FABRICATION OF NANO-PATTERN LIBRARIES AND THEIR APPLICATIONS IN MODE-SELECTIVE SERS

A Dissertation

by

ZHI ZHAO

Submitted to the Office of Graduate Studies of
Texas A&M University
in partial fulfillment of the requirements for the degree of

DOCTOR OF PHILOSOPHY

Chair of Committee,	Paul S. Cremer
Committee Members,	David H. Russell
	Dong Hee Son
	Igor Lyuksyutov
Head of Department,	David H. Russell

August 2013

Major Subject: Chemistry

ABSTRACT

Patterned arrays of metallic nanostructures are commonly used in photonics, electronics, as well as functional materials and biotechnology because of their unique electronic and optical properties. Although great effort has been devoted to the development of nano-patterning techniques in the past decades, there are still existing challenges for nano-fabrication to achieve fine resolution and complex features over macroscopic areas in a reasonable time period. Herein, we devise two versatile patterning strategies, namely indentation colloidal lithography (ICL) and oblique colloidal lithography (OCL), for the stepwise patterning of planar substrates with numerous complex and unique designs. Those strategies combine colloidal self-assembly, imprint molding in conjunction with capillary force lithography and reactive ion etching, all of which are simple and straightforward.

Hexagonal arrays of symmetric and nonconcentric gold features are fabricated on glass substrates with highly controllable geometric parameters. The width, size and asymmetry of each surface structure could be tuned down to the ~10 nm level while the scale of the patterned area could exceed 1 cm^2. Moreover, our technique also leads to the ability to develop an enormous variety of patterns through stepwise amplification of feature types. In particular, some of the features are fabricated for the first time, including target-triangle, hexagram, hexagram-dot and triangle-dot. Distinctive surface plasmon resonance (SPR) properties, such as higher order surface plasmon modes and Fano resonances are both observed from our patterns, which would be highly desired for

the study of plasmonic coupling. In addition, we have demonstrated a surface orientation dependent Raman selectivity on two nano-structures for the first time. Molecular vibrations with opposite symmetries can be selectively enhanced on different substrates. As a demonstration, this property is applied to the odd-even effect of n-alkanethiol self-assembly monolayers (SAMs) on the gold surface. The alternative alternation of the intensity ratios of two vibration pairs have been shown by surface enhanced Raman spectroscopy (SERS) as a function of the number of carbon atoms. The results obtained exhibit high sensitivity and excellent agreement with previous publications.

ACKNOWLEDGEMENTS

I would like to thank my committee chair, Dr. Cremer, and my committee members, Dr. Russell, Dr. Son and Dr. Lyuksyutov, for their guidance and support throughout my Ph.D. study.

Thanks also go to my friends and colleagues and the department faculty and staff for making my time at Texas A&M University a great experience. I also want to extend my gratitude to the Welch foundation and Norman Hackerman Advanced Research Program, which provided the research funding and instrumentation.

Finally, thanks to my mother and father for their encouragement and to my wife for her patience and love.

NOMENCLATURE

4-ATP	4-Aminothiolphenol
AAA	Annular aperture arrays
AFM	Atomic force microscope
CFL	Capillary force lithography
CL	Colloidal lithography
DAR	Disk and the antibonding ring dipolar plasmon
DBR	Disk and bonding ring dipolar plasmon
DMAB	4,4'-Dimercaptoazobenzene
e	Eccentricity
EBL	Electron beam lithography
F	Force
FDTD	Finite difference time domain
FEM	Finite element modeling
FIB	Focused ion beam lithography
FOM	Figure of merit
FR	Fermi resonance
FWHM	Full width at half maximum
ICL	Indentation colloidal lithography
IR	Infrared
LSPR	Localized surface plasmon resonance

NIR	Near-infrared
OCL	Oblique colloidal lithography
PDMS	Polydimethylsiloxane
PL	Photolithography
PML	Perfect matched layer
PS	Polystyrene
PSPR	Propagating surface plasmon resonance
RI	Refractive index
RIE	Reactive ion etching
SAM	Self-assembly monolayer
sccm	Standard cubic centimeter per minute
SERS	Surface enhance Raman spectroscopy
SFG	Sum frequency generation
SPR	Surface plasmon resonance
T_g	Glass transition temperature

TABLE OF CONTENTS

LIST OF FIGURES

LIST OF TABLES

CHAPTER I

INTRODUCTION AND LITERATURE REVIEW*

Patterned arrays of metallic nanostructures are commonly used in photonics,[1, 2] electronics,[3] as well as functional materials[4] and biotechnology[5-11] because of their unique electronic and optical properties. Much of this behavior results from surface plasmons, which represent the collective oscillation of conducting electrons on metal surfaces.[11] Multiple modes of surface plasmons, including localized surface plasmon resonance (LSPR) and propagating surface plasmon resonance (PSPR), can be tuned in metal films as a function of structural and chemical properties. As a result, specific geometries and architectures are chosen and optimized for each application. For example, structures that are rich in edges or sharp crevices are believed to be useful for surfaced enhanced Raman spectroscopy by providing a greater number of hot spots.[12, 13] By contrast, the period and size of surface features are more essential for optical applications which require a precise match between external excitation fields and surface plasmon modes.[14, 15] The ability to create a library of surface structures through a combinatorial patterning technique would be highly desirable for screening the most efficient structures for a given individual purpose.

---

*Part of the data reported in this chapter is reprinted with permission from "Stepwise Molding, Etching, and Imprinting to Form Libraries of Nanopatterned Substrates" by Zhao,Z.; Cai, Y.; Liao, W.; Cremer, P. S., 2013. *Langmuir*, 29, 6737-6745, Copyright [2013] by American Chemical Society.

nanoscale platforms. This includes, among others, colloidal lithography, photolithography, soft lithography and scanning beam lithography approaches.[16] The advantage of these methods is that they afford high reproducibility and good control over surface morphology. Despite their success, there are still substantial barriers for achieving very fine scale structures and complex designs over macroscopic areas in a reasonable time period. In principle, it is possible to fabricate almost any arbitrary feature with 10 nm resolution or better with the help of electron beam lithography (EBL)[17-19] and focused ion beam lithography (FIB).[20] Nevertheless, the amount of time and cost rises tremendously as the patterned area increases and the features become more complex. By contrast, more rapid methods, such as photolithography (PL)[21] readily allow for the fabrication of complex structures over large areas, but have more difficulty producing very small objects due to the diffraction limit. Patterning methods including colloidal lithography (CL)[22, 23] and soft lithography[24] generally meet the resolution, large area, cost and time requirements. However, the types of features which can easily be produced are typically much more limited. As such, CL and soft lithography approaches are often combined with PL or EBL in order to fabricate fine surface features,[25-28] although some of the inherent disadvantages remain in place.

To expand the variety of architectures which can be inexpensively and rapidly fabricated, additional methods need to be pursued that can provide both large area patterning and small feature sizes. One idea would be to employ a step-wise or combinatorial approach for creating large libraries of patterns. The key is to incorporate steps that do not require PL, EBL and FIB and, therefore, don't reduce the resolution or

require specialized facilities and high costs. As a step toward realizing this goal, we introduce an indentation colloidal lithography method to create complicated architectures in a polydimethylsiloxane (PDMS) template through a combination of self-assembly, molding, and reactive ion etching (RIE). By integrating PDMS templating with capillary force lithography (CFL), a large number of patterns could be generated in a polystyrene (PS) layer. An even greater variety of Au features could then be generated by tuning the time employed for oxygen plasma etching of the PS layer, which was followed by wet chemical etching to transfer the pattern to an underlying thin Au film. By doing this, dots, triangles, circles, lines and related patterning units could be formed individually or in combination with each other. Each surface element could be tuned from the micron scale to well below the 100 nm level, while the size of the patterned area was about 1 cm^2.

The collective oscillation of conducting electrons supported by metallic surface is known as surface plasmons.[11] Local electromagnetic field of metallic structures will be significantly enhanced at the frequency of surface plasmon resonance (SPR), which depends on the chemical and geometric characters of nanostructures. Great benefit has been demonstrated in photonics,[1, 2] electronics,[3] as well as functional materials[4] and biotechnology[5-10, 12] with the application of plasmonic devices. Specifically, sensitive, label free detection of molecules has been proposed by measuring the shift of SPR frequencies or intensities of certain types of nano-structures.[29,30] The major advantages of SPR sensors include their short response time, easy to miniaturize and being able to detect both non-aqueous and aqueous samples.[31] People have already demonstrated

several SPR sensor designs based on metallic structures, including aggregation of nanoparticles,[32] nano-hole array[33] and nanorods.[34] Despite the demonstration of these methods, the limit of detection for SPR sensors, which is determined by the value of figure of merit (FOM), is still lower than the satisfied level as compared to other sensing technologies such as fluorescence based techniques, microcantilevers and electrochemical methods.[35]

FOM is defined as:

$$FOM = \frac{\Delta\lambda_{peak}}{\mathrm{FWHM}}$$

in which $\Delta\lambda_{peak}$ is the shift of plasmonic resonance frequency per refractive index (RI) unit and FWHM is the full width at half maximum for the corresponding plasmonic peak.[35] Current value of $\Delta\lambda_{peak}$ is typically in the range from hundreds of to a couple of thousands of nanometers per RI unit while most FWHM is equal to hundreds of nanometers.[32-36] As a result, the corresponding limit of detection is typically around a few nM for most current SPR sensors.[35] In order to improve the limit of detection, either a narrower peak width or a greater RI sensitivity is required.

Recently, the fabrication and unique SPR properties of asymmetric patterns have been shown by several research groups.[37-39] Nano-systems will benefit from the break of symmetry in terms of getting more spectrally observable oscillations. It is well known that the plasmonic resonance could be classified as either light modes or dark modes according to their coupling efficiency with the excitation beam.[40] Compared to the light mode, the charge distribution in dark mode SPR possesses a center of symmetry and has

no net charge separation, which eliminates its coupling with light.[41] For most of the cases, the center of the charge distribution is also the geometric center of the nano-feature. Therefore, it is possible to create a net charge separation through the break of structural symmetry. The excitation of more than a single SPR mode increases the number of bands that could be applied in sensing applications. This kind of multi-frequency optics is of highly importance for the spectroscopic characterization and phase imaging of materials which exhibit distinctive absorption or spectral characters at multi-frequencies.[42, 43]

One of the most attractive characters of asymmetric structures is the possession of Fano resonance. Fano resonance is a special type of plasmonic coupling phenomenon with a distinctly asymmetric profile which originates from the constructive and destructive interference of a narrow discrete resonance with a broad spectral line or continuum.[44] The presence of Fano resonance requires the break of symmetry in plasmonic systems.[45] The presence of Fano resonance can now be found experimentally in plasmonic materials and metamaterials.[37, 38, 46] Compared to the typical bright SPR modes, Fano resonance owns a much narrower peak width and response to environmental changes more sensitively, which are ideal for high-FOM-value sensors. Therefore, asymmetric features are taken as a promising candidate in the design of ultra-sensitive biosensors. Cetin et al. has demonstrated that, for example, a FOM value of 72 was reached in nonconcentric ring-disk system which is tens of times higher than average.[47] As a result, more attention has been attracted to the fabrication of asymmetric plasmonic structures for sensing purpose. In addition, other optical behaviors including

plasmon induced transparency[48] and polarization dependent transmittance[37] are revealed for Fano resonances which are promising to be integrated in optics and electronics.[49]

The majority of asymmetric substrates are fabricated by electron beam lithography (EBL)[17-19] owing to the requirement of a decent morphology control. In particular, all the non-concentric plasmonic structures can only be created by EBL at present. While it is possible to fabricate almost any arbitrary feature with 10 nm resolution or better by EBL, the time and cost for making patterns rises tremendously as the patterned area increases and the features become more complicated. Therefore, there are still existing challenges for finding out alternative techniques to achieve fine resolution and complex features over macroscopic areas in a reasonable time period. Colloidal lithography (CL)[22, 50] is a simple, cost-effective method that generally meets the resolution, large area, cost and time requirements. Numerous structures, such as disks,[51, 52] circular rings,[53−56] triangles,[22] and crescents[57] have been generated at nanoscale using spherical colloids as templates. Nevertheless, CL lacks the ability of a precise control over the surface symmetries for the reason that the structure of colloidal template is fixed and hard to change.

As a step toward, we demonstrate a strategy to overcome the problems in asymmetric nano-feature fabrication and generate libraries of symmetry breaking features with large scale, high resolution and low cost. A new technique named oblique colloidal lithography (OCL) is developed to fabricate PDMS templates with asymmetric contours which allow us to create nonconcentric polymer features. A decent structural control over surface units is realized by reactive ion etching, imprinting molding as well

as capillary force lithography. By conducting a wet chemical etching, each polymer feature is able to be transferred onto a metal film, thus enables the fabrication of plasmonic structures. The advantage of this technique also lies in that the stepwise patterning procedure offers magnifications of pattern variety. Multiple types of features are able to be created from a single starting structure by applying slightly different experimental conditions. Consequently, an exponential magnification of feature variety is observed in our patterning strategy which greatly contributes to the number of systems that could be applied for developing plasmonic theory and applications.

Optical measurements are the most common approaches to characterize surface plasmon resonance among which extinction spectroscopy and reflection spectroscopy are two of the most popular techniques.[11, 58] Extinction is defined as the absorption and scattering of electromagnetic radiation by matter between an emitting object and the observer. The magnitude of extinction could be used to quantify how light is lost when passing through an object. It has been well known both theoretically and experimentally that plasmonic structures possess several peaks and dips in extinction spectrum.[59-65] Besides material and geometric dependence, the profile of extinction spectra is also determined by the refractive index of surrounding medium.[29, 36] In particular, a functional expression of relationships between SPR and the medium has already been obtained for a couple of simple metallic structures, including nano-hole arrays[59-61, 63] and annular aperture arrays.[62] The profile of extinction spectra plays an essential role in the understanding of quantum mechanics of plasmonic structures.[45, 65] The shape, location and magnitude of plasmon resonances could also provide insights into the coupling

between surface units. Therefore, the measurement of extinction spectra for nano-features is of great importance.

Raman scattering is the inelastic scattering of photons and was discovered in 1905 by C. V. Raman.[66] The Raman scattered light is sensitive to the vibrational structure of a molecule and has been widely applied in chemical analysis. However, the typical molecular Raman cross section is only about 10^{-30} to 10^{-25} cm^2,[67] which limits its further application in the detection of low concentration species. Surface-enhanced Raman spectroscopy (SERS) was discovered at 1977 by using silver electrode in the Raman detection.[68, 69] The enhancement of signal is mainly coming from the local electromagnetic field generated by SPR yet is also influenced by several other factors, including chemical enhancement and charge transfer.[70] Strong signal enhancement up to 10^{15} has been observed in SERS, which greatly extends the potential area of application for Raman spectroscopy.[71, 72] Till now, SERS has been applied as a noninvasive and sensitive tool for chemical,[72,73] material,[74] biological,[75] and pharmaceutical[76] applications. One of the most attractive characteristics of SERS lies in its potential for detecting single molecules.[72] As a type of Raman spectroscopy, SERS possesses the ability to obtain vibrational spectra from adsorbates.[72-76] Consequently, it provides chemically specific information for analytes and is compatible with biomolecular studies.[75]

Despite such advantages, there is still considerable concern about the reproducibility of SERS spectra. It is widely thought that the major source of SERS signal comes from molecules in a few hot spots where the electric fields are significantly

larger than at other locations.[77] The origin of hot spots is usually believed to involve edges or sharp crevices between adjacent metallic structures.[12] As a result, fractals and metal nanoparticle assemblies are often used as high efficiency SERS substrates to exploit the gaps between their nanoscale features.[13, 78] The challenge, of course, is to obtain repeatable signals from these randomly assembled structures, since the topology of the hot spots may vary from sample to sample. Therefore, efforts to fabricate metal structures in a more reproducible fashion are drawing increasing attention. Another factor that affects the reproducibility of SERS lies in the intrinsic mechanism that contributes to signal enhancement. It is widely accepted that signal enhancement could be reached through electronic enhancement, chemical enhancement and charge transfer processes which will be both molecule and substrate dependent.[70] Consequently, the Raman profile may change dramatically when a variant in substrate, excitation light or other conditions changes.[79-82]

In the past, we showed a strategy to fabricate libraries of patterned nano-structures on the surface.[83] The main advantage of our technique is that it offers high reproducibility and good control over the surface morphology with a low time and money cost. Therefore, the films we created should be ideal for high reproducibility SERS measurements and the investigation of the relationships between the surface morphology and Raman signal.

The selectivity of Raman spectra has been demonstrated by several researches.[79-82] Nevertheless, no investigation has been carried out in the study of Raman selectivity on various surface patterns. Herein, we demonstrate a detailed study on surface

morphology dependence of SERS spectra. The model molecule 4-ATP is test on various substrates to investigate the relative intensity change of each vibrational mode as a function of surface morphologies. The results have shown that by varying the surface structure, a selective enhancement of either perpendicular or tangential resonance could be individually achieved. Simulations have demonstrated that the origin of this phenomenon comes from the orientation difference of local E-field on various nano-patterns. To the best of our knowledge, this is the first example of a surface morphology dependent Raman selection. In addition, this mode-selective SERS is extremely sensitive to the orientations of molecular vibrations and should be ideal to examine structures of analytes absorbed on the surface.

Odd-even effect is a widely existed phenomenon in nature. Generally, it describes an alternative alteration of material structures and/or properties depending on the odd or even number of structural units in a molecule.[84] One of the most frequently studied system of odd-even effect is the SAM of functionally terminated alkyl molecules on silver or gold substrates. Nearly 30 years ago, Nuzzo and Allara discovered that when gold was immersed in a dilute organosulfur solution, an uniform monolayer was spontaneously chemisorbed on the surface of the gold, producing a self-assembled monolayer.[85] Such coatings are promising to be used in corrosion inhibition,[86] lubrication,[87] and organic sensors.[88] During the past few decades, numerous experiments have been carried out to characterize n-alkanethiol SAMs on gold surface. Their structures[89-98] as well as physical and chemical properties, such as contact angle,[89] electrical resistances[96] and ionization efficiencies[97] have been carefully examined. The

major characterization approaches involve scan probe microscopy,[90, 95] electrochemical techniques,[93, 97] electron diffraction[94] and optical techniques, such as ellipsometry,[93, 98] infrared spectroscopy,[89, 93] Raman spectroscopy[91] and SFG.[92] Among others, several experiments have revealed the chain-length dependence of the properties of n-alkanethiol SAMs due to odd-even effect.[89, 93, 95-98]

Compared to scan probe microscopy or electron diffraction techniques,[90, 94, 95] vibrational spectroscopy is of low cost and compatible with bio-samples because of its non-invasive nature. Recently, more effort has been put on investigating odd-even effect by IR, SFG and Raman spectroscopy.[89, 93, 99, 100] In all cases, the signal intensity varies alternatively according to the change of methylene numbers in the alkyl chains, which clearly demonstrates the influence of odd-even effect on molecular vibrations. The study of odd-even effect by vibrational spectroscopy, however, faces some intrinsic problems in obtaining a good contrast between odd and even SAMs. For example, the absorbent difference between odd and even n-alkanethiols in IR is only about 10^{-4},[89, 93] which is neither easy to detect nor good enough to rely on. Also, the intensity of SFG signals varies only 0.1 to 0.2 from odd to even n-alkanethiols. This could be mainly attributed to a surface lack of structural selectivity. Indeed, typical substrates in vibrational spectroscopies are aimed at the detection of universal resonances and not able to provide satisfied results on structural specific applications. Therefore, it is necessary to find a way that can introduce structural selectivity when measuring spectra from odd and even n-alkanethiol SAMs. The determination of molecular conformation by SERS has been briefly proposed in which the intensity ratio of two vibrational modes of know spatial

relation is used to establish the orientation of a surface spices based on the assumption that the electromagnetic enhancement is predominant.[100] However, there are a few disadvantages of this method which prevents its wide application. This technique obtains SERS information from a single metallic surface. Further comparison between the SERS spectrum and solid Raman spectrum from pure analyte has to be carried out before any structural information could be concluded, which increases the amount of analyte required. In addition, the selectivity of a single SERS substrate is still relatively low for the discrimination of molecular conformations.

To solve the problems mentioned above, we proposed a protocol which could provide the structural information of SAMs through mode-selective SERS. Odd and Even carbon n-alkanethiols are simultaneously examined on two nano-patterned substrates with known SPR properties. As mentioned previously, by creating some distinctive local E-field, resonances with different orientations could be selectively enhanced on corresponding nano-patterns. This is extremely useful in odd-even systems because it is highly responsive to the molecular orientation on the surface. We demonstrate here that the alternative relative intensity alterations of two orthogonal vibrational pairs with known spatial relations are clearly observed on our SERS substrates. Two opposite trends are revealed on different nano-features which could be readily predicted by simulations based on electromagnetic enhancement. The results well match previous studies yet are more sensitive. Relative intensity ratio change up to a factor of 2 is recorded. We believe this technique could also be applied in other fields where structural information is required by a highly sensitive and non-invasive method.

CHAPTER II

EXPERIMENTAL SECTION*

2.1 Fabrication of symmetric nano-pattern libraries

2.1.1 Formation of the polystyrene sphere monolayer

PS beads of certified size standards were purchased from Duke Scientific Corporation with diameters of 400 nm, 800 nm and 2 μm. The beads were centrifuged five times with copious amounts of water to remove surfactants and other impurities that were present from the manufacturer. They were then re-dissolved in purified water (Barnstead nanopure water system, 18 MΩ/cm resistivity). The concentration of PS spheres was maintained at 4×10^7/ μL for all sizes. Triton X-100, laboratory grade, was purchased from Sigma-Aldrich. PS bead suspensions were mixed with a 0.1% (volume percentage) Triton X-100 solution in a 4:1 ratio to yield a final surfactant concentration of 0.020 vol%. PDMS molds were made by mixing Sylgard 184 silicone elastomer with 10 wt. percent of the Sylgard 184 curing agent. The mixture was then cured at 70 °C for 3 hours. Before introducing the aqueous PS sphere suspension, the PDMS surface was treated with an oxygen plasma for 15 s to increase its hydrophilicity. The PDC-32G plasma cleaner/ sterilizer was from Harrick Plasma (Ithaca, NY).

---

*Part of the data reported in this chapter is reprinted with permission from "Stepwise Molding, Etching, and Imprinting to Form Libraries of Nanopatterned Substrates" by Zhao,Z.; Cai, Y.; Liao, W.; Cremer, P. S., 2013. *Langmuir*, 29, 6737-6745, Copyright [2013] by American Chemical Society.

2.1.2 PDMS templates

A March CS-1701 reactive ion etcher was used to create PDMS templates. To do this, a PDMS film coated with a monolayer of PS spheres was exposed to a carbon tetrafluoride (CF_4)/oxygen (O_2) plasma at 270 W in the reactive ion etcher for varying time periods. The total flow rate of the etchant was kept at 40 standard cubic centimeters per minute (sccm) while the etchant composition was varied for creating various pillar spacings. After treatment, the PS spheres were removed from the PDMS surface by sonication first in toluene followed by acetone and water. Toluene was bought from EMD and acetone was purchased from Fisher Scientific. Both were ACS grade. PDMS template was heated under 130 °C for 30 min to further remove any absorbed solvent before use.

2.1.3 Polystyrene and Au features

Glass slides (VWR, No. 2 micro cover slides) were treated with piranha solution to remove organics from the surface. This solution was a 3:1 mixture of sulfuric acid (EMD, ACS grade) and hydrogen peroxide (Acros Organics, 35%) (caution: piranha solutions are extremely corrosive, reactive, potentially explosive and need to be handled with care in a fume hood). The glass slides were then washed with water and baked in an oven (Orton, Sentry Xpress 2.0) at 500 °C for 5 hours. A 50 nm-thick Au layer (Alfa Aesar, 99.999%) was thermally evaporated onto the glass slides using a 5 nm-thick chromium layer as an adhesive. This was done in a BOC Edwards metal evaporator (Auto 360). Polystyrene powder (Scientific Polymer, M.W. =97400) was first dissolved in toluene and then spin-coated onto the planar Au surface using a WS-400B-6NPP/ LITE spin coater (Laurell Techonologies Corporation). The spinning rate was set to

3000 rpm/min, while the concentration of the PS solution was tuned between 5 mg/mL and 50 mg/mL depending on the thickness of the PS film which was desired. Detailed parameters for this setup can be found in Table 2.

The PDMS template was placed on a polymer layer and an iron block was used to adjust the applied pressure. The applied pressure was set to ~7.9×10^3 Pa by placing an 80 g iron block on a 1 cm×1 cm PDMS mold. Next, the system was annealed at 130 °C for time periods ranging from 30 min to 1 hr and then cooled back to room temperature in air. After peeling away the PDMS layer, the nascently formed polymer features were treated in an oxygen plasma to completely remove the thinnest portions of the PS film. The power of the RIE was set to 60 W and the oxygen flow rate was 20 sccm, which initially corresponded to a removal rate of 2 nm/s. Finally, the whole chip was immersed in a mixture of 50 mM iron nitrate (Alfa Aesar, 98+%) and 50 mM thiourea (Alfa Aesar, 99%). After removing the unprotected Au, the chip was rinsed with purified water and treated with chromium etchant 1020AC (Transene Company Inc.) for 1 min to dissolve the exposed chromium. The remaining PS layer was removed by toluene before each gold feature was examined by AFM (Digital Instrument, multimode scanning probe microscope) in tapping mode to explore the surface topography.

2.2 Fabrication of non-concentric nano-pattern libraries

2.2.1 Oblique colloidal lithography

Polystyrene beads of certified size standards were purchased from Duke Scientific Corporation with diameters of 2 μm. The beads were centrifuged five times

with copious amounts of water to remove surfactants and other impurities that were present from the manufacturer. They were then re-dissolved in purified water (Barnstead nanopure water system, 18 MΩ/cm resistivity). The concentration of PS spheres was maintained at 4×10^7/ μL. Triton X-100, laboratory grade, was purchased from Sigma-Aldrich. PS bead suspensions were mixed with a 0.1% (volume percentage) Triton X-100 solution in a 4:1 ratio to yield a final surfactant concentration of 0.020 vol%. Polydimethylsiloxane (PDMS) molds were made by mixing Sylgard 184 silicone elastomer with 10 weight percent of the Sylgard 184 curing agent. The mixture was cured at 70 °C for 3 hours. Before introducing the aqueous PS sphere suspension, the PDMS surface was treated with an 18 W oxygen plasma for 15 s to increase its hydrophilicity. The PDC-32G plasma cleaner/ sterilizer was from Harrick Plasma (Ithaca, NY). The PDMS substrate was tilted by inserting a PDMS wedge of desired size under one of its edges. Two tilted angle, namely 5° and 10° were applied in the follow experiments which were measured the by a protractor.

2.2.2 PDMS templates

A March CS-1701 reactive ion etcher was used to create PDMS templates. To do this, a PDMS film coated with a monolayer of PS spheres was exposed to a CF_4/oxygen plasma at 270 W in the reactive ion etcher for varying time periods. The total flow rate of the etchant was kept at 40 standard cubic centimeters per minute (sccm) while the etchant composition varied for creating different surface morphologies. After treatment, the polystyrene spheres were removed from the PDMS surface by washing with toluene and acetone. Toluene was bought from EMD and acetone was purchased from Fisher

Scientific. Both were ACS grade. The cleaned PDMS template was incubated at 130 °C for 30 mins in order to remove any remaining solvent.

2.2.3 Polystyrene and Au features

Glass slides (VWR, No. 2 micro cover slides) were treated with piranha solution to remove organics from the surface. This solution was a 3:1 mixture of sulfuric acid (EMD, ACS grade) and hydrogen peroxide (Acros Organics, 35%) (caution: piranha solutions are extremely corrosive, reactive, potentially explosive and need to be handled with care in a fume hood). The glass slides were then washed with water and baked in an oven (Orton, Sentry Xpress 2.0) at 500 °C for 5 hours. A 50 nm-thick Au layer (Alfa Aesar, 99.999%) was thermally evaporated onto the glass slides using a 5 nm-thick chromium layer as an adhesive. This was done in a BOC Edwards metal evaporator (Auto 360). Polystyrene powder (Scientific Polymer, M.W. =97400) was first dissolved in toluene and then spin-coated onto the planar Au surface using a WS-400B-6NPP/ LITE spin coater (Laurell Techonologies Corporation). The spin rate was set to 3000 rpm/min, while the concentration of the PS solution was tuned between 5 mg/mL and 25 mg/mL depending on the thickness of the PS film which was desired.

The PDMS template was placed on a polymer layer and an iron block was used to adjust the applied pressure. The applied pressure was set to ~7.9×10^3 Pa by placing an 80 g iron block on 1 cm×1 cm PDMS mold. Next, the system was annealed at 130 ℃ for one hour and then cooled to room temperature in air. After peeling away the PDMS layer, the nascently formed polymer features were treated in an oxygen plasma to completely remove a desired portion of the PS film. The power of the RIE was set to 60

W and the oxygen flow rate was 20 sccm, which initially corresponded to a removal rate of 2 nm/s. Finally, the whole chip was immersed in a mixture of 50 mM iron nitrate (Alfa Aesar, 98+%) and 50 mM thiourea (Alfa Aesar, 99%). After removing the unprotected Au, the chip was rinsed with purified water and treated with chromium etchant 1020AC (Transene Company Inc.) for 1 min to dissolve the exposed chromium. The remaining PS layer was removed by toluene before each gold feature was examined by AFM (Digital Instrument, multimode scanning probe microscope) in tapping mode to explore the surface topography.

2.3 Extinction spectra of nano-features

2.3.1 Extinction spectroscopy

Extinction spectra in visible-NIR range were recorded by a Hitachi 4100 UV-vis-NIR spectrometer. Glass slides (VWR, No. 2 micro cover slides) were treated with piranha solution to remove organics from the surface. This solution was a 3:1 mixture of sulfuric acid (EMD, ACS grade) and hydrogen peroxide (Acros Organics, 35%) (caution: piranha solutions are extremely corrosive, reactive, potentially explosive and need to be handled with care in a fume hood). The glass slides were then washed with water and baked in an oven (Orton, Sentry Xpress 2.0) at 500 °C for 5 hours before used as references in spectral measurements. Each spectrum was recorded from 400 nm to 3000 nm at the speed of 750 nm/min in 850 nm to 3000 nm region and 600 nm/min for wavelengths below 850 nm. Optical silt was fixed at 2 nm below 850nm and auto-changed in 850 nm to 3000 nm region to achieve an optimized sensitivity.

The incident angle dependence of extinction spectra was measured by varying the orientation of the nano-patterns. To do this, PDMS wedges with different angles were made by mixing Sylgard 184 silicone elastomer with 10 weight percent of the Sylgard 184 curing agent in glass molds. The mixture was cured at 70°C for 3 hours and wedges with 15°, 30°, 45°, 60° and 75° angles were fabricated. Each wedge was stuck under the nano-patterned chip to achieve a desired incident angle. In order to investigate the effect of polarization on the non-concentric nano-features, a polarizer was inserted in the light path in front of the sample.

2.3.2 Surface morphology measurement

Each extinction spectrum was correlated with its surface morphology to investigate the geometrical dependence of SPR. To do this, the measured region was first checked under an Olympus BX 41 microscope to determine the uniformity of certain area. A 50x object was used and the lateral resolution was about 1 μm. Each area with good quality was labeled on the back. Next, the label region was explored by tapping mode AFM (Digital Instrument, multimode scanning probe microscope) to acquire the surface morphology data.

2.3.3 Simulations

Commercial software FDTD Lumerical 7.5.3 had been used to calculate extinction spectra of nano-features. Periodic boundary condition was set in the x-y plane and Perfect Matched Layer (PML) boundary condition was applied in the z direction to eliminate numerical artifacts at the simulation boundary. The nanostructures' material is Palik Gold. Semi-infinite silica substrate was applied just below the gold nanostructures.

The minimum repeat cell for each periodic array was defined as the simulation domain and a polarized incident plane wave was defined in accordance with the experimental incidence angle. The electric field of the polarized light was defined in such a way that its orientation is parallel to the deviation of the inner disk. Next, the transmitted field was solved by using Stratton-Chu formula. The procedure was repeated over a set of wavelengths to compile a full scattering spectrum.

2.4 Mode-selective SERS

2.4.1 Fabrication of patterned SERS substrates

The detailed method is published in previous article.[83] Generally, polystyrene beads with diameters of 2 μm were cleaned and dispersed in a 0.020 vol% Triton X-100 solution. This suspension was then deposited on a PDMS surface. Next, The PS sphere coated PDMS surface was exposed to a CF_4/oxygen plasma at 270 W in the reactive ion etcher for varying time periods. After treatment, the polystyrene spheres were removed from the PDMS surface by washing with toluene and acetone.

A 50 nm-thick Au layer (Alfa Aesar, 99.999%) was thermally evaporated onto glass slides using a 5 nm-thick chromium layer as an adhesive. Polystyrene powder (Scientific Polymer, M.W. =97400) was first dissolved in toluene and then spin-coated onto the planar Au. The PDMS template was placed on the polymer layer and annealed at 130 ℃ for 1 hr before cooled to room temperature in air. After peeling away the PDMS layer, the nascently formed polymer features were treated in an oxygen plasma to completely remove a desired portion of the PS film. Finally, the whole chip was

immersed in a mixture of 50 mM iron nitrate (Alfa Aesar, 98+%) and 50 mM thiourea (Alfa Aesar, 99%) to conduct a wet chemical etching.

2.4.2 Extinction spectroscopy

Extinction spectra in visible-NIR range were recorded by a Hitachi 4100 UV-vis-NIR spectrometer. Glass slides (VWR, No. 2 micro cover slides) were treated with piranha solution to remove organics from the surface. This solution was a 3:1 mixture of sulfuric acid (EMD, ACS grade) and hydrogen peroxide (Acros Organics, 35%) (caution: piranha solutions are extremely corrosive, reactive, potentially explosive and need to be handled with care in a fume hood). The glass slides were then washed with water and baked in an oven (Orton, Sentry Xpress 2.0) at 500 °C for 5 hours before used as references in optical measurements. Each spectrum was recorded from 400 nm to 3000 nm at the speed of 750 nm/min in 850 nm to 3000 nm region and 600 nm/min for wavelengths below 850 nm. Optical silt was fixed at 2 nm below 850nm and auto-changed in 850 nm to 3000 nm region to achieve an optimized sensitivity.

2.4.3 Surface preparation procedures in SERS measurements

Each patterned gold substrate was first sonicated in pure ethanol (200 proof, KOPTEC) for 5 min followed by a sonication in purified water (Barnstead nanopure water system, 18 MΩ/cm resistivity) in order to removed absorbed organic and inorganic contaminations. After dried in air, the chip was then cleaned in a 60 W oxygen plasma (March CS-1701 reactive ion etcher) for 50 s to remove any remaining contaminations. The oxygen flow was set at 20 sccm while the pressure was 80 mTorr for the system. After that, the chip was immediately immersed into pure ethanol for 20 min to reduce

the oxygen containing gold layer generated by plasma etching. Each substrate was tested by Raman spectrometer under the same conditions used in sampling to make sure that no residue was left. No peak is observable in phenyl ring vibrational region (1000 cm^{-1} to 1600 cm^{-1}) or C-H stretching region (2800 cm^{-1} to 3100 cm^{-1}) after the cleaning procedure.

2.4.4 Mode-selective surface enhanced Raman spectroscopy

4-aminothiolphenol (4-ATP, 97%) was purchased from Alfa Aesar. Solutions containing 100 μM 4-ATP were made by dissolving the solid in pure ethanol. 1-octanethiol (≥98.5%), 1-decanethiol (96%), 1-tetradecanethiol (≥98%), 1-pentadecanethiol (98%) and 1-hexdecanethiol (99%) were purchased from Aldrich. 1-heptanethiol (98%) was purchased from SAFC. 1-nonanethiol (98%) was purchased from Alfa Aesar. 1-undecanethiol (>95.0%) was purchased from TCI-EP. 1-dodecanethiol (98%) was purchased from Acros. N-tridecyl mercaptan was purchased from Pfaltz & Baner. Solutions of n-alkanethiols were prepared by dissolving each pure n-alkanethiols in pure ethanol. The concentration was 10 mM for all the analytes. Cleaned gold chips were dipped into the solution overnight. A self-assembly monolayer (SAM) of thiol terminated molecules was spontaneously absorbed onto the gold features during this process. Next, Each chip was washed with copious amounts of ethanol to remove unbound molecules and dried in air before data collection. Raman spectroscopy was performed using a Horiba Jobin-Yvon LabRam IR system with a linearly polarized 633 nm laser. SERS spectra of 4-ATP were recorded with a 1.91 mW 633 nm laser for nine cycles with 60 s collection times for each cycle. SERS spectra of n-alkanethiols

were recorded with a 4.02 mW 633 nm laser for nine cycles with 60 s collection times for each cycle.

2.4.5 Simulations of molecular orientations and surface plasmon resonance

Commercial software FDTD Lumerical 7.5.3 had been used to calculate extinction spectra of nano-features. Periodic boundary condition was set in the x-y plane and Perfect Matched Layer (PML) boundary condition was applied in the z direction to eliminate numerical artifacts at the simulation boundary. The nanostructures' material is Palik Gold. Semi-infinite silica substrate was applied just below the gold nanostructures. The minimum repeat cell for each periodic array was defined as the simulation domain and a polarized incident plane wave was defined in accordance with the experimental incidence angle. The electric field of the polarized light was defined in such a way that its orientation is parallel to the asymmetry. Next, the transmitted field was solved by using Stratton-Chu formula. The procedure was repeated over a set of wavelengths to compile a full scattering spectrum.

Theoretical data for molecular vibrations were calculated numerically using commercial finite element modeling (FEM) software (COMSOL Multiphysics 4.2 with the 3D RF module).

CHAPTER III

RESULTS AND DISCUSSION*

3.1 Stepwise molding, etching and imprinting to form libraries of nano-patterned substrates

Our patterning procedure consisted of consecutive colloidal lithography and reactive ion etching steps. To do this, a flat PDMS substrate was cured at 70 °C for 3 hours. It was then rendered partially hydrophilic in an O_2 plasma and used immediately. Next, a monolayer of polystyrene (PS) spheres was assembled via deposition from an aqueous suspension onto the planar PDMS surface.[101-103] The spheres had a diameter of 2 μm and formed a closely packed hexagonal monolayer on the surface upon evaporation of the water solution (Fig. 1A). This process typically took ~2 hours. It should be noted that a close packed self-assembled monolayer of PS spheres on PDMS has not been previously demonstrated. These experimental conditions represented a significant modification of deposition techniques previously employed to deposit PS spheres on glass or silicon substrates.[104, 105] Specifically, the production of PDMS surfaces of intermediate hydrophobicity was the key to forming a high quality self-assembled colloidal sphere monolayer. Moreover, the introduction of 0.020 vol% triton X-100 to the deposited aqueous droplet facilitated the formation of a uniform single

---

* Part of the data reported in this chapter is reprinted with permission from "Stepwise Molding, Etching, and Imprinting to Form Libraries of Nanopatterned Substrates" by Zhao,Z.; Cai, Y.; Liao, W.; Cremer, P. S., 2013. *Langmuir*, 29, 6737-6745, Copyright [2013] by American Chemical Society.

monolayer. For these experiments, a contact angle for water of ~40 degrees with the PDMS worked well. To obtain this degree of hydrophobicity, the elastomeric substrate was treated in an 18 watt O_2 plasma for 15 sec with the initial O_2 pressure of 0.1 bar.

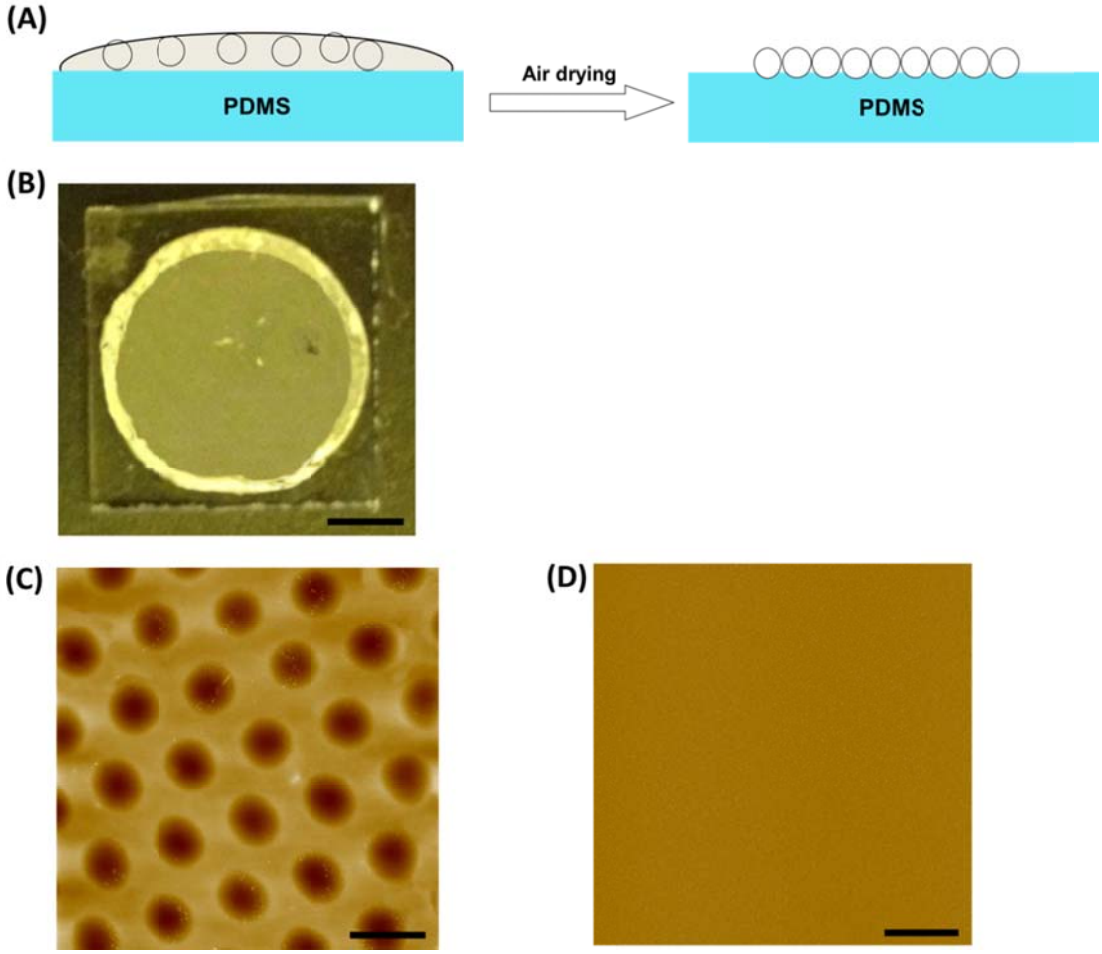

Figure 1. (A) Schematic diagram for forming a PS sphere monolayer. (B) An optical image of the self-assembled PS sphere layer on PDMS. Scale bar: 2 mm. (C) A tapping mode AFM image of the PDMS surface after removal of the PS sphere monolayer in which the PDMS is cured for 24 h at 70 °C. Scale bar: 2 μm, (D) An AFM image of the PDMS surface after removal of the PS sphere monolayer whereby the PDMS is cured for only 3 h at 70 °C. Scale bar: 2 μm. (C) and (D) are in the same height scale.

When the PDMS surface was made more hydrophobic, it led to colloidal multilayer formation. By contrast, when it was made more hydrophilic, increasing disorder in the colloidal array was found. The area that could be patterned with PS spheres depended on the total volume of the liquid solutions that was introduced onto the PDMS surface. In particular, a coating with an approximately 1 cm diameter could be made by introducing a 30 μL volume solution. An optical image of the dried film is shown in Figure 1B. As can be seen, the film was thicker near the rim, but otherwise a single monolayer was achieved.

The colloidal sphere layer created a dimple array in the underlying PDMS substrate when left in contract with the substrate overnight. To demonstrate this, the PS spheres could be removed and the substrate subsequently imaged. Removal was performed by sonication in a bath with a 50/50 volume mixture of acetone and water for 1 min. The PDMS slab was then washed with water and dried in flowing nitrogen. AFM imaging revealed that an array of dimples was formed in the PDMS surface (Fig. 1C). If we employed PDMS that was cured at 70 °C for 24 hours instead of 3 hours and kept other conditions the same, no dimple array pattern was found after sonication (Fig. 1D). As such, it is believe that uncross-linked PDMS strands are keys to forming the dimples by molding around the PS spheres after assembly. Also, this molding process did not occur immediately as removal of the colloidal array by sonication only a few minutes after the self-assembly process was completed did not leave the dimple pattern behind.

A simple calculation was carried to demonstrate the mechanism for this indentation of PDMS surface based on material mechanics. The surface profile of PDMS

after the removal of PS spheres was monitored by AFM (Fig. 2). The figure clearly showed that the surface was indented by PS spheres. From the measured depth and width of each indent, it is easy to find out that the profile of each dimple didn't follow the contour of the PS sphere. Consequently, we could rule out the possibility that the dimples were generated by the polymerization of PDMS oligomers around the PS spheres. Next, we assumed that the surface feature was created during an elastic contact between PDMS and PS sphere. In this case, the PDMS was treated as an elastomer and no adhesion between the two materials was taken into consideration. Assume the PS-PDMS system followed the Hertz contact model for non-adhesive elastic contact (Fig. 3), the contact area and the applied force could be correlated by the following equations:

$$F = \frac{4}{3} E^* R^{1/2} d^{3/2} \quad (1)$$

where F is the applied force, R is the radius of an elastic sphere, d is the displacement of the elastic half space under the presence of F and E* is the combined elastic moduli which can be expressed by the equation below:

$$\frac{1}{E^*} = \frac{1-\nu_1^2}{E_1} + \frac{1-\nu_2^2}{E_2} \quad (2)$$

E_1, E_2 and ν_1, ν_2 are the elastic moduli and the Poisson's ratios associated with each body, respectively. The value of Young's modulus for PS and PDMS is 2.66 MPa and 3.25 GPa, respectively[106, 107] and the Poisson's ratios is 0.33 for PS and 0.5 for PDMS.[108] The forced applied on each sphere (F) was a summation of its gravity and the pressure from the top solution. The pressure could be estimated by assuming that the added solution (30 μL) was extended into a column with a 1 cm diameter.

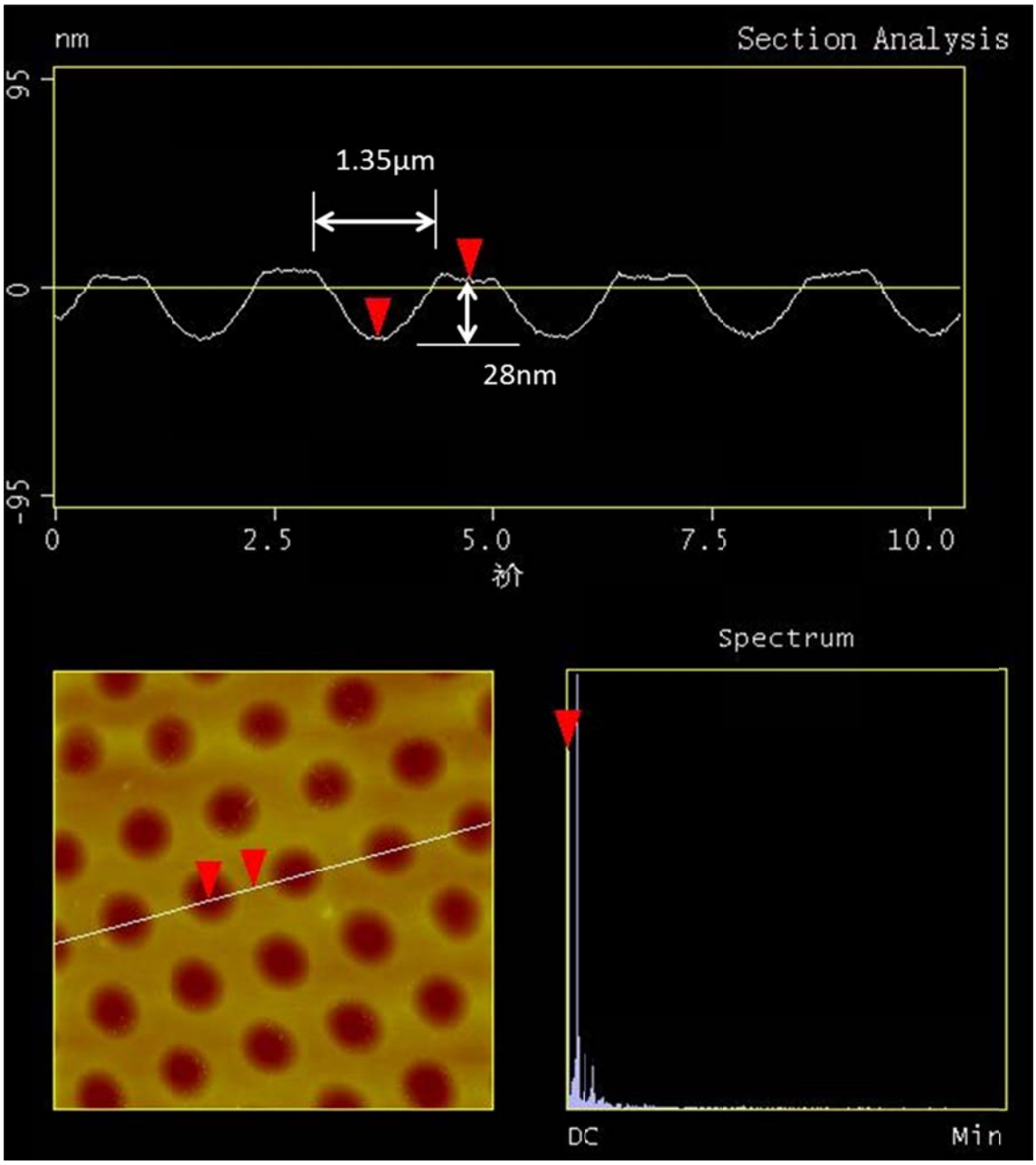

Figure 2. Tapping mode AFM image of the morphology and corresponding cross section of the indented PDMS surface.

By replacing the parameters in equation (1) and (2), we could figure out that the combined elastic moduli of PDMS is 1.9×10^3 Pa, which was significantly smaller than typical bulk Young's modulus of PDMS cured for 3 hours.[108] This indicated that the surface layer of PDMS hadn't fully cross-linked during the contact with PS spheres. As a result, its mechanical strength was significantly lower compared to the bulk PDMS which made it possible to create dimples at the PDMS surface simply by a colloidal assembly process. The formation of dimples was probably caused by the crosslinking of uncured surface PDMS molecules under the effect of elastic contact between PS sphere and PDMS. The external force induced a redistribution of surface PDMS molecules and their new positions would be fixed after the long time incubation.

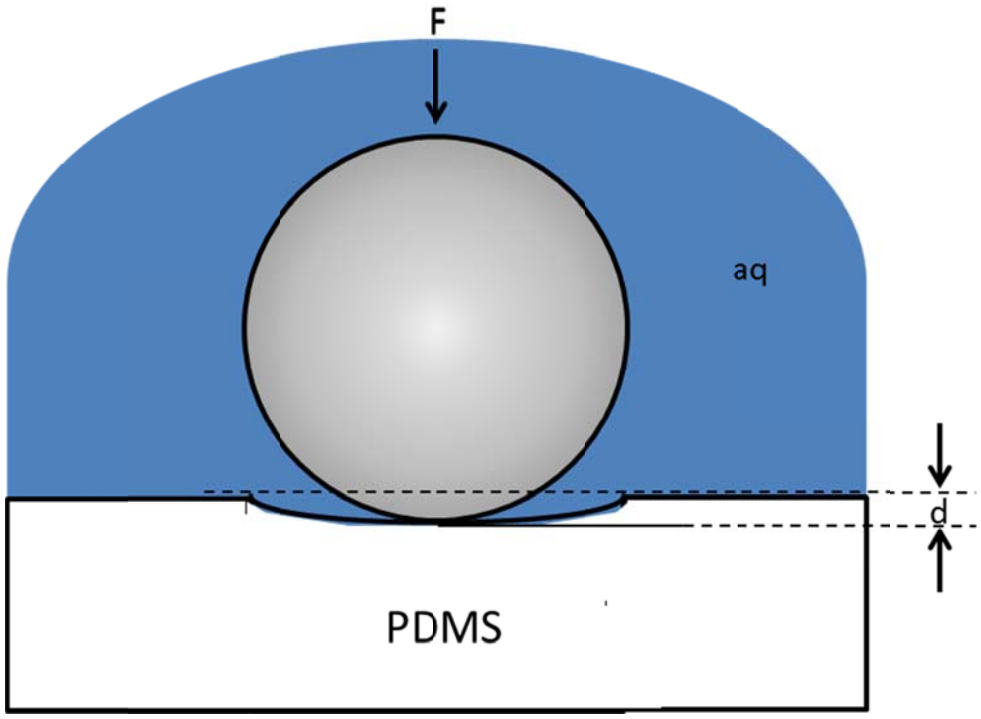

Figure 3. A proposed mechanism for the PDMS indentation based on the Hertz contact model.

In a next step, a PS sphere-covered PDMS substrate was subjected to plasma etching (Fig. 4A). The etchant in the RIE procedure consisted of 39:1 mixture of CF_4 and O_2.[109] The total flow rate was 40 standard cubic centimeters per minute (sccm) at a pressure of 80 mTorr. Etching was conducted for 30 sec with a 270 W plasma. It should be note that only the PDMS surface that was not shielded by the PS spheres was etched, which corresponded to the area under the three-fold hollow site of PS sphere SAM (Fig. 4B). The reactivity of PDMS and PS are quite different for these two gasses. The Si-O backbone of PDMS (Fig. 4C) primarily reacted with F•, while the PS was relatively stable in F•.[109, 110] As a result, a hexagonal array of pillars was formed. A schematic view of this process was shown in Figure 5A. After the pattern was formed, the PS spheres were dissolved with toluene and the PDMS template was cleaned by acetone and water. An optical image of the entire substrate after this procedure is shown in Figure 5B. The sample could then be imaged microscopically by AFM. This revealed that an array of PDMS pillars was formed (Fig. 5C). The hexagonal pillar array was characterized by the height of the PDMS pillars (H), the depth of the indent on top of the pillars (h), the width of the pillars at half height (d) and the periodicity of the pillar array. The period was determined by the original size of PS spheres, while all the other parameters could be tuned in a very broad range by controlling the RIE time, O_2 concentration, and the size of the PS spheres.

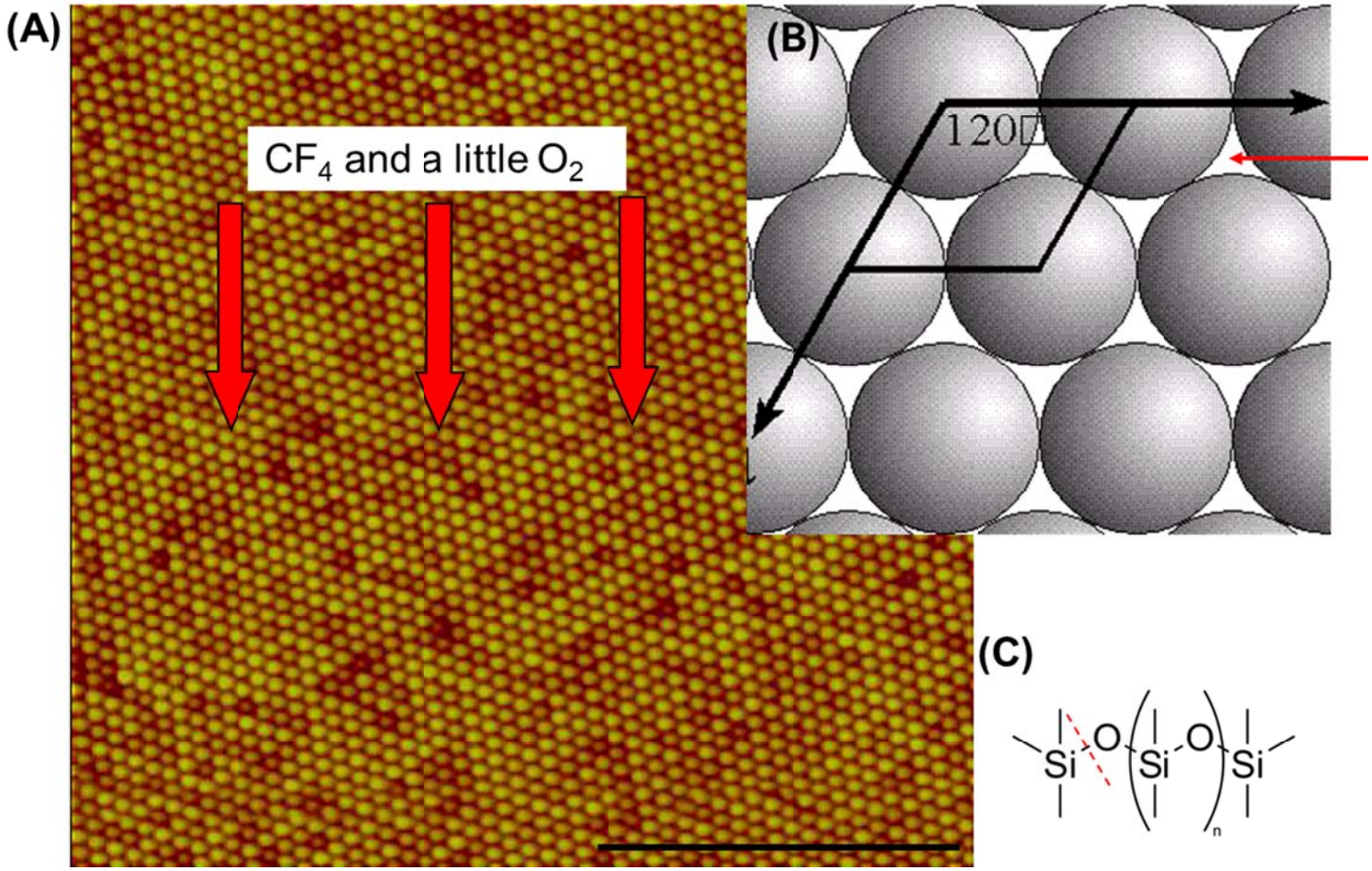

Figure 4. (A) AFM image of a self-assembly monolayer of PS spheres. Scale bar: 2 μm, (B) A schematic view of the PS sphere SAM and the three fold hollow site, (C) The structure of the Si-O backbone in PDMS.

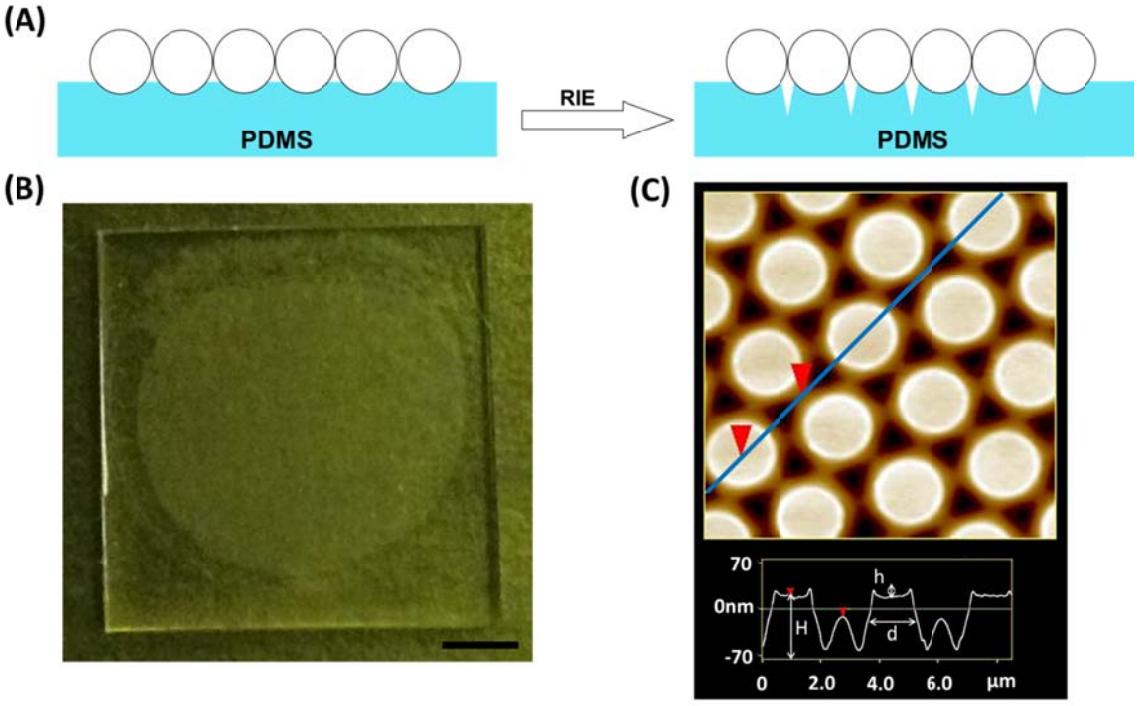

Figure 5. (A) Schematic diagram of the binary reactive ion etching step. (B) An optical image of the PDMS template after RIE and removal of the PS sphere monolayer. Scale bar: 2 mm, (C) A representative view of the surface of the PDMS template with a height profile shown beneath it.

The relative amount of O_2 was the most essential parameter for tuning the features of the pillar array (Fig. 6). Indeed, varying the concentration of O_2 drastically changed the morphology of the PS sphere mask. As is well known, the C-C backbone of PS can be etched quickly in oxygen.[111] As a result, we could partially oblate the PS spheres by adding more oxygen to the etchant gas. This served to uncover more of the PDMS surface. Depending on the etching conditions, the PS sphere diameter could be tuned to leave the spheres touching or widely separated. Since the underlying PDMS

substrate was simultaneously being etched by CF_4 (and to a lesser extent by O_2), the resulting pattern in the underlying substrate would change. The total flow rate of etchant was kept constant at 40 sccm at a total pressure of 80 mTorr under all conditions. AFM images of the surface topography of the patterned PDMS surface after etching with various O_2 to CF_4 ratios and etching times are shown in Figure 6. The images were taken after subsequent removal of the PS spheres by dissolving them with toluene. As can be seen, increasing the ratio of O_2 to CF_4 (left to right) created more room between the pillars. On the other hand, increasing the time of plasma etching create deeper valleys in the PDMS (bottom to top images).

A hexagram pattern was formed in the three-fold hollow sites between the locations of the PS spheres under conditions where the O• concentration was relatively low. This can be seen by the dark triangular regions in the lower left-hand image (green arrow). As the oxygen ratio was increased, the etching rate of the spheres increased relative to that of the PDMS substrate. This led to bridge-shaped dips descending between adjacent spheres. As a result, the height difference between the top of the pillars and the top of the bridges became larger as the etching time increased. Moreover, the triangular regions became deeper and the diameter of the spherical pillars became smaller as the etching time was increased under all conditions. Depending on the plasma etching time, the pillars in the PDMS templates could be defined as well separated (type I), closely separated (type II) or overlapping (type III) based on the interpillar separation. This classification is reflected in the top, middle, and bottom rows of images in Figure 6, respectively.

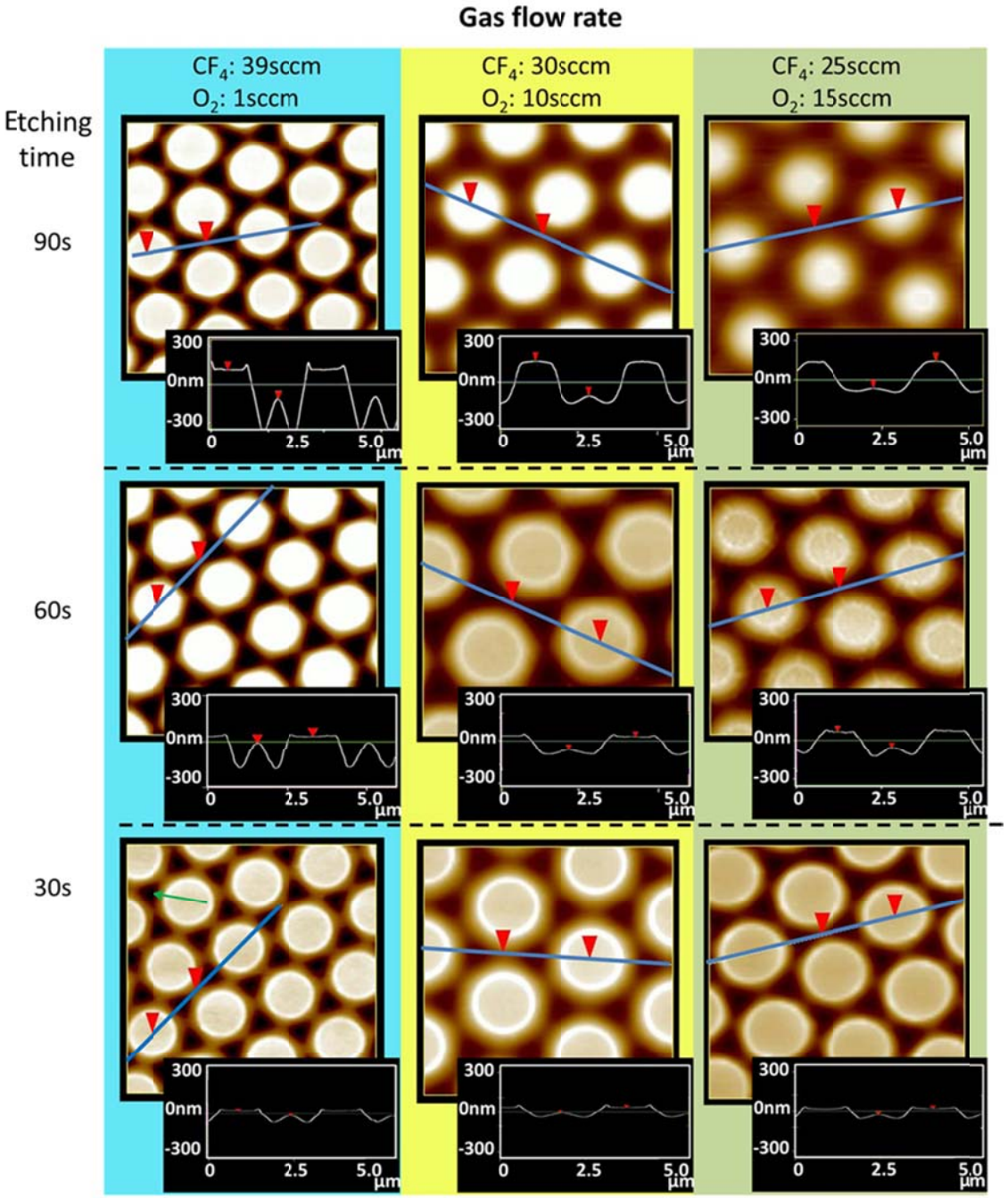

Figure 6. AFM images and line profiles of the PDMS molds with various O_2 to CF_4 ratios and etching times. A three-fold hollow site is pointed out in the lower-left image by a red arrow. The red triangles in each image denote positions along the line profile over the blue line. Each line profile is displayed as an inset.

Next, the patterned PDMS substrates were used to create arrays of complex nanoscale features in both PS and Au thin films. The system used for these experiments consisted of a 10 to 50 nm PS layer, which was spin coated onto a 50 nm thick Au layer on a planar glass substrate. An intervening 5 nm Cr layer was used to wet the Au onto the glass (Fig. 7A). It was worthwhile to note that each PDMS template was washed with both water and organic solvents before applied in the following steps (see experimental section). As a result, no PS or Triton X-100 should leave on the surface and affect the patterning.

The PS layer was patterned first by capillary force lithography.[112] To do this, the PDMS mold was placed onto a polystyrene-coated planar glass substrate. An iron block was placed on top of the mold to ensure close contact between the mold and the polymer as well as to adjust the pressure applied to the substrate. The whole system was then heated for a fixed period of time at 130 ºC, which was above the glass transition temperature (T_g) of PS.[113] PS features were formed as the polymer melt climbed up the walls under the influence of capillary forces.[114, 115] As the temperature rose above the T_g, the PS layer was melted and accumulated around the edge of the PDMS pillars. This kind of capillary rise was mainly driven by the surface tension as the initial contact angle between the PDMS walls and the PS layer was 90°, which is far from contact equilibrium.[114, 115]

Distinct patterns in the PS layer could be generated by changing the pillar spacing (Fig. 7B), varying the heating time and the PS layer thickness (Fig. 7C). For example, when the width of capillary rise was smaller than the gap (g) between adjacent

PDMS pillars (type I), circular rings were generated (Fig. 7B, left). The PS film employed here was ~20 nm thick and a heating time of 30 minutes was used. If the gap between the pillars was reduced to a range that was comparable to the size of the PS features (type II template), connected structures such as hexagrams were formed in the PS surface (Fig. 7B, middle). The film thickness in this case was 12 nm for optimized overlap. Finally, if only a small portion of the three-fold hollow site was etched (type III), triangular hexagram structures were formed using 10 nm thick PS films (Fig. 7B, right). The red outlines in Figure 7B denote filling regions into which PS material would flow around the circular pillars (gray). Specifically, those three conditions corresponded to PS patterns in Figure 8A, 8B and 8C, respectively.

As noted above, the PS film thickness was a critical parameter with a greater capillary rise occurring for thicker films. For example, if one increased the PS film from 20 to 30 nm and kept other parameters identical, nanowells were generated instead of rings for Type I conditions (Fig. 8D). Indeed, the thicker PS film more completely filled the voids in the template compared with Figure 8A. Similarly, hexagonal wells were formed by using a type II template and a 15 nm PS film (Fig. 8E vs. Fig. 8B). Such differences, however, were smaller with type III features as the void space in the PDMS molds was considerably smaller (Fig. 8F vs. 8C).

In addition to the patterns described above, it was found that the heating time of the PS layer also played an important role. In fact, a central dimple could be introduced by increasing this time to ~1 h from ~30 min under otherwise identical conditions. This is shown in Figure 8G-8I, which correspond to Figure 8A, 8B, and 8C, respectively.

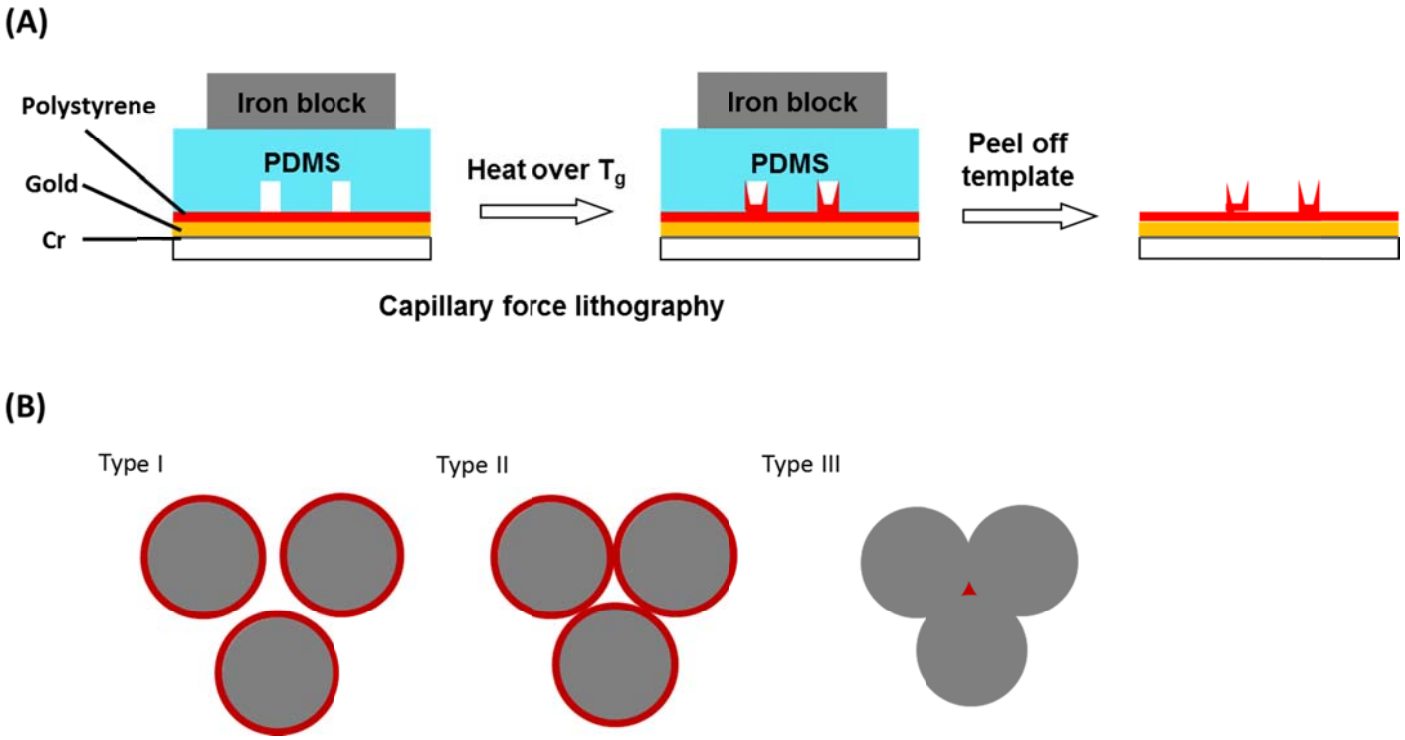

Figure 7. (A) A schematic diagram of the layered substrate used in capillary force lithography and the procedure for creating PS patterns. (B) Schematic diagrams of the three types of spacings for the PDMS pillars. (C) Schematic diagrams showing the influence of PS film thickness (in red) and annealing times on the PS film structures that are obtained. Left: features formed by using a thinner film with a 30 min. annealing time; middle: formed by using a thicker film with a 30 min. annealing time; right: features formed by using a thinner film with a 60 min. annealing time.

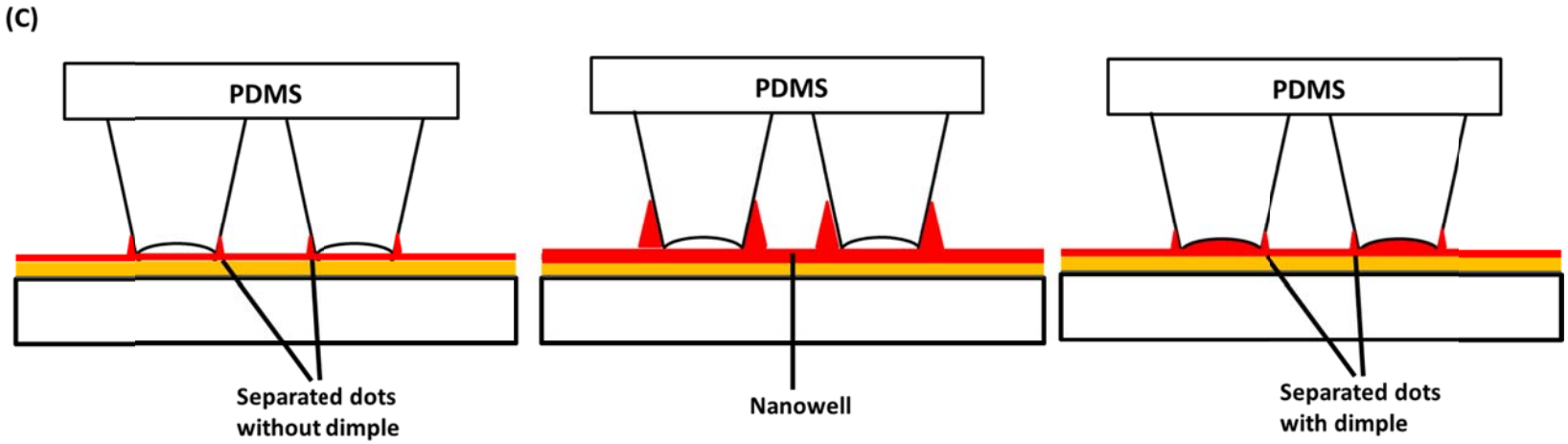

Figure 7. continued.

Apparently, PS was initially excluded from rising into the indented portion of the pillars over the first 30 minutes of the capillary rise process. After 60 minutes, however, the polymer melt filled this region too. This time dependent annealing feature may be related to gas trapped between the top of the PDMS pillars and the PS layer that initially prevents dimple formation. The influence of both film thickness and heating time on the molding of PS features is illustrated schematically in Figure 7C.

Finally, the PS patterns could also be transferred into an underlying Au layer. This was done by treating the PS pattern with an oxygen plasma for a fixed amount of time in order to expose the desired parts of the metal layer. Then, the chip was immersed into a 1:1 (volumetric) mixture of 50 mM ferric nitrate and 50 mM thiourea to conduct a wet chemical etch. After removal of the exposed Au, the chip was treated with chromium etchant for 1 minute to dissolve the subsequently exposed chromium adhesion layer beneath the Au film. Finally, the chip was washed with toluene and copious amounts of acetone and deionized water to remove the polymer layer.

In order to faithfully transfer the polymer features into the Au film, the plasma etching time was carefully controlled so that only the planar portions of the polymer layer were removed, while leaving the raised areas behind. This was done by adjusting the plasma etching time. The plasma etching speed was approximately 2 nm/s under our conditions. Therefore, the amount of PS that was ultimately removed was easy to control. The resulting Au layer patterns are shown in Figure 9. Each image in the three by three array corresponds to its PS template in Figure 8. For example, Figure 9A was obtained by using the PS pattern in Figure 8A. As can be seen, a rich variety of Au

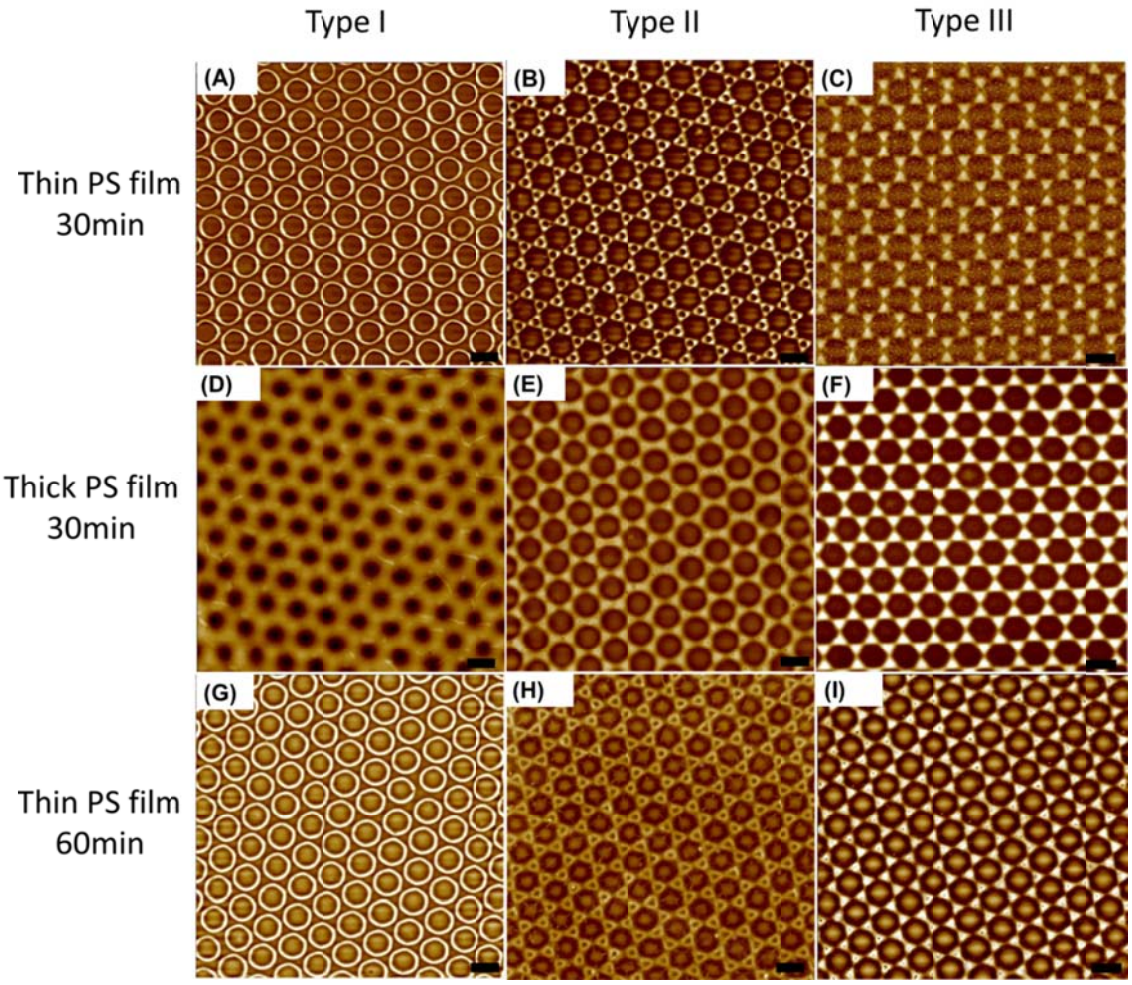

Figure 8. Various PS patterns obtained by adjusting the PS film thickness and annealing time. Scale bars: 2 μm.

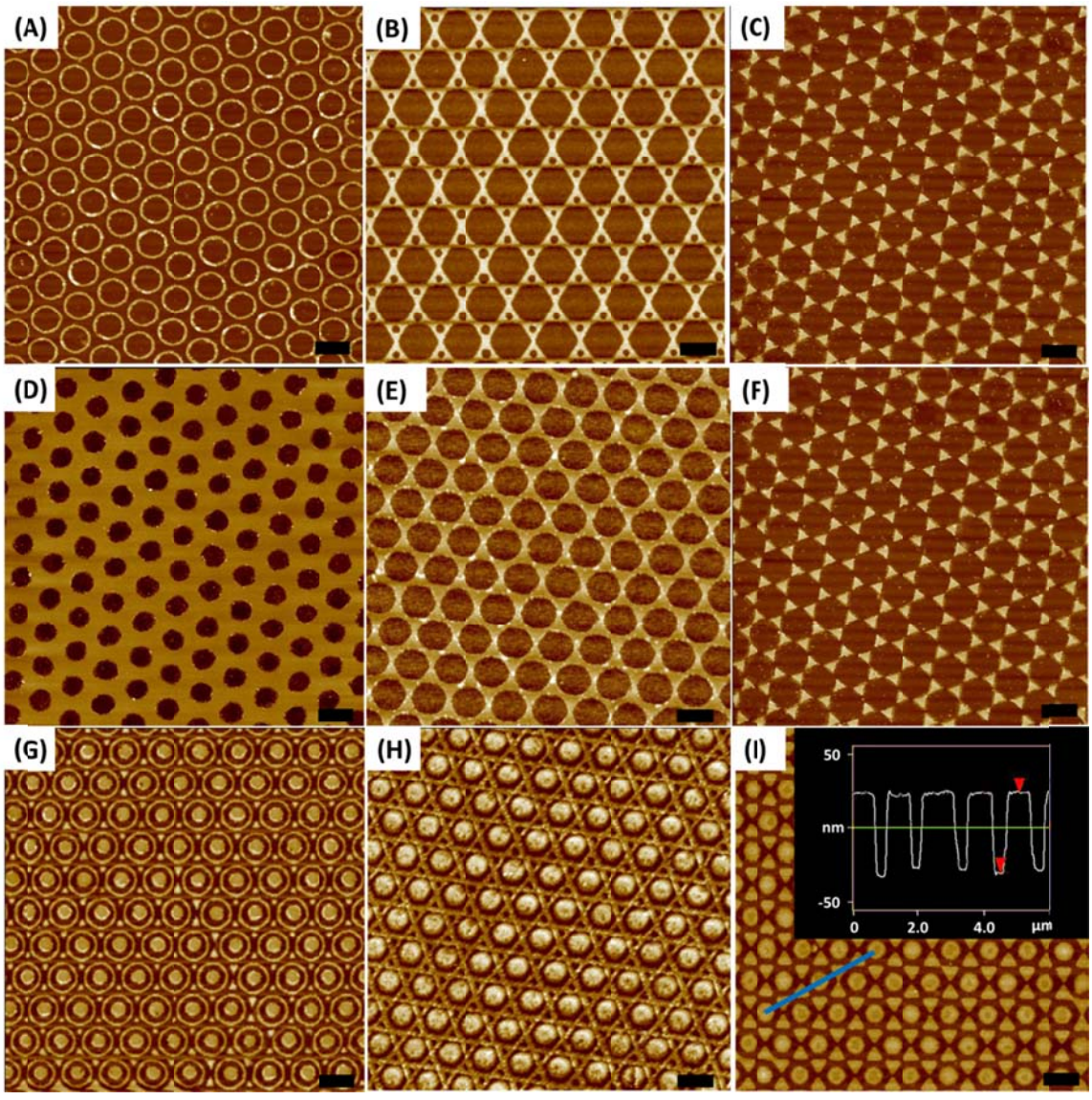

Figure 9. Au nanopatterns created from the respective PS templates in Figure 5. (A-H) various gold features. Scale bars: 2 µm. (I) triangle-dot gold feature. The height information of the region under blue line is displayed in the inset. Scale bar: 2 µm.

patterns can be created. This includes rings, triangles, targets, wells, lines, and complex combinations of these features. Many of these large scale Au patterned elements should be unique to this patterning method, including the hexagonal web (Fig. 9B), the targets surrounding by triangles (Fig. 9G) and hexagonal web with dots (Fig. 9H). The height of gold features shown here is equal to 55 ± 5 nm, which was obtained from AFM measurements and demonstrated typically in Figure 6i. This number is coincident with the total thickness of deposited gold (50 nm) and Cr (5 nm) layers.

It is also possible to develop an even richer array of Au patterns by varying the etching time of the PS film. For example, the removal of some of the raised portions of the PS pattern can be achieved by over-etching. As a result, the gold patterns can have different topologies from the original PS templates. Figure 10 shows three distinct Au patterns made from the same PS template by varying the plasma etching time. The original PS pattern was composed of three moieties with different heights: small triangular dots, dimples, and ring structures. The triangles were thinnest, while the rings were the tallest features as shown by a line scan of the PS template (Fig. 10, top image and corresponding line scan). Using a minimum etching time (10 sec), all features were preserved in the Au layer including the small triangles, while a longer etching time left just the rings (20 sec). An intermediate etching time (15 sec) removed the small triangles, but not the center dot (Fig. 10, three lower images, left to right). Exact details for the etching times and other fabrication conditions are provided in Table 1. The height of gold features shown here is equal to 55 ± 5 nm. The corresponding patterning conditions for PS features can be found in Table 2.

Table 1. Patterning conditions for each type of gold feature

pattern	corresponding PS pattern	etching time by RIE	etching time by wet etching method
9A	8A	40 s	12 min
9B	8B	15 s	10 min
9C	8C	15 s	12 min
9D	8D	>30 s	15 min
9E	8E	20 s	15 min
9F	8F	20 s	12 min
9G	8G	10 s	7 min
9H	8H	15 s	7 min
9I	8I	15 s	12 min
10 (left)	8G	10 s	7 min
10 (middle)	8G	15 s	12 min
10 (right)	8G	20 s	12 min
12D	12A	30 s	10 min
12E	12B	15 s	7 min
12F	12C	20 s	11 min

Table 2. Patterning conditions for each type of polymer feature

Pattern[a]	polystyrene film thickness	time heated[b]	template fabrication condition
8A	<20 nm	30 min	CF_4 35 sccm, O_2 5 sccm, 270 W etch 60 s
8B	12 nm	30 min	CF_4 35 sccm, O_2 5 sccm, 270 W etch 50 s
8C	10 nm	30 min	CF_4 35 sccm, O_2 5 sccm, 270 W etch 40 s
8D	>30 nm	30 min	CF_4 35 sccm, O_2 5 sccm, 270 W etch 60 s
8E	15 nm	30 min	CF_4 39sccm, O_2 1 sccm, 270 W etch 60 s
8F	>10 nm	30 min	CF_4 35 sccm, O_2 5 sccm, 270 W etch 40 s
8G	<20 nm	60 min	CF_4 35 sccm, O_2 5 sccm, 270 W etch 60 s
8H	12 nm	60 min	CF_4 35 sccm, O_2 5 sccm, 270 W etch 50 s
8I	15 nm	60 min	CF_4 35 sccm, O_2 5 sccm, 270 W etch 60 s

Table 2. continued

Pattern[a]	polystyrene film thickness	time heated[b]	template fabrication condition
12A	10 nm	30 min	CF_4 39 sccm, O_2 1 sccm, 270 W etch 55 s
12B	10 nm	60 min	CF_4 39 sccm, O_2 1 sccm, 270 W etch 45 s
12C	10 nm	60 min	CF_4 39 sccm, O_2 1 sccm, 270 W etch 40 s

[a] The patterns are listed according to the figure number in which they appeared.

[b] The temperature was 130 ℃.

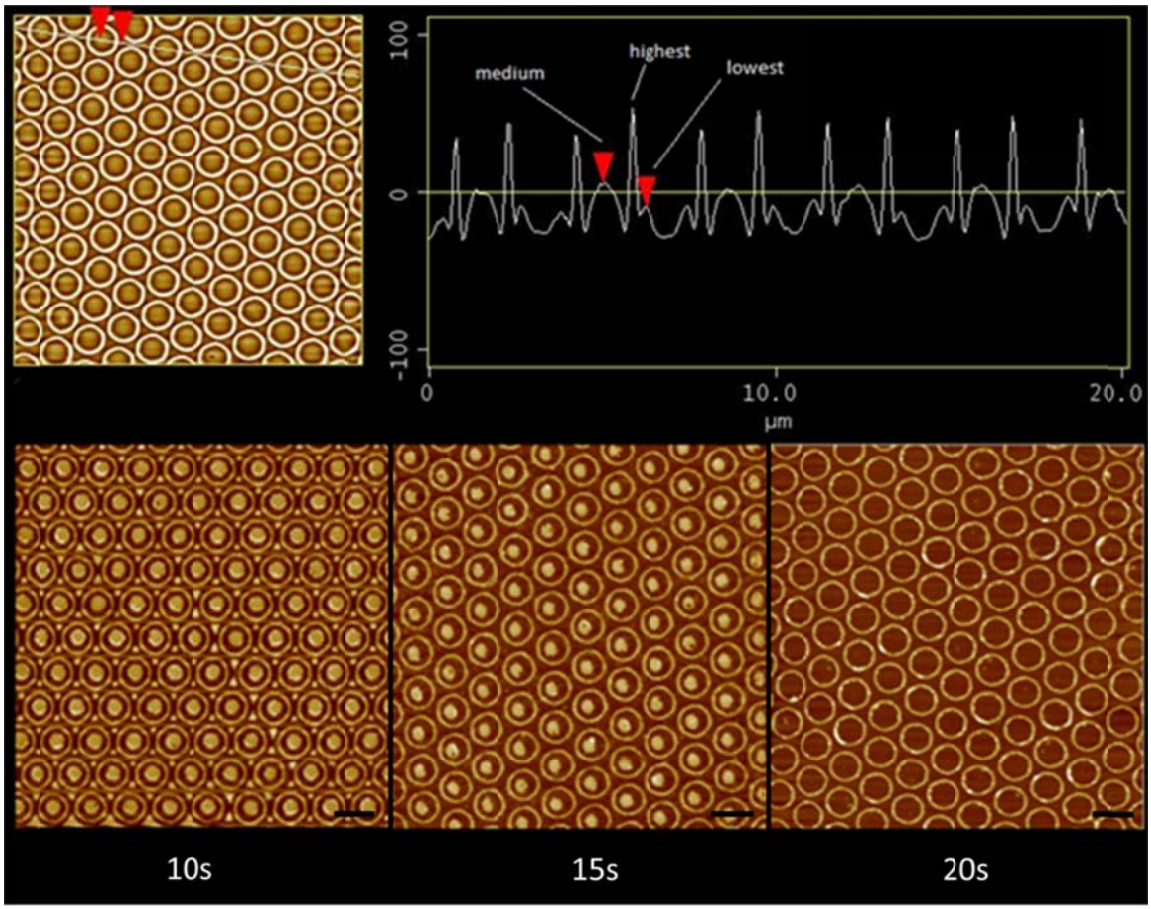

Figure 10. Three Au patterns (bottom row) fabricated from the same PS template (upper-left image) by control of the etching time in RIE. The etching time is listed under each image. The period for the patterns is 2 μm and a line profile is shown next to the PS template. Scale bars: 2 μm.

The most significant advantage of our method is that one can make a very large variety of patterns. A branching tree is provided to summarize the conditions for creating specific motifs (Fig. 11). In fact, the ability of our method to fabricate different feature types and patterns in Au is even greater than what is shown here. Indeed, since the RIE gas composition, plasma etching time, capillary force lithography time, PS film thickness, and Au etching time can each be controlled separately, a very large library of distinct features can be formed. Moreover, the patterning method described above was performed with 2 micron colloidal spheres. The size of these spheres, of course, can be varied as well to change the element size and spacing. In fact, we have repeated these methods with 800 nm and 400 nm PS spheres. In the latter case, the line widths of the PS features were about 35 nm (Fig. 12). Again, the height of gold features shown here is equal to 55 ± 5 nm. Theoretically, spheres down to 100 nm in diameter were still able to be deposited on PDMS surface. However, this would require extremely tricky conditions.

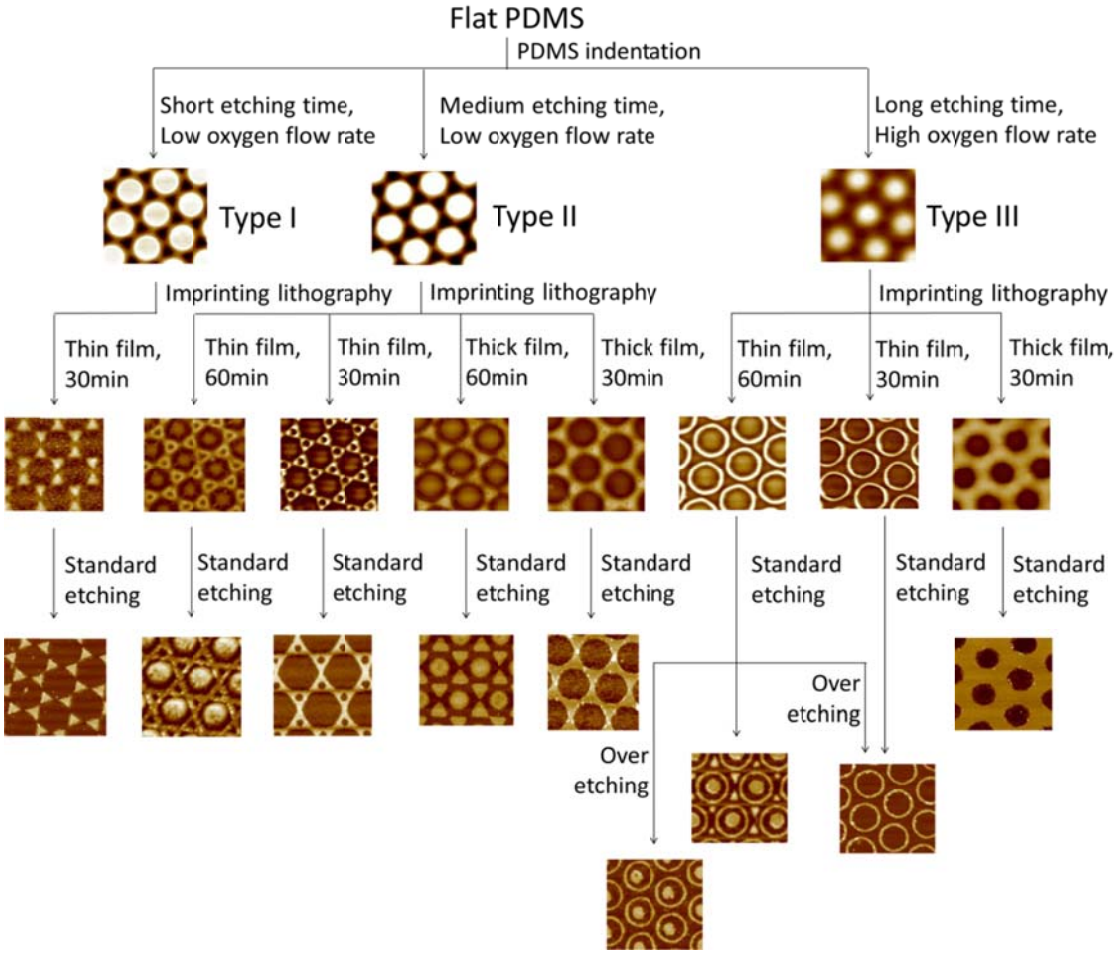

Figure 11. A branching tree guide to the strategies employed for fabricating various Au pattern motifs by the stepwise templating method. All patterns shown here are of 2 μm period.

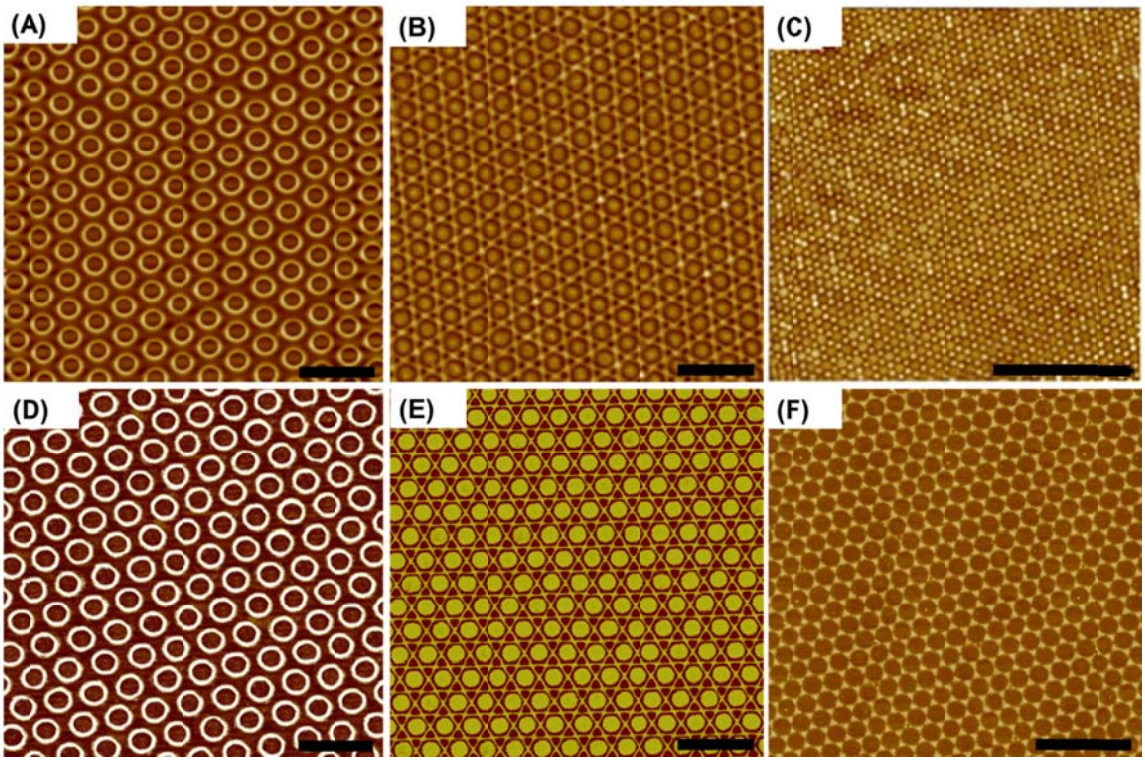

Figure 12. PS thin film features created with (A & B) 800 nm and (C) 400 nm PS spheres. Type I features are shown in (A), while type II features are shown in (B). (D-F) The corresponding Au features generated from the PS templates in (A-C). Scale bars: 2 μm.

3.2 Fabrication of non-concentric nano-pattern libraries through oblique colloidal lithography (OCL)

Oblique colloidal lithography is a modification of conventional colloidal lithography in terms of changing the substrate to a hydrophobic elastomer and tilted the substrate to create asymmetry. PDMS was chosen as the substrate because it is a robust, simple and inexpensive tool with well-studied properties.[108, 116] In a previous study, we showed that by leaving a SAM of PS sphere in touch with pristine PDMS surface for a certain amount of time, shallow and uniform dimple array could be formed.[83] This was probably caused by the redistribution and crosslinking of uncured PDMS molecules under the effect of elastic contact between PS sphere and PDMS surface. As a step forward, we applied this property to create asymmetric features on the surface by tilting the PDMS substrate to a certain angle in the air drying process of colloidal lithography (Fig. 13A). Generally, a flat PDMS substrate was first made and rendered hydrophilic in an O_2 plasma. Next, a self-assembled monolayer of polystyrene (PS) spheres was deposited from an aqueous suspension onto the tilted planar PDMS surface.[83, 101-103] The spheres had a diameter of 2 μm and formed a closely packed hexagonal monolayer on the surface during drying in ambient condition.

The external force (F) played an essential role during this process as it induced a redistribution of surface PDMS molecules. For an oblique planar surface, F could be divided into two components, namely $F_{\perp}$ that was perpendicular to the surface and $F_{//}$ that was parallel to the surface. $F_{\perp}$ created dimple arrays during the normal elastic contact while the parallel component of $F_{//}$ induced the formation of surface asymmetry.

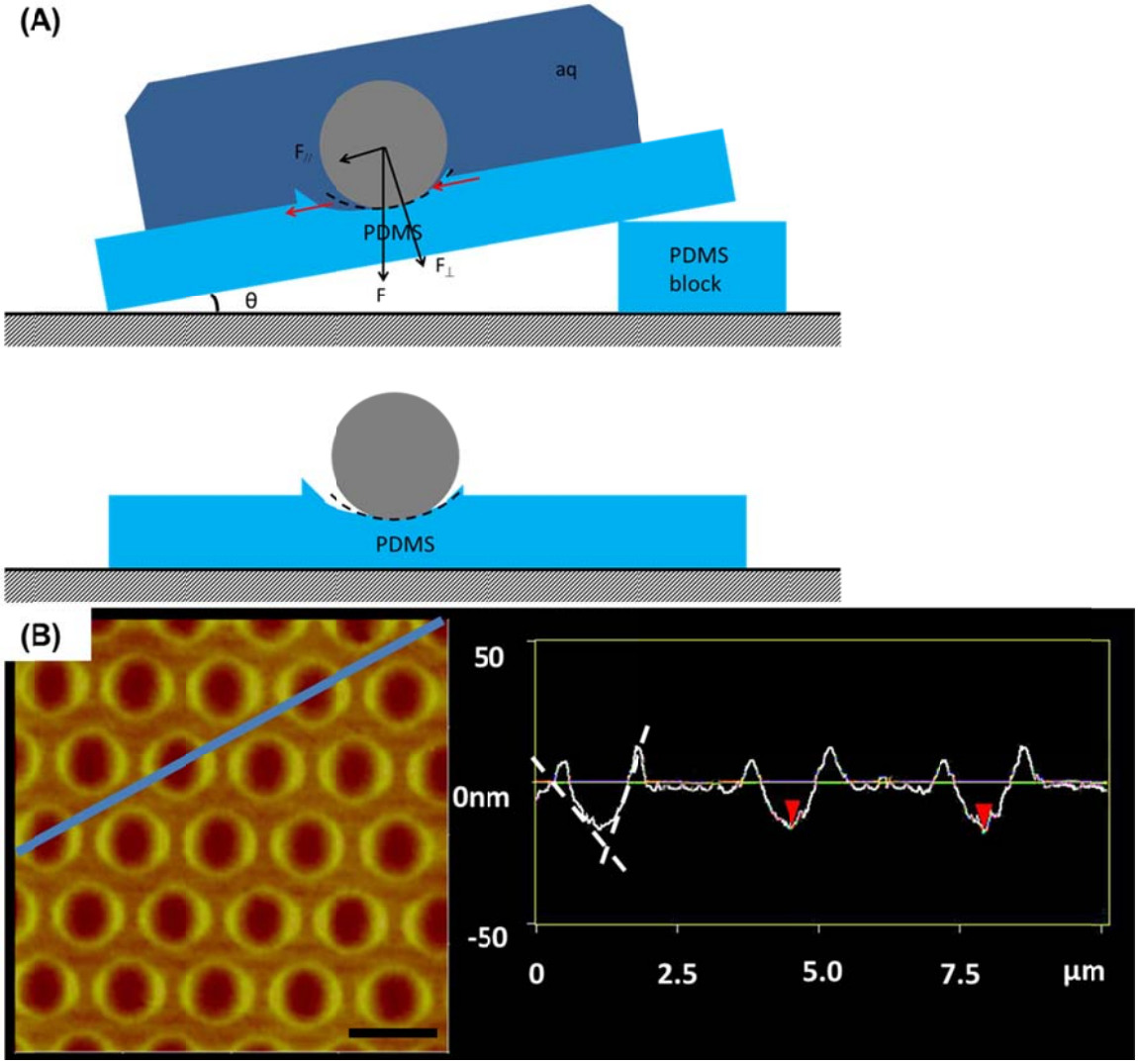

Figure 13. (A)Schematic illustration of the formation of asymmetric PDMS wells by oblique colloidal lithography. (B) AFM image of PDMS substrate surface after the removal of PS spheres. Scale bar: 2 µm.

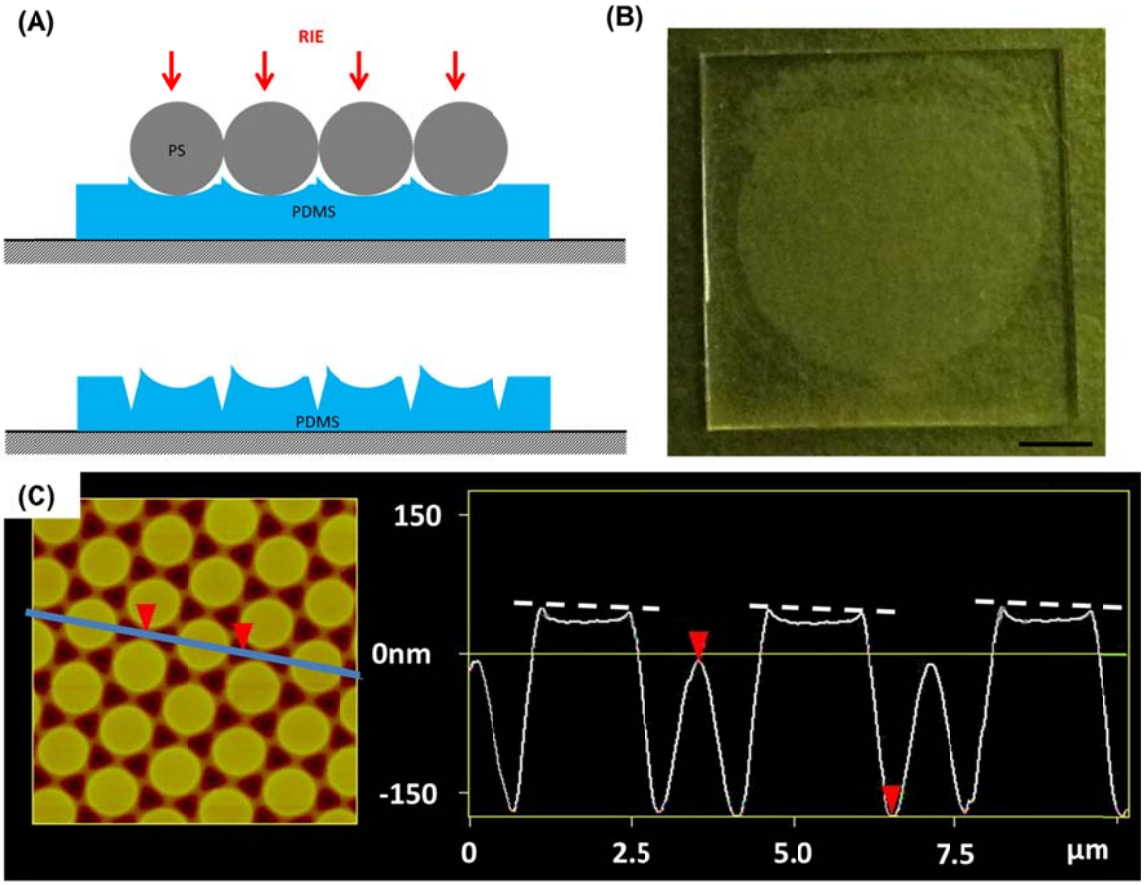

Figure 14. (A) A scheme of the binary reactive ion etching step. (B) Optical image of PDMS template after RIE and removal of PS spheres. Scale bar: 2mm, (C) A representative view of the as formed PDMS template.

Generally, a symmetric dimple would be formed during the normal elastic contact between PS sphere and PDMS surface (Fig. 13A, dashed curve). Meanwhile, this virtual dimple was distorted by $F_{//}$ in the direction parallel to the surface. The higher right side of PDMS was dragged towards PS sphere while the lower left side was pushed away, as was indicated by the red arrows in Figure 13A. As a result, the space between

PS sphere and PDMS surface became narrower on the right side and wider on the opposite side. The left edge of the dimple would also be higher than the right one due to the accumulation of more material during this surface distortion. Consequently, an asymmetric dimple was formed on PDMS after the removal of PS spheres, which could be directly observed under AFM (Fig. 13B). It is worthwhile to note that the tilted angle should be carefully controlled as the parallel F component would also influence the self-assembly of PS spheres. Basically, if the tilted angle was not too big (≤10°), the influence of $F_{//}$ could be omitted for the sake that individual particles would still be held together under the effect of surface tension and frictions. However, if the tiled angle went beyond that point, the magnitude of $F_{//}$ would become comparable with other forces. Consequently, disorder in the SAM would be observed by then.

In the next step, the PS sphere covered PDMS was subjected to binary plasma etching in the same way as we used in the previous publication (Fig. 14A).[83] Generally, reactive radicals yielded from etchant containing CF_4 and O_2 were applied vertically onto the PS covered PDMS. Only the surface region that was not shielded by the PS spheres was etched, which led to a hexagonal array of PDMS pillars. The asymmetric dimple was protected in this process. After the formation of PDMS pattern, PS spheres were dissolved with toluene and the PDMS template was cleaned by acetone and water followed by drying under 130 °C for 15 minutes. Optical and AFM image of the as formed PDMS template was shown in Figure 14B and 14C. As can be seen, PDMS pillar array with asymmetric dimple could be created in a cm^2 scale. The removed parts on PDMS corresponded to the three-fold hollow site in PS sphere SAM. Note that the left

and right edge of each dimple has a small height difference, as shown by the white dashed line in Figure 14C. As we pointed out previously, the morphology of PDMS pillars could be tuned by RIE time, O_2 concentration, and the size of the PS spheres. This type of control also worked for this system, which meant the shape of each PDMS pillar, the height of PDMS pillars as well as the gap between adjacent pillars were all tunable. Moreover, all the PDMS dimples were sitting under the PS spheres therefore would not be affected by the plasma etching operation. As a result, we could easily combine the inner asymmetric dimple with various types of outer PDMS surface structures within a single step.

Nonconcentric features would be formed when the as prepared PDMS template was introduced to capillary force lithography. To do this, the PDMS mold was placed onto a polystyrene-coated planar glass substrate. An iron block was placed on top of the mold to ensure close contact between the mold and the polymer as well as to adjust the pressure applied to the substrate. The whole system was then heated for a fixed period of time to 130 ºC, which was above the glass transition temperature (T_g) of polystyrene.[113] The polystyrene features were formed as the polymer melt climbed up the walls under the effect of capillary forces. As the temperature rose above the T_g of polystyrene, the PS layer melted and accumulated around the edge of the PDMS pillars. This kind of capillary rise was mainly driven by the surface tension as the initial contact angle between the PDMS walls and the PS layer was 90°, which is far from contact equilibrium (~76°). [114, 115] In addition, more material would accumulate under the side with a taller roof than the other side because of the tendency for a system to minimize its

surface tension. As a result, a polymer disk with an asymmetric height distribution would be formed, which could be further verified by AFM (Fig. 15B). As can be seen, a major portion of the polymer in the central disk was confined at the left half, leaving a faint color on the right side corresponding to the less steep part in the line profile. It should also be noted that the center of the disk, which is the tallest point in Figure 15B, deviated from the center of the outer ring. This served as the key part to introduce nonconcentricity to metallic structures.

In the next step, PS patterns were transferred onto an underlying gold layer through plasma etching and wet etching steps (Figure 16). The perpendicular plasma etching speed was approximately 2 nm/s under our conditions; therefore, the amount of PS that was ultimately removed was easy to control. Exposed gold layer was removed by immersing the chip into a 1:1 (volumetric) mixture of 50 mM ferric nitrate and 50 mM thiourea to conduct a wet chemical etch, leaving some patterns on the surface.

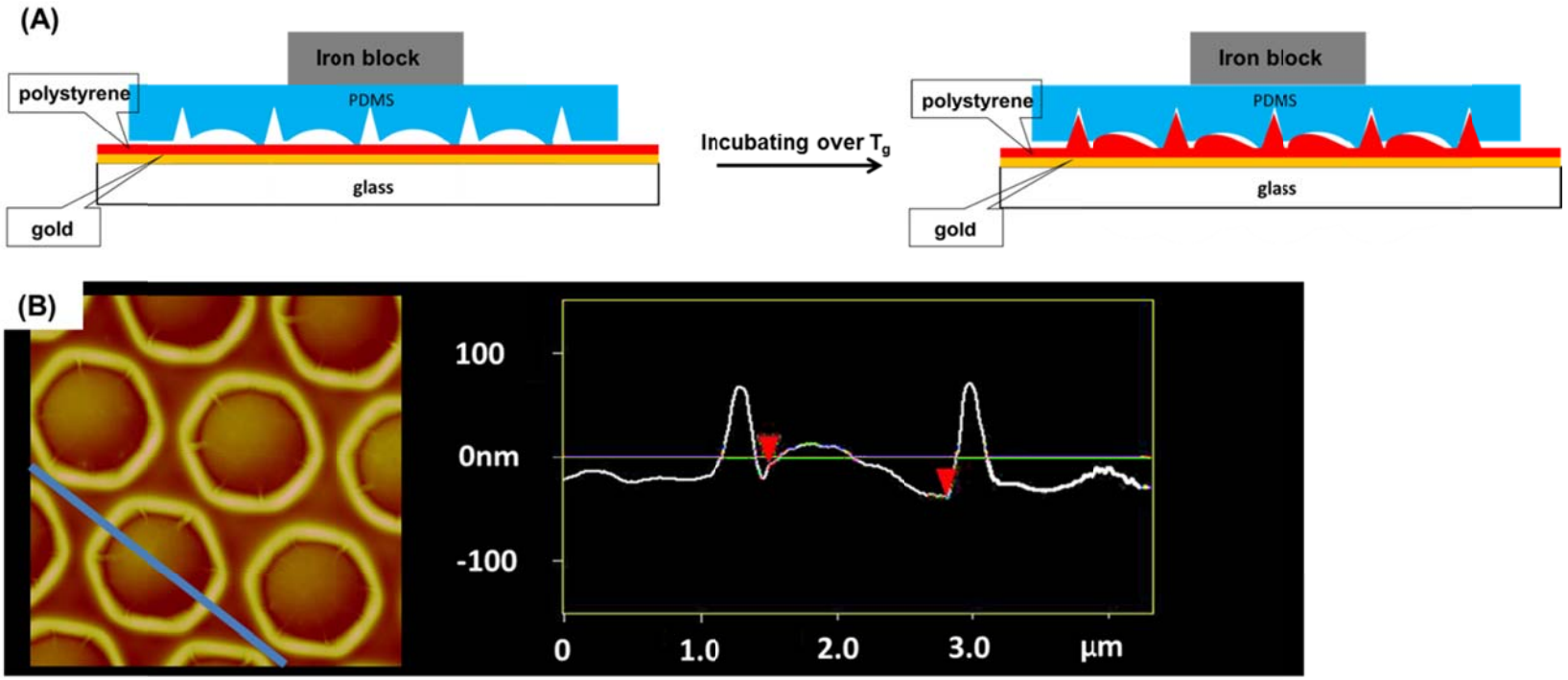

Figure 15. A scheme of the capillary force lithography step with asymmetric PDMS template.

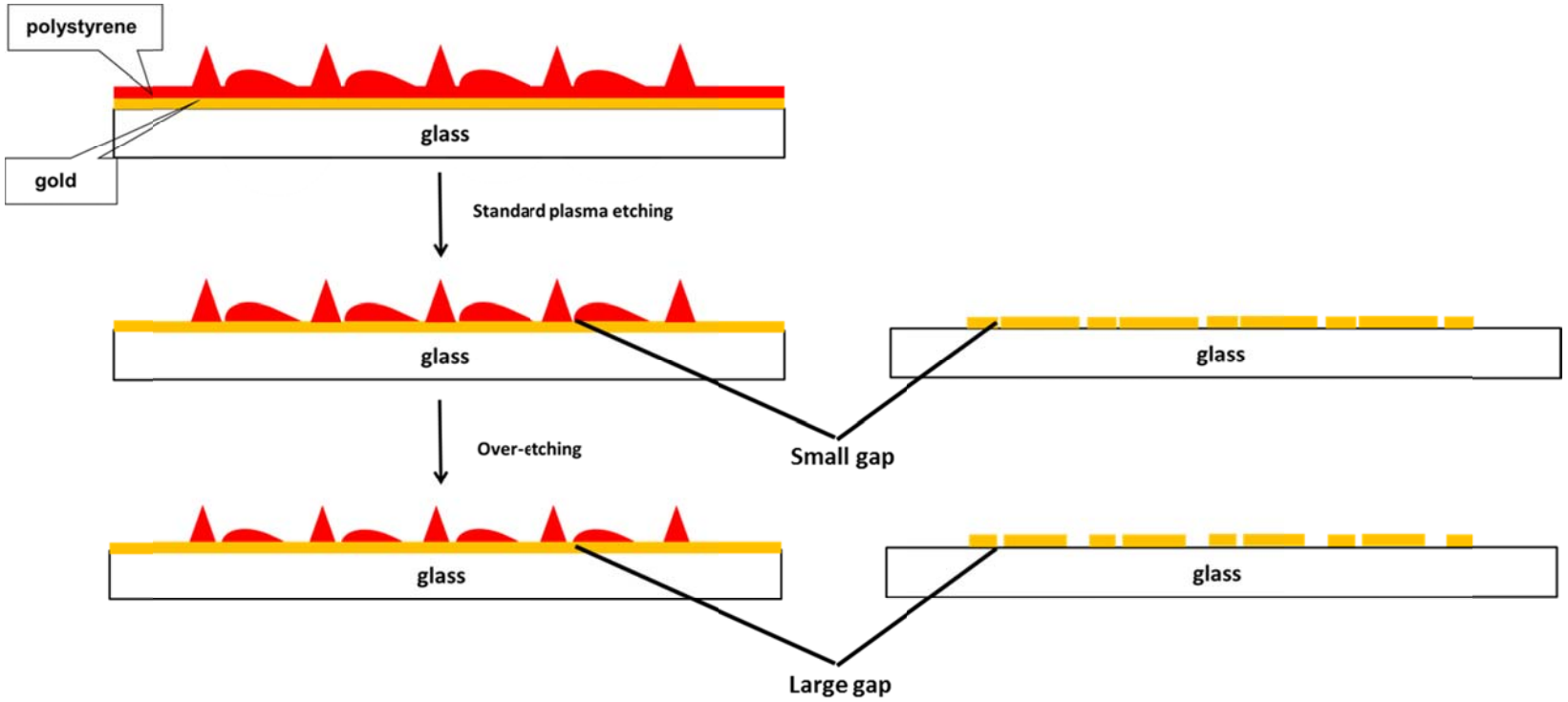

Figure 16. The influence of plasma etching time on the morphology of PS and Au patterns.

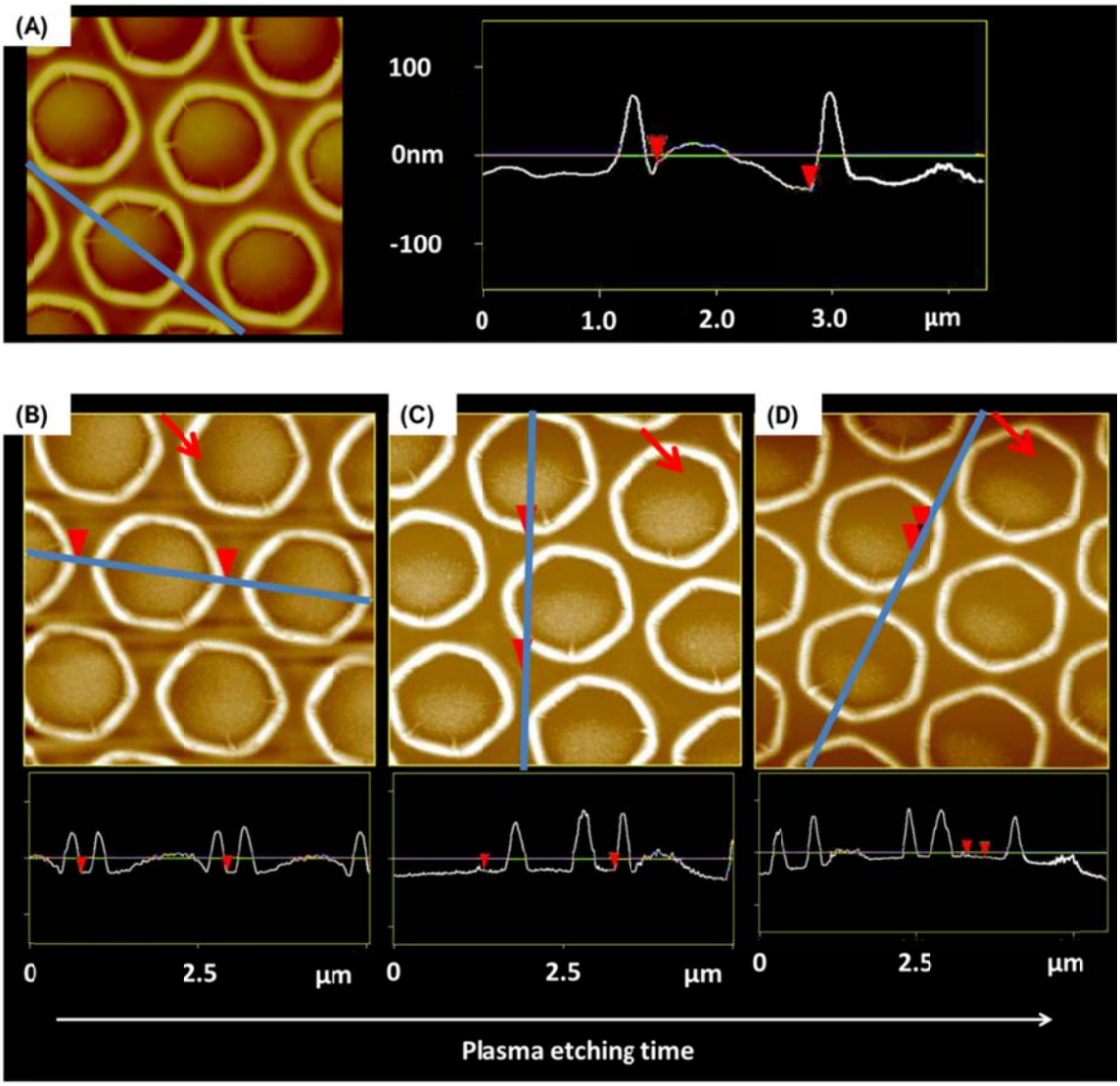

Figure 17. AFM image and line profiles of (A) PS target created by capillary force lithography. (B) plasma etching of the same PS feature by 20s; (C) 30s and (D) 40s. Surface areas removed most rapidly were pointed by the green arrows.

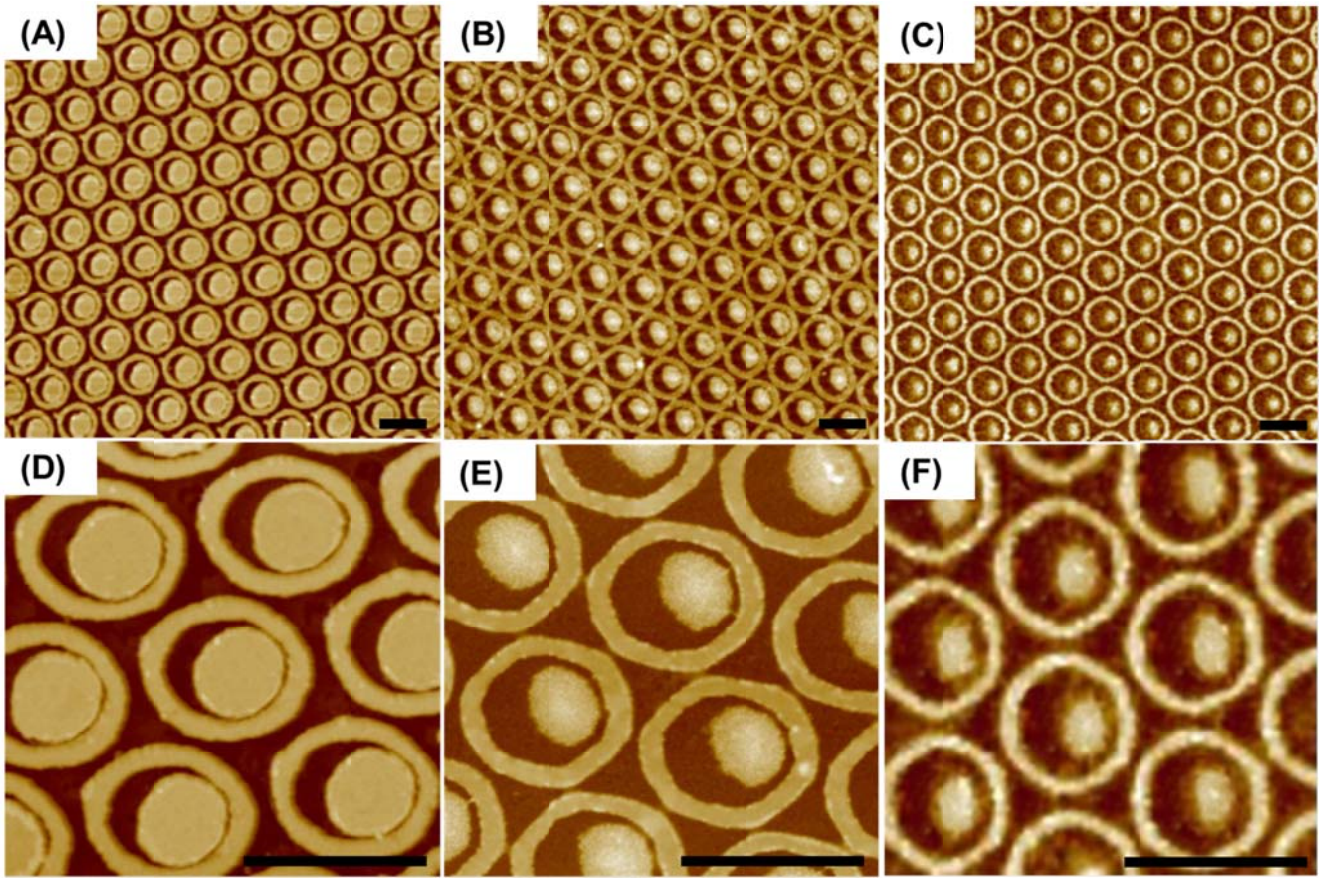

Figure 18. Au nanopatterns created from the PS templates in Fig. 17. (A)-(C) in the upper line were generated from (B)-(D) in figure 5, respectively and (D)-(F) at the bottom are magnified of image of the corresponding figure on their top. Scale bars: 2 μm.

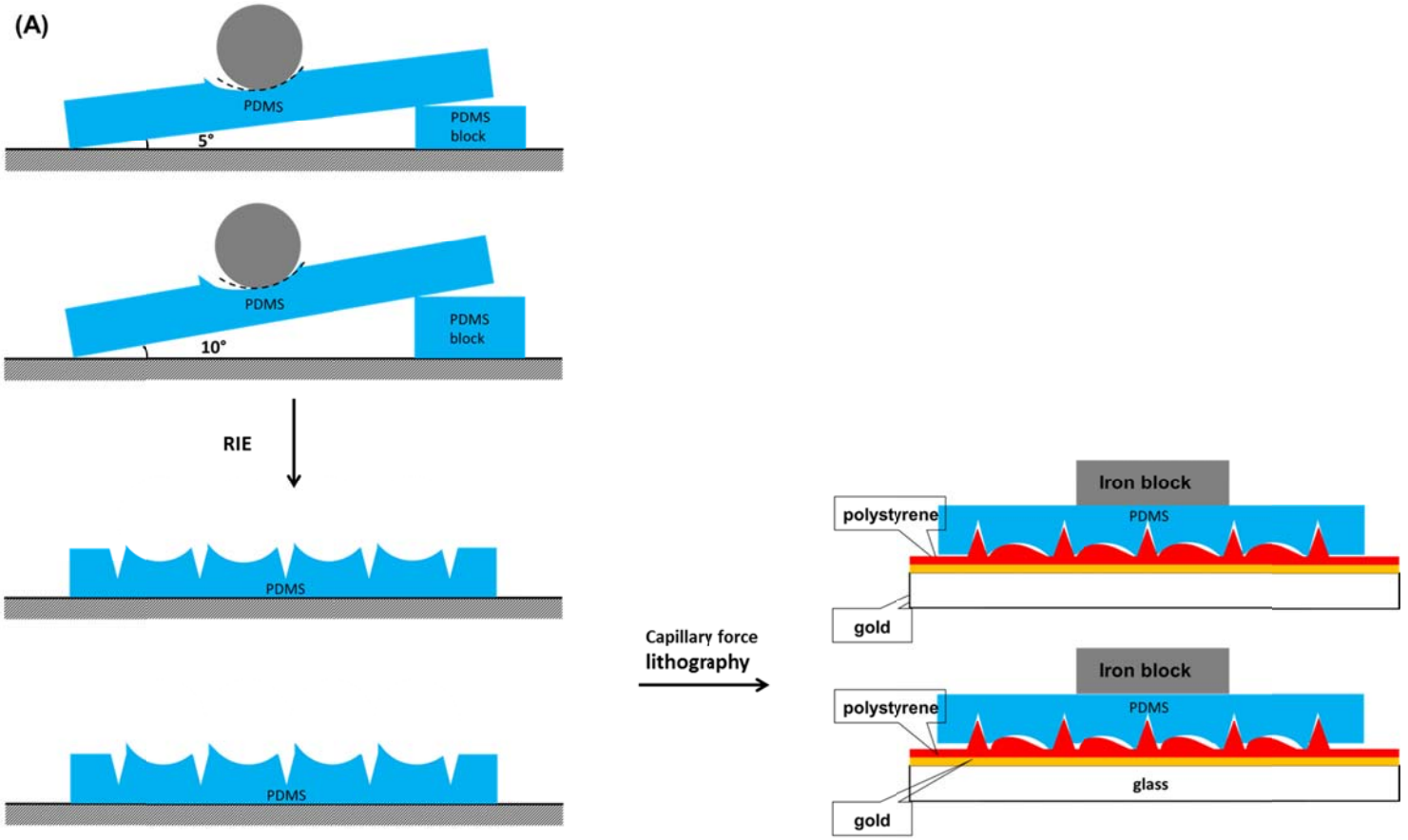

Figure 19. (A) The influence of tilted angle on the asymmetry of PDMS template and the corresponding PS feature. (B) PS feature made from PDMS template with small tilted angle and its line profile. (C) PS feature made from PDMS template with large tilted angle and its line profile. (D) The definition of parameters a and b.

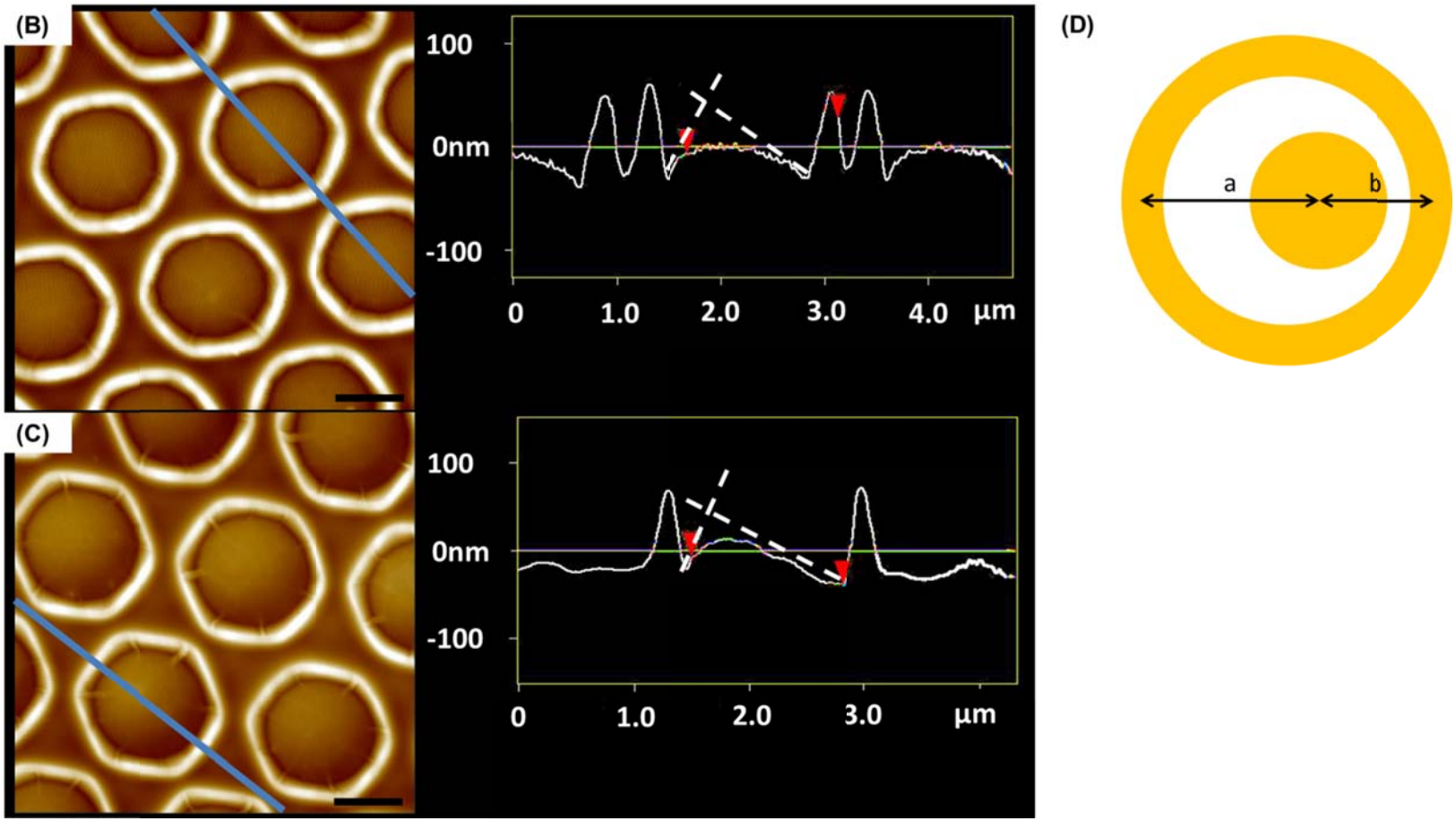

Figure 19. continued.

Interestingly, due to the asymmetry of PS features, the tangential etching rate became anisotropic with a much higher speed at the smoother part. Given the fact that a constant vertical etching was maintained in RIE, a smaller slope of PS feature meant that a larger tangential distance was required to cause the same height variation. As a result, an extended etching time led to the asymmetric exposure of the underlying metal layer (Fig. 17). The longer the etching time, the more significant this phenomenon would be (Figure 17B-17D). As can be seen, the part pointed by the red arrows was removed significantly quicker compared to other regions with the increase of etching time. This allowed us to fabricate nonconcentric gold features by creating anisotropic gap size around the inner disk. Also, the size ratio between the inner disk and the outer ring was tuned in the same process way, which is shown in Figure 18. The size of the inner disk was reduced dramatically from 20 s etching to 40s etching while the ring moiety didn't change much. This was also attributed to the difference in the slope of each structural unit. The ring feature possessed the highest slope, leading to the slowest tangential etching rate.

The tilted angle of PDMS substrate provided another dimension to control the surface morphology of gold patterns. As is shown in figure 19A, the difference in tilted angle affected the magnitude of $F_{//}$ which defined the asymmetry of dimples. It is not difficult to imagine that the bigger the angle was, the larger $F_{//}$ would be, which proportionally took effect on the asymmetry of PDMS features. When two PDMS templates with either small or large asymmetry were applied in CFL with the other conditions the same, two types of PS features would be generated, namely the one with

milder asymmetry (Fig. 19B) and the one with a very significant asymmetric profile (Fig. 19C). Note that the outer moiety of both patterns is identical. In order to quantify this difference in the structure of nano-features, we borrowed the concept of eccentricity (e) from astronomy. Eccentricity was originally used to describe the amount by which the orbital of an astronomical object around another body deviated from a perfect circle. Similarly, we defined the distance from the center of the inner disk to two opposite edges of the outer ring in the direction of deviation as a and b, respectively (Fig. 19D). The eccentricity of the nonconcentric patterns could be expressed as:

$$e = \sqrt{1 - \frac{b^2}{a^2}} \tag{3}$$

Two gold patterns with e=0.6 and e=0.8 were fabricated by a wet etching process from PS features in Figure 19. (Fig. 20A & 20B). The detailed patterning conditions were listed in Table 3.

Multiple types of non-concentric features could be fabricated with our method by varying the outer moiety of structure. This could be simply done through applying PDMS template of different morphology. We had defined three kinds of PDMS template according to their interpillar distance in an earlier publication.[83] Each type of template was able to create a group of distinctive PS features. The interpillar distance had nothing to do with the shape of the central dimple but only related to the etching conditions in RIE. Therefore, we could accurately repeat the outer feature by using the same RIE conditions in creating symmetric PDMS template and the same parameters in CFL. Moreover, with each type of outer patterns, inner dish with various eccentricities could

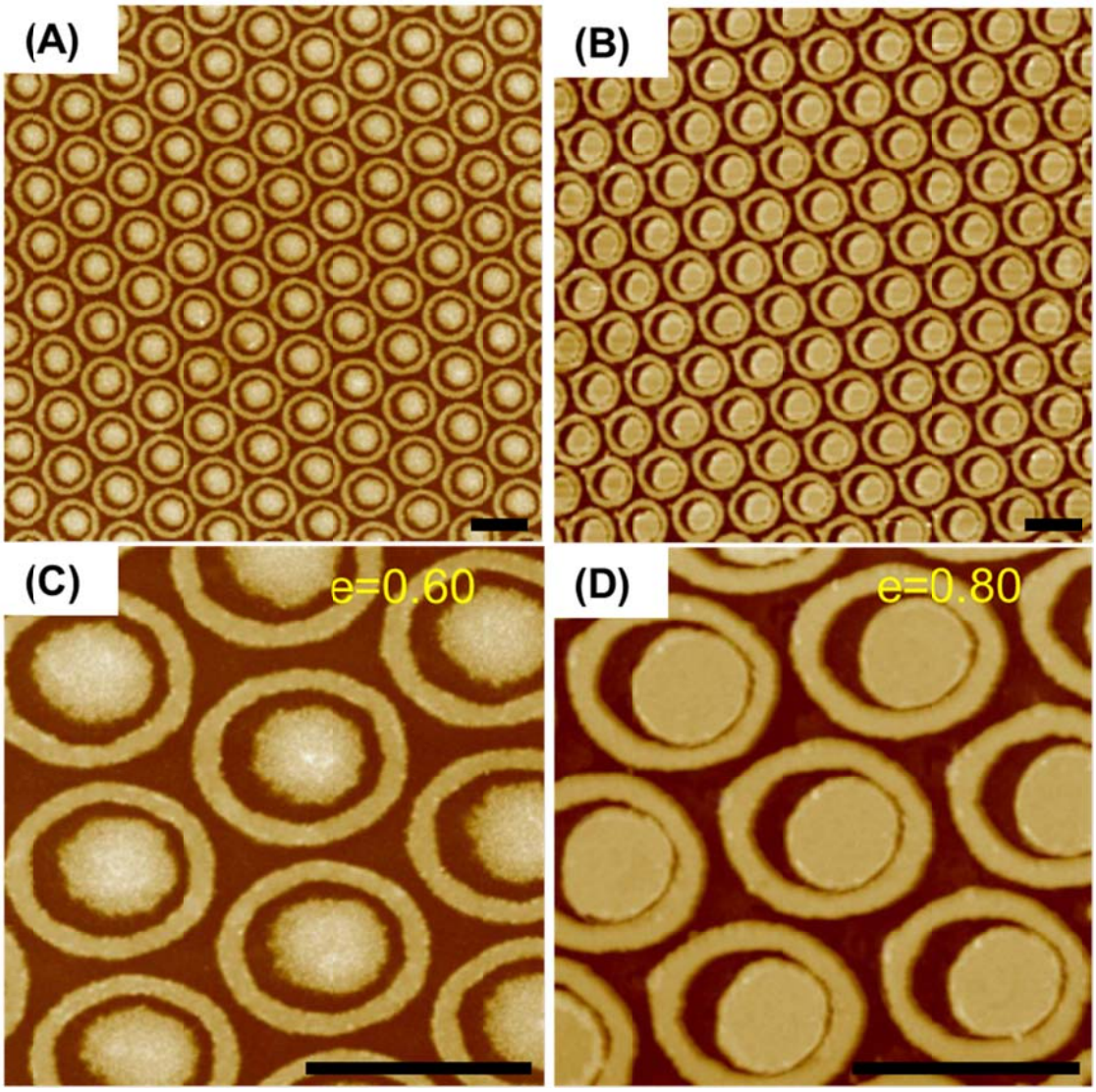

Figure 20. Nonconcentric gold patterns with different eccentricity created from the PS templates in Fig. 19. (A) gold pattern from PS figure in Fig. 7B; (B) gold pattern from PS figure in Fig. 7C; (C) and (D) magnified image of (A) and (B), respectively. Scale bars: 2 μm.

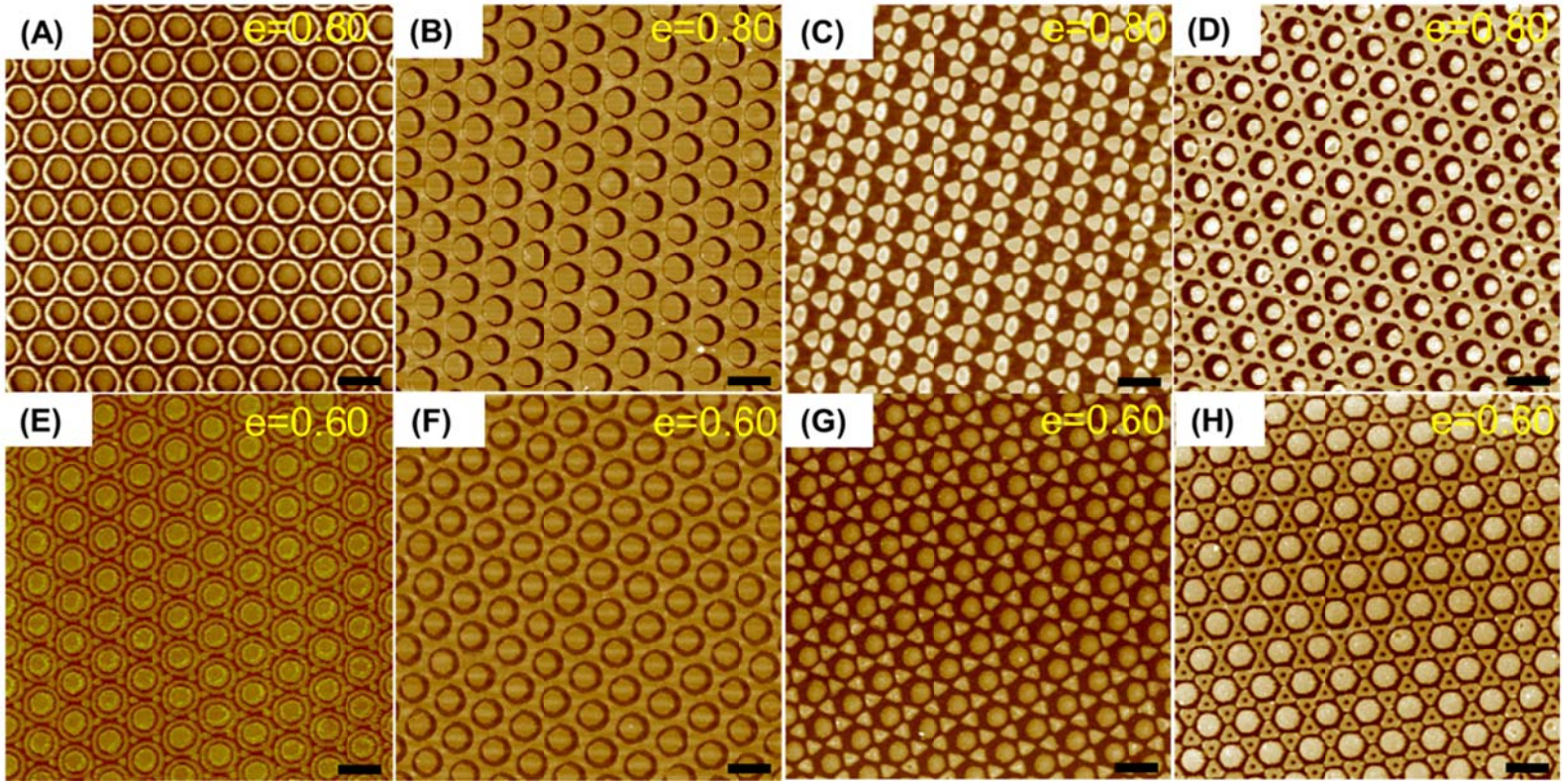

Figure 21. Other four types of nonconcentric gold features with (A)-(D) large eccentricity and (E)-(H) small eccentricity. Scale bars: 2 μm

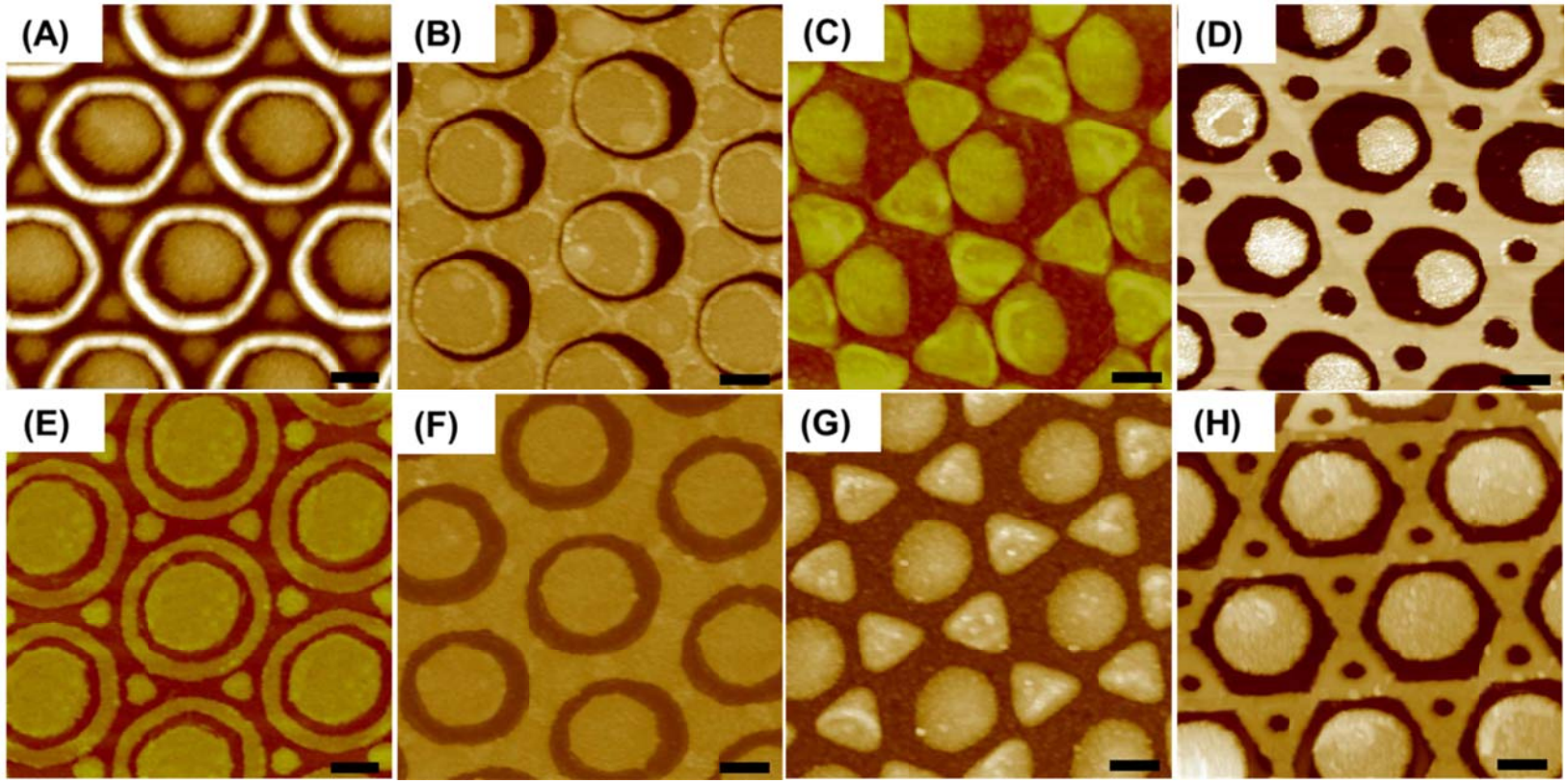

Figure 22. Magnified image of figure 21. Scale bars: 500nm

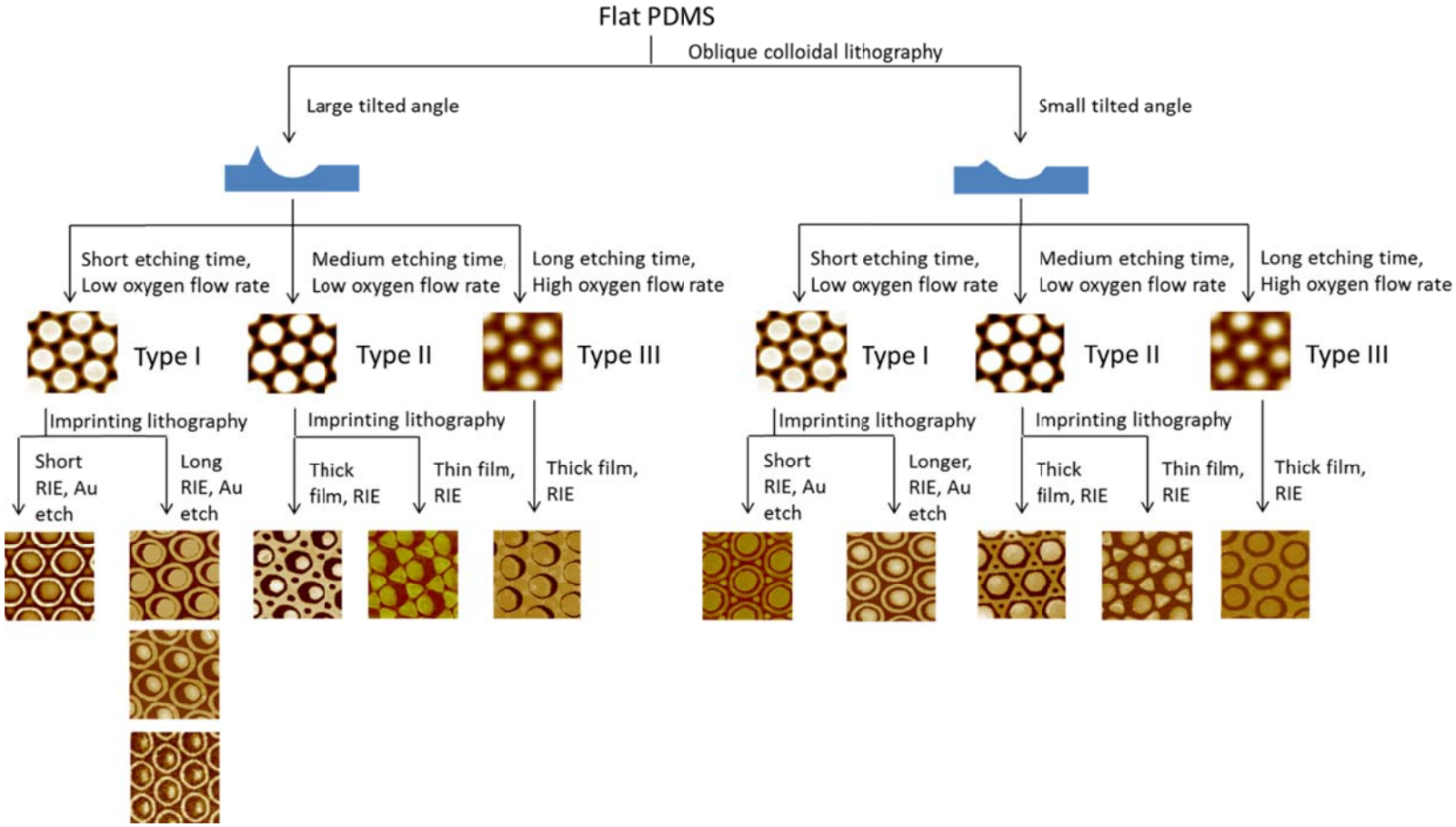

Figure 23. A guide to the strategies employed for fabricating various Au pattern motifs.

also be switched freely through adjusting the tilted angle in the OCL step. The summation of those two independently controlled mechanisms led to a huge number of structures that were able to be fabricated by our technique. Eight representative gold features were listed in Figure 21 and detailed experimental conditions could be found in Table 3. The vertical row showed two nonconcentric features with the same outer pattern but different while the horizontal line compared four types of structures with the same eccentricity. Magnified image of all the patterns was listed in Figure 22. It is worthwhile to mention that we could fabricate gaps down to 30 nm with a careful control of plasma and wet etching time (Fig. 22). The size of gaps was mainly restricted by the diffusion of etchant in the wet chemical etching step. With the use of a highly anisotropic etching method, the fabrication of sub 20 nm features should be possible. A tree guide to the strategies employed for fabricating various Au pattern motifs was listed in Figure 23. Detailed patterning parameters for PS patterns can be found in Table 3.

Table 3. Patterning conditions for each type of non-concentric gold feature

pattern[a]	polystyrene feature fabrication conditions[b]	Plasma etching time	wet etching time	template fabrication conditions[c]
18A	20 nm, 1h incubation	20s	9 min	10°, CF_4 35 sccm, O_2 5 sccm, 270 W etch 72 s
18B	20 nm, 1h incubation	30s	9 min	10°, CF_4 35 sccm, O_2 5 sccm, 270 W etch 72 s
18C	20 nm, 1h incubation	40s	9 min	10°, CF_4 35 sccm, O_2 5 sccm, 270 W etch 72 s
20A	20 nm, 1h incubation	20s	9 min	5°, CF_4 35 sccm, O_2 5 sccm, 270 W etch 72 s
20B	20 nm, 1h incubation	20s	9 min	10°, CF_4 35 sccm, O_2 5 sccm, 270 W etch 72 s
20A	18 nm, 1h incubation	17s	9 min	10°, CF_4 39 sccm, O_2 1 sccm, 270 W etch 70 s
21B	50 nm, 1h incubation	35s	11 min	10°, CF_4 35 sccm, O_2 5 sccm, 270 W etch 85 s
21C	26 nm, 1h incubation	25s	9 min	10°, CF_4 35 sccm, O_2 5 sccm, 270 W etch 72 s

Table 3. continued

pattern[a]	polystyrene feature fabrication conditions[b]	Plasma etching time	wet etching time	template fabrication conditions[c]
21D	20 nm, 1h incubation	20s	10 min	10°, CF_4 35 sccm, O_2 5 sccm, 270 W etch 72 s
21E	18 nm, 1h incubation	17s	9 min	5°, CF_4 39 sccm, O_2 1 sccm, 270 W etch 70 s
21F	50 nm, 1h incubation	35s	11 min	5°, CF_4 35 sccm, O_2 5 sccm, 270 W etch 85 s
21G	26 nm, 1h incubation	25s	9 min	5°, CF_4 35 sccm, O_2 5 sccm, 270 W etch 72 s
21H	20 nm, 1h incubation	20s	10 min	5°, CF_4 35 sccm, O_2 5 sccm, 270 W etch 72 s

[a] The patterns are listed by the figure number they appeared in.

[b] The Temperature was 130℃.

[c] The first number indicated the tilted angle in OCL process.

3.3 SPR properties of nano-features

The extinction spectrum for each nano-pattern was first recorded at normal incidence under unpolarized light. The extinction spectra of several symmetric patterns had been previously studied, including target,[46] triangles,[64, 117] annular apertures[118-120] and nano-well.[11, 59-63] Therefore, their spectral characters in the visable-NIR range could be applied to inspect the quality of our patterning technique over the macroscopic scale

As a well-studied structure, the hexagonal hole array owns two transmission minimum and several plasmon peaks. The corresponding wavelength of the maximum transmittance of a hexagonal hole array could be expressed as:[59-63]

$$\lambda_{\max} = \frac{P}{\sqrt{\frac{4}{3}(i^2 + ij + j^2)}} \sqrt{\frac{\varepsilon_m \varepsilon_d}{\varepsilon_m + \varepsilon_d}} \tag{4}$$

where P is the period of the array, ε_m and ε_d are respectively the dielectric constants of the metal and the adjacent dielectric medium and i and j are the scattering orders of the array. This equation didn't take into consideration the interference between holes therefore the calculated number would be slightly smaller than observed value.[121, 122] We examined our nano-well arrays with 2 μm period and the result showed a good match with the theoretical expression (Fig. 24). The maximum in transmission would transform to the minimum in extinction. Accordingly, the dip at around 2136nm could be assigned to the (1, 0) peak at air-metal interface. The tiny dip observed at 1233nm would most probably to be the $(1, 1)_{air}$ transmission while the two minimums appeared at 2955 nm and 1511 nm are the $(1, 0)_{glass}$ and $(2, 0)_{glass}$ plasmon resonance, respectively.

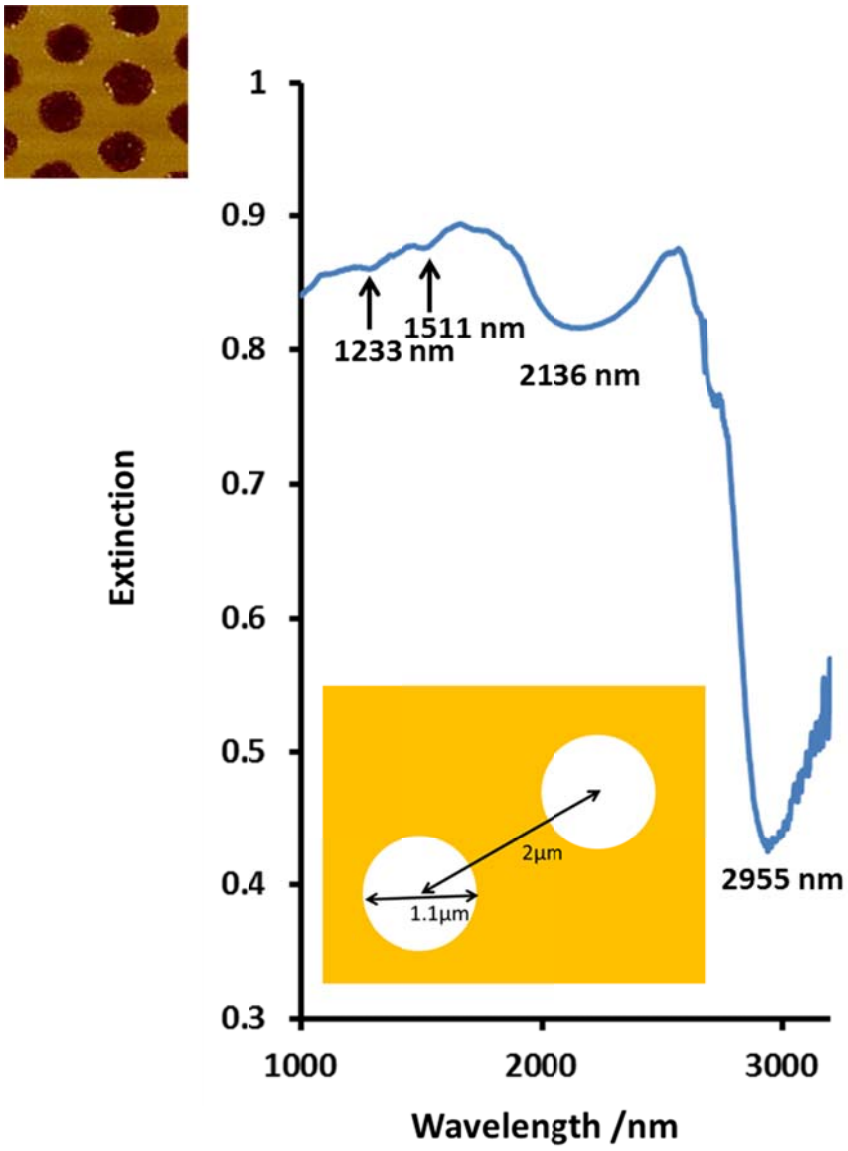

Figure 24. The extinction spectrum of symmetric nano-hole array.

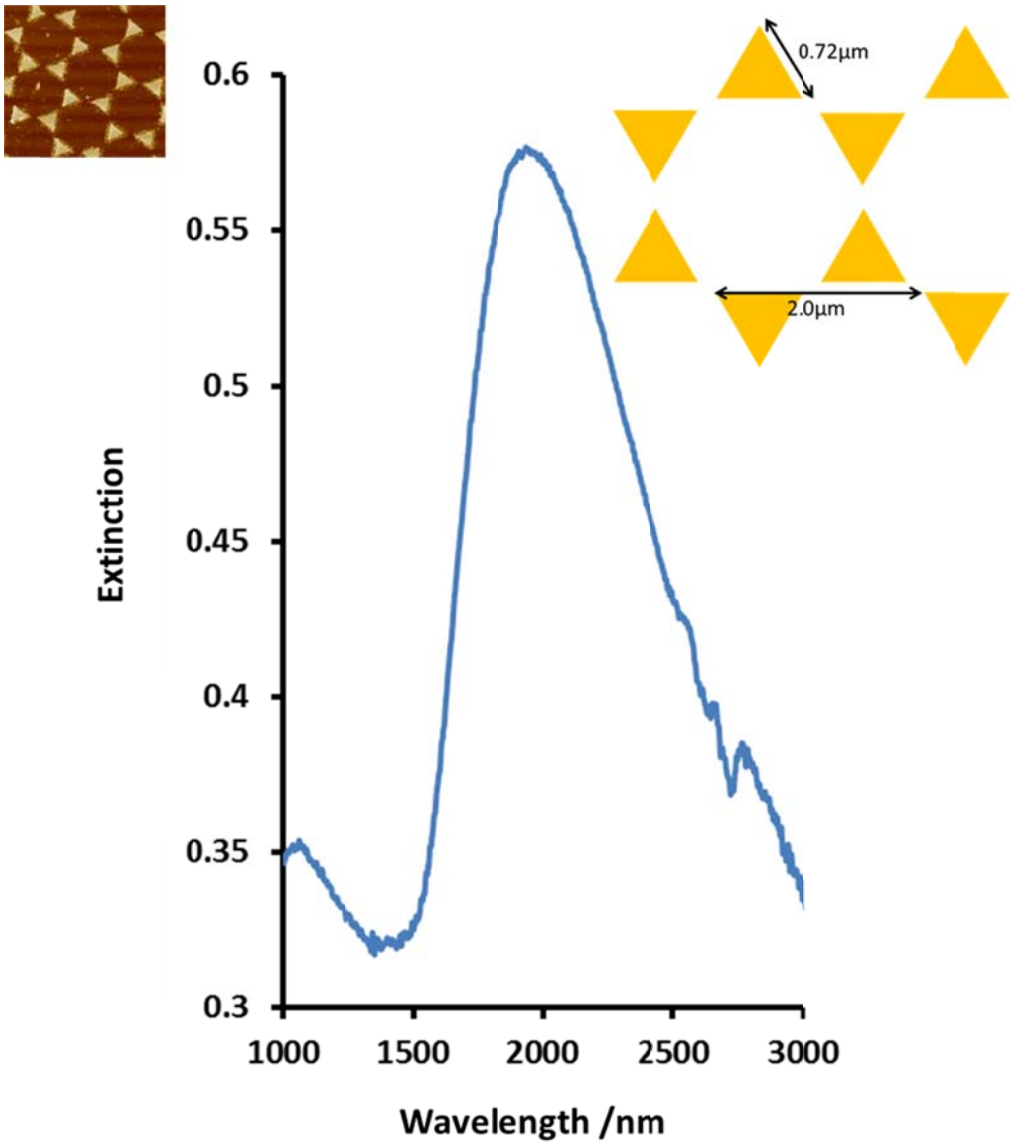

Figure 25. The extinction spectrum of symmetric triangle array.

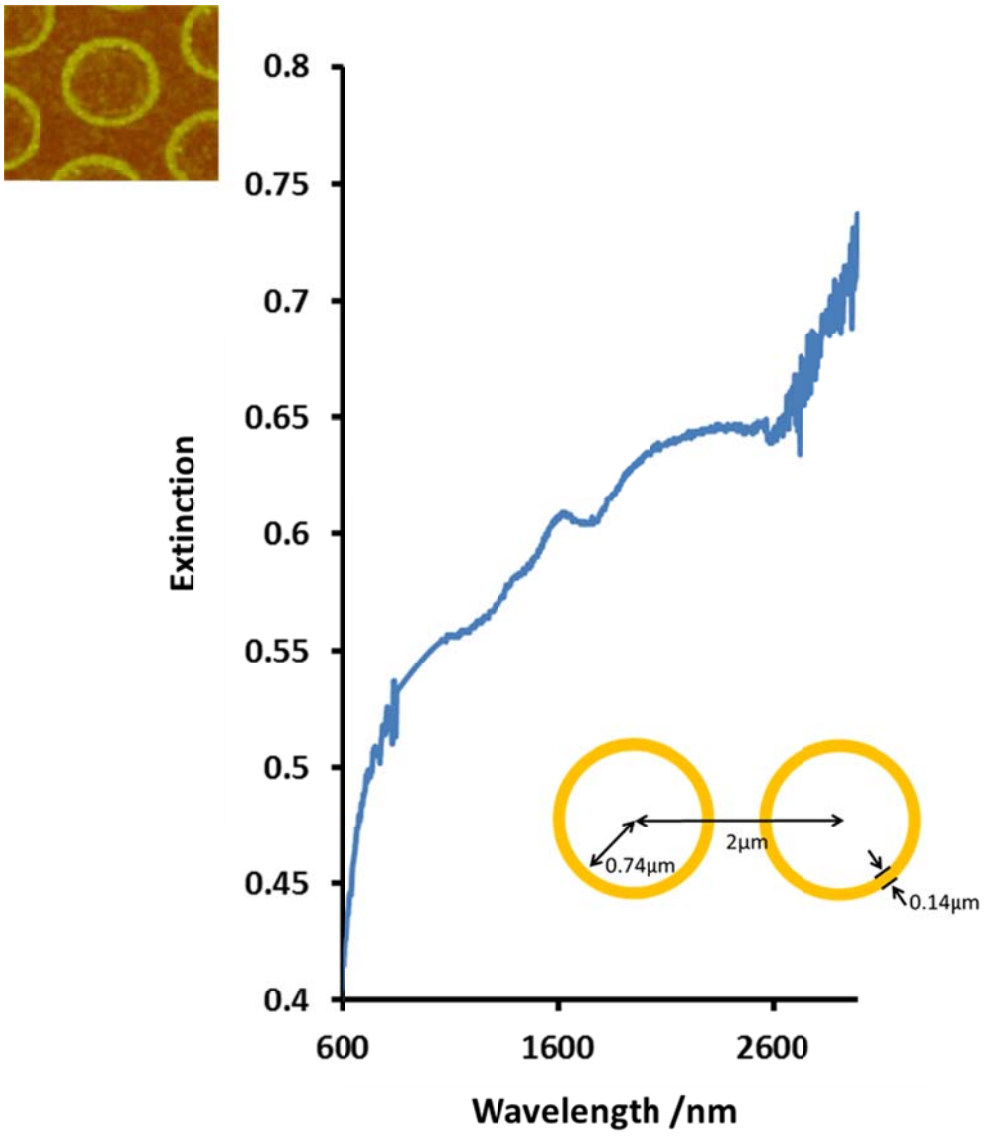

Figure 26. The first extinction spectrum of symmetric nano-ring array with labeled geometric parameters.

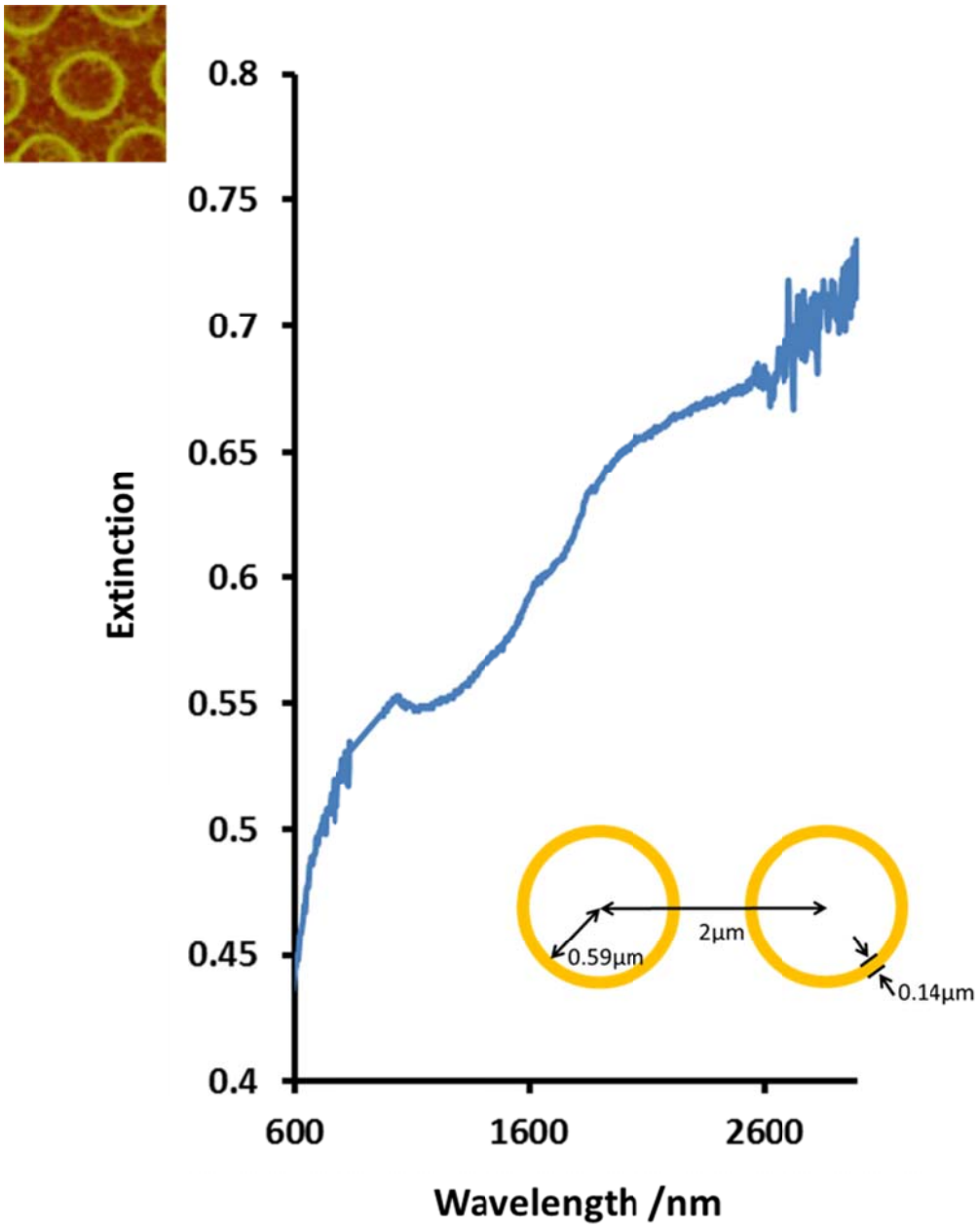

Figure 27. The second extinction spectrum of symmetric nano-ring array with labeled geometric parameters.

The plasmonic behavior of nano-triangles was relatively simpler compared to the hexagonal hole array.[64, 117] Basically, a single maximum was observed in the extinction spectrum which was sensitive to the variation in shape, gap distance, and other inhomogeneities. As a result, the peak was usually broadened under the presence of several types of defects, such as undesired connections between triangles. The extinction spectrum of triangles with 2 μm period was shown in Figure 25. As can be seen, a single broad maximum was found at 1989 nm and the shape of the spectral profile well fitted previous studies.

The optical behavior of nano-ring array had been predicted by FDTD simulations.[123, 124] There were two modes for a single isolated ring structure, namely the bonding ring dipole mode and the antibonding ring dipole mode. The antibonding mode had a higher energy than the bonding mode and located at a short wavelength. Our results clearly showed that two major peaks were observed in the extinction spectra of nano-ring array (Fig. 26). Their positions were measured at 1670 nm and 2450 nm. Interestingly, the first peak that corresponded to the antibonding plasmon mode almost disappeared when the diameter of the ring decreased from 1.76 μm to 1.44 μm but remaining a constant thickness (Fig. 27). This result might indicate that some sort of coupling between adjacent antibonding ring plasmons was happened during the first case to increase its extinction cross section. After all, the extinction cross section of isolated antibonding ring dipole mode should be pretty small according to simulations.[123, 124]

The extinction spectra of symmetric ring/disk cavity had been calculated by FDTD theory by several groups.[123, 124] In general, two plasmon resonances were found to

dominant the spectral region The subradiant (DBR) mode at longer wavelength for the target structure resulted mainly through bonding-type hybridization of oppositely aligned (bonding) ring and disk dipoles while the superradiant (DAR) mode of shorter wavelength was mainly a result from bonding combination of the antibonding ring dipole and the primitive disk dipole. Two maximums were found to appear at ~1500 nm and 2900 nm in the spectrum of our nano-target structures, which matched the theoretical prediction (Fig. 28). The 1500 nm peak should be identified as the DAR mode and the 2900 nm mode was attributed the DBR plasmon resonance.

A super-transmission has been reported for the annular aperture arrays (AAA) during the past decade[118-120]. Similarly, we also found a corresponding extinction minimum located at ~1520 nm (Fig. 29). Interestingly, a Fano-like peak was observed for the annular aperture pattern at around 1800 nm. There should be no Fano resonance for the annular aperture due to the lack of symmetry breaking. The peaks we observed might be attributed to the asymmetry caused by the semi-hexagonal shape of the outer profile of the aperture (Fig. 29, upper left icon). As a result, the depth of the Fano-like peak was relatively small because the asymmetry was not very significant.

Several symmetric nano-patterns, including triangle-target, hexagram-dot, triangle-dot, were fabricated for the first time. In order to investigate the structural dependence of surface plasmon resonances, features belonging to the same type but with slightly different geometrical parameters were fabricated and tested.

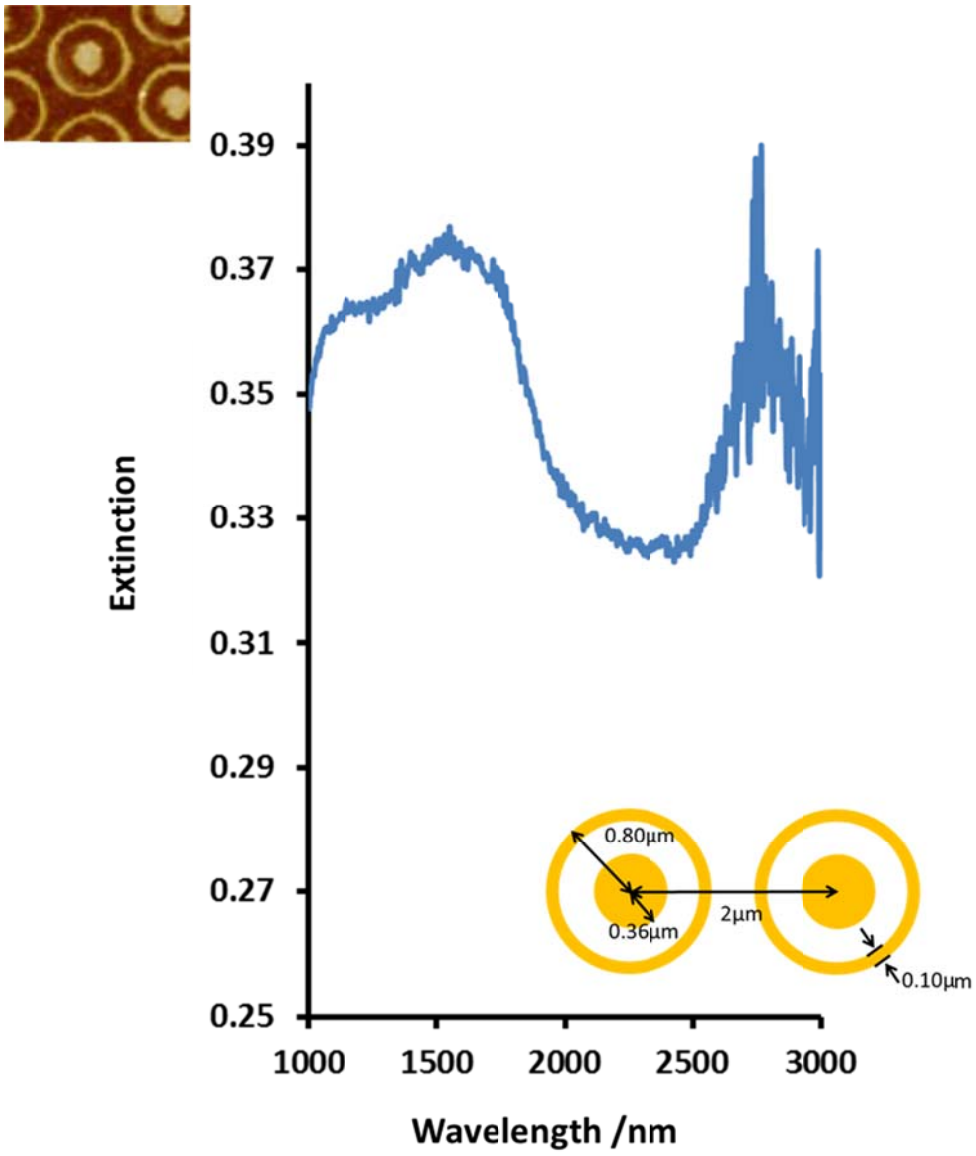

Figure 28. The extinction spectrum of symmetric target array.

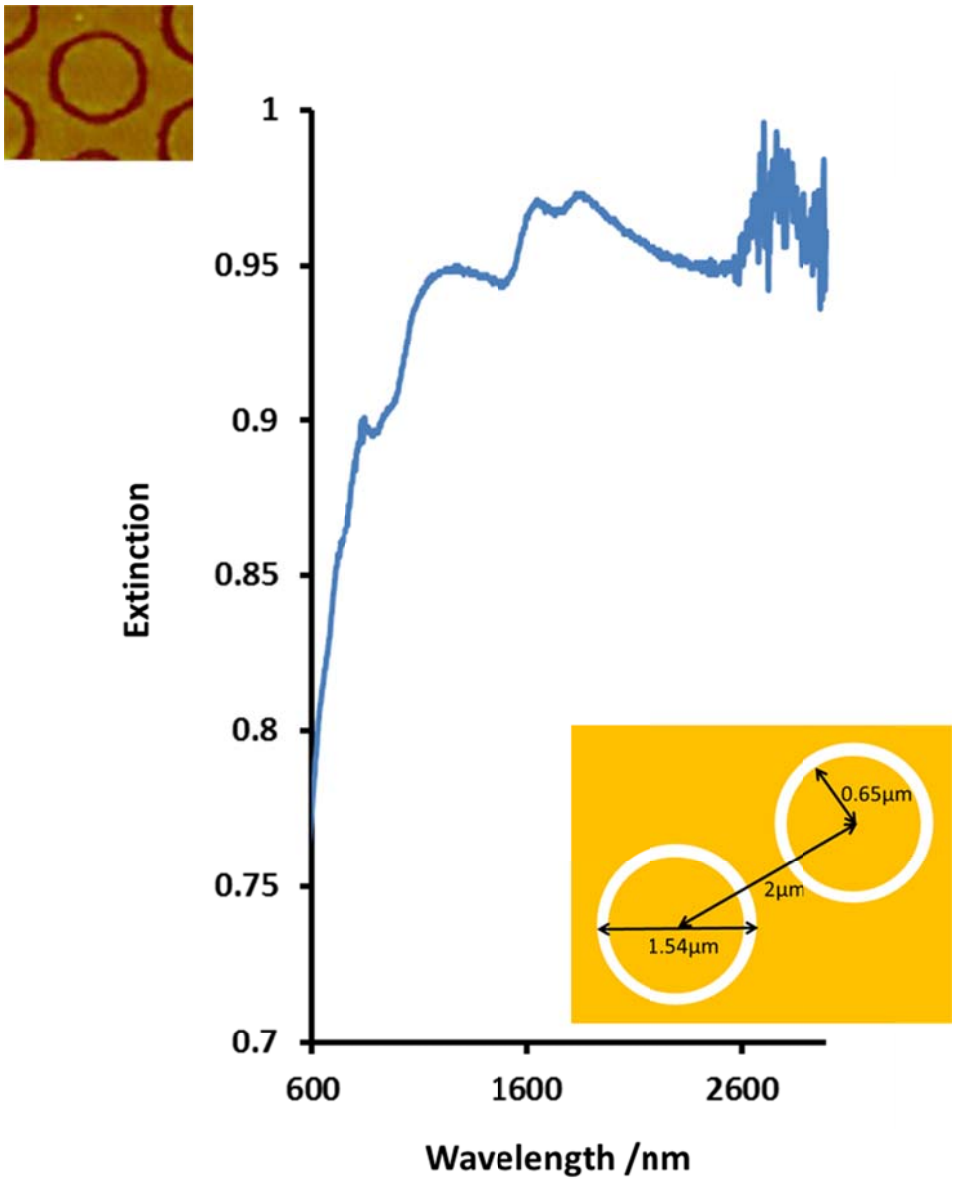

Figure 29. The extinction spectrum of symmetric annular aperture array.

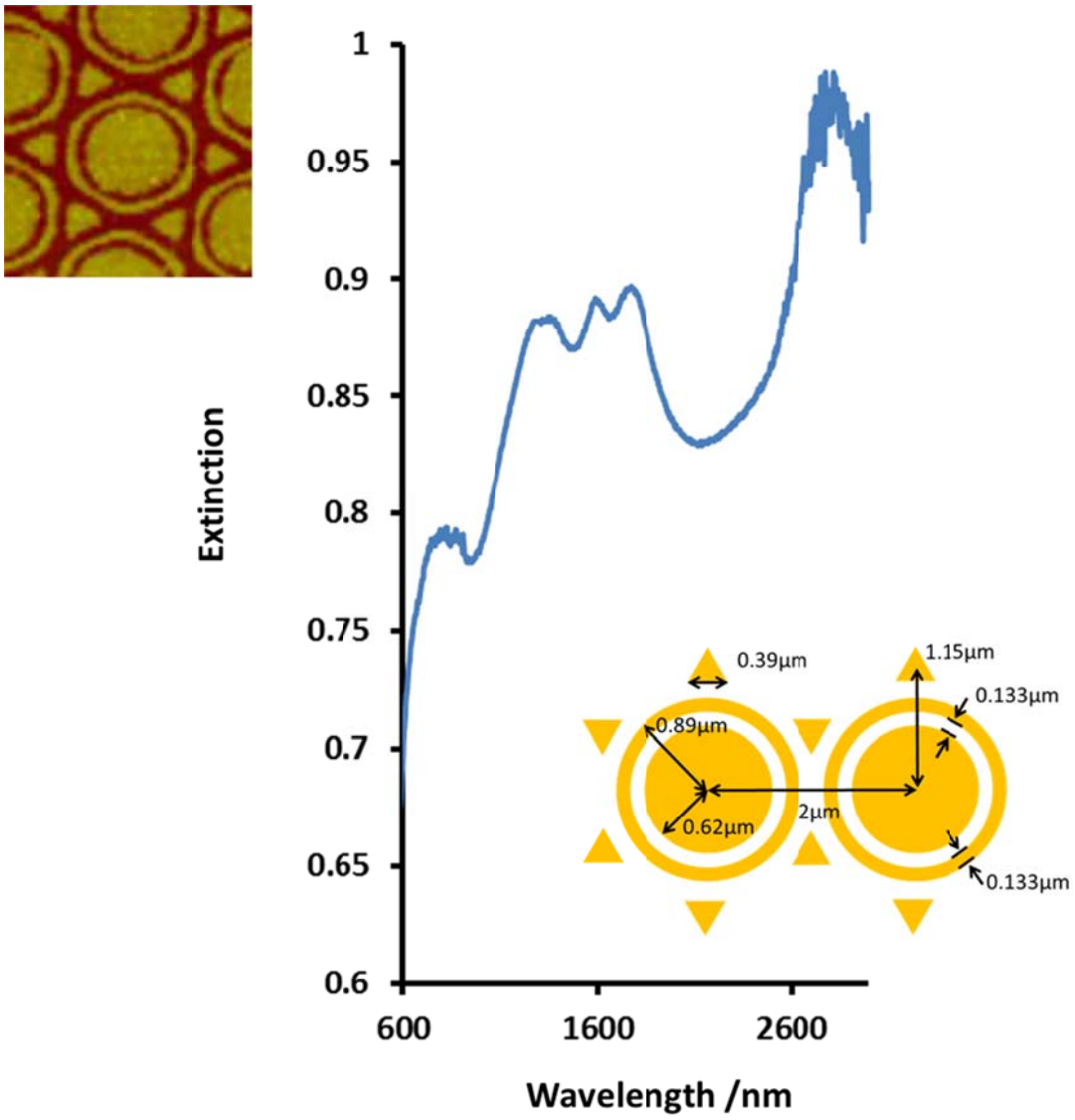

Figure 30. The first extinction spectrum of symmetric triangle-target array with labeled geometric parameters.

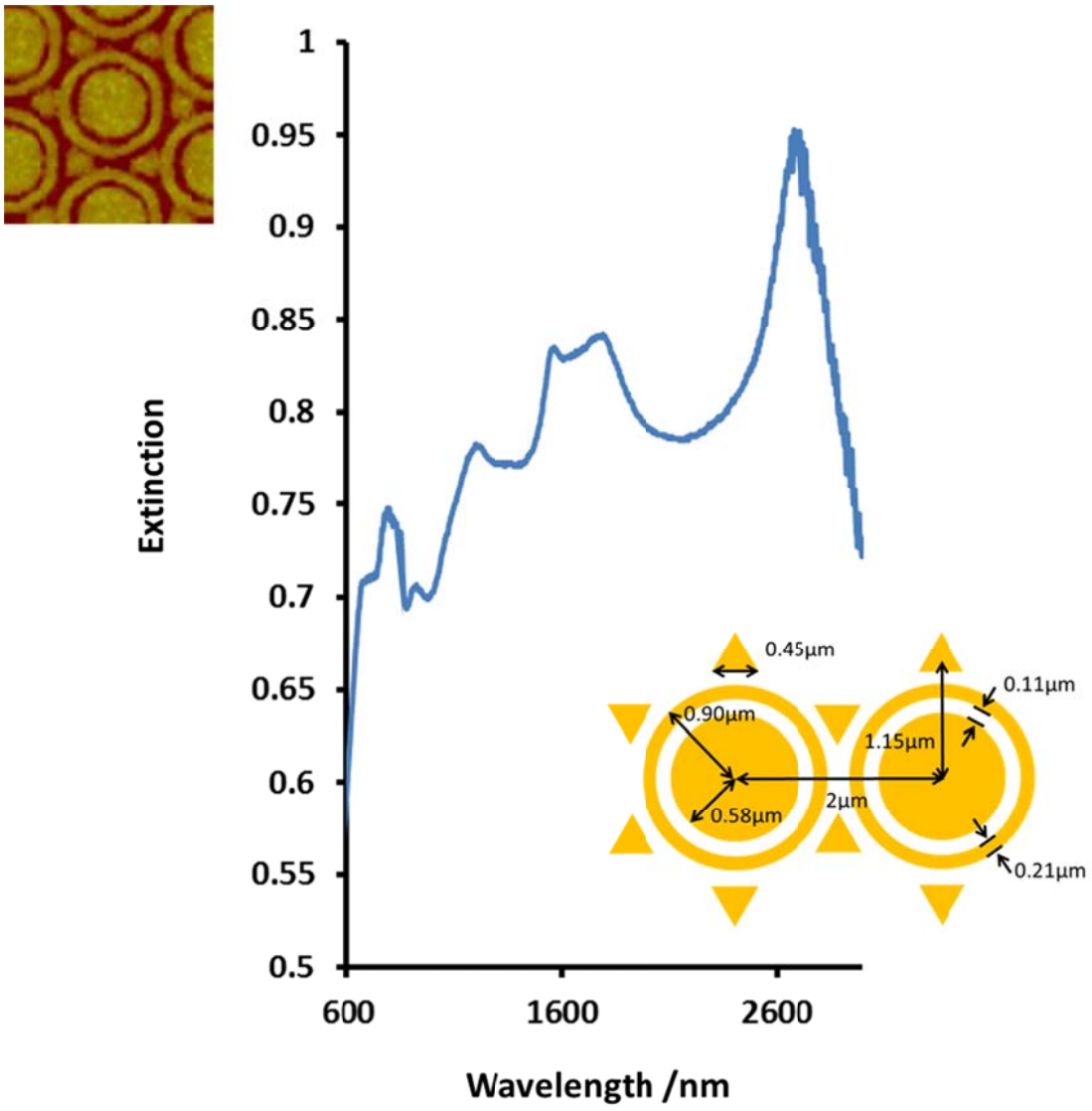

Figure 31. The second extinction spectrum of symmetric triangle-target array with labeled geometric parameters.

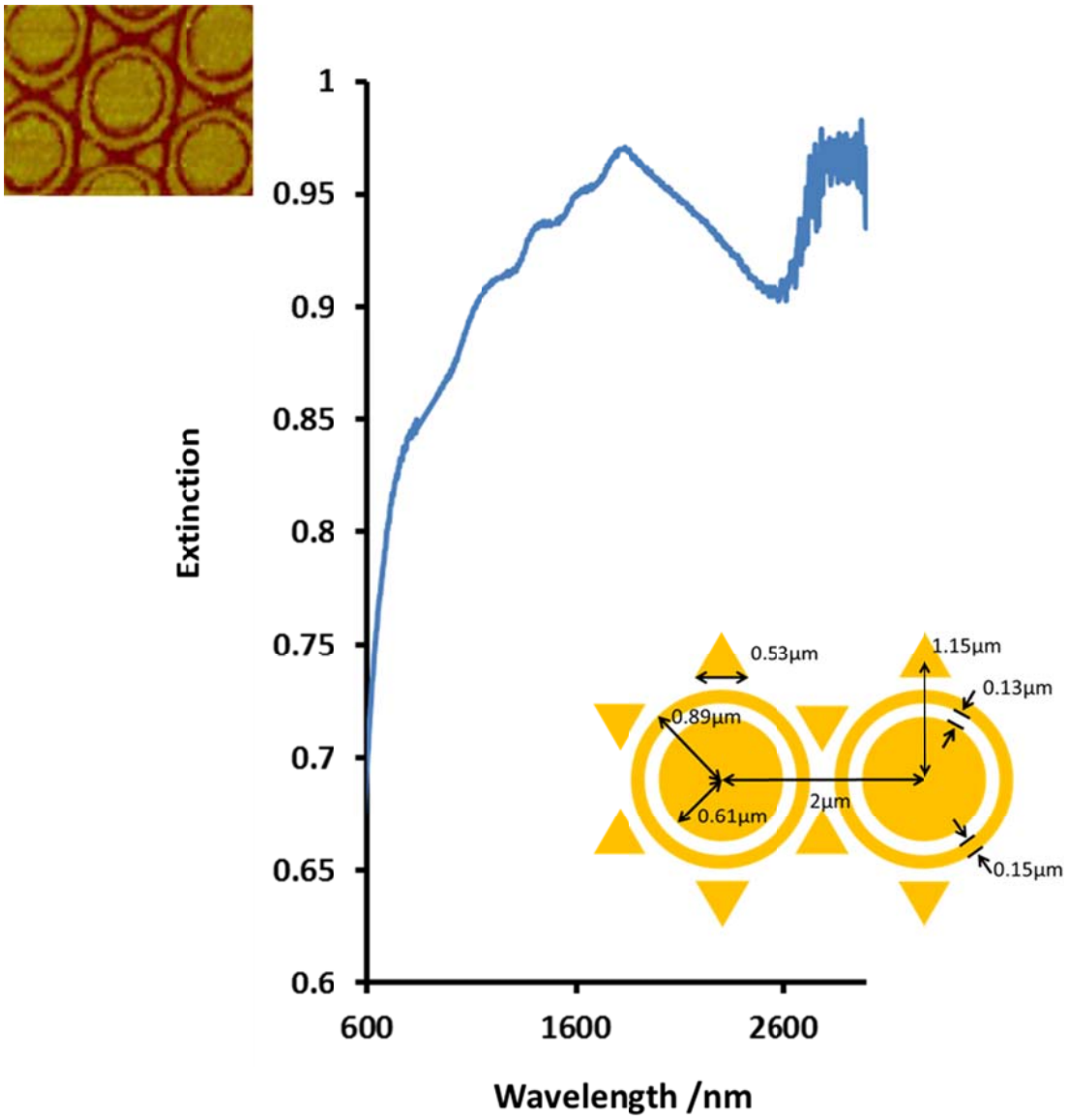

Figure 32. The third extinction spectrum of symmetric triangle-target array with labeled geometric parameters.

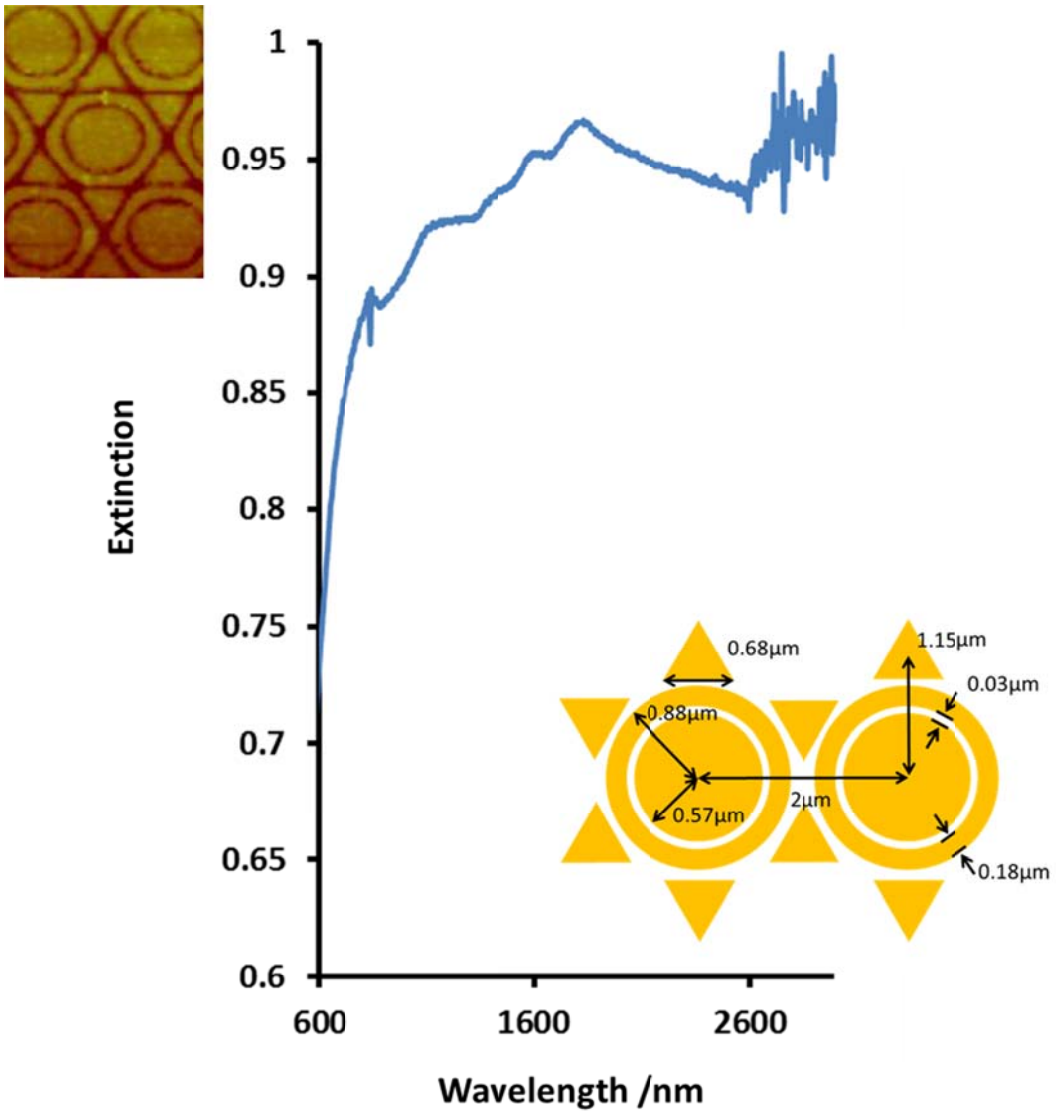

Figure 33. The fourth extinction spectrum of symmetric triangle-target array with labeled geometric parameters.

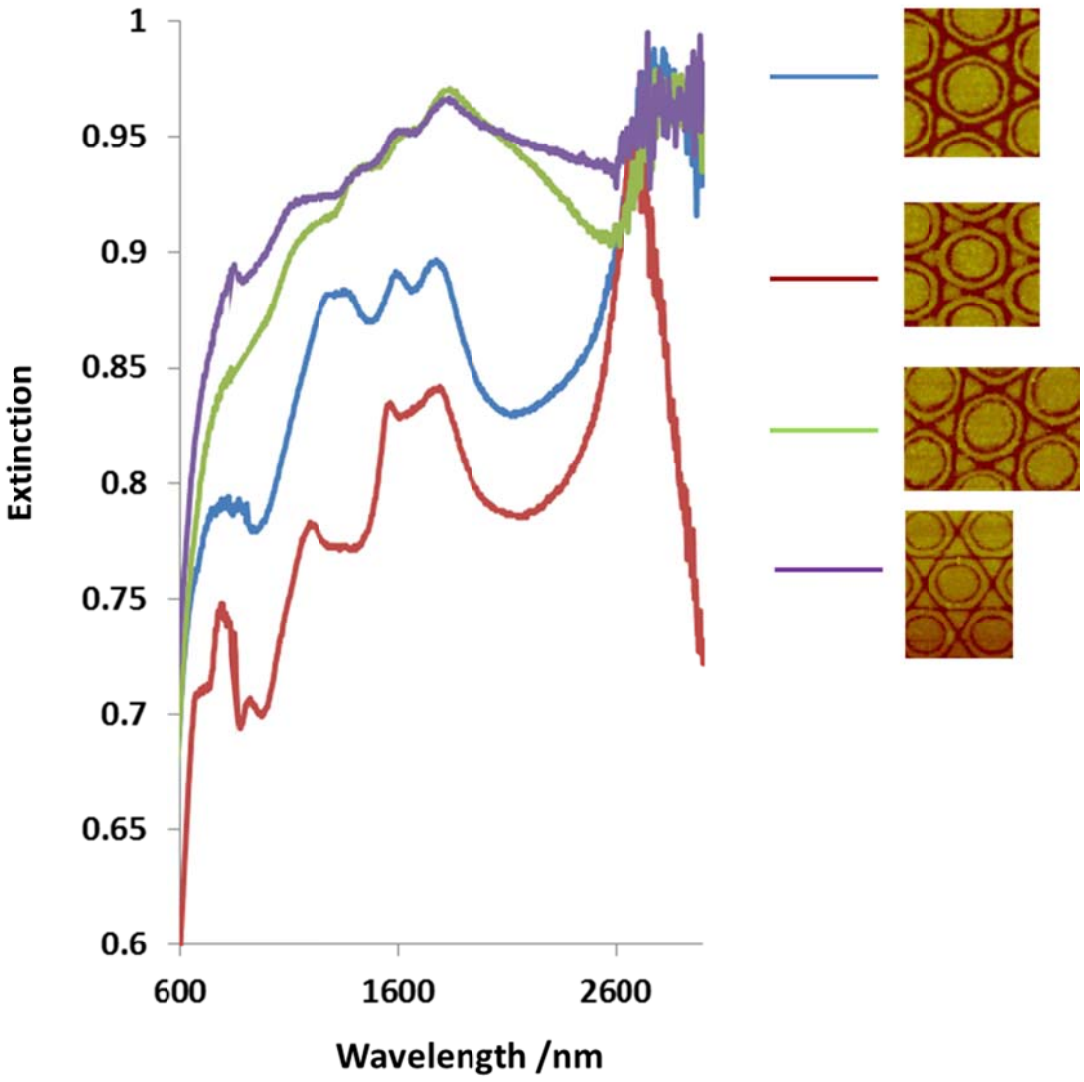

Figure 34. The structural dependence of extinction spectra for triangle-target arrays with different geometric parameters.

Four well isolated plasmon resonances located at 960 nm, 1480 nm, 1680 nm and 2150 nm were observed in the extinction spectrum of the target-triangle feature (Fig. 30). The high number of observable plasmon mode was apparently due to the

complexity its structure. The depth of 960 nm and 2150 nm dips were significantly deeper than the other two minumums. As a comparison, the ~1480 nm dip became much deeper when the gap between the outer triangles and inner targets got smaller, indicating this mode involved some sort of interactions between ring mode and triangle mode (Fig. 31). Moreover, its position also shifted a little to the blue side, indicating an increasing energy of the corresponding plasmon mode. Another small dip appeared at ~880 nm which was not observed in the previous case (Fig. 31). Apparently, a smaller gap size led to a much stronger coupling between plasmonic structures and resulted in more observable surface plasmon resonances. However, when the size of the outer triangles exceeded a certain range, the extinction spectra were only characterized by a few very weak minimums (Fig. 32 & Fig. 33). It seemed that the growth of the outer triangles led to a mismatch of the previously coupled plasmon modes. Consequently, the spectra changed to a smoother curve with only a single major dip. The overlap of spectra under all geometrical parameters was shown in Figure 34.

There are two extinction minimums located at around 1015 nm and 1510 nm for the hexagram-dot pattern (Fig. 35). The height of those dips became shallower as the line width of the hexagram web getting narrower. (Fig. 35 vs. Fig. 36). This phenomenon got even clearer as the line width becoming much broader (Fig. 37). Also, the 1015 nm dip was also blue shifted to 967 nm and a new peak appeared at around 1800 nm when the gap between the central disk and the hexagram got down to 100 nm level (Fig. 37). Therefore, the Fano-shape feature around 1800 nm was most likely to

originate from the coupling of these two moieties. An overlap of all the spectra was demonstrated in Figure. 38.

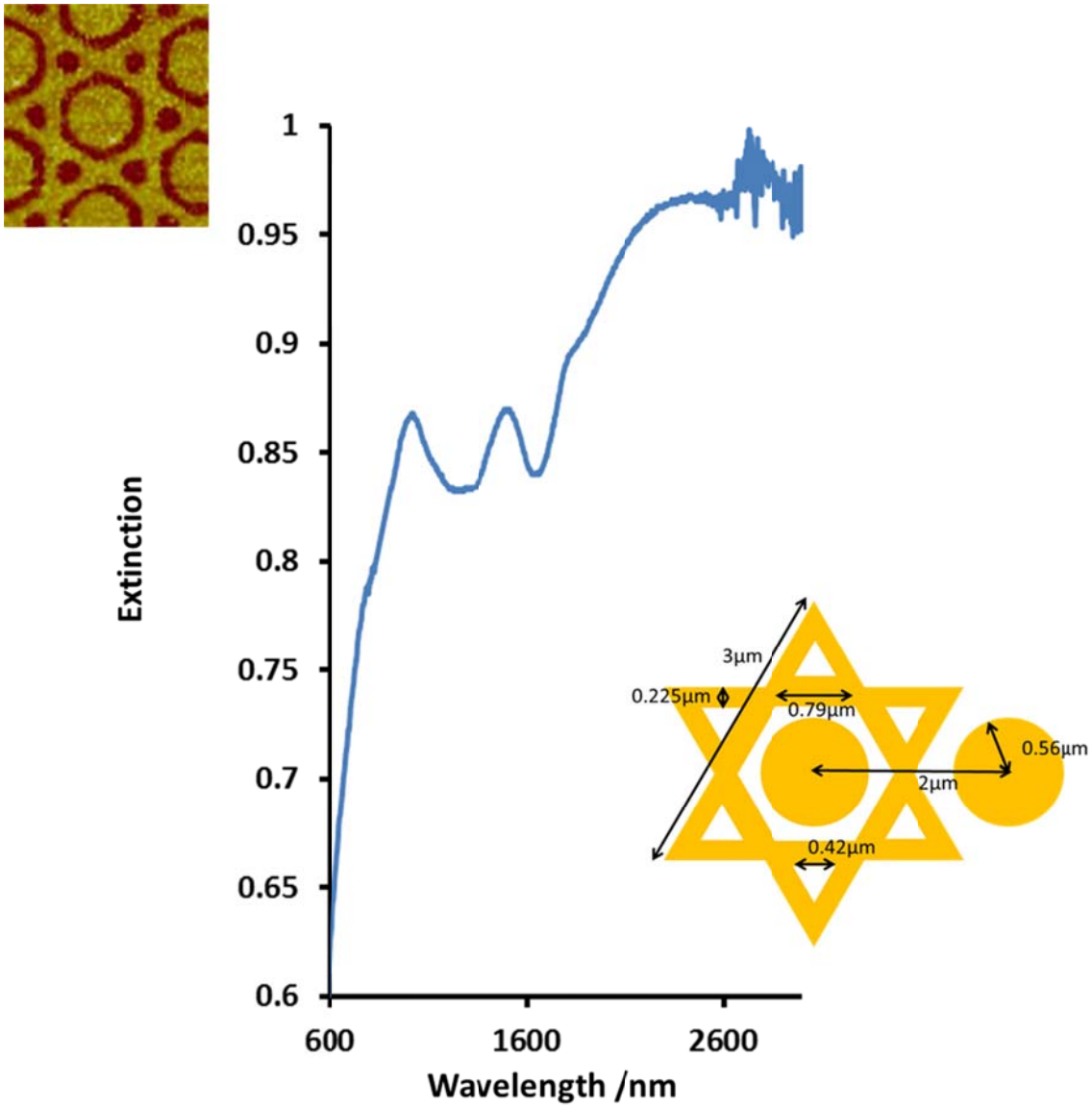

Figure 35. The first extinction spectrum of symmetric hexagram-dot array with labeled geometric parameters.

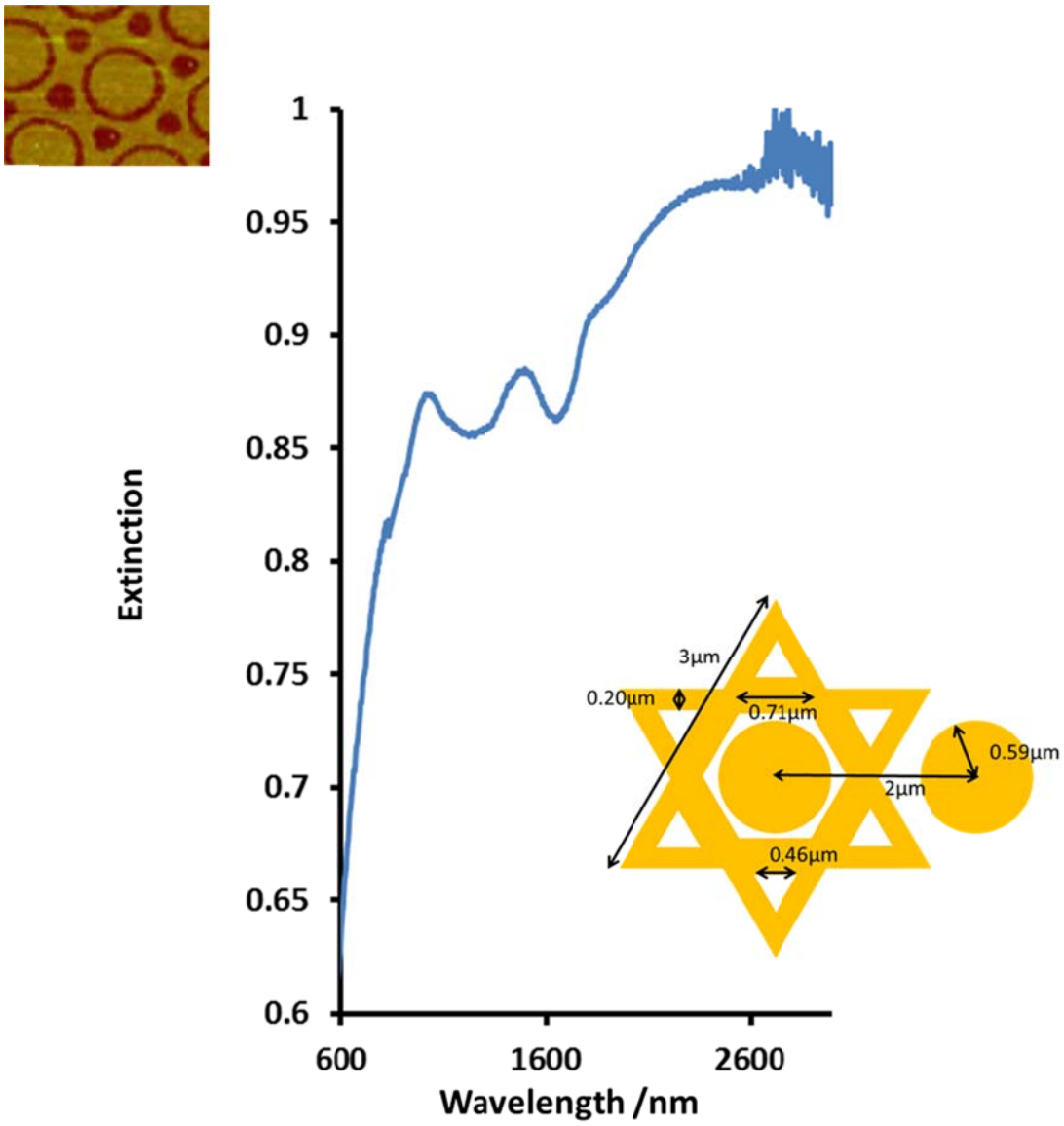

Figure 36. The second extinction spectrum of symmetric hexagram-dot array with labeled geometric parameters.

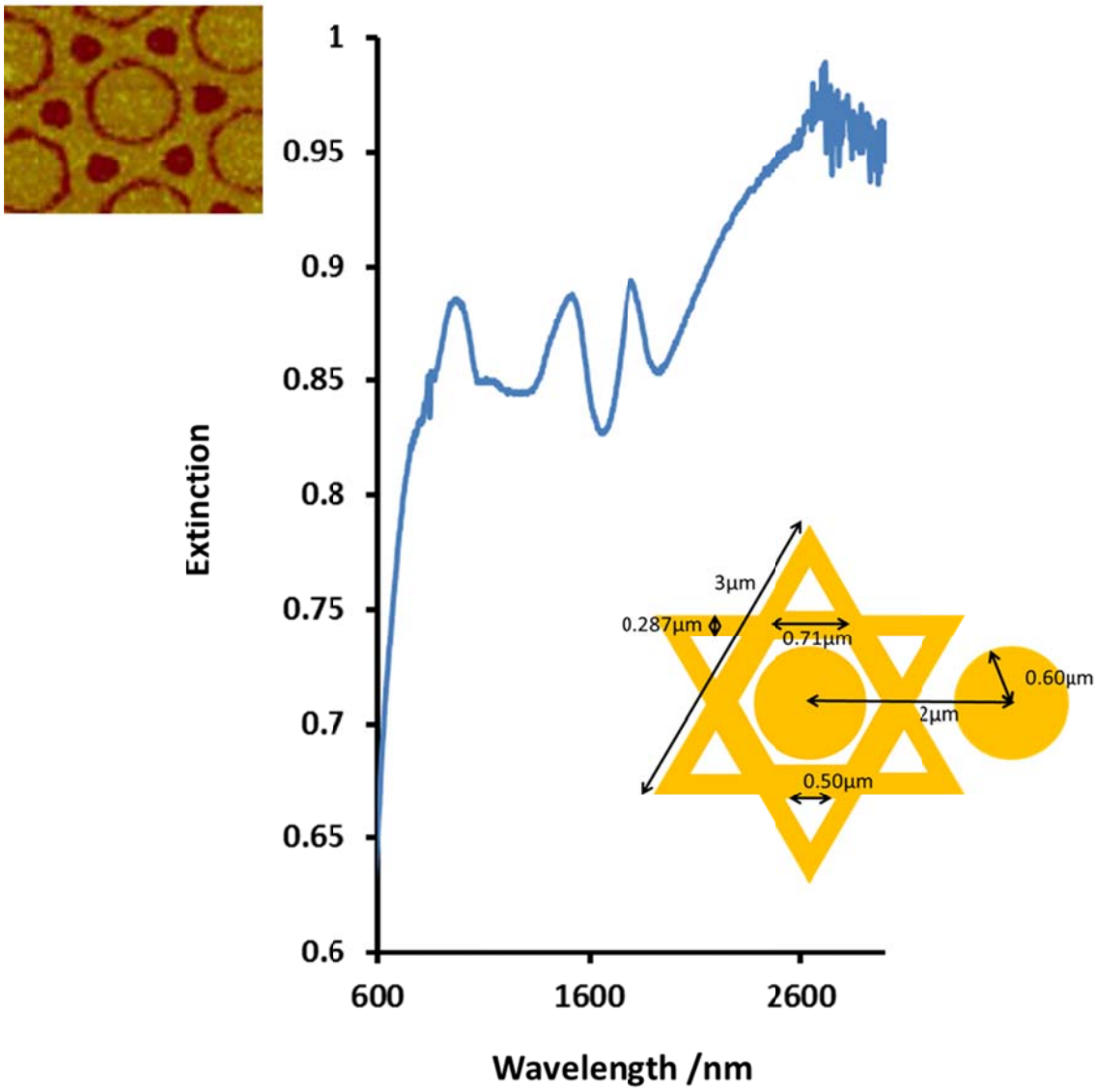

Figure 37. The third extinction spectrum of symmetric hexagram-dot array with labeled geometric parameters.

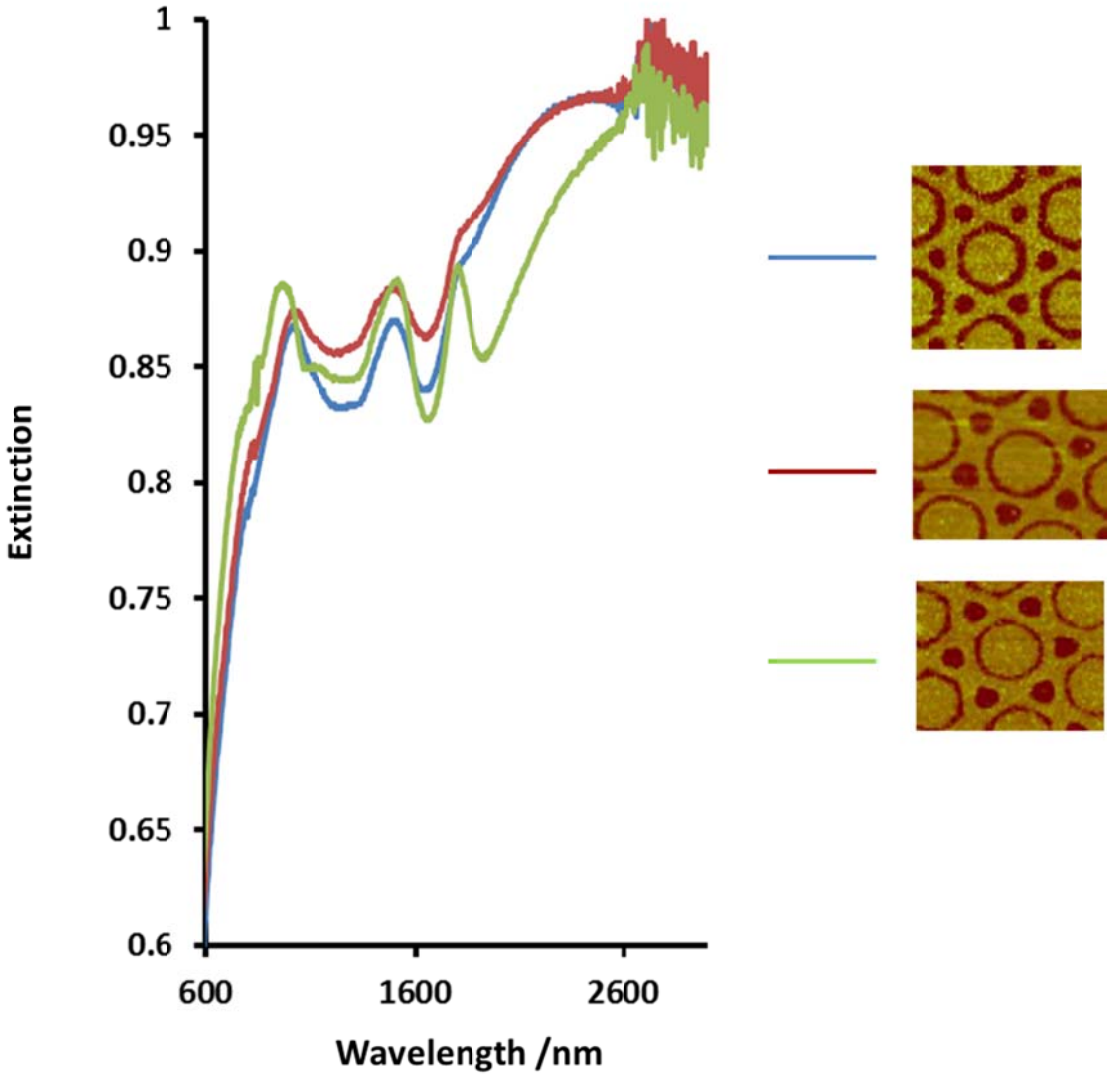

Figure 38. The structural dependence of extinction spectra for hexagram-dot arrays with different geometric parameters.

The extinction spectra of triangle-dot structure was characterized by a minimum at ~1520 nm and a broad peak right to the dip (Fig. 39 & Fig. 40). The symmetry group of this structural type was D_{6h}. Therefore, the collective modes that would couple

efficiently to light were the E_{1u} modes using the plasmon hybridization concept.[65] The minimum at ~1520 nm should be the Fano resonance from the interference of a bonding bright (superradiant) mode where the dipolar plasmons of all nanoparticles oscillated in phase and in the same direction and the antibonding dark (subradiant) mode, where the dipolar moment of the center particle opposeed the dipole moment of the surrounding triangles. The broad shape of this Fano peak was probably due to the significant size dependence of the subradiant mode. Because of the stronger hybridization of the higher order modes, the subradiant mode would red shift more significantly than the superradiant mode for an increasing feature size. Therefore, the gap between the two plasmon resonances would become pretty wide for triangles over 800 nm in size.[65] The superradiant bonding E_{1u} mode was located at 1160 nm for the case in which the six triangles were separated by a small gap (Fig. 39 & Fig. 40). A red shift of the superradiant mode was observed in case when the triangles were connected (Fig. 41). Larger triangles resulted in stronger hybridization between the individual units and induced this red-shift of the corresponding plasmonic mode.[102k] In addition, a Fano peak also appeared at around 1830 nm. This character was similar as the Fano-resonance in annular aperture structure, indicating that this structure could be taken as a transit between annular aperture and the triangle-dot feature. When we further shrank down the size of triangles, the curve became quite smooth with only tiny dips which indicated that the plasmonic coupling was actually broken by a huge gap (Fig. 42). The overlapped spectra for all the triangle-dot features could be found in Figure 43.

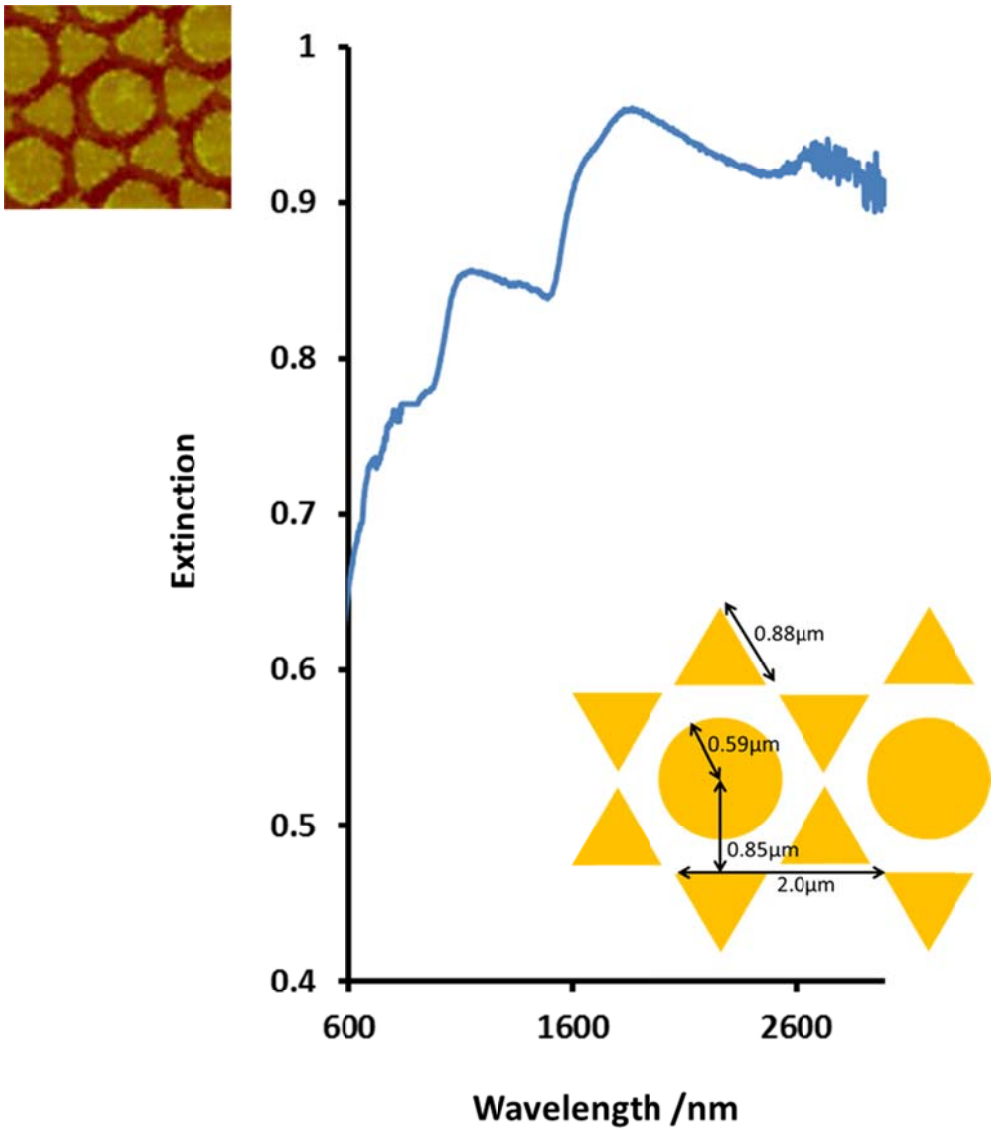

Figure 39. The first extinction spectrum of symmetric triangle-dot array with labeled geometric parameters.

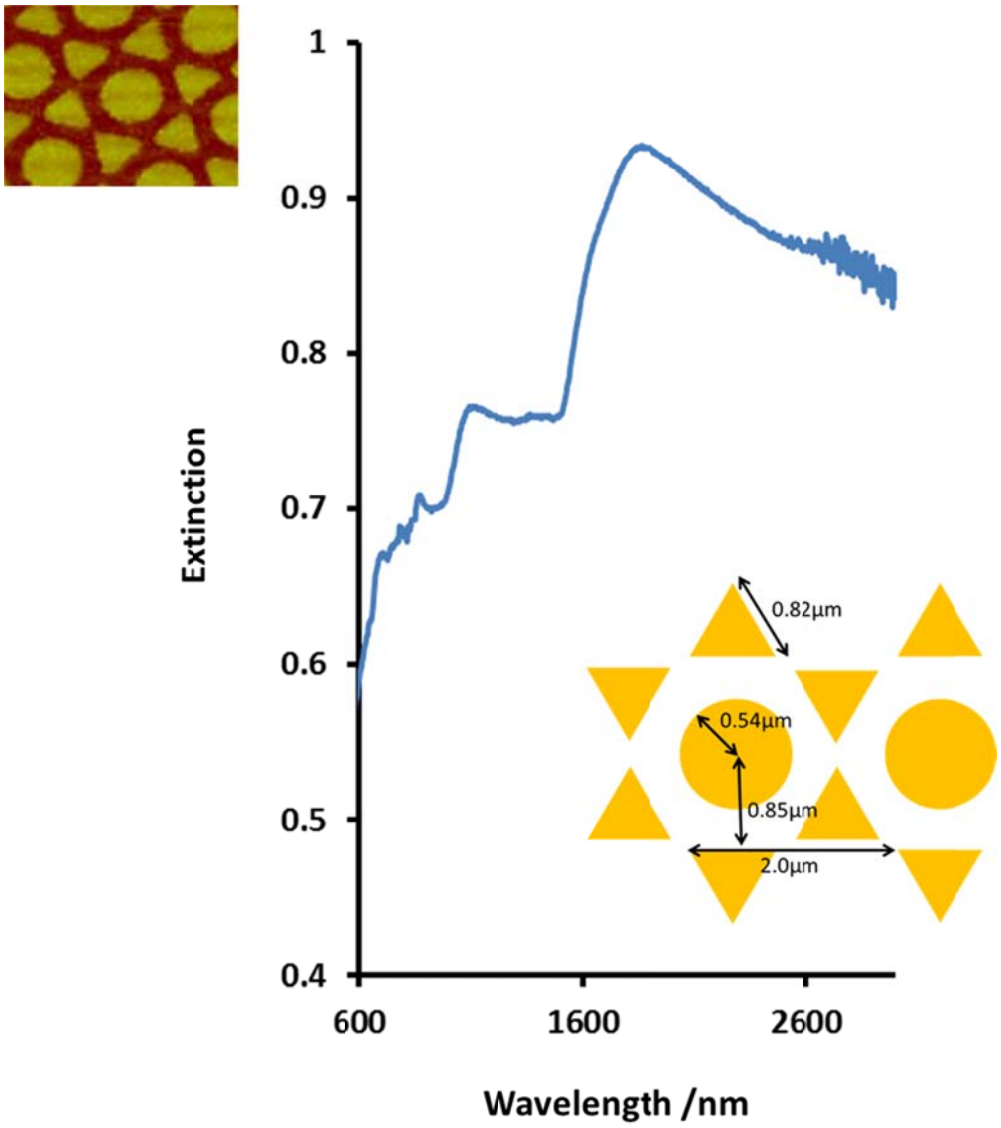

Figure 40. The second extinction spectrum of symmetric triangle-dot array with labeled geometric parameters.

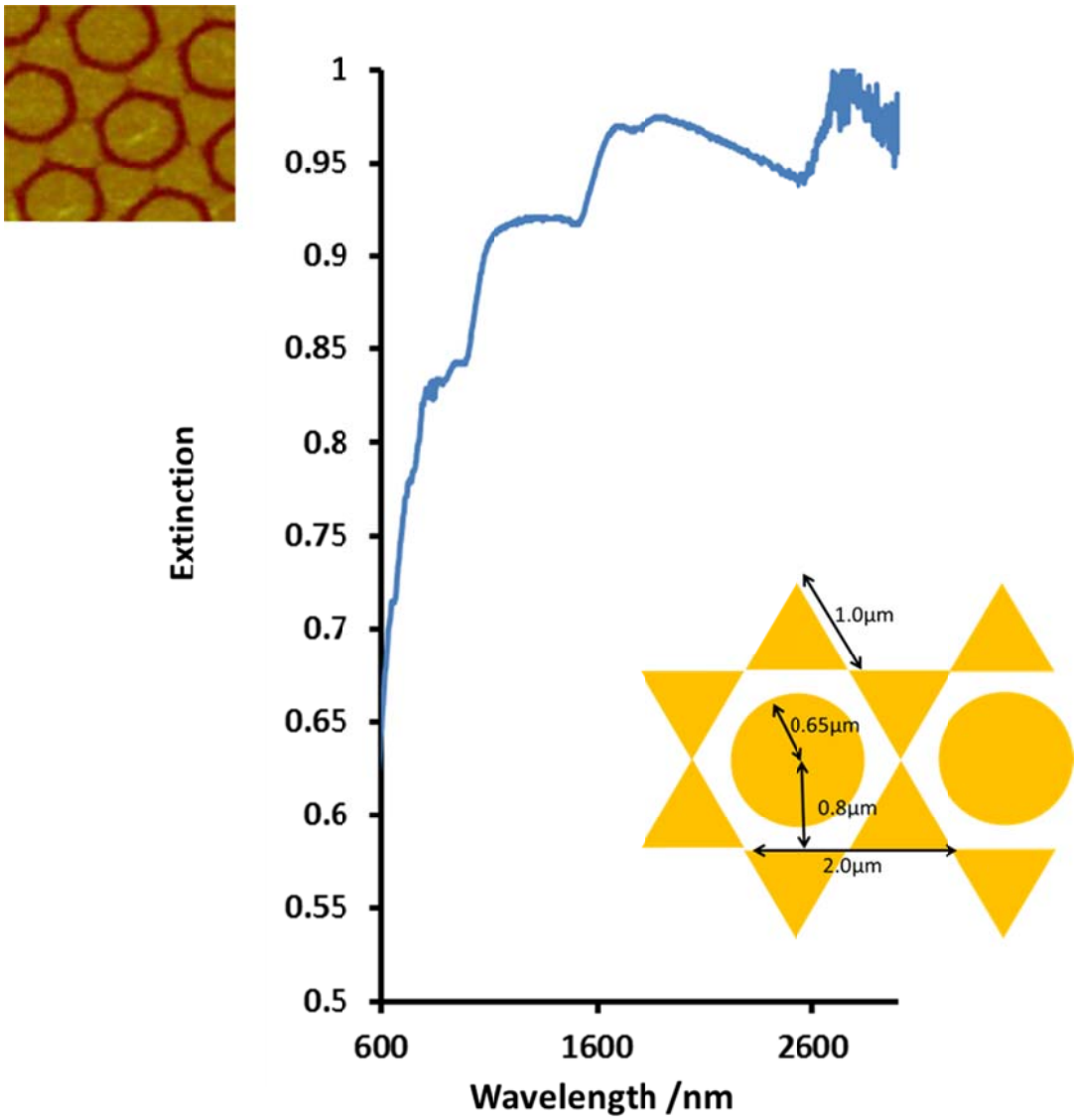

Figure 41. The third extinction spectrum of symmetric triangle-dot array with labeled geometric parameters.

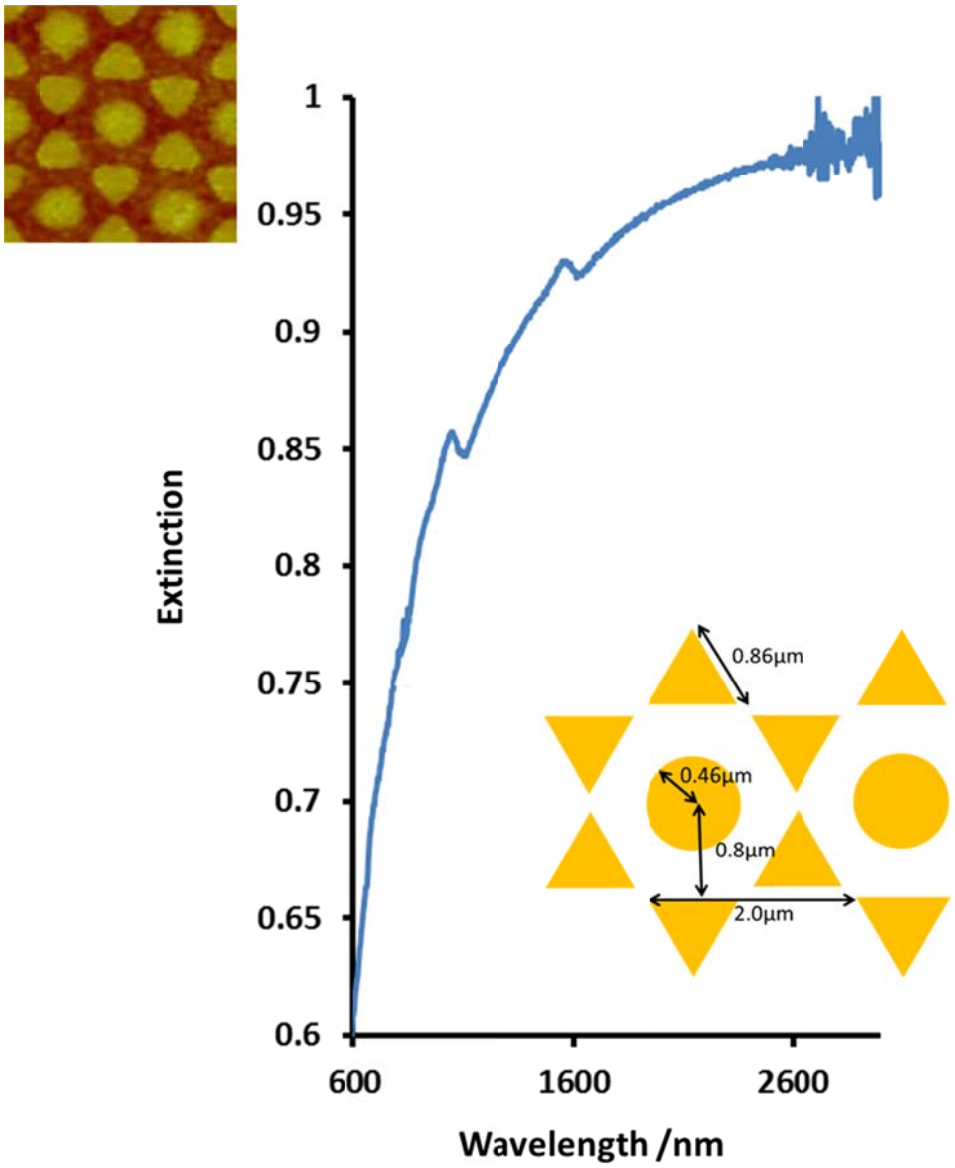

Figure 42. The fourth extinction spectrum of symmetric triangle-dot array with labeled geometric parameters.

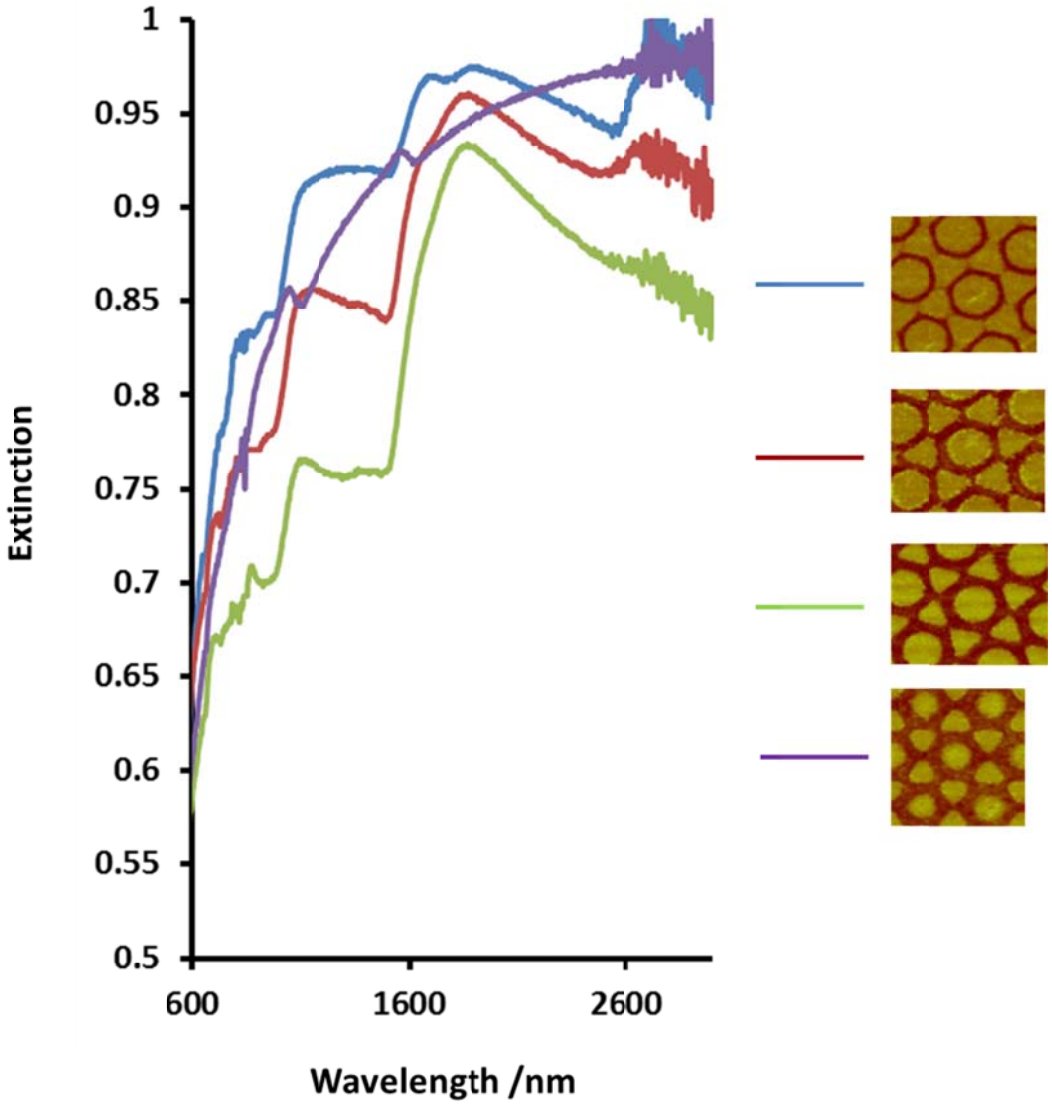

Figure 43. The structural dependence of extinction spectra for triangle-dot arrays with different geometric parameters.

The non-concentric target feature had been fabricated and well investigated.[46, 123] In general, it possessed a clear Fano-resonance which depended on coupling between the dark quadrupolar ring plasmon and the superradiant antibonding dipolar disk-ring mode.

As a result, the Fano peak appeared at ~1400 nm for a single nonconcentric target.[46, 123] Similarly, we observed the Fano resonance at around 1600 nm which was probably due to a larger size of our nano-patterns (Fig. 44). Simulations showed that for a larger pattern, the Fano peak would be shifted to a longer wavelength (Fig. 45). The profile of our extinction spectrum generally matches simulations which demonstrated the capability of our technique in the fabrication of asymmetric features.

Extinction spectra of nonconcentric annular apertures with different eccentricity were shown in Figure 46 & 47. Besides the expected extraordinary optical transmission at ~1560 nm, a Fano-like resonances was also identified from the curve at 1780 nm. Compared to the feature with a smaller eccentricity, the other pattern exhibited much narrower Fano-like peak (Fig. 47). Moreover, the peak was also deeper, indicating a stronger coupling between plasmonic modes (Fig. 48). We attributed this to the stronger coupling due to the smaller gap size in the feature. However, if we further shrank the gap on all the directions of the inner disk, the transmittance would become very weak (Fig. 49 & Fig. 50). This would be easy to understand because in those cases the gaps were too small (<1/10) compared to the wavelength of incident light.

Two non-concentric triangle-dot patterns were examined by UV-visible-NIR spectrometer (Fig. 51 & Fig. 52). Their extinction spectra were similar as those of symmetric triangle-dot features. The Fano minimum was found at ~1520 nm for both of the structures we tested. Moreover, the subradiant mode right to the dip was much broader than those in symmetric patterns. This might indicate that the hybridization of the higher order modes was more complicated in the asymmetric case which broadened

the corresponding plasmonic mode. A comparison between the optical properties of non-concentric triangle dot arrays was shown in Figure 53.

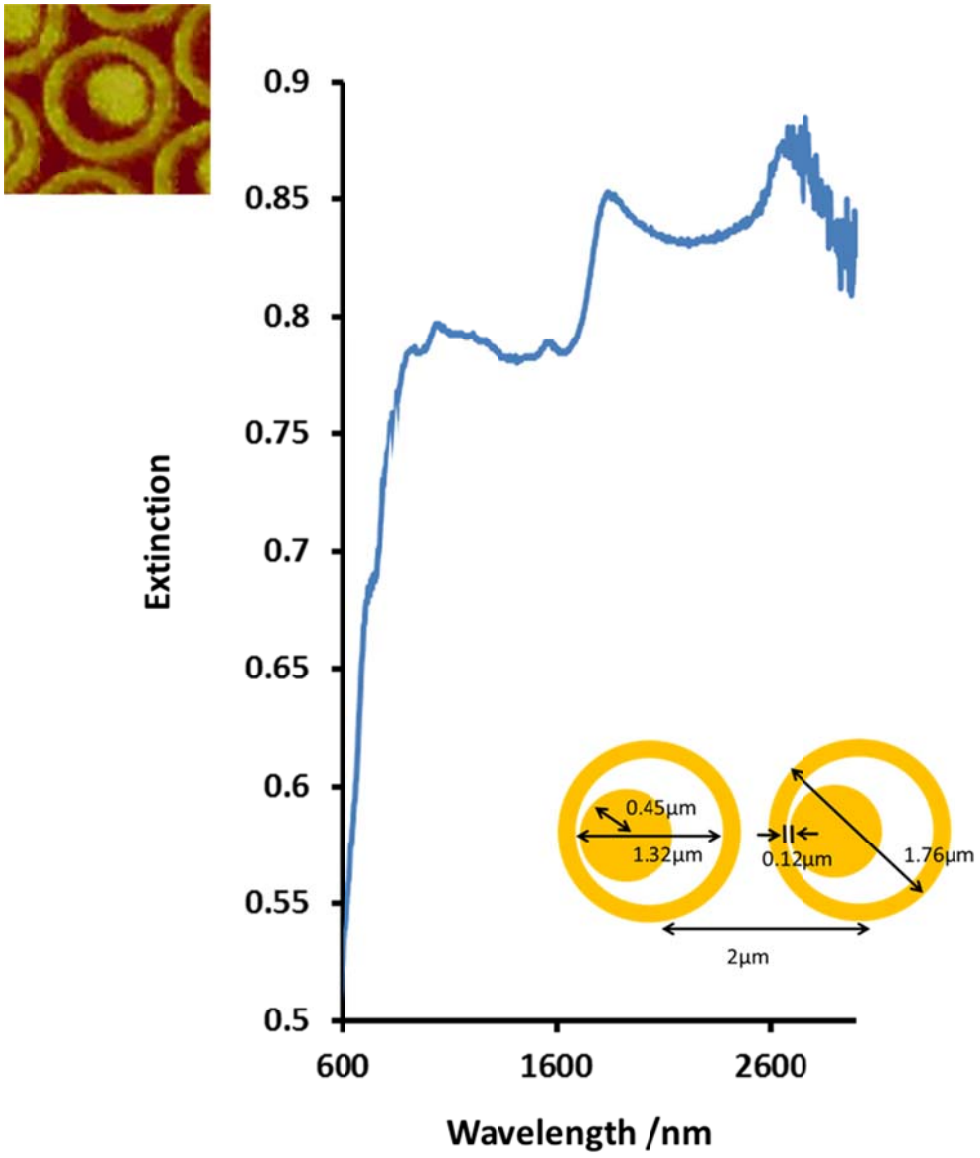

Figure 44. The extinction spectrum of asymmetric target array.

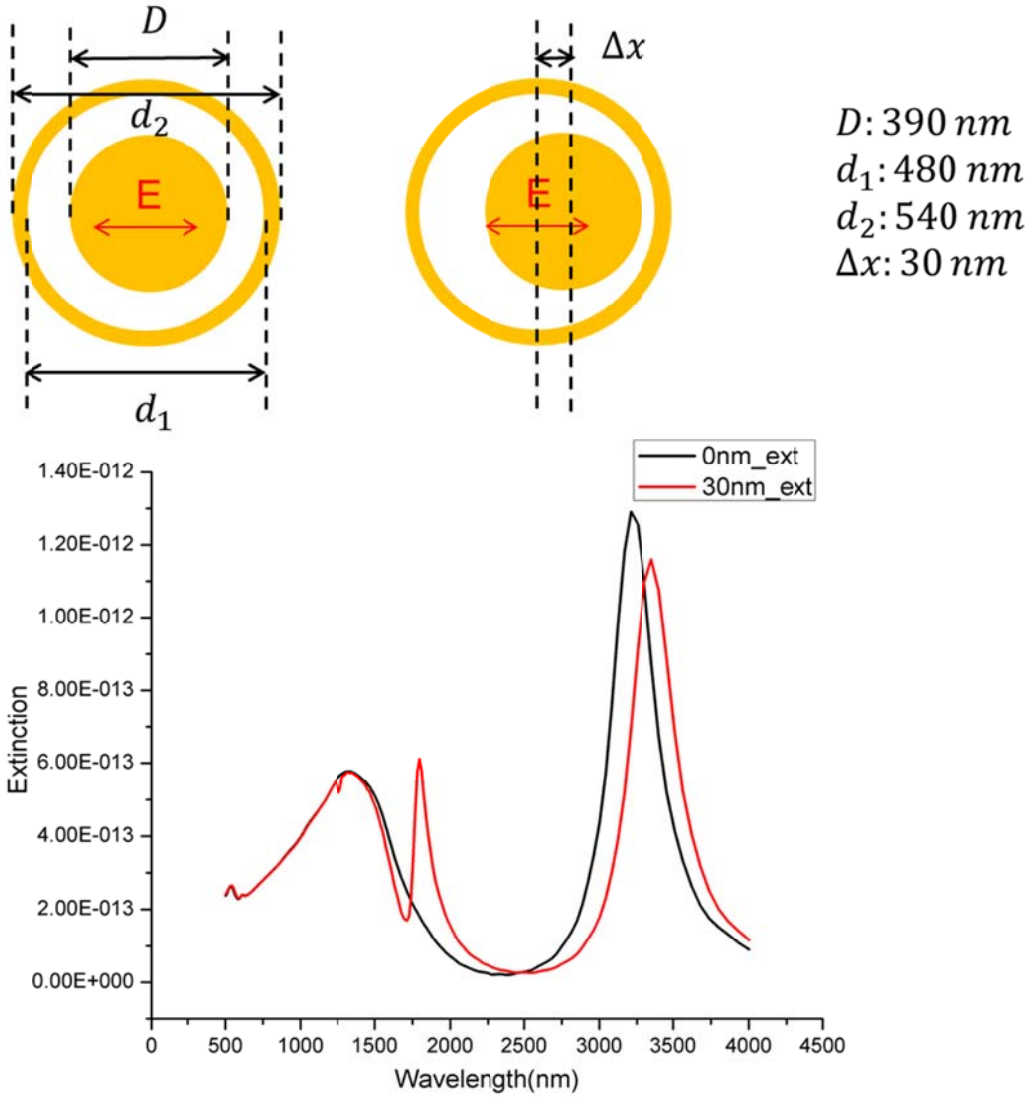

Figure 45. Simulated extinction spectra of symmetric and asymmetric target array.

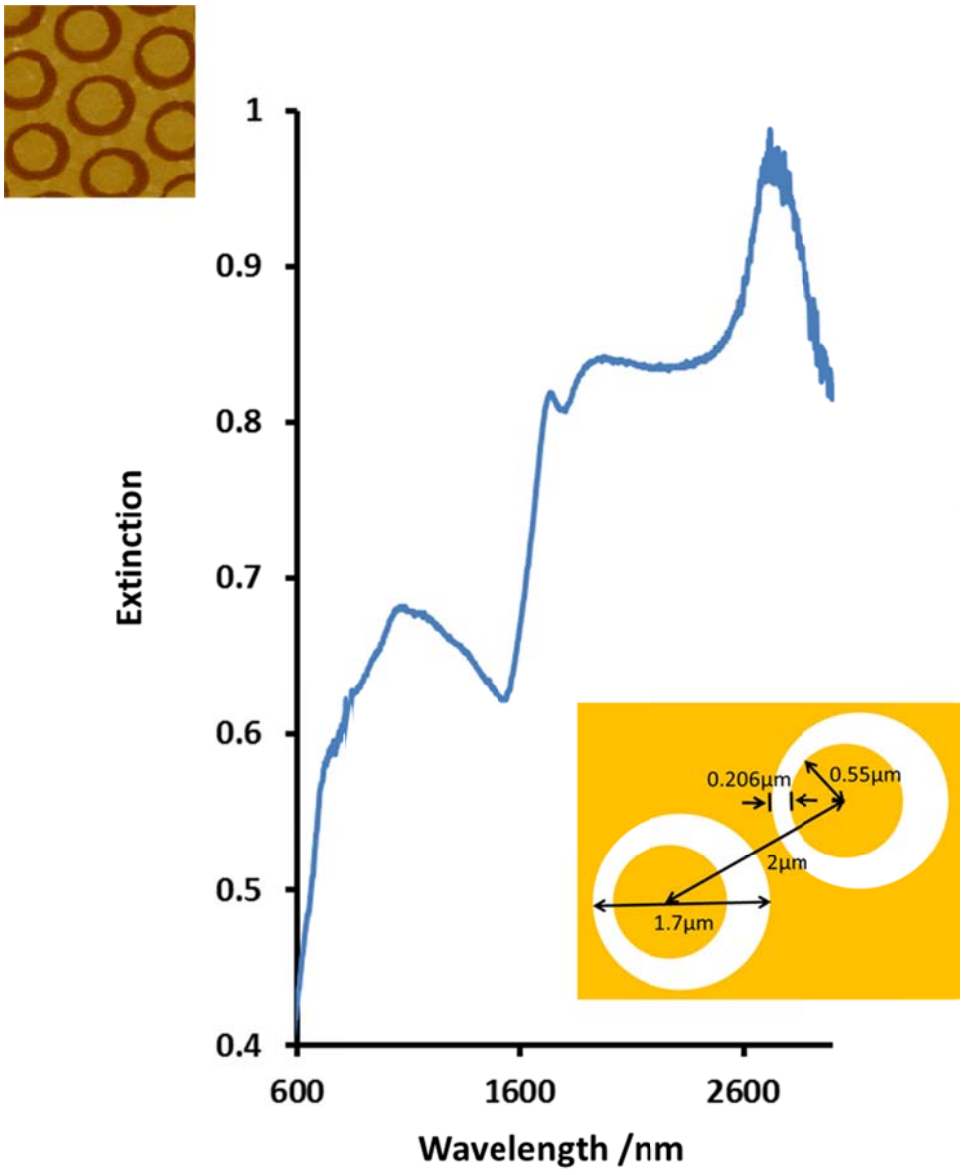

Figure 46. The first extinction spectrum of asymmetric annular aperture array with labeled geometric parameters.

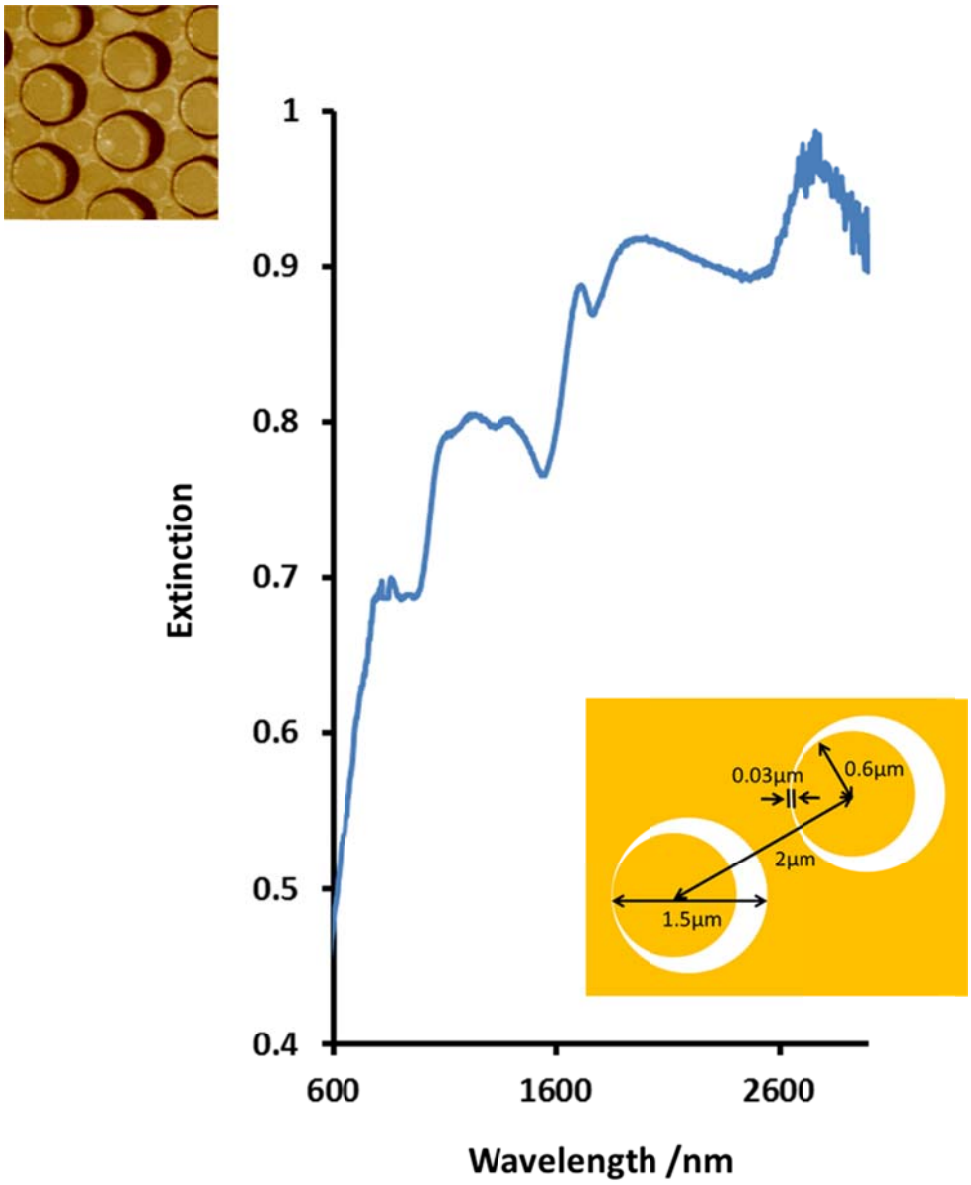

Figure 47. The second extinction spectrum of asymmetric annular aperture array with labeled geometric parameters.

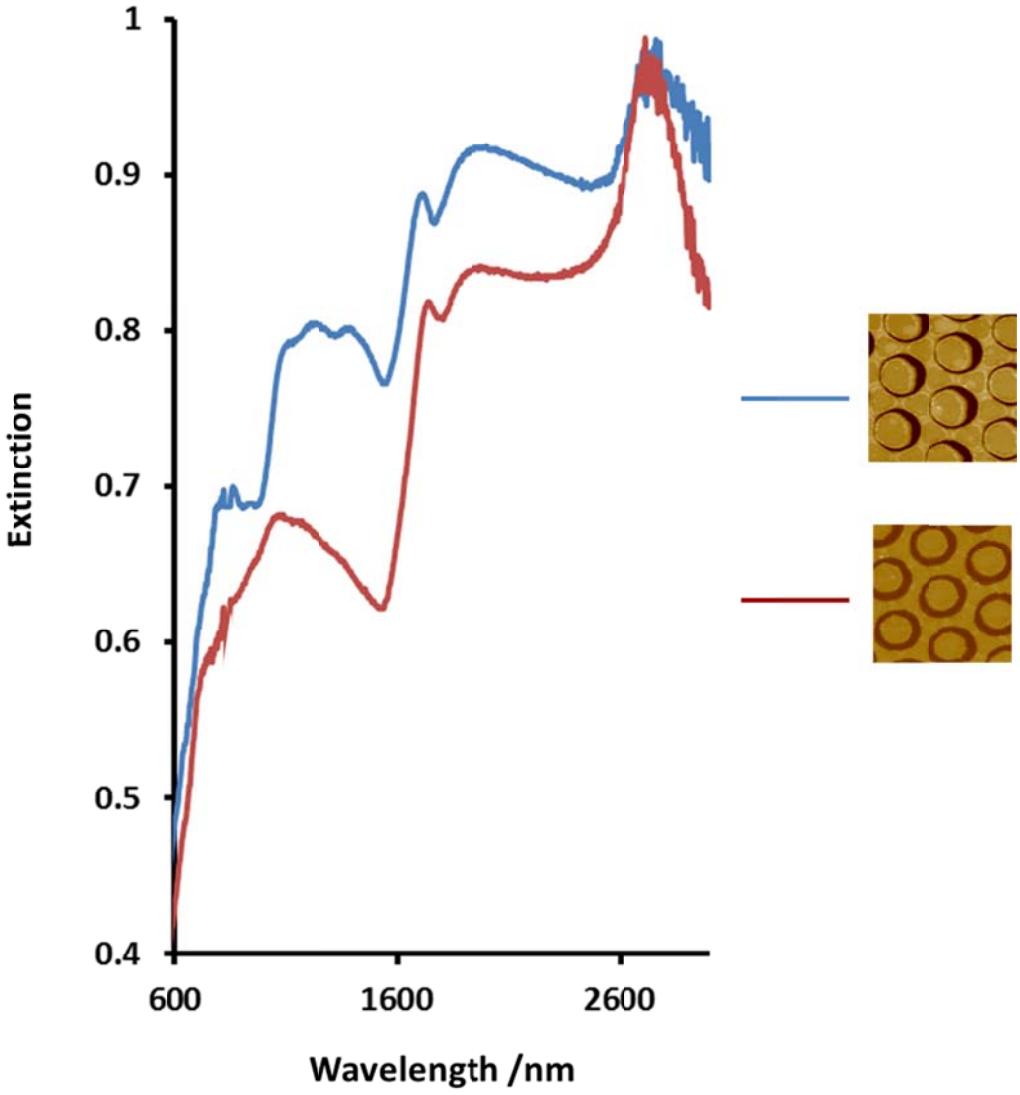

Figure 48. The structural dependence of extinction spectra for asymmetric annular aperture arrays with different geometric parameters.

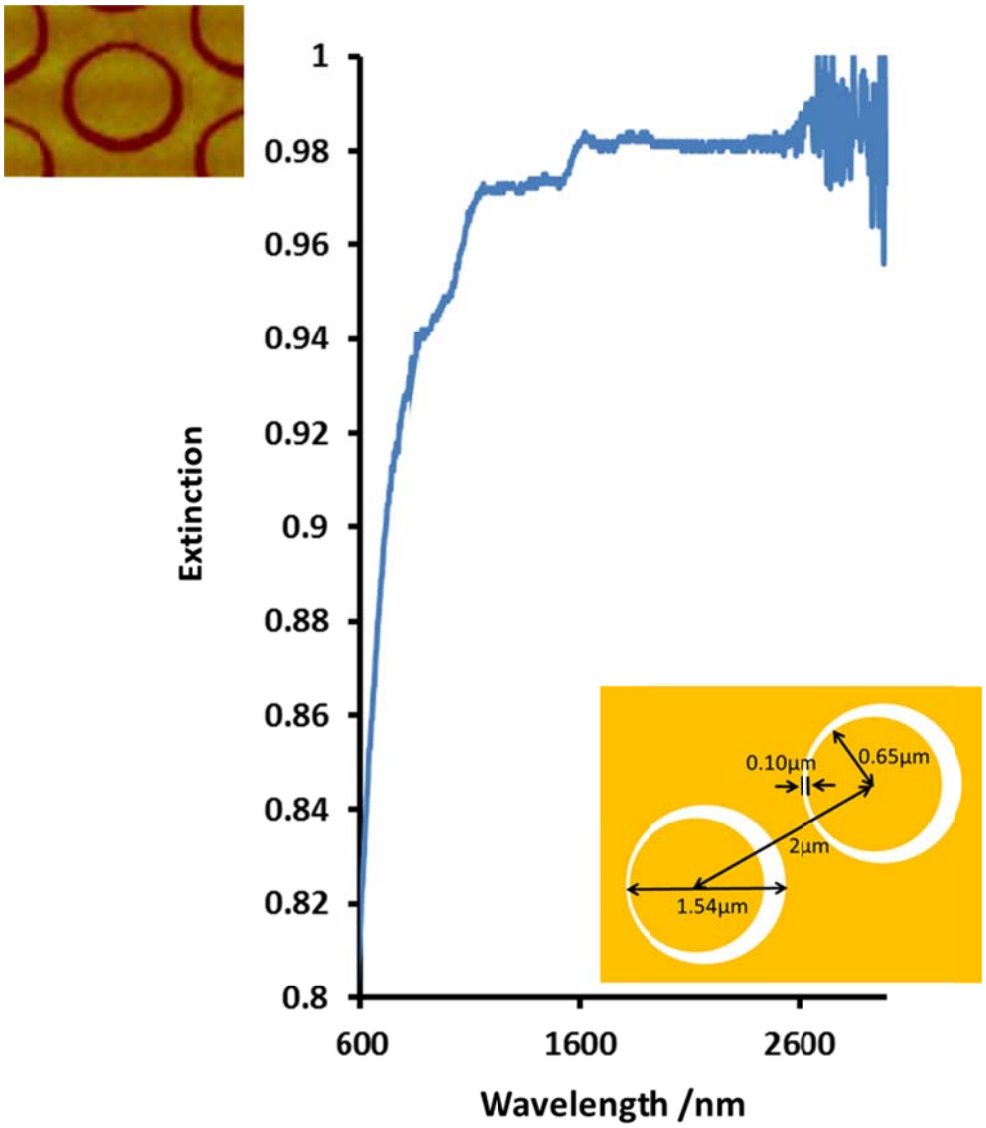

Figure 49. The third extinction spectrum of asymmetric annular aperture array with labeled geometric parameters.

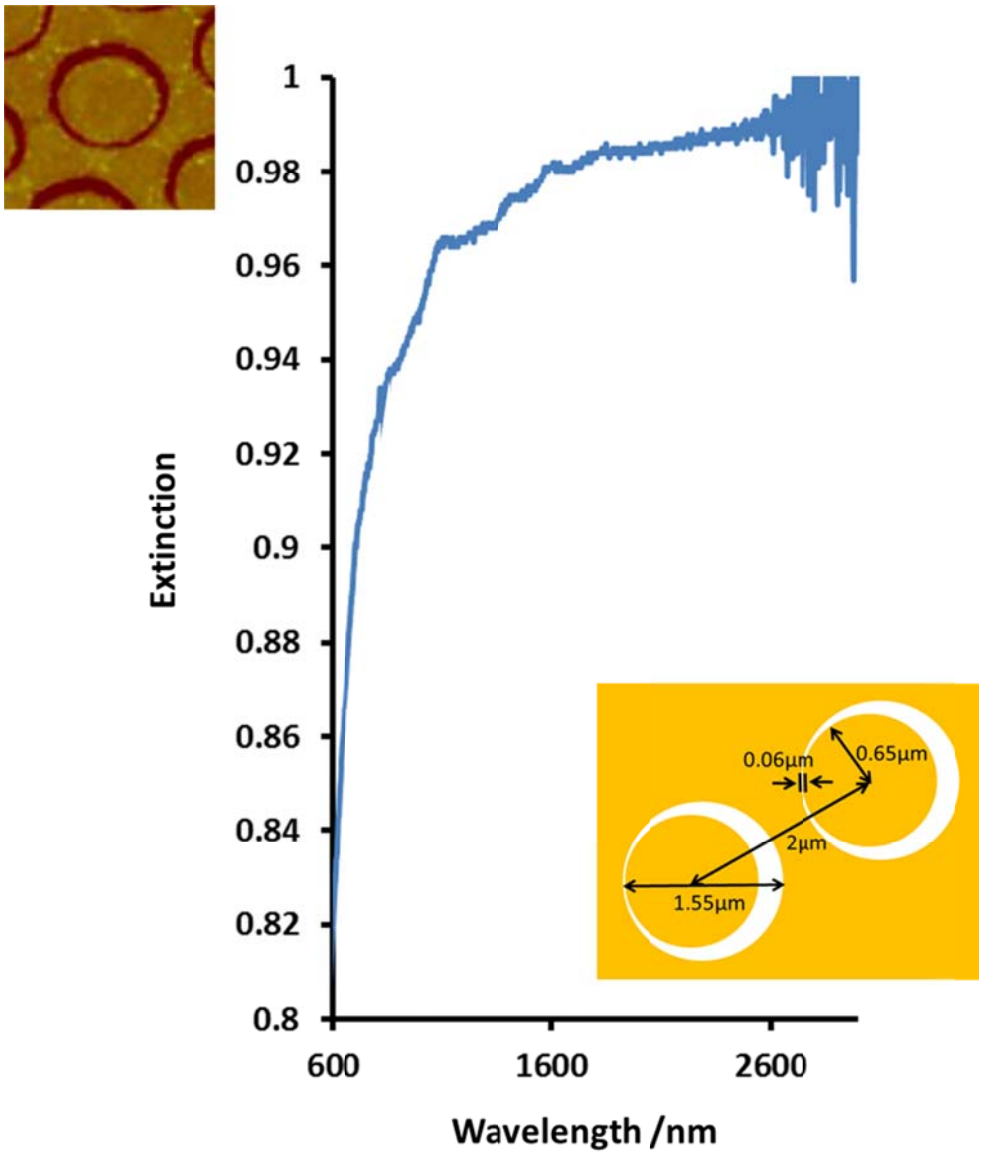

Figure 50. The fourth extinction spectrum of asymmetric annular aperture array with labeled geometric parameters.

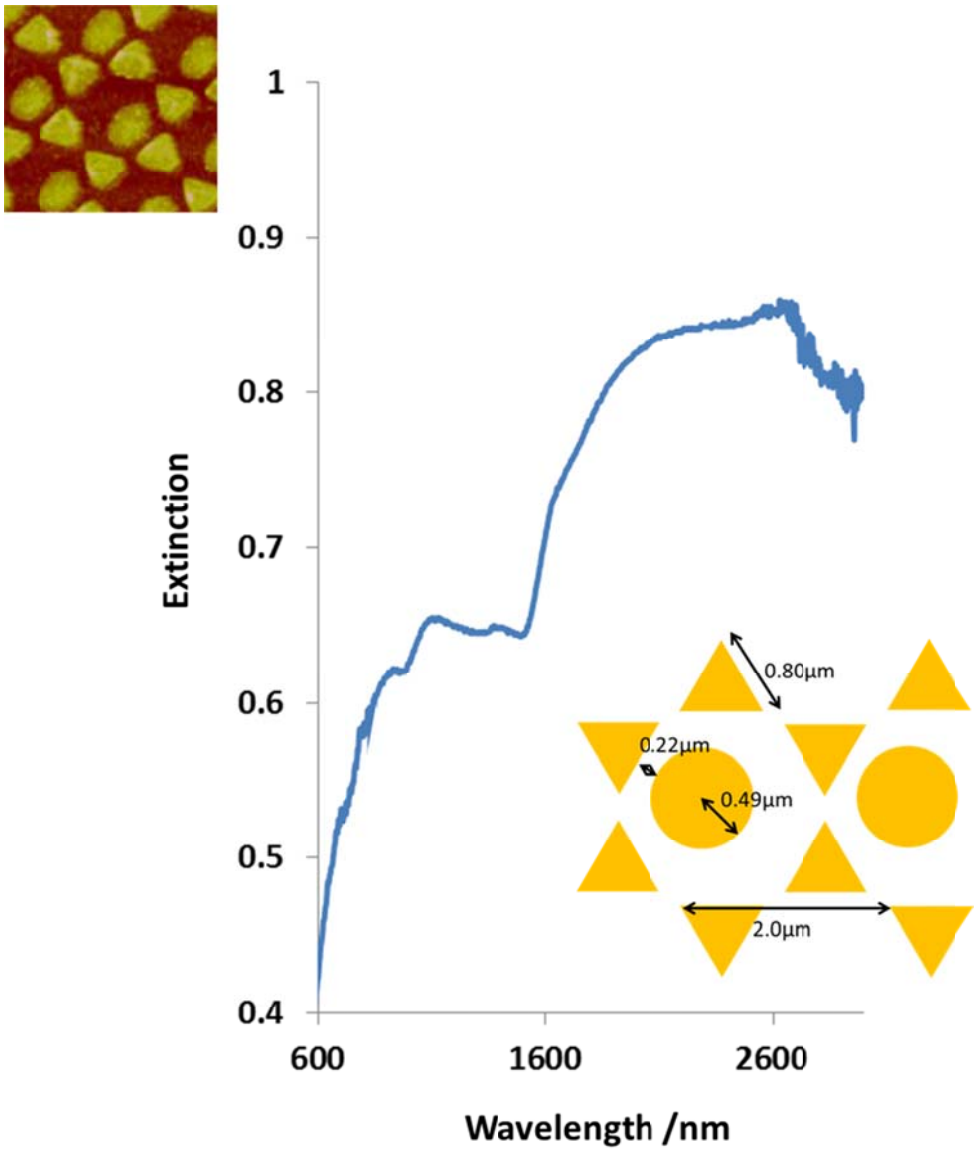

Figure 51. The first extinction spectrum of asymmetric triangle-dot array with labeled geometric parameters.

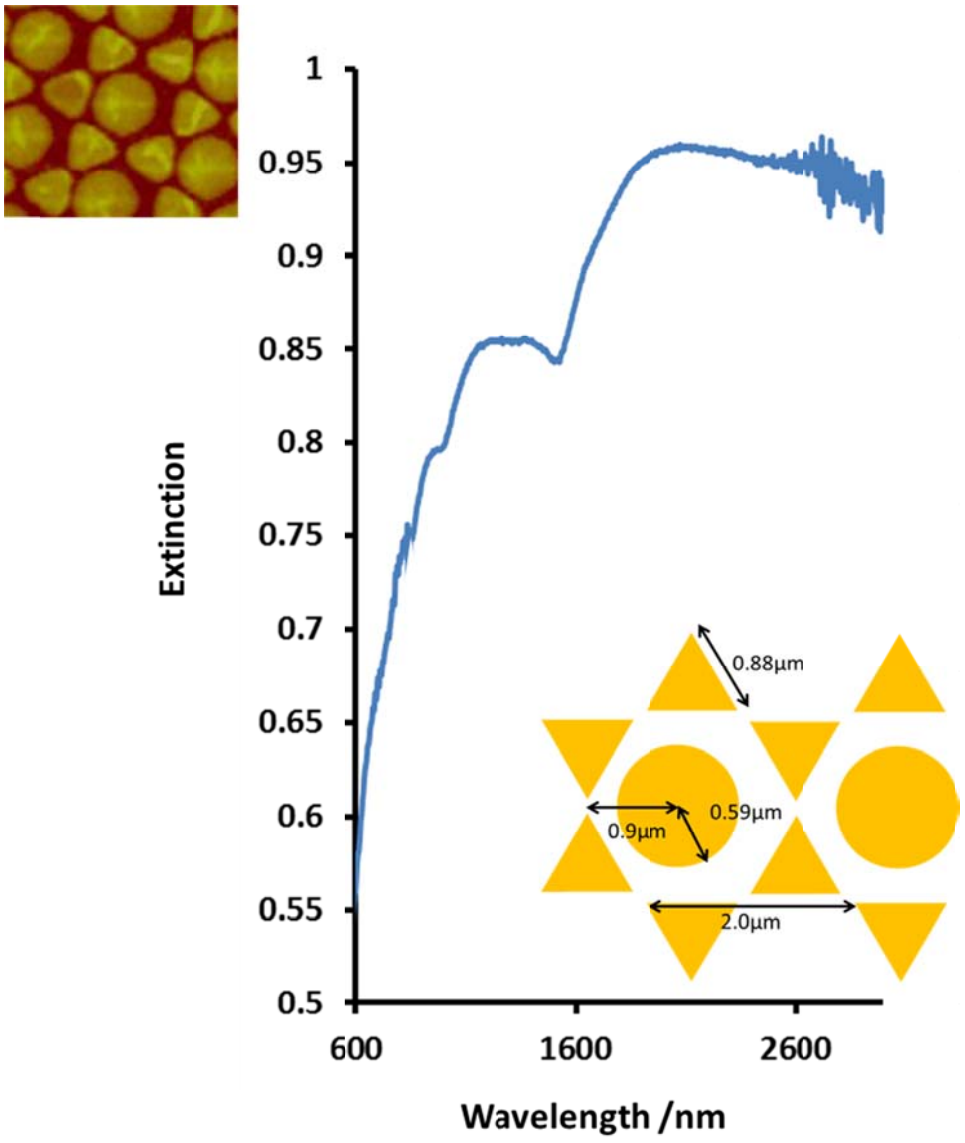

Figure 52. The second extinction spectrum of asymmetric triangle-dot array with labeled geometric parameters.

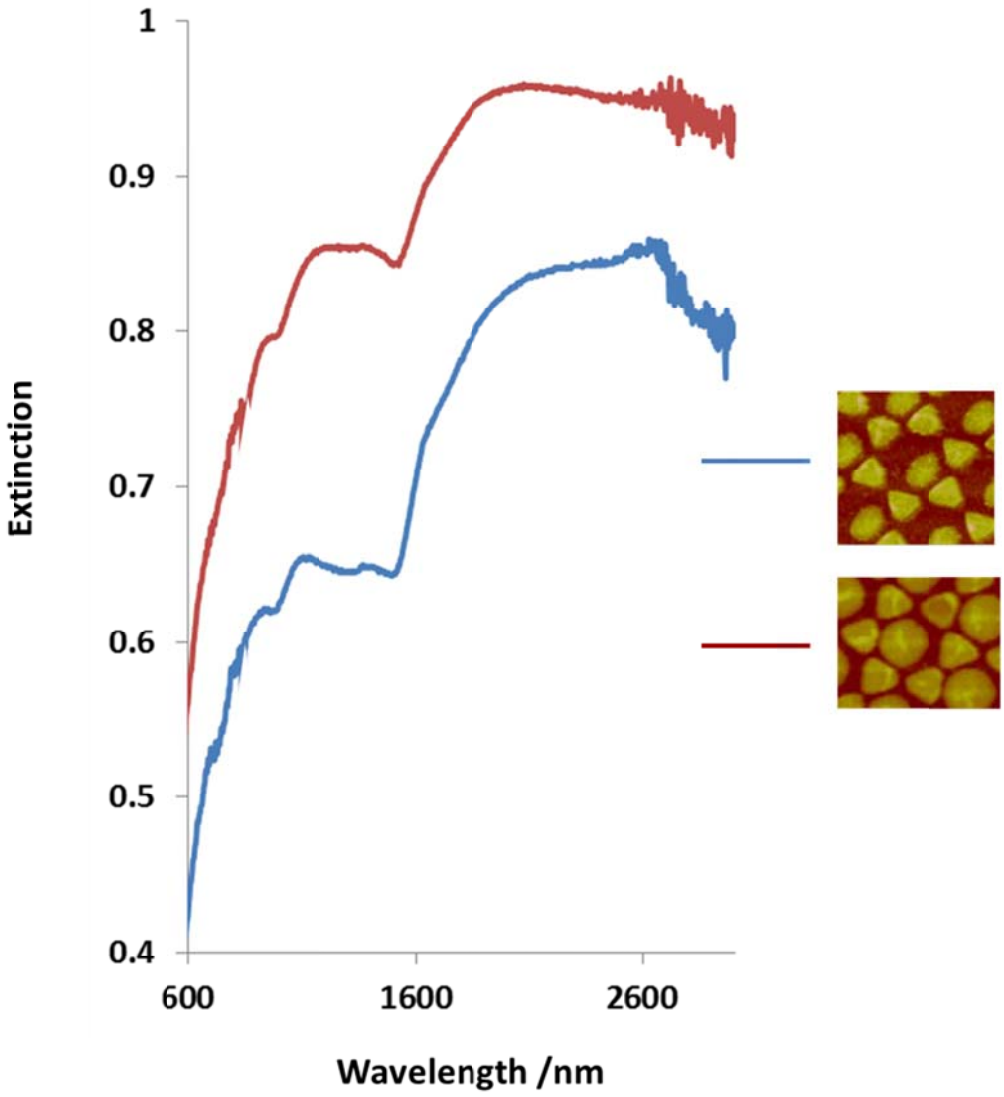

Figure 53. The structural dependence of extinction spectra for asymmetric triangle-dot arrays with different geometric parameters.

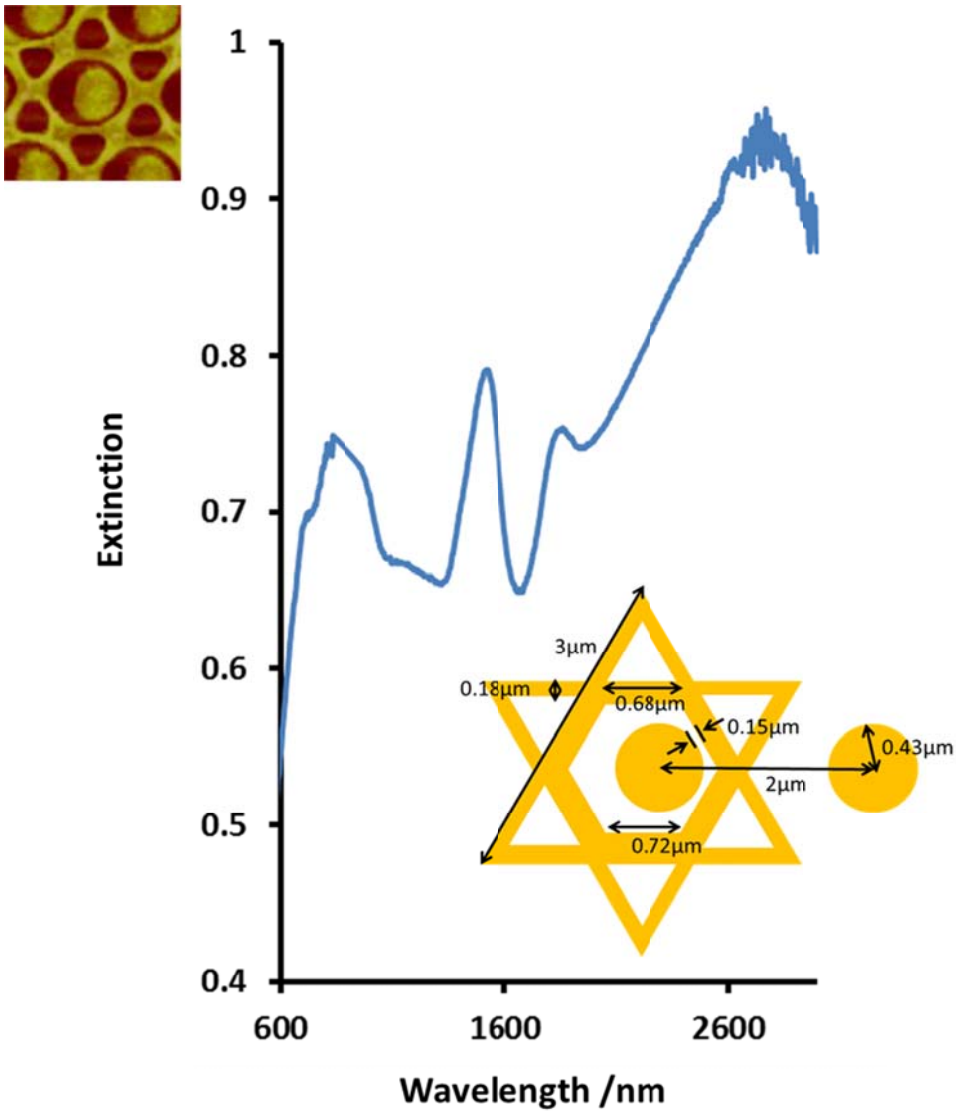

Figure 54. The first extinction spectrum of asymmetric hexagram-dot array with labeled geometric parameters.

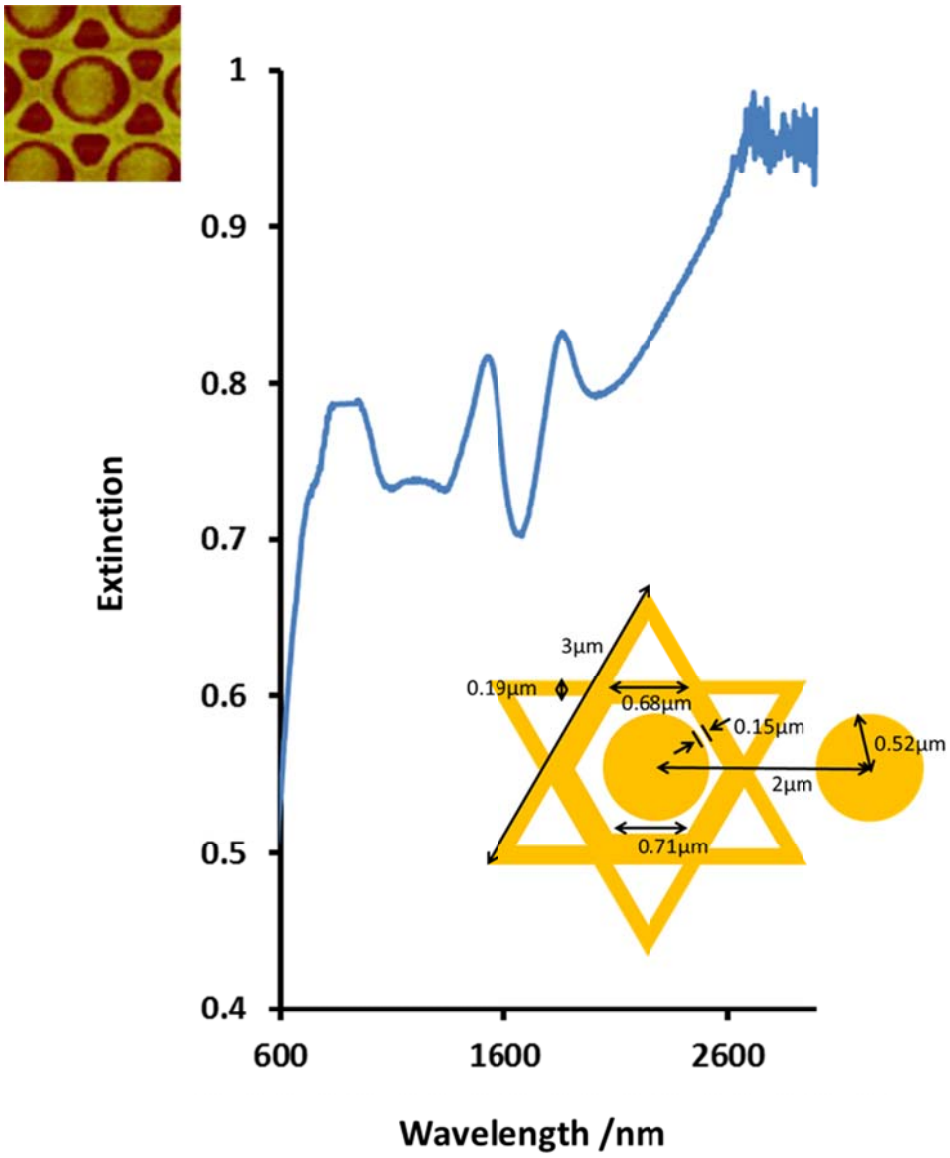

Figure 55. The second extinction spectrum of asymmetric hexagram-dot array with labeled geometric parameters.

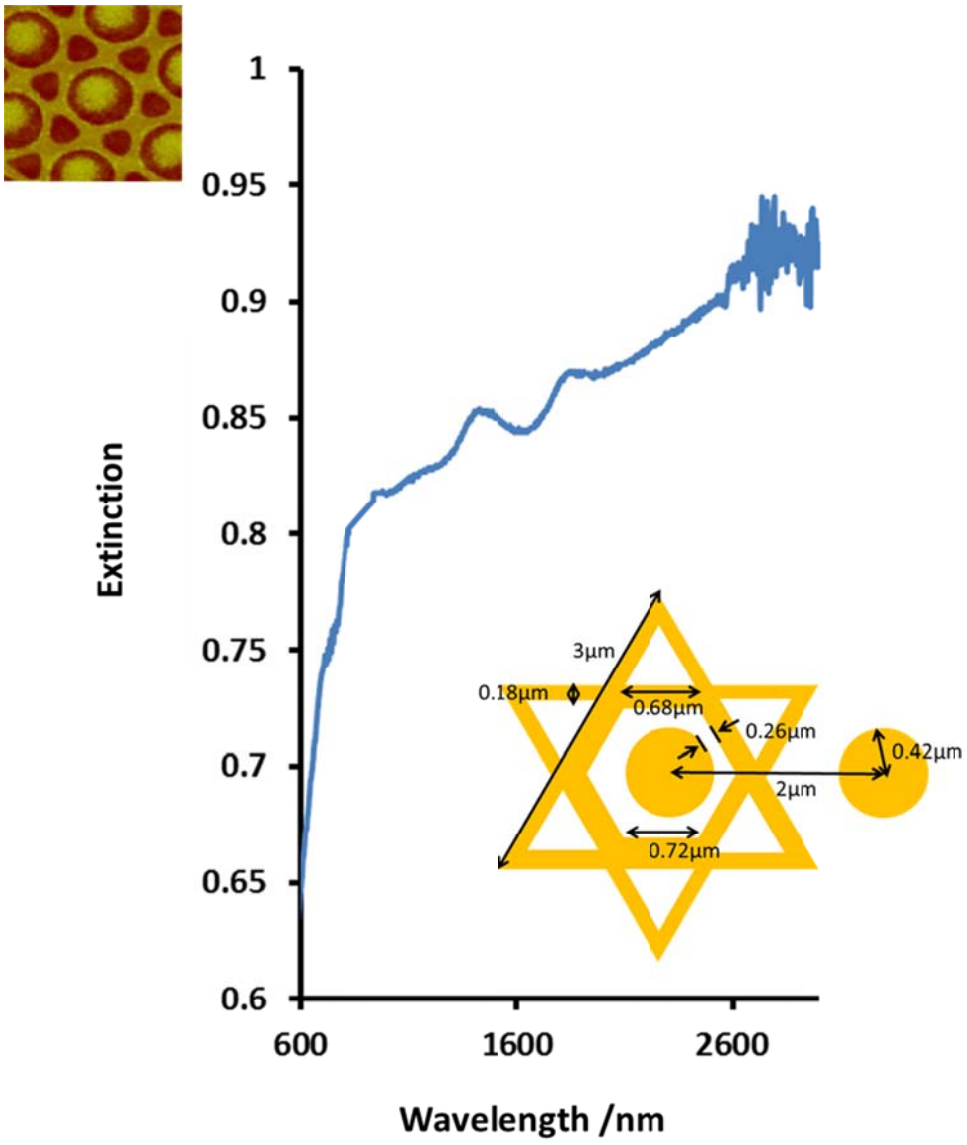

Figure 56. The third extinction spectrum of asymmetric hexagram-dot array with labeled geometric parameters.

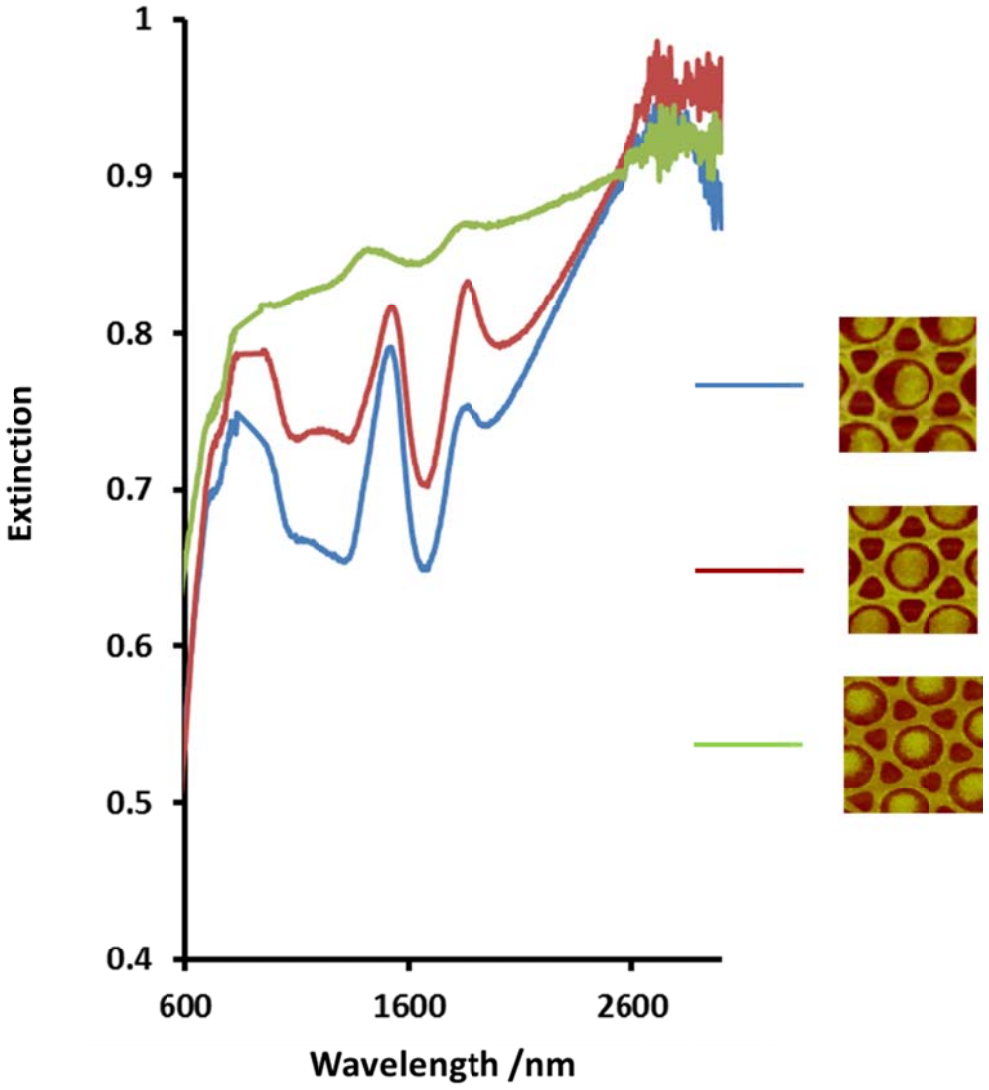

Figure 57. The structural dependence of extinction spectra for asymmetric hexagram-dot arrays with different geometric parameters.

Asymmetric hexagram-dot patterns possessed a sharp dip at ~1700 nm. Moreover, five major peaks were seen at about 800 nm, 1260 nm, 1500 nm, 1900 nm and 2800 nm among which the 1900 nm peak possessed a Fano-shaped curve (Fig. 54 &

Fig. 55). Compared to the symmetric centerpiece, the 1900 nm peak was much clearer in non-concentric hexagram-dot structures. We assumed that this character should come from the interference between the hexagram web and the central disk, which was coincident with our discoveries for the symmetric patterns. The peak at ~1260 nm should also originate from this interference since it didn't show up in symmetric patterns. The 800 nm peak was most likely to be the blue-shifted 1070 nm peak in symmetric hexagram-dot features. Accordingly, we assigned the 1260 nm and 1900 nm peak to be the hybridization of hexagram mode and disk mode while other peaks were mainly from some modes of the hexagram. When the size of the disk shrunk, the spectrum became much smoother (Fig. 56). An overlap of all the spectra was shown in Figure 57.

Four extinction peaks were also observed in the spectra of asymmetric triangle-target feature, which is similar as the spectral characters of symmetric triangle-target. The positions of those dips are 1294 nm, 1670 nm, 1940 nm and 2830 nm (Fig. 58, Fig. 59 & Fig. 60). It should be note that a Fano-shaped character was found for the ~1700 nm dip which was not seen in the cases of symmetric pattern. Therefore, this character was probably coming from the asymmetric inner disk. Consequently, we could assign the origin of each plasmon mode from their structural dependence. The 1294 nm peak should involve mainly the subradiant mode of the middle ring structure while the 2830 nm peak was most likely from the dipole mode of the triangles. As a comparison, the 1670 nm and 1940 nm peaks should come from the interference between the asymmetric inner disk and the dipole mode of the ring. Moreover, no significant change of the extinction spectra was found when the geometric parameters changed for this type of

structure. The positions of the peaks and dips slightly shifted from feature to feature yet the overall profile was kept the same. The structural dependence of all asymmetric triangle-target patterns was shown in Figure 61.

In order to acquire more insights into the structural dependence of symmetric and asymmetric, we picked up a reprehensive spectrum from each feature type and compared them in the same figure (Fig. 62 to Fig. 65).

The line shape of Fano resonances would change dramatically with the variations of incident angle and polarization.[44, 46] As such, we tested the extinction spectra of each type of novel asymmetric nano-pattern under different excitation. The results of the incident angle dependence were shown through Figure 66 to Figure 69 in which the expected position of Fano resonances were labeled by a vertical dashed line. It was found that the incident angle becomes more grazing, the line shape of the Fano resonance becomes more symmetric. The Fano-shaped character disappeared for incident angles larger than 30° in all the cases.

Significant polarization dependence was also revealed for all the non-concentric features (Fig. 70, Fig 72 to Fig. 74). For example, the Fano-resonance was only observed under the 0° polarization for the asymmetric annular aperture, as was pointed by the green arrow. As a comparison, the peak became more symmetric when a 90° polarization was applied in the direction orthogonal to the asymmetry (Fig. 70). This spectral behavior was also predicted by numerical simulation (Fig. 71).

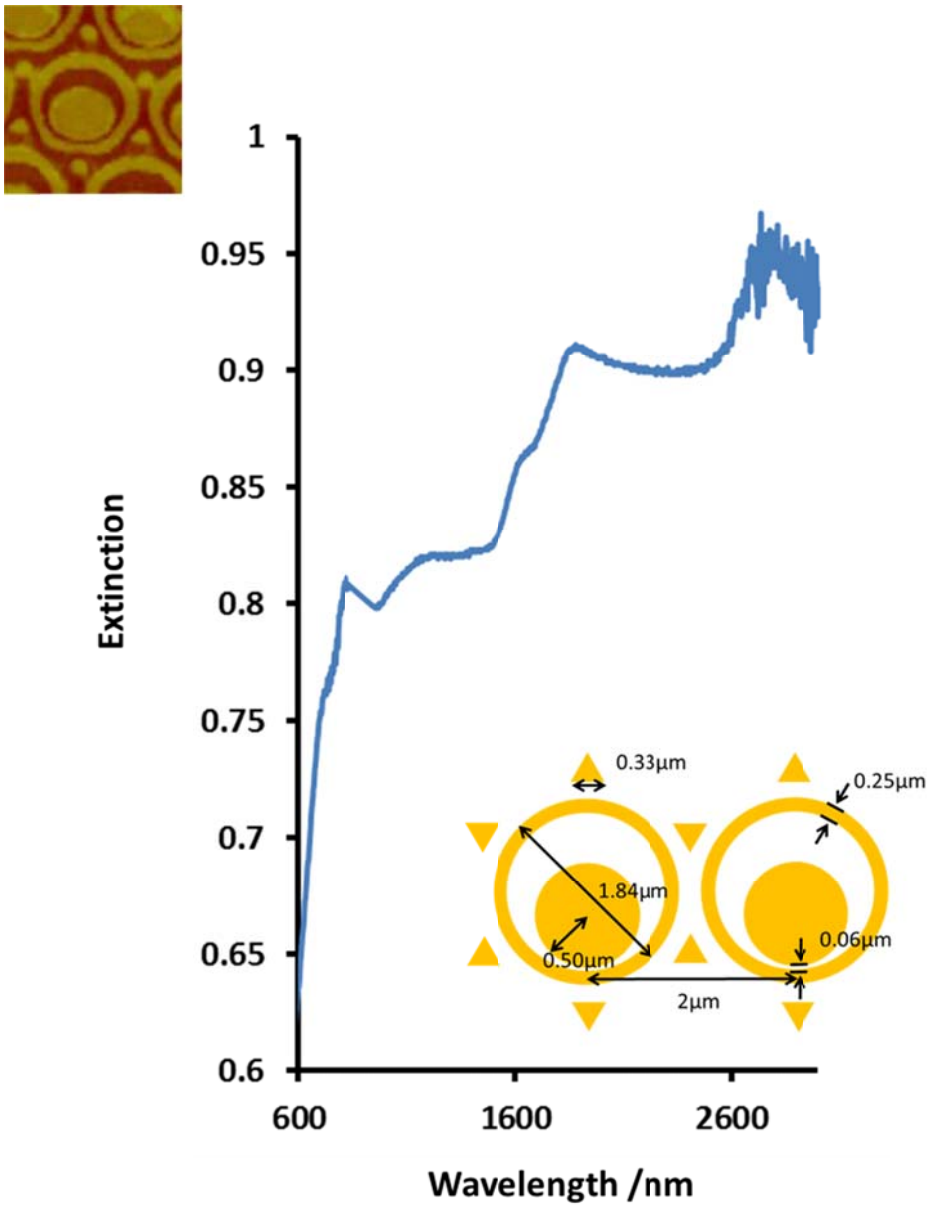

Figure 58. The first extinction spectrum of asymmetric triangle-target array with labeled geometric parameters.

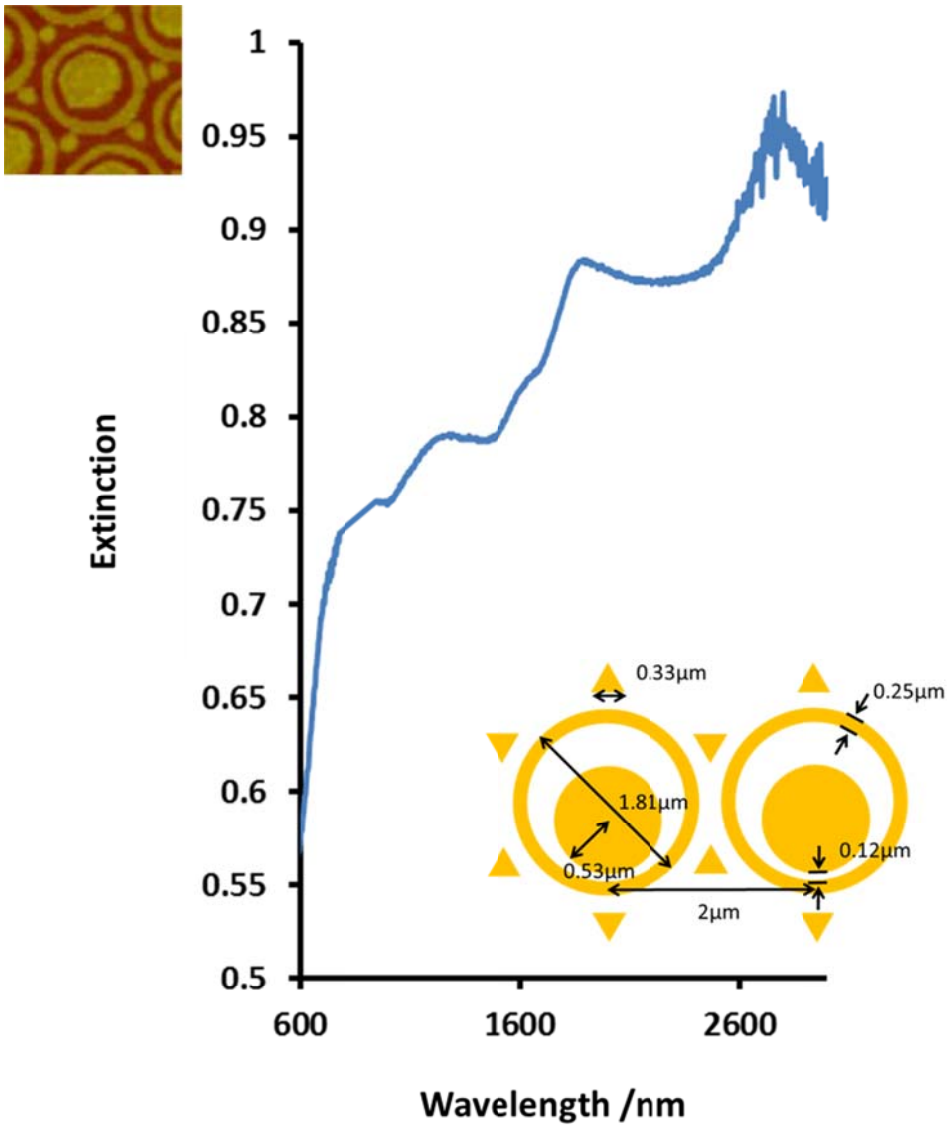

Figure 59. The second extinction spectrum of asymmetric triangle-target array with labeled geometric parameters.

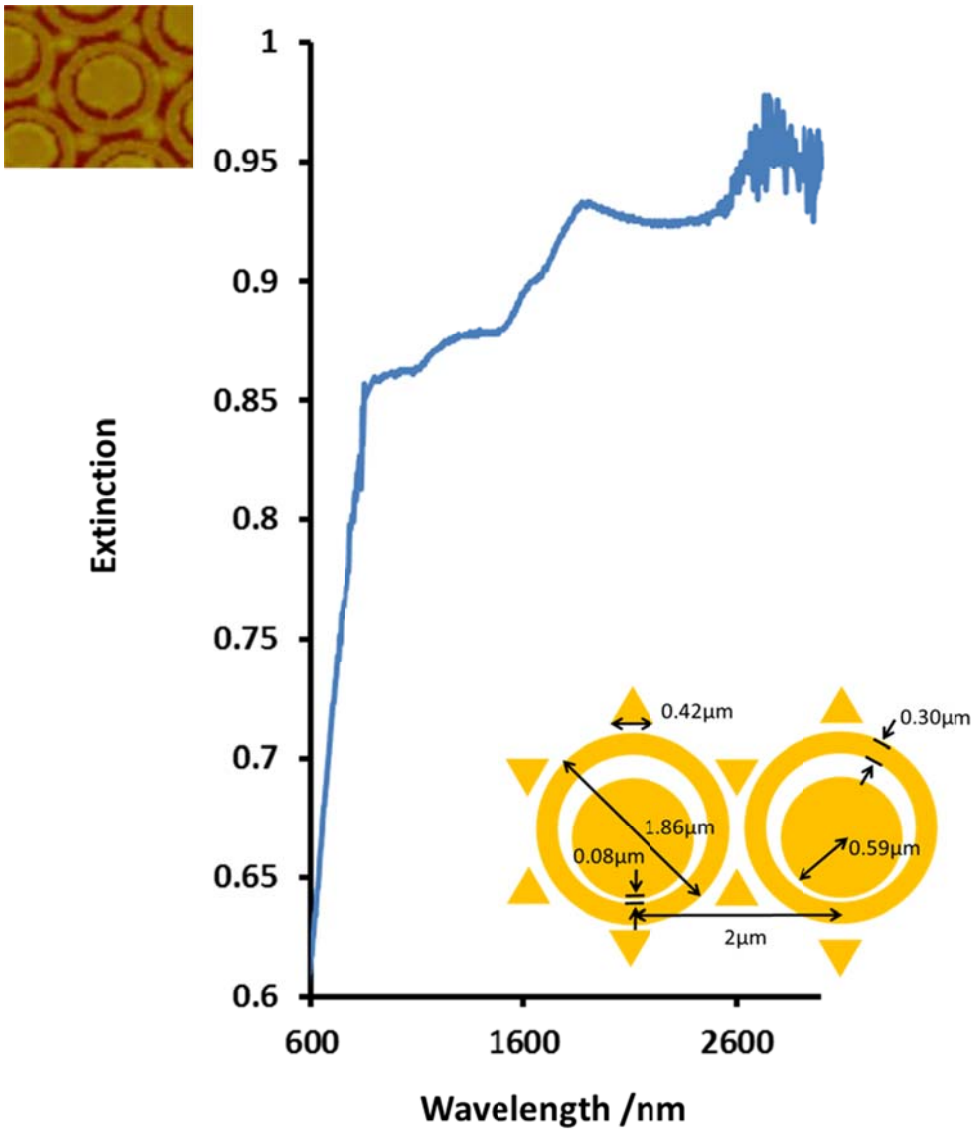

Figure 60. The third extinction spectrum of asymmetric triangle-target array with labeled geometric parameters.

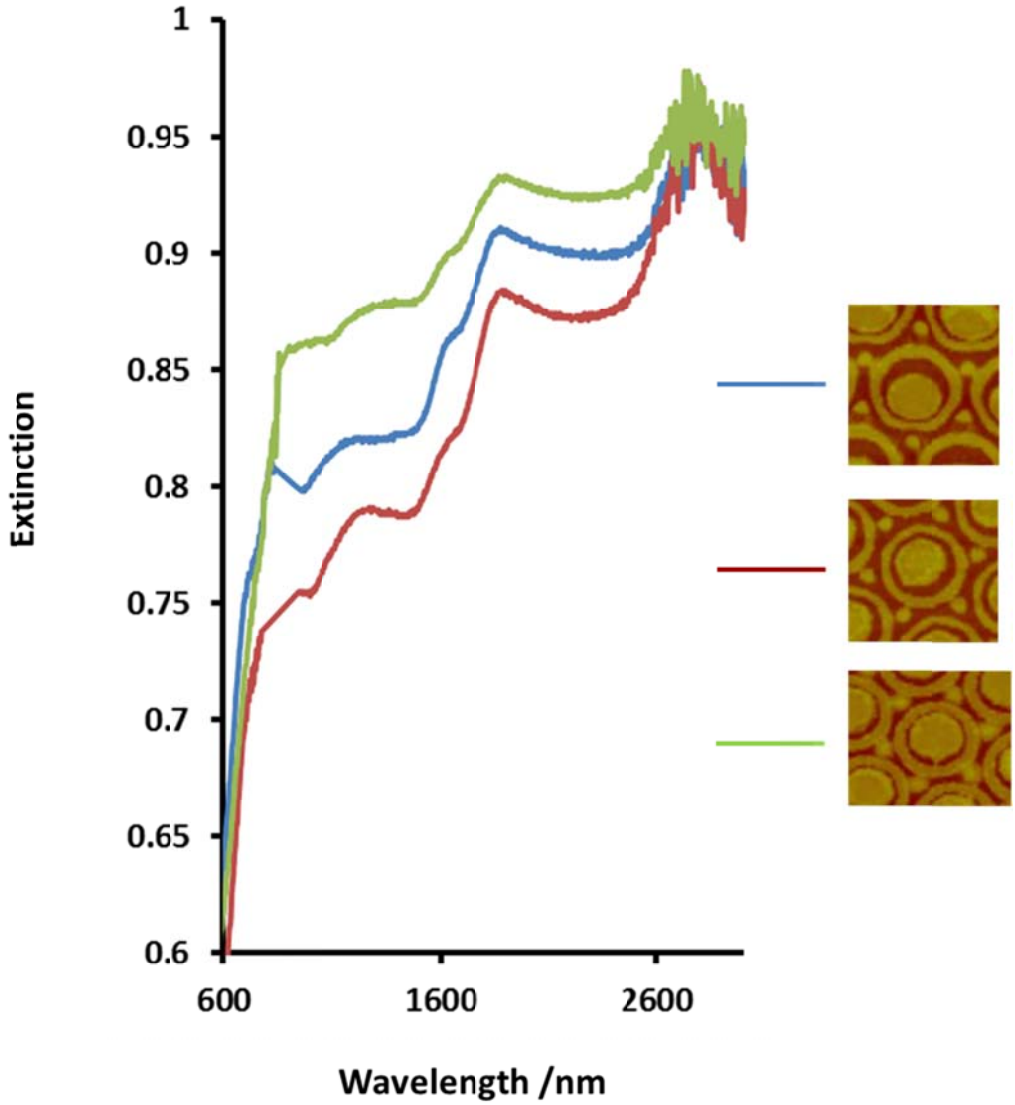

Figure 61. The structural dependence of extinction spectra for asymmetric triangle-target arrays with different geometric parameters.

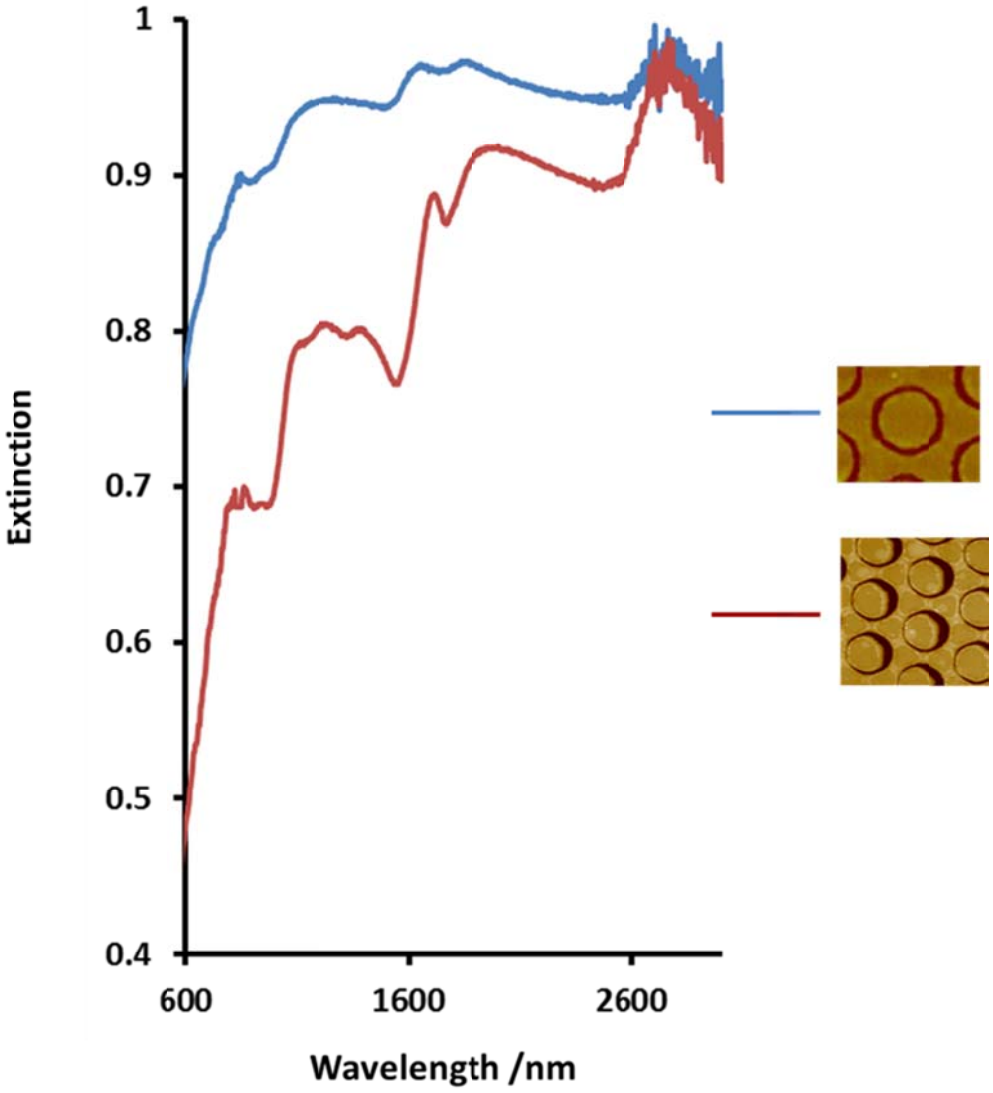

Figure 62. A comparison between the optical properties of symmetric and asymmetric annular aperture arrays.

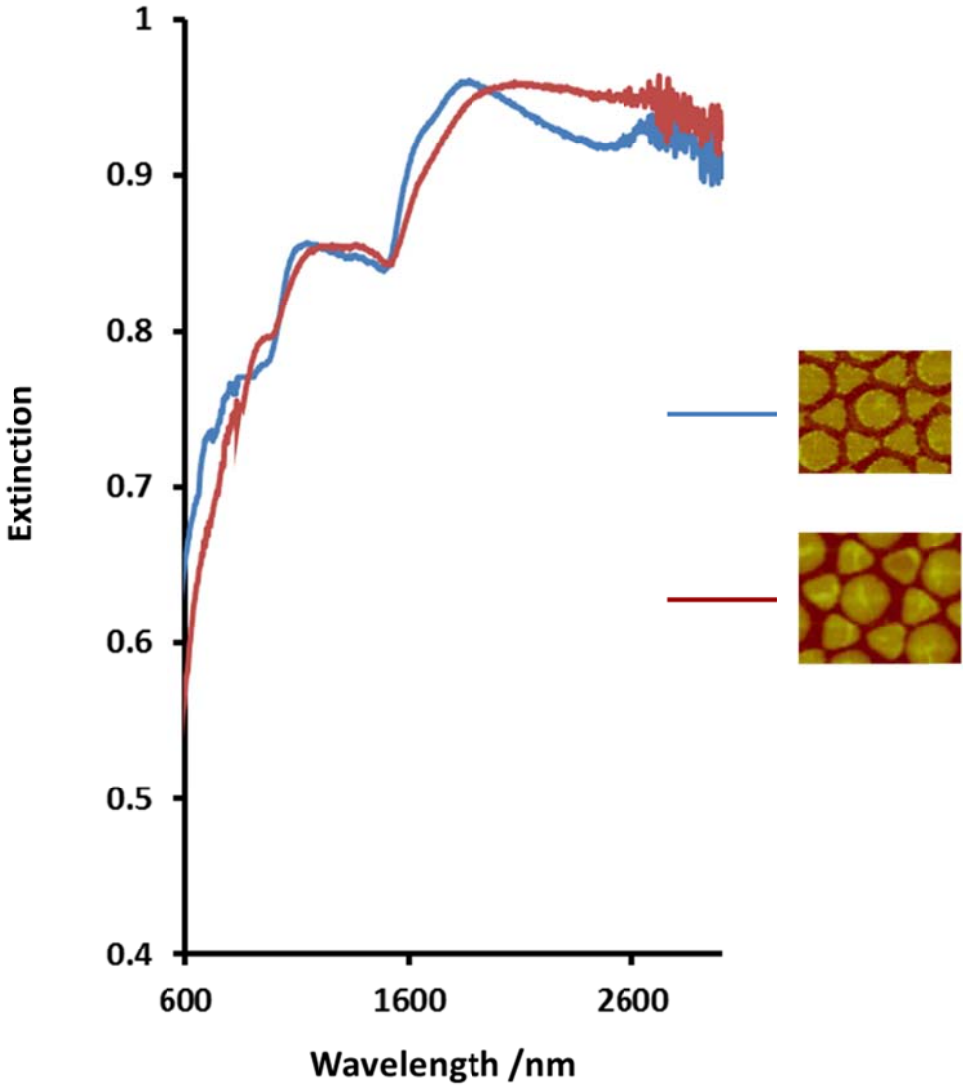

Figure 63. A comparison between the optical properties of symmetric and asymmetric triangle-dot arrays.

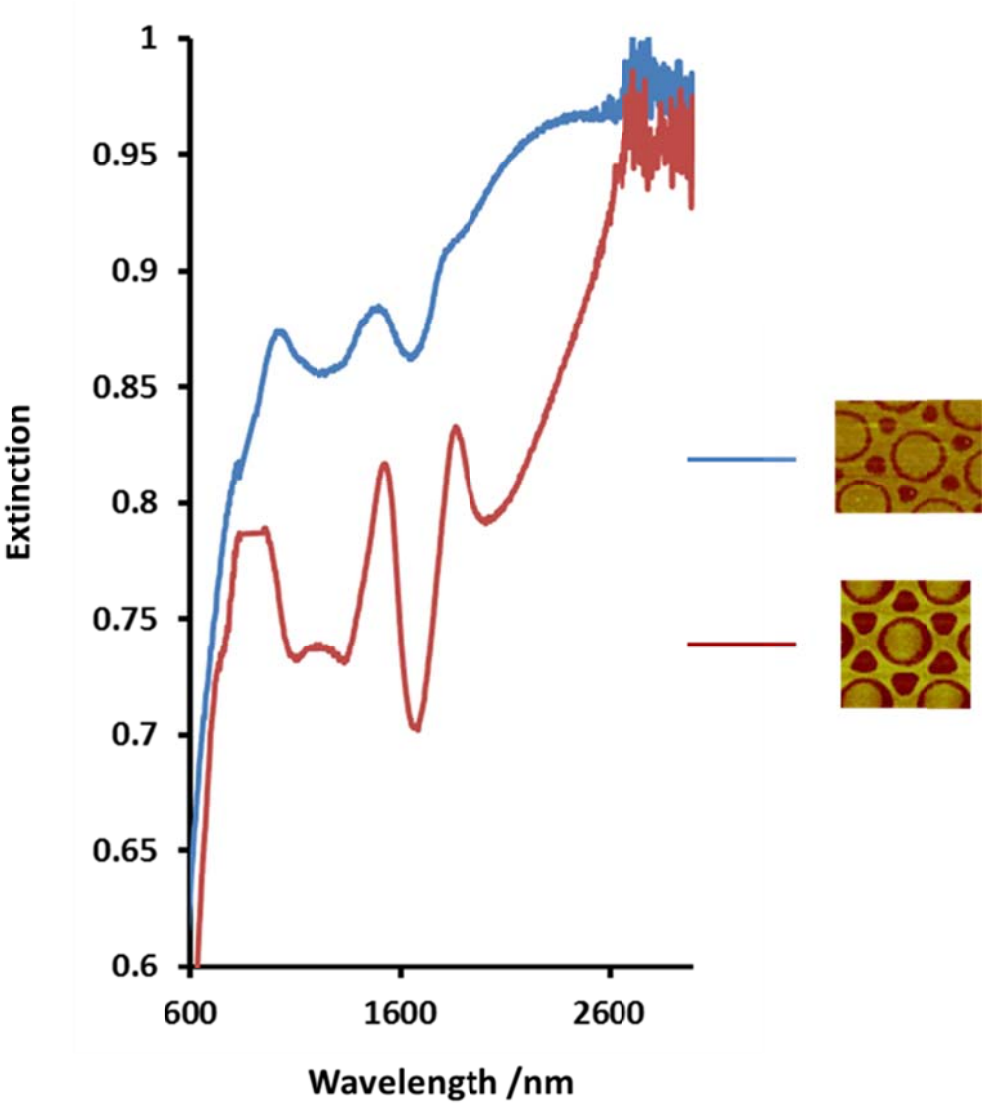

Figure 64. A comparison between the optical properties of symmetric and asymmetric hexagram-dot arrays.

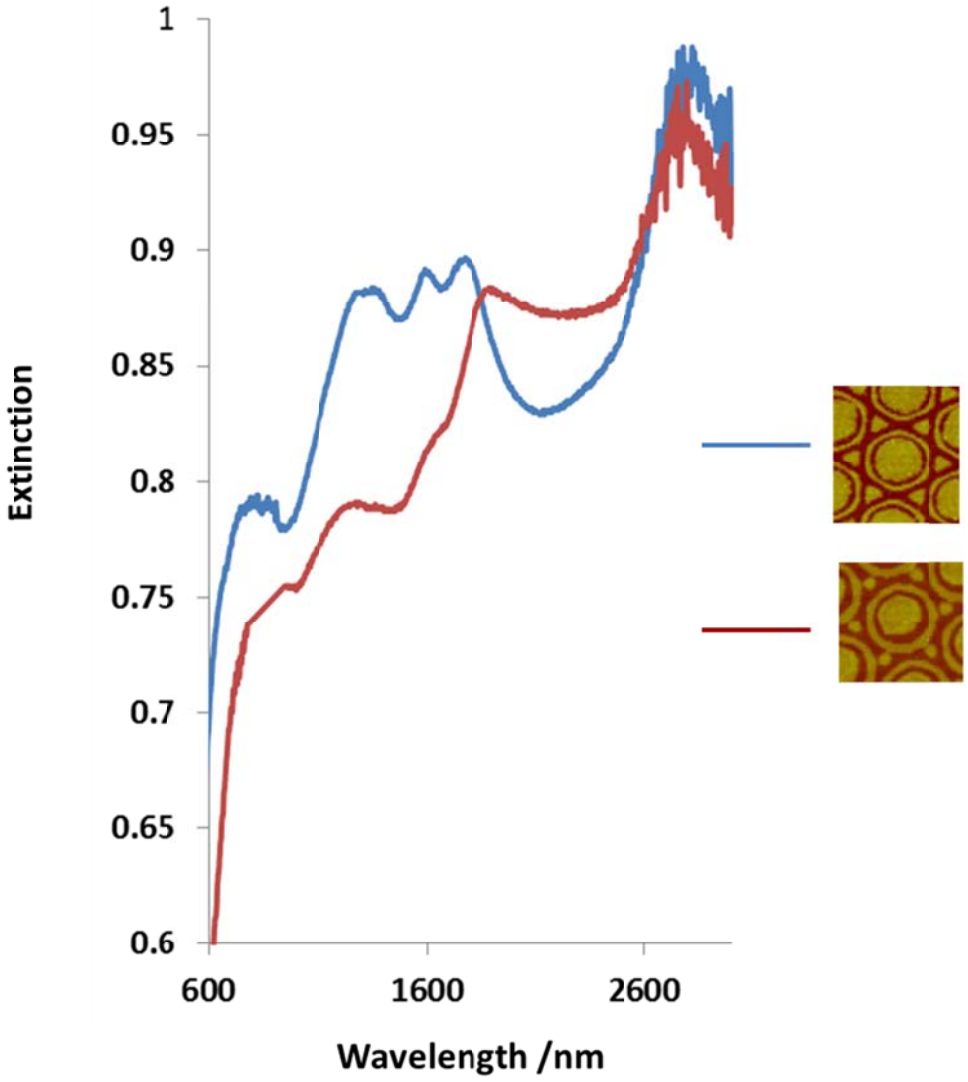

Figure 65. A comparison between the optical properties of symmetric and asymmetric triangle-target arrays.

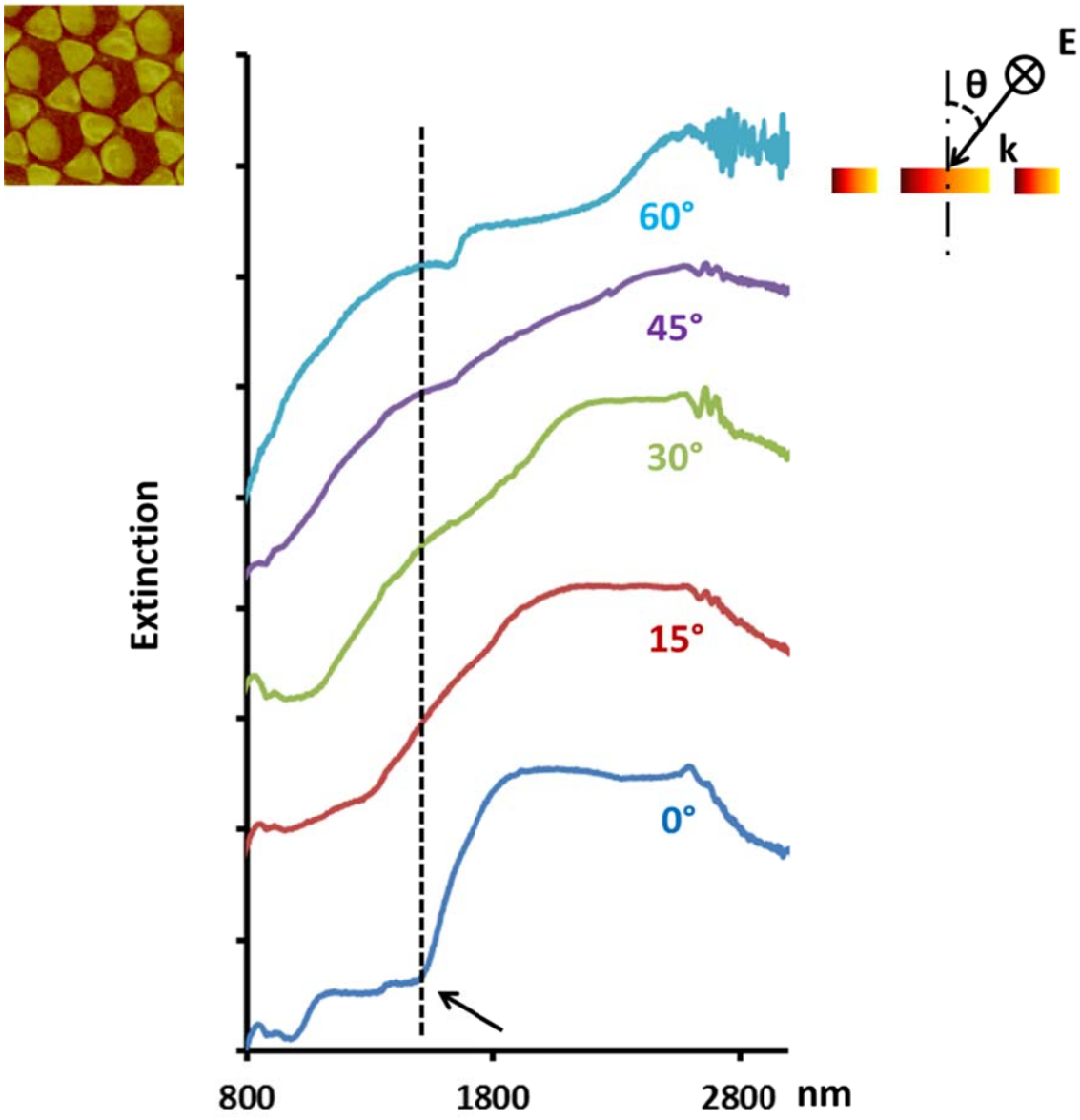

Figure 66. The change of extinction spectrum for asymmetric triangle-dot arrays under various incident angles.

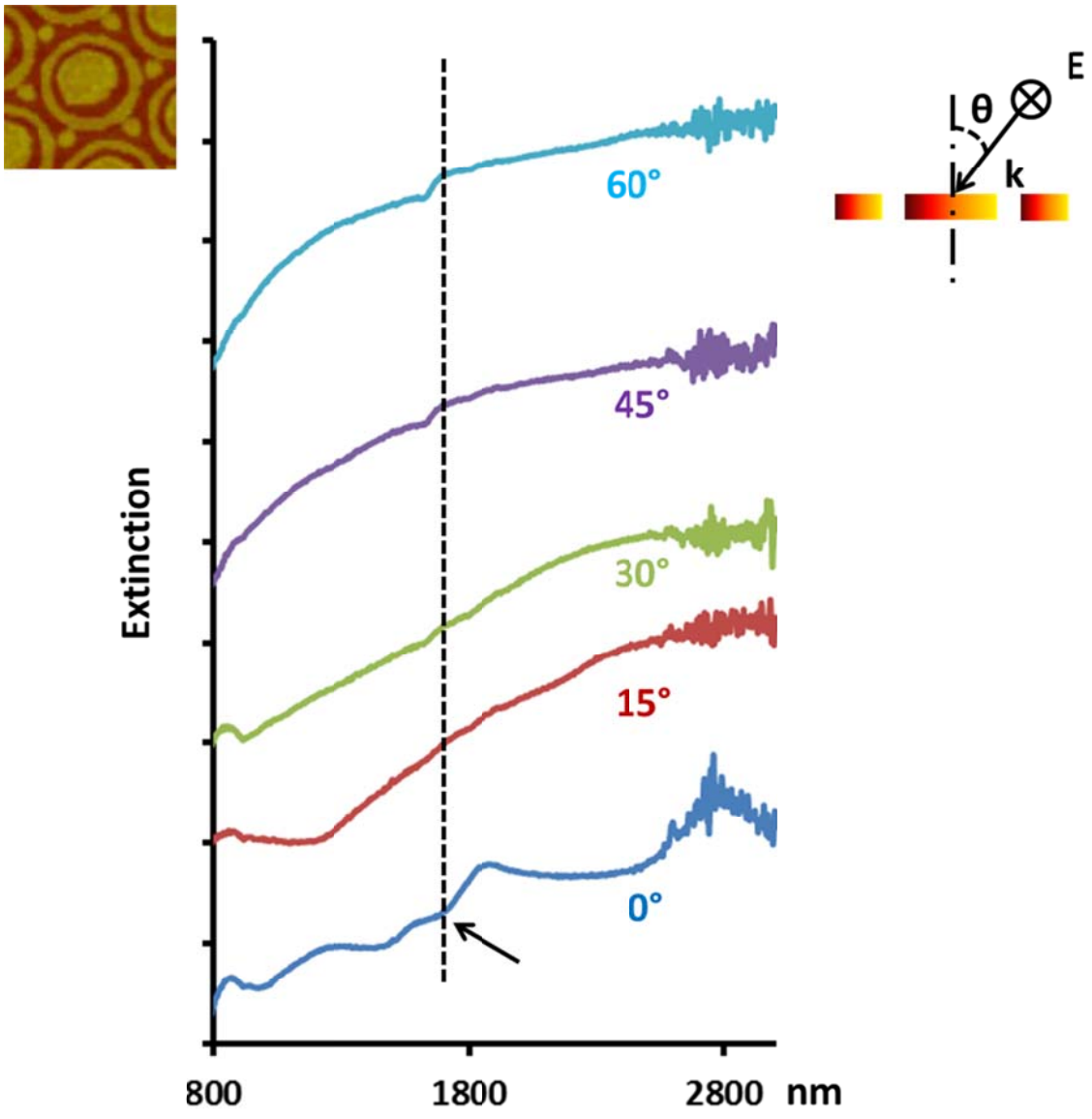

Figure 67. The change of extinction spectrum for asymmetric triangle-target arrays under various incident angles.

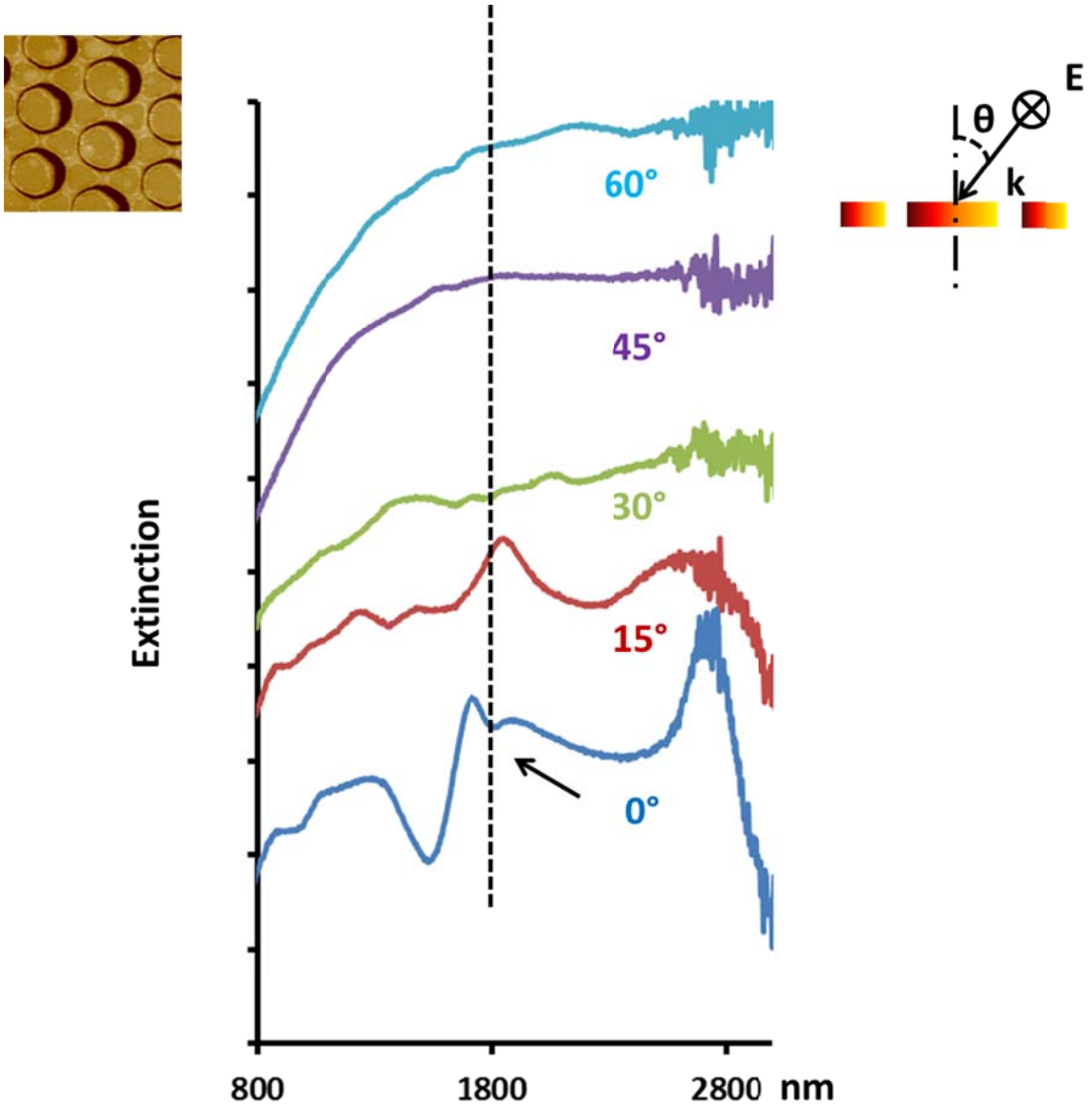

Figure 68. The change of extinction spectrum for asymmetric annular aperture arrays under various incident angles.

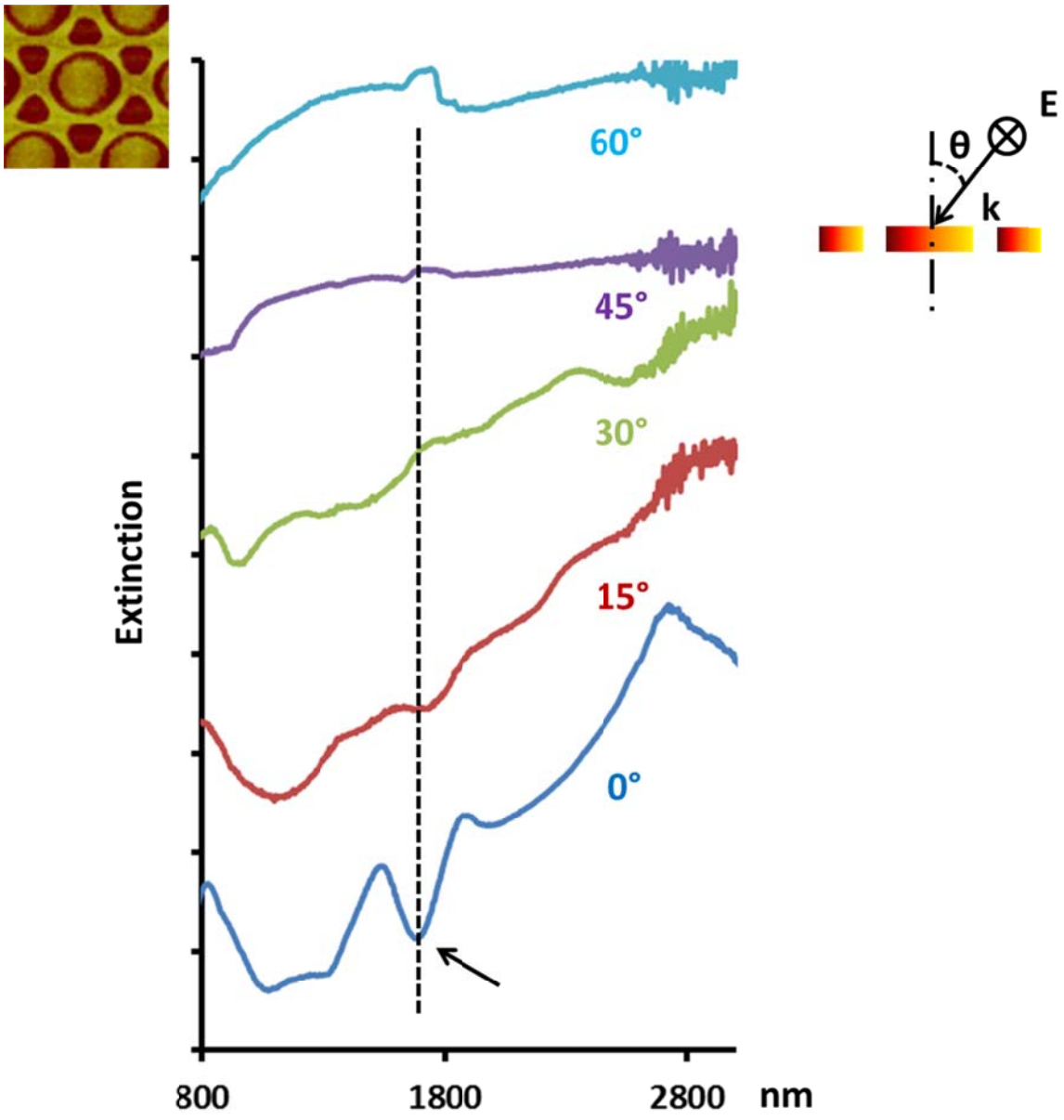

Figure 69. The change of extinction spectrum for asymmetric hexagram-dot arrays under various incident angles.

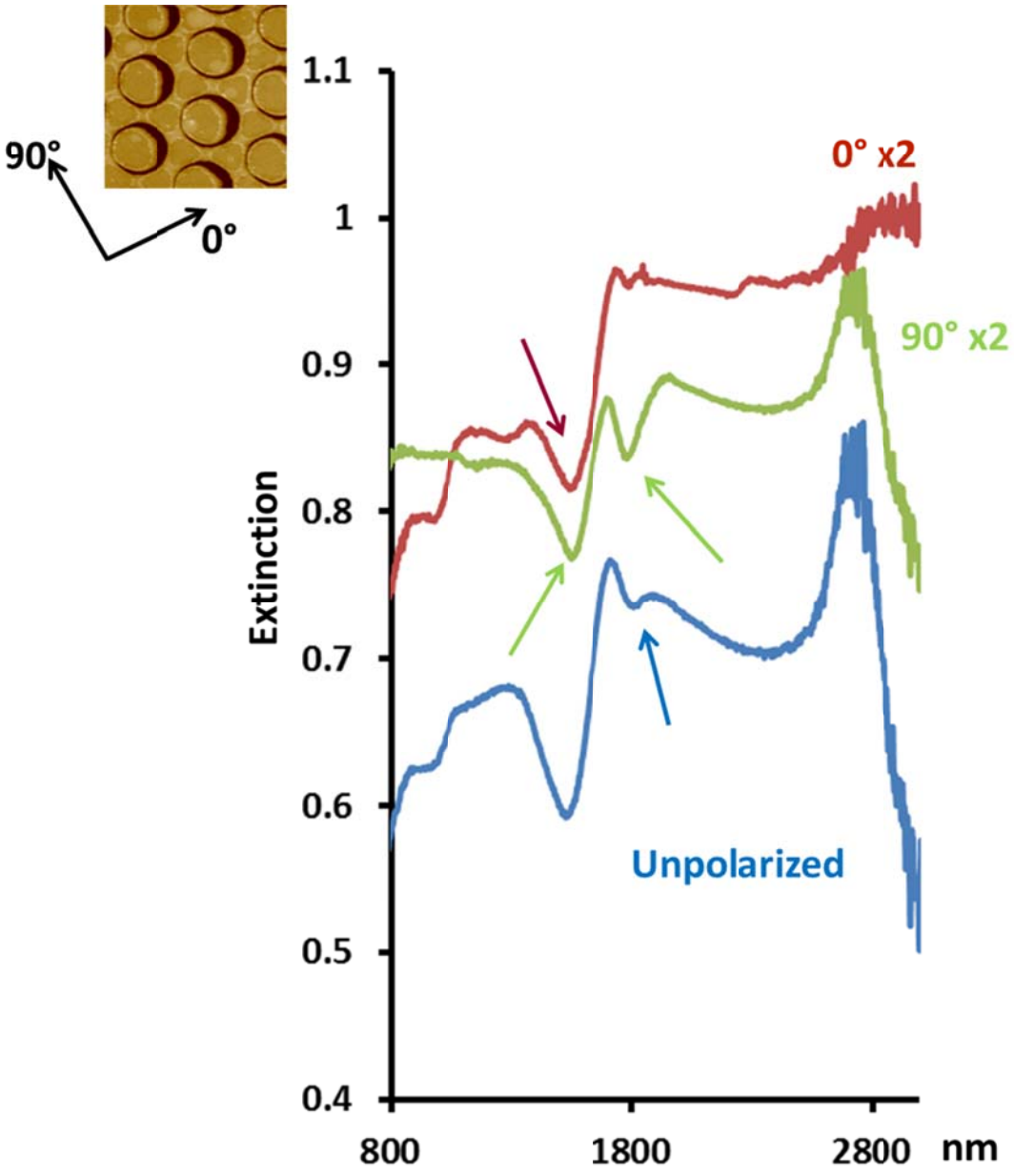

Figure 70. The polarization dependence of extinction spectra of non-concentric annular aperture arrays.

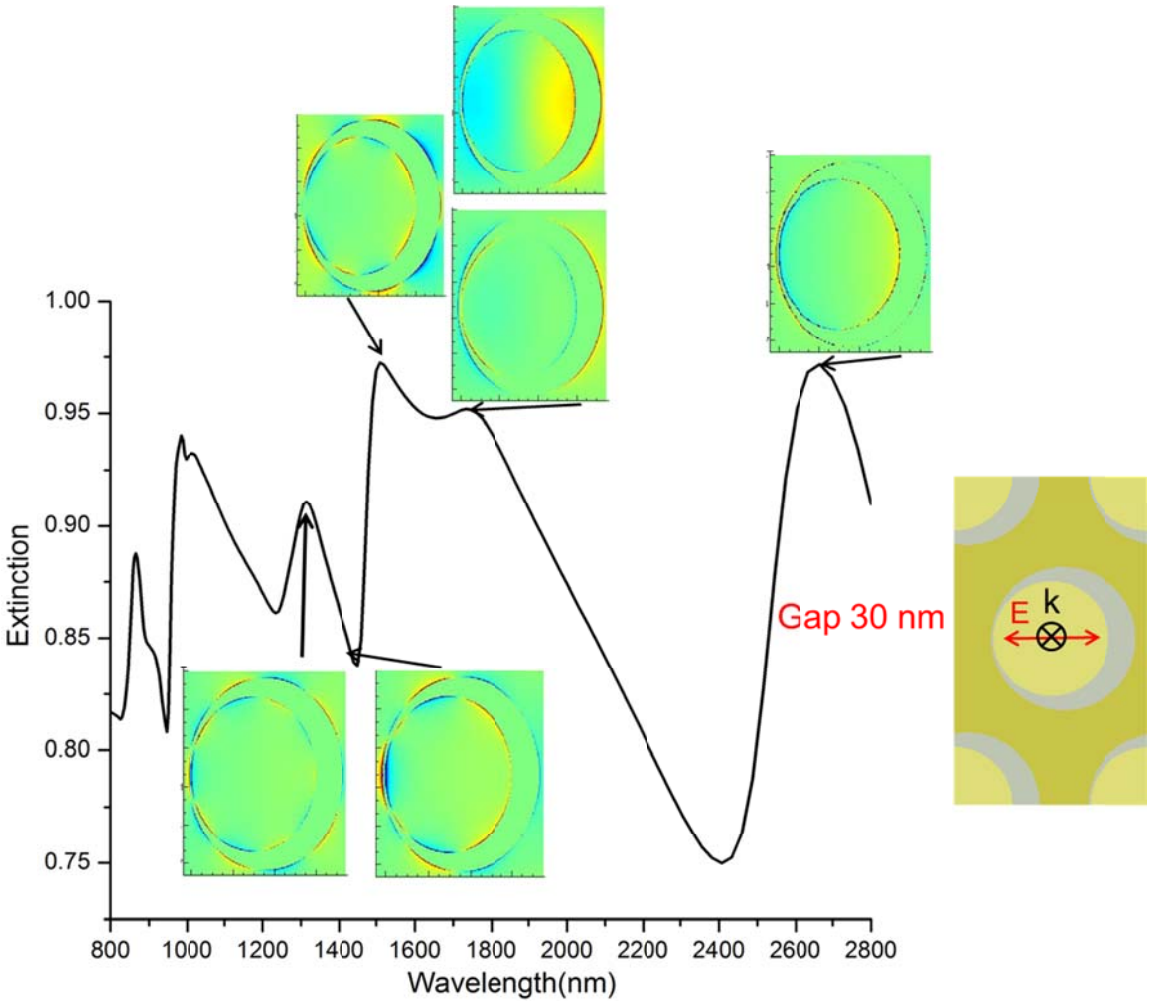

Figure 71. The simulated extinction of nonconcentric annular aperture array under 0° polarization.

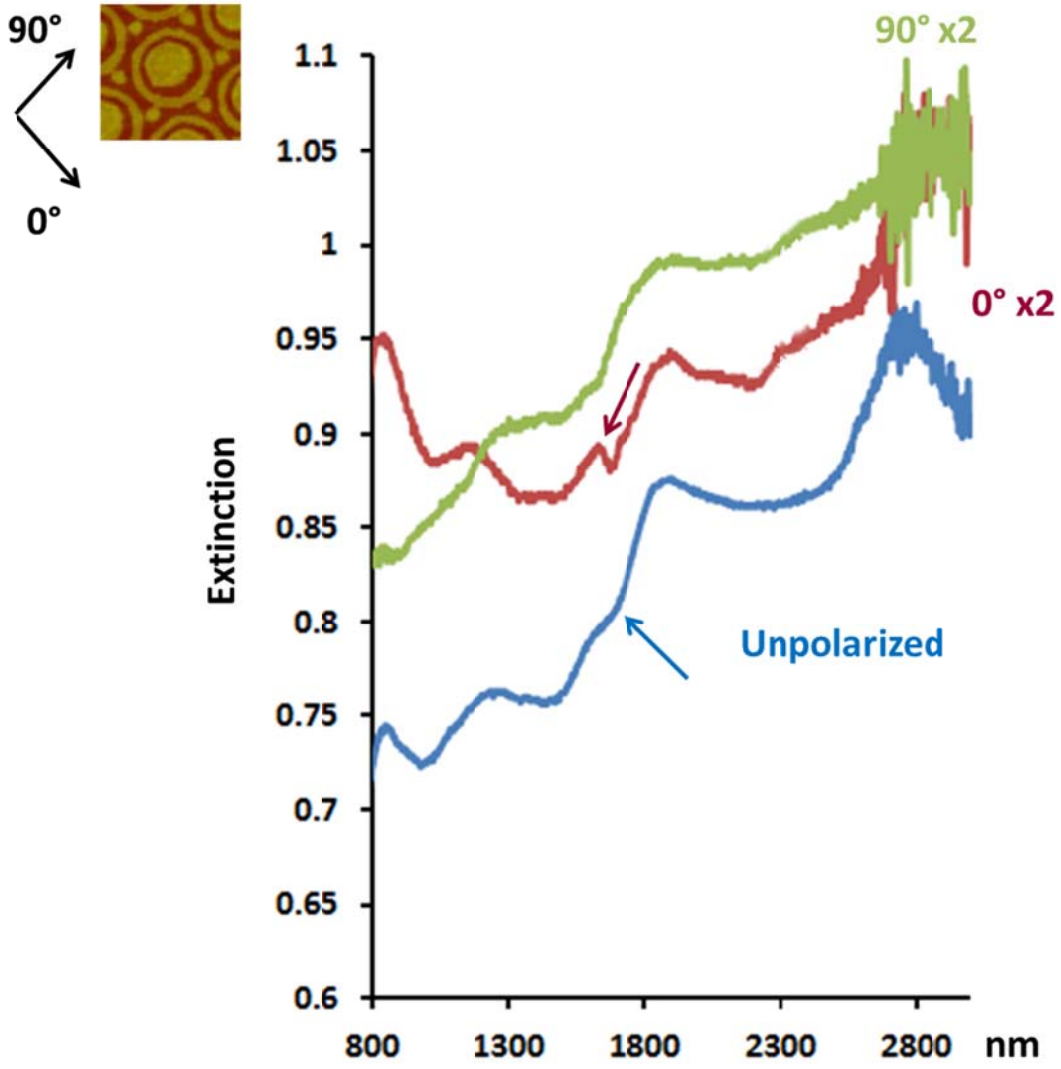

Figure 72. The polarization dependence of extinction spectra of non-concentric triangle-target arrays.

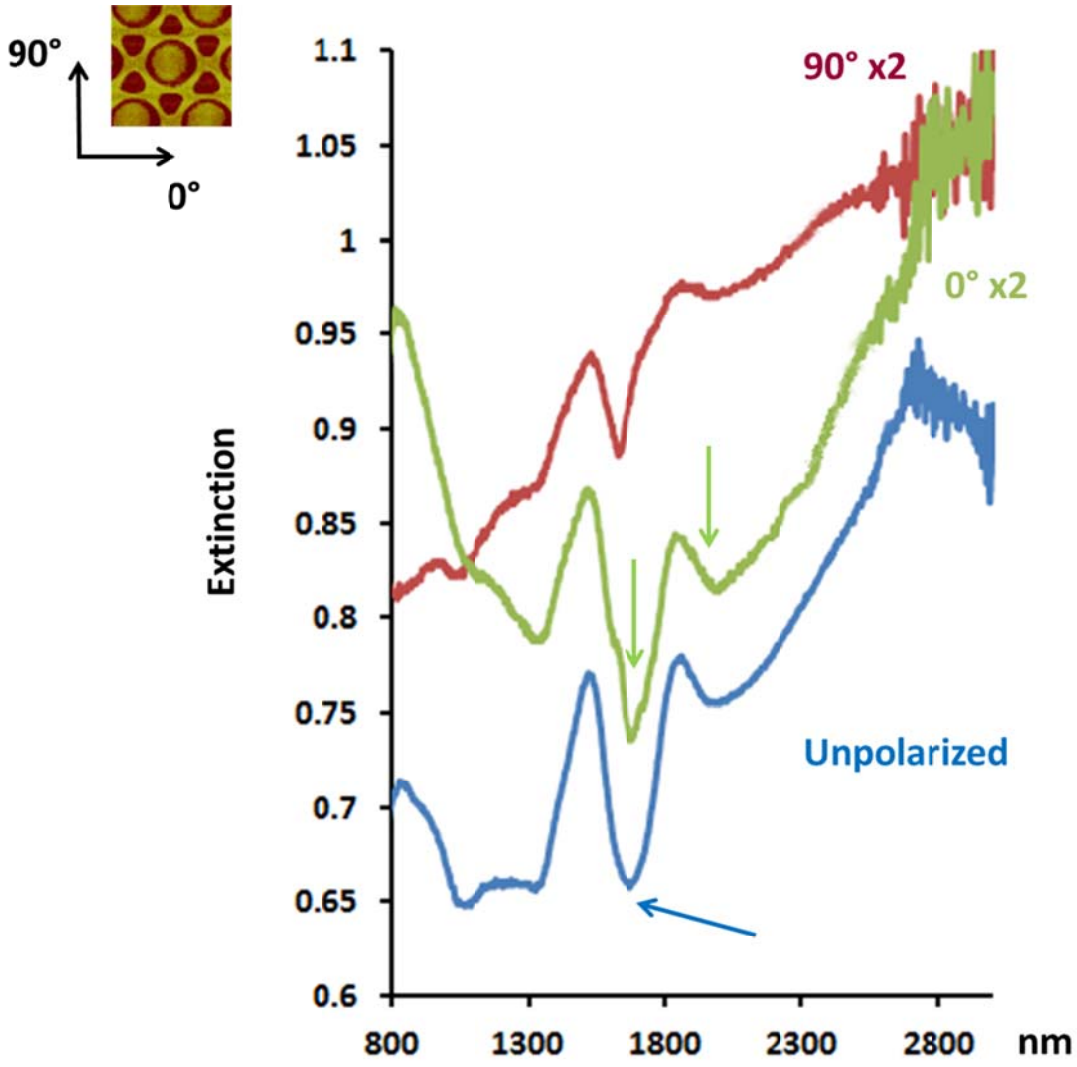

Figure 73. The polarization dependence of extinction spectra of non-concentric hexagram-dot arrays.

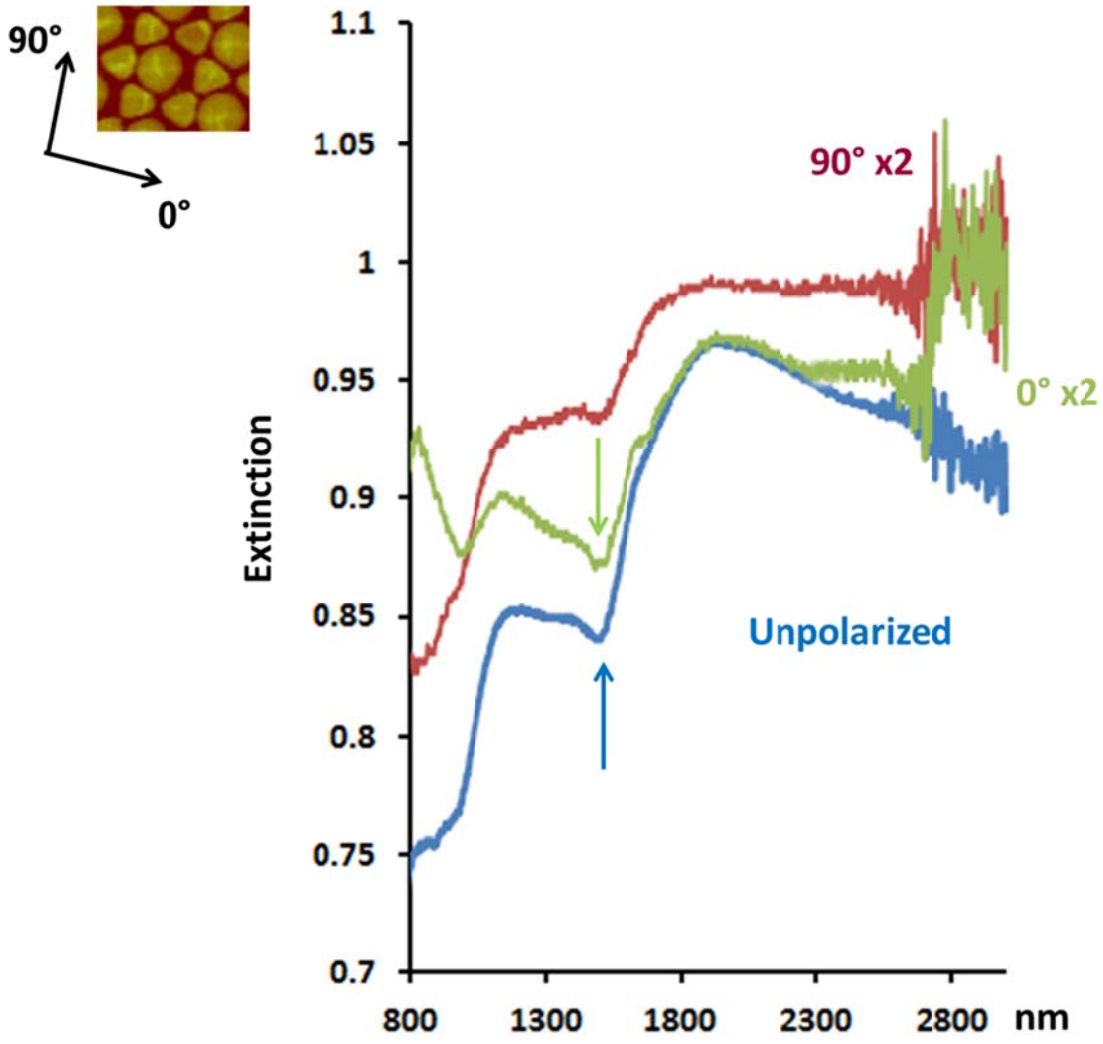

Figure 74. The polarization dependence of extinction spectra of non-concentric triangle-dot arrays.

3.4 Mode-selective SERS and its application in the detection of odd-even effect

The substrates used in SERS were made from previously developed procedures.[83] Two patterns were chosen to demonstrate the mode-selective SERS because they gave the best selectivity and signal to noise ratio (Fig. 75A). The Raman spectrum was collected in a confocal Raman system. A 10x objective was used to focus the laser beam onto patterned area which resulted in an approximate 4 μm lateral resolution. The advantage of confocal Raman system lay in that it allowed the selection of a defect-free area under microscopy that is larger than the size of focused laser spot. The focused laser spot was approximately 8 μm in diameter which is smaller than the average grain size that can be patterned (~50 μm×50 μm). As a result, the error from surface defects could be eliminated.

Raman spectra of 4-ATP on triangle-target feature and dot-hexagram feature were collected (Fig. 75B). All the peaks observed could be identified according to previous literatures.[125] Specifically, each resonance could be classified as either a_1 or b_2 vibrations according to their symmetries. The major peaks between 1000 and 1700 cm^{-1} were: νCC (1574 cm^{-1}, a_1), δCH+νCC (1430 cm^{-1}, b_2), νCC+δCH (1377 cm^{-1}, b_2), δCH (1165 cm^{-1}, a_1), δCH (1134 cm^{-1}, b_2), and νCS (1070 cm^{-1}, a_1). As a comparison, the resonance positions were the same in both cases, but the ratios of the peak intensities were strikingly different. Notably, the a_1 peaks were substantially more intense on the first surface relative to the b_2 peaks while b_2 resonances became stronger on the second surface. For example, the 1070 cm^{-1}: 1134 cm^{-1} intensity ratio on the first pattern was about twice as that of the second pattern. However, this ratio dropped to about 1 on the

dot-hexagram feature. In order to get a more quantitative view, the SERS spectra of 4-ATP SAM on two were compared. The detailed summary of peak intensity ratio was listed in Figure 76. As can be seen, the intensity ratios of resonances with the same symmetry were close to a constant for all the conditions (Fig. 76A & Fig. 76B). In contrast, the ratio between a_1 and b_2 vibrations varied dramatically from pattern to pattern (Fig. 76C). However, a general trend for all the vibrations was still easy to find in which the a_1:b_2 value followed the order: feature 1>>feature 2. As such, the a_1 vibrations appeared to be selectively enhanced on the first surface and b_2 vibrations were selectively enhanced on the second feature. These results were highly repeatable from sample to sample. We named this phenomenon mode-selective SERS.

Recently, the oxidation of 4-ATP under high laser power has been demonstrated by calculation and spectroscopic data.[126] The product 4,4'-dimercaptoazobenzene (DMAB) exhibited several resonances in Raman spectra at the same wavenumbers as b_2 modes of 4-ATP molecule. As a result, we need to consider the possibility whether the b_2 signals in our experiments were from DMAB. It was well recognized that the oxidation of 4-APT was dependent on the laser power. Accordingly, the signal from DMAB should roughly be the same on the two of our substrates under the same experimental conditions. Moreover, the total Raman intensity of 4-ATP SAMs on the two substrates were about identical, which demonstrated that the local E-field had no obvious difference between patterns. It is also worth to mention that the power density in our experiment (~3×10^6 mW/cm^2) was an order of magnitude smaller than the power density used to induce 4-ATP oxidation.[126] Therefore, the striking difference between

spectrums should not be observed if the Raman selectivity were identical on all of our substrates.

The selective enhancement of a specific vibrational mode in Raman spectroscopy had been shown by previous publications. Generally, this goal could be realized by varying excitation wavelength[79, 80] or applying an external E-field.[81, 82] A quantum theory model had been proposed by Moskovits. et al to illustrate the selection rule for surface enhanced Raman spectroscopy under different excitation wavelengths.[78, 79] According to this theory, the E-field distribution induced by surface plasmon would be different with an excitation red or blue to the plasmonic peak. The E-field could be divided into three components, namely the one fully perpendicular to the surface, the one partially perpendicular to the surface and the one parallel to the surface. Each type of E-field would mainly enhance molecular resonances that had the same orientation. The ratio of three E-field components could be varied by applying different excitation wavelengths. As a result, a_1 or b_2 vibrations were able to be selectively enhanced dependents on whether the excitation is red or blue to the plasmon resonance. A surface Raman selection rule was also proposed according to this theory.

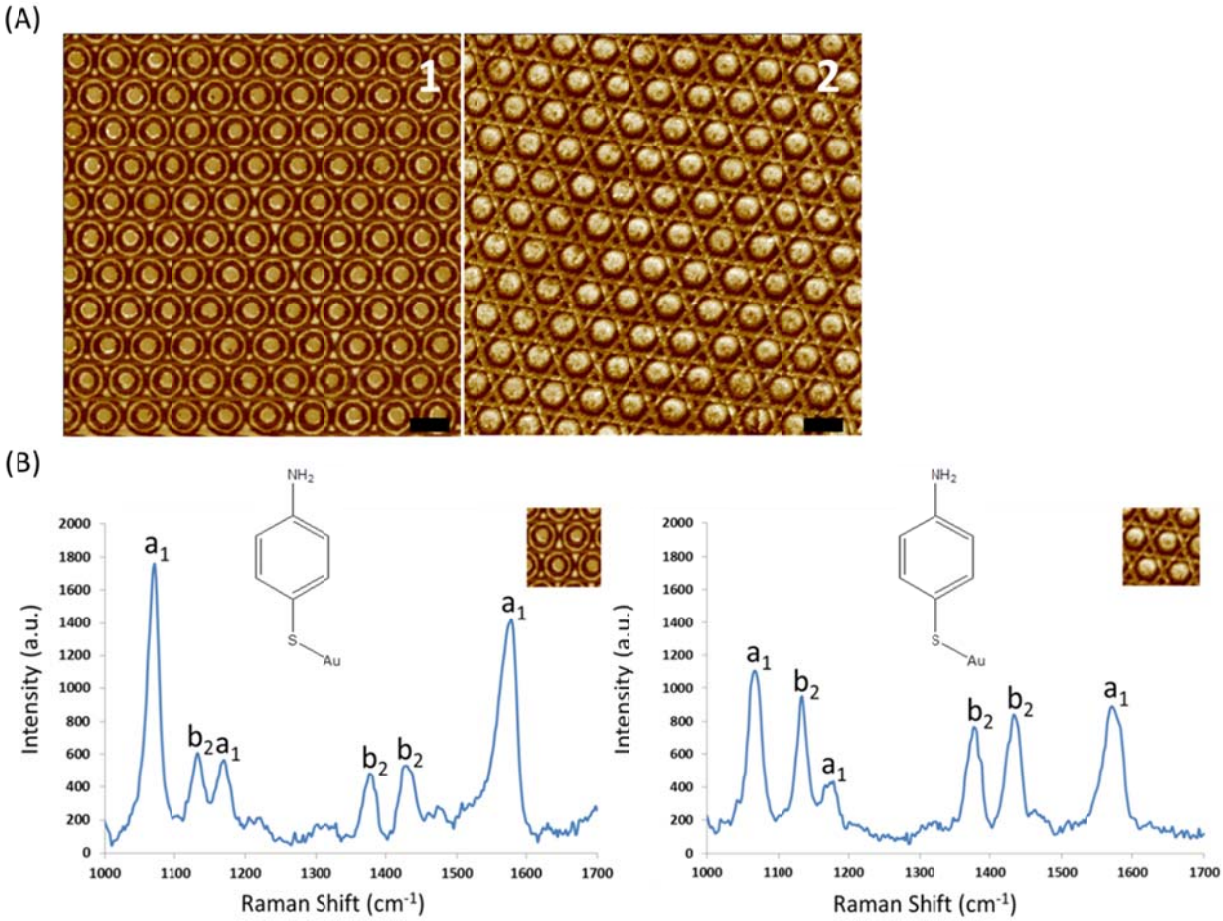

Figure 75. (A) AFM image of nano-patterned gold substrates applied in the SERS experiments. Scale bars: 2 μm, (B) SERS spectra of 4-ATM molecular absorbed on two substrates.

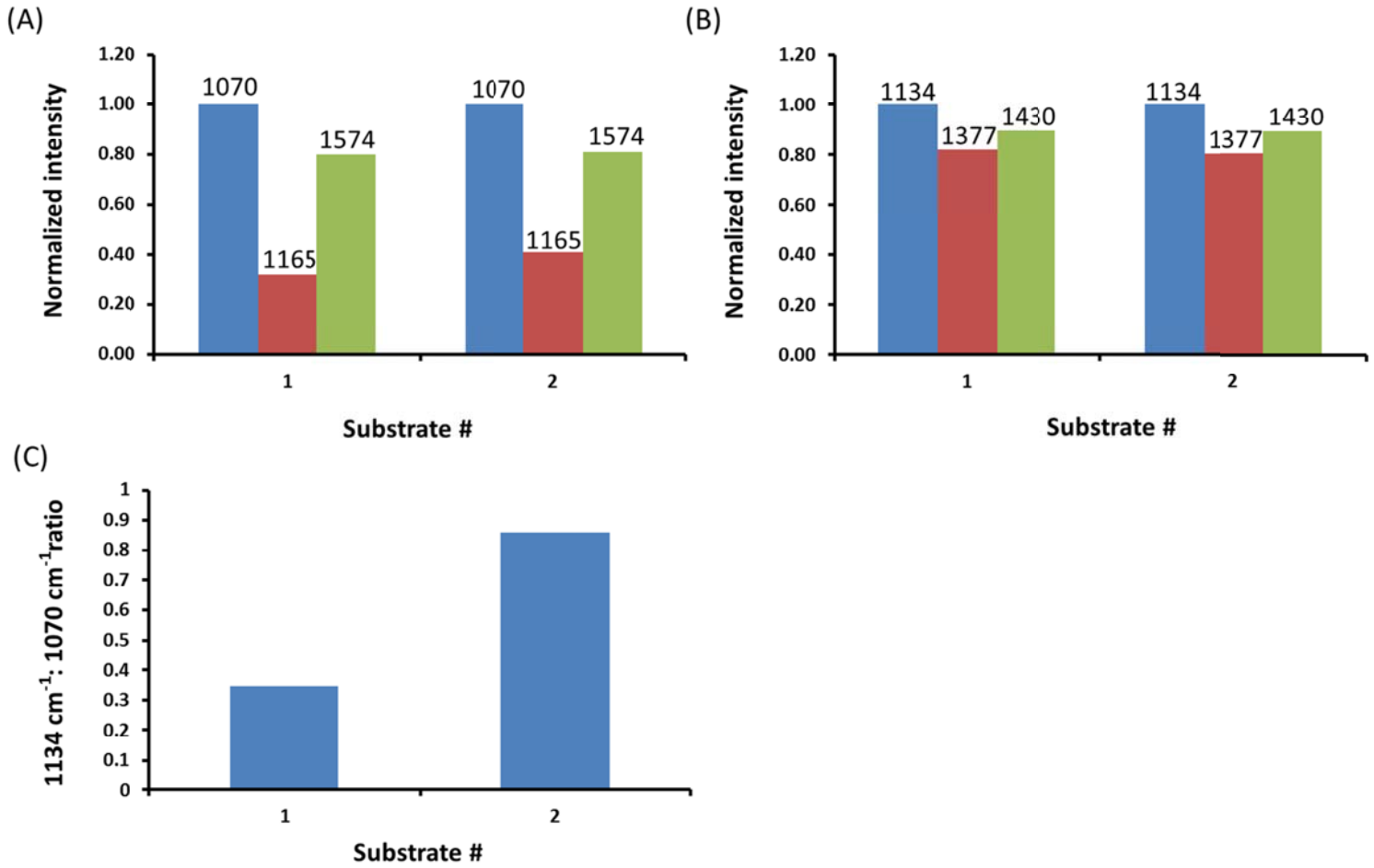

Figure 76. (A) Normalized intensity of a_1 vibrations on both substrates. (B) Normalized intensity of b_2 vibrations on both substrates. (C) The intensity ratio of 1134 cm^{-1}: 1070 cm^{-1} on two substrates.

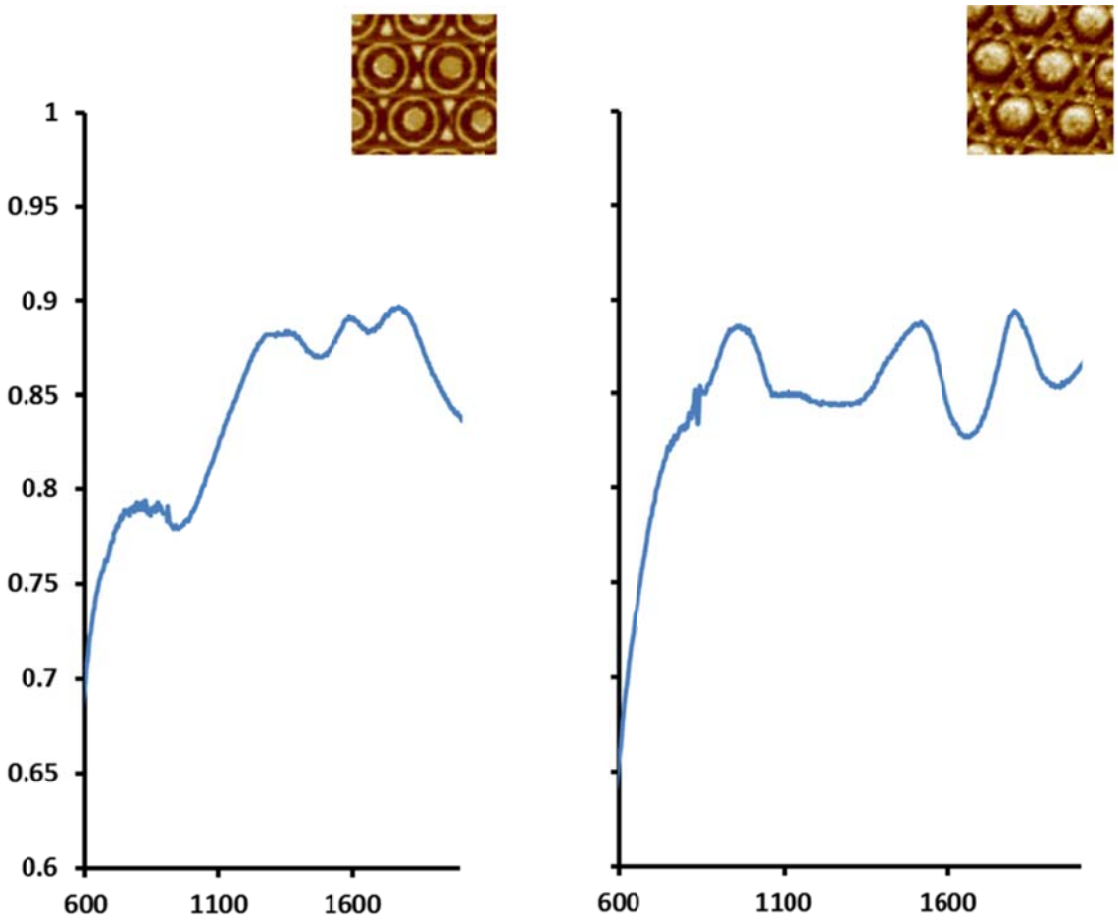

Figure 77. The extinction spectrum of both substrates in the visible-NIR range.

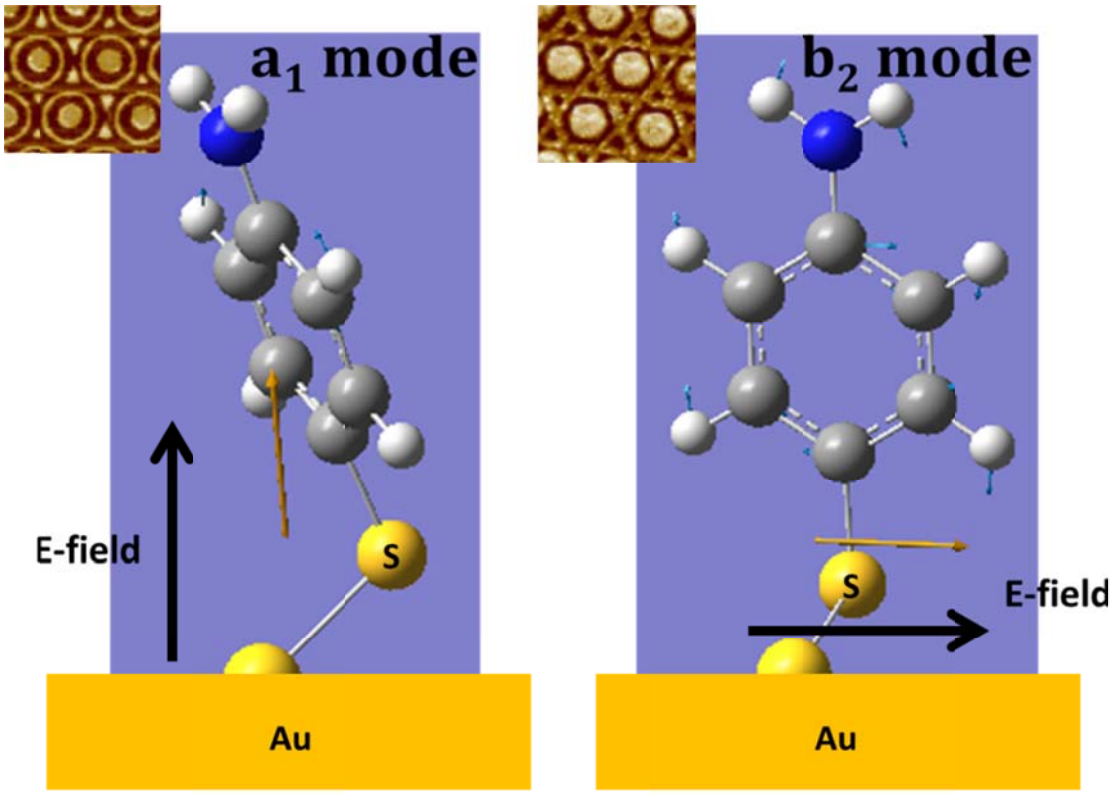

Figure 78. Simulated molecular vibrations of 4-ATP molecule and the proposed mechanism of mode-selective enhancement. The yellow arrows indicate the orientation of dipole changes for each type of vibrations.

However, our results demonstrated that the mode selectivity varied on different substrate under the same excitation light. Extinction spectrums of the two features are shown in Figure 77. It is easy to find out that the collecting window of Raman spectrums corresponded to 633 nm to 785 nm, which was red to any observed plasmon peak. Therefore, the selective enhancement of Raman resonances should be the same on both features if it was only determined by excitation wavelength. As a result, the phenomenon we observed should come from a different mechanism.

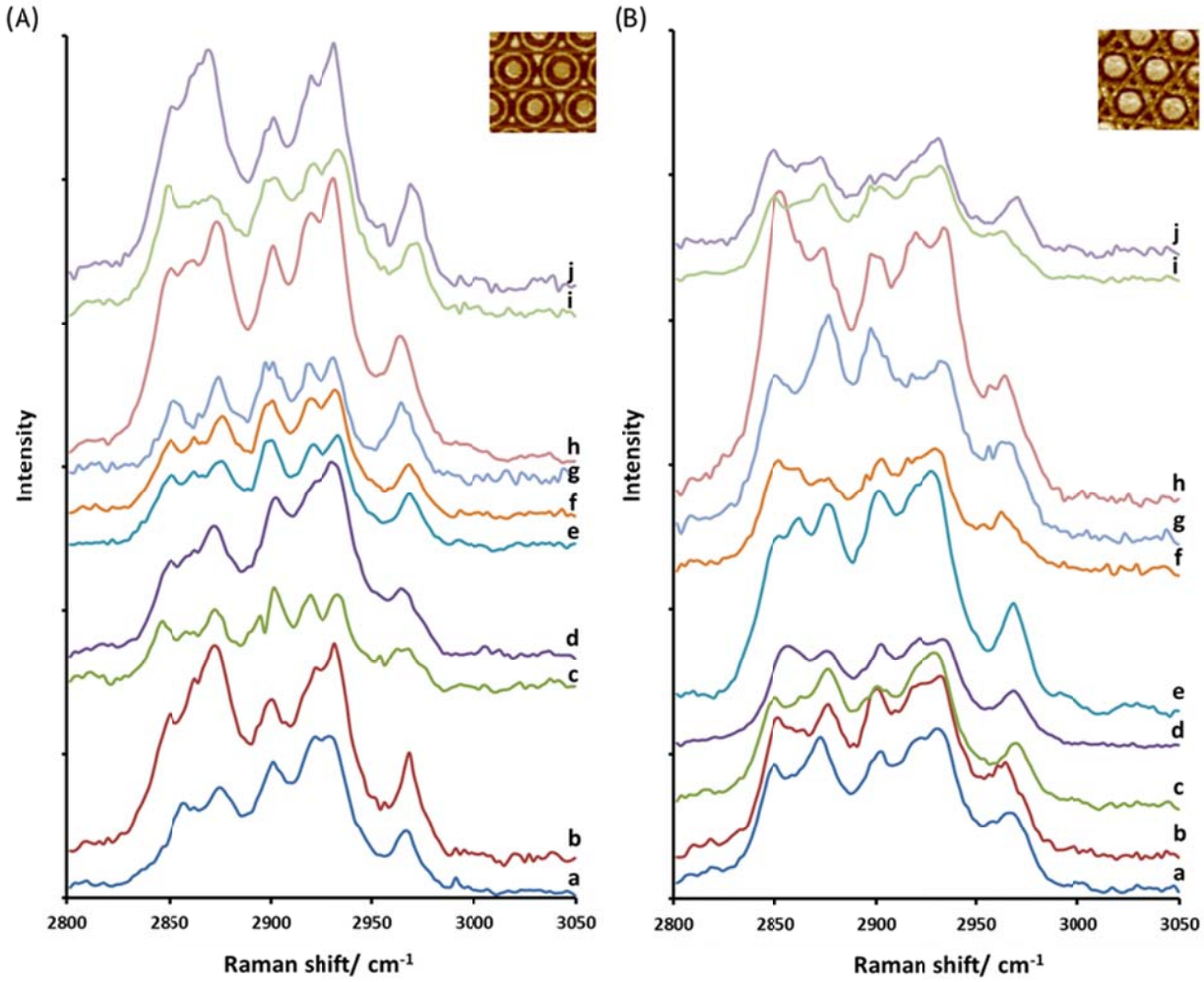

Figure 79. (A) SERS spectra of alkanethiol SAMs on nano-patterned gold substrate 1. (a) 1-heptanethiol, (b) 1-octanethiol, (c) 1-nonanethiol, (d) 1-decanthiol, (e) 1-undecanethiol, (f) 1-dodecanethiol, (g) 1-tridecanethiol, (h) 1-tetradecanethiol, (i) 1-pentadecanethiol, (j) 1-hexadecanethiol, (B) SERS spectra of alkanethiol SAMs on nano-patterned gold substrate 2. (a) 1-heptanethiol, (b) 1-octanethiol, (c) 1-nonanethiol, (d) 1-decanthiol, (e) 1-undecanethiol, (f) 1-dodecanethiol, (g) 1-tridecanethiol, (h) 1-tetradecanethiol, (i) 1-pentadecanethiol, (j) 1-hexadecanethiol.

The molecular orientations of 4-ATP SAM on gold surface have been well studied.[127, 128] In summary, 4-ATP molecules tended to maintain an almost upright conformation with a small tilted angle (~15°) relative to surface normal. Therefore, the dipole moment change in each vibrational mode was easy to calculate. Our simulation showed that the dipole change of a_1 resonances was close to perpendicular to the surface. As a comparison, dipole variation of b_2 modes possessed a direction nearly parallel to the surface. This result is also coincidence with results from other groups.[127, 128] Therefore, we could correlate our data with molecular vibrations. That is, resonances perpendicular to the surface would be enhanced more on the first substrate while parallel vibrations would be selectively enhanced on the second substrate. It is worthwhile to note that this type of selection was under the same experimental conditions. In other words, the mode selectivity of surface enhanced Raman spectroscopy changed in our experiments. To the best of our knowledge, the demonstration of mode-selective Raman under the same experimental conditions has never been shown previously.

The intensity in Raman spectra could be defined as:

$$\boldsymbol{I_{Raman} \propto \omega^4 \times \sigma \times I_o}$$

in which ω is the frequency of incident light, σ is the Raman cross section of a particle and I_0 is the initial intensity of incident beam. The Raman cross section for a specific vibration was typically isotropic, with the highest value appeared when the direction of external excitation is identical to the orientation of dipole change.[129] Therefore, it is possible to shift the intensity of a band in Raman spectra by simply changing the polarization state of excitation light. According to previous researches, the signal

enhancement in SERS was mainly caused by electronic enhancement, which was two orders of magnitude higher than other possible enhance mechanisms.[70, 130-132] Therefore, we assume our results should be mostly attribute to different electronic fields induced by surface plasmon. It is possible that 4-ATP adopts different orientations on the two substrates, leading to the various Raman mode enhancements. This, however, seems somewhat unlikely as the curvature of the features was quite large compared to the scale of the molecule's size. More likely, the different mode enhancements were intrinsic to the variations in the electric fields on the two substrate surfaces. As the surface plasmon is highly dependent on the geometric factors of the surface pattern, we believe that the mode selectivity was attributing to the different orientation of E-field on two substrates. It is most likely that the major component of E-field is perpendicular to the surface on the triangle-target pattern, which resulted in the selectively enhancement of a_1 resonances. By contrast, the E-field should be parallel to the surface for the hexagram-dot in order to selectively enhance b_2 resonances (Fig. 78).

Raman spectra in the ν(C-H) region from n-$CH_3(CH_2)_6SH$ to n-$CH_3(CH_2)_{15}SH$ were shown in Figure 78 where seven different modes were included. Two $\nu_{sym}(CH_2)$ bands were seen at 2850 and 2861 cm^{-1}. The 2861 cm^{-1} band corresponded to the $\nu_{sym}(CH_2)$ adjacent to the methyl group, while the other band corresponded to the remaining methylene groups. The lower frequency band was more intense in the long-chain n-alkanethiols because of the dominant number of methylene units. A band due to the Fermi resonance of the $\nu_{sym}(CH_2)$ and with the overtone of the $\delta(CH_2)$ band appeared at 2920 cm^{-1} and while the Fermi resonance of the $\nu_{sym}(CH_3)$ was located at 2935 cm^{-1}.

The $\nu_{asym}(CH_2)$ band appeared at 2900 cm^{-1} and the $\nu_{sym}(CH_3)$ band appeared at 2875 cm^{-1}. The $\nu_{asym}(CH_3)$ band appeared at 2965 cm^{-1} in these spectra. Both the $\nu_{sym}(CH_3)$ and $\nu_{asym}(CH_3)$ bands decreased in intensity relative to the methylene bands as the chain length increased, reflecting the increase in number of methylene groups. The vibrational modes and there approximate wavenumbers were listed in Table 4.

The structure of n-alkanethiol SAMs was well characterized by several groups.[89-98, 133] In general, the orientation of the head methyl group is nearly perpendicular to the surface for even-number n-alkanethiols and oblique to the surface for odd-number n-alkanethiols (Fig. 80A & 80B). This fixed molecular conformation allowed us to pick up two vibrational pairs whose intensity ratio would alternate alternatively with the increase of carbon numbers. In particular, the symmetric methyl stretching and the symmetric methylene stretching are orthogonal to each other (Fig. 80A). Consider the well structures of the n-alkanethiol SAMs, we would expect two opposite trends for the ratio of $\nu_{sym}(CH_3)$: $\nu_{sym}(CH_2)$ vs. carbon numbers in the molecule due to the distinctive plasmon field on the two substrate. Specifically, the ratio of $\nu_{sym}(CH_3)$: $\nu_{sym}(CH_2)$ would increase from odd-carbon n-alkanethiols to even-carbon n-alkanethiols or vice versa on substrate 1 for the reason that the symmetric methyl stretching would be selectively enhanced over the $\nu_{sym}(CH_2)$ on substrate 1 when it was perpendicular to the surface. As a comparison, the opposite trend would be anticipated on substrate 2 because the $\nu_{sym}(CH_3)$ of even carbon n-alkanethiols is orthogonal to the E-field in this case which gave it a weaker enhancement relative to $\nu_{sym}(CH_2)$. Similarly, we could predict the intensity ratio change when the substrate was changed for the same even carbon n-

Table 4. Raman shifts and the corresponding vibrational mode for n-alkanethiols

Vibrational mode	Raman shift /cm^{-1}
CH_2 symmetric stretching	2850
CH_2 symmetric stretching	2861
CH_3 symmetric stretching	2875
CH_2 asymmetric stretching	2900
CH_2 symmetric stretching, FR	2920
CH_3 symmetric stretching, FR	2935
CH_3 asymmetric stretching	2965

alkanethiol. An opposite variation would also be expected for odd and even carbon n-alkanethiols. In order to better demonstrated our theory as well as eliminate experimental error, we picked up another vibrational pairs for further analysis, that is, the ratio of $\nu_{sym}(CH_3)$: $\nu_{asym}(CH_3)$. The prediction of intensity ratio changes was summarized in Figure 81.

Following the data given in Table 4, we deconvolved the wide CH stretching region into seven Lorentzian peaks regarding the CH stretching mode positions. Such a deconvolution allows us to extract information on the signals of each individual CH stretching modes. An example demonstrating this fitting was shown in Figure 82. With this deconvolution, we could clearly see that the intensity ratio change for odd- and even-carbon n-alkanethiols on two substrates did match our theoretical prediction. For example, the ratio of both $\nu_{sym}(CH_3)$: $\nu_{sym}(CH_2)$ and $\nu_{sym}(CH_3)$: $\nu_{asym}(CH_3)$ increased from 1-heptanethiol to 1-octanethiol on substrate 1. As a comparison, both ratios decreased from 1-heptanethiol to 1-octanethiol on substrate 2. We also noticed that the ratios for octanethiol on substrate 1 is bigger than those on substrate 2 (Fig. 83). Similar comparisons for all the other n-alkanethiols could be found in Figure 83 to Figure 87.

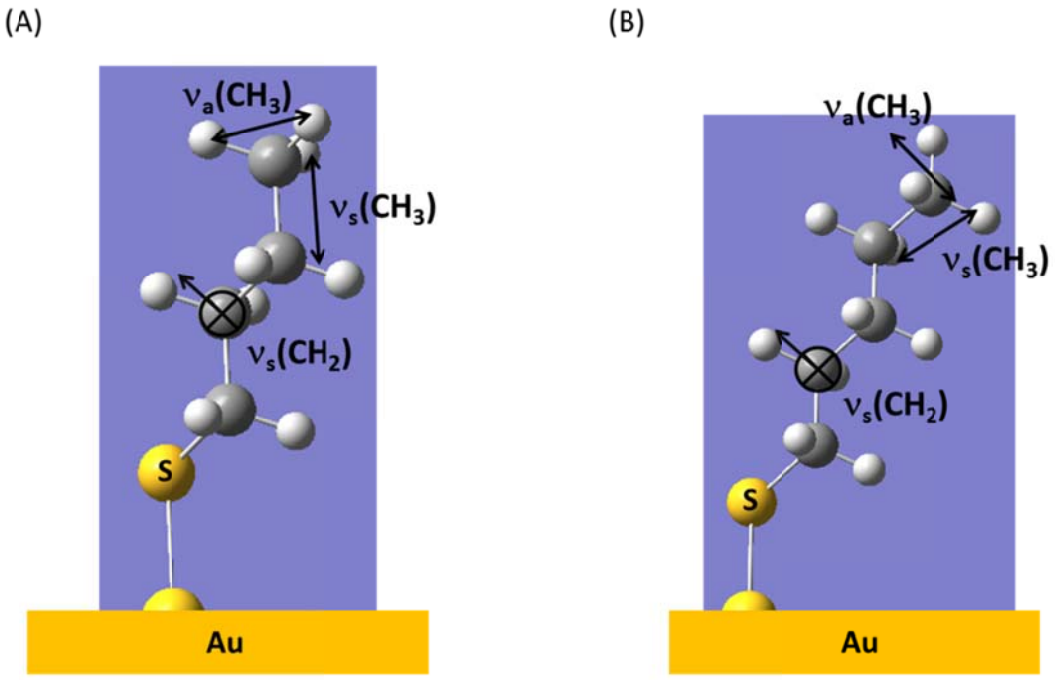

Figure 80. Molecular structures of absorbed odd- and even-carbon alkanethiols on gold surface and the orientations of vibrations selected for mode-selective SERS experiments.

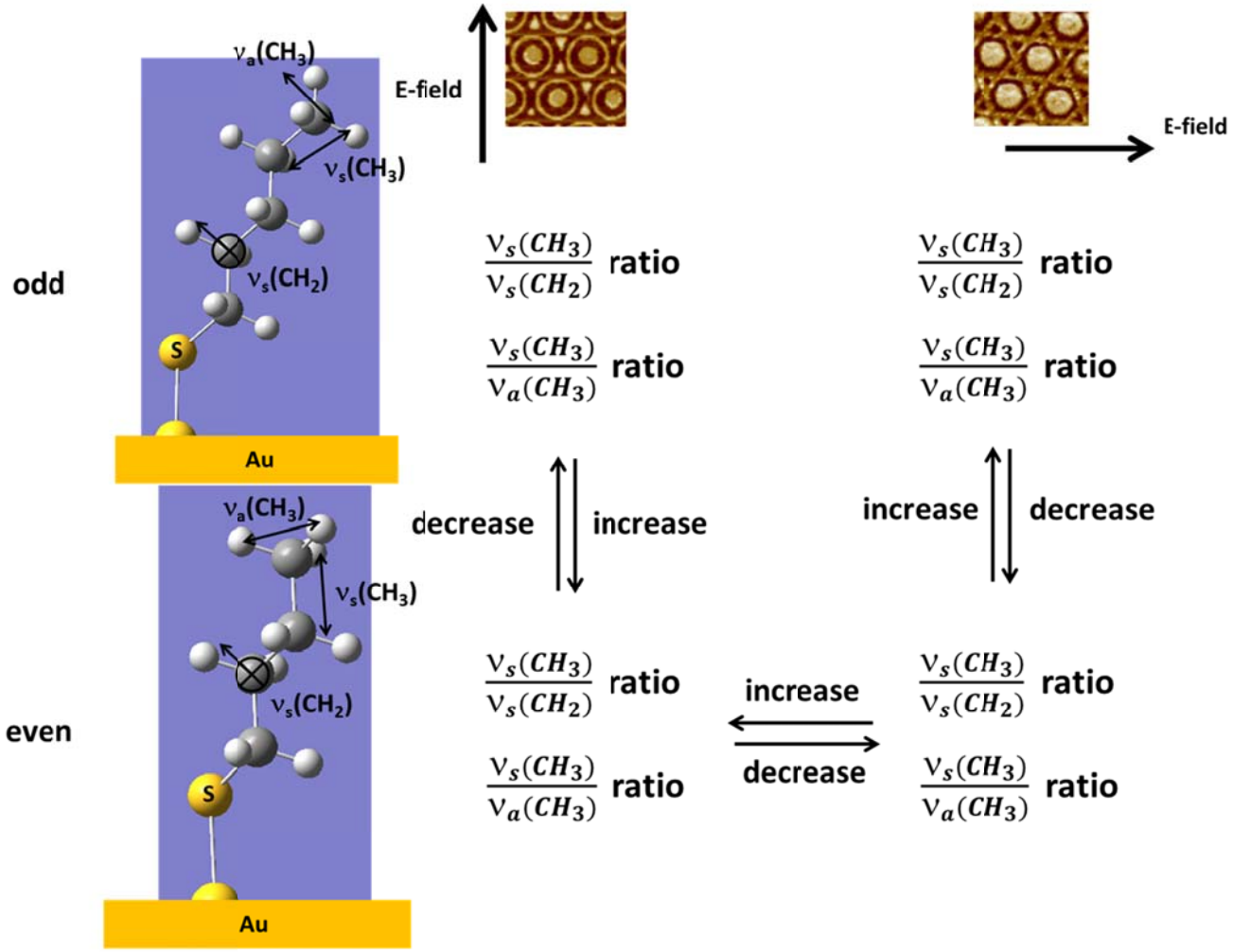

Figure 81. The predicted intensity ratio change of each orthogonal vibration pair.

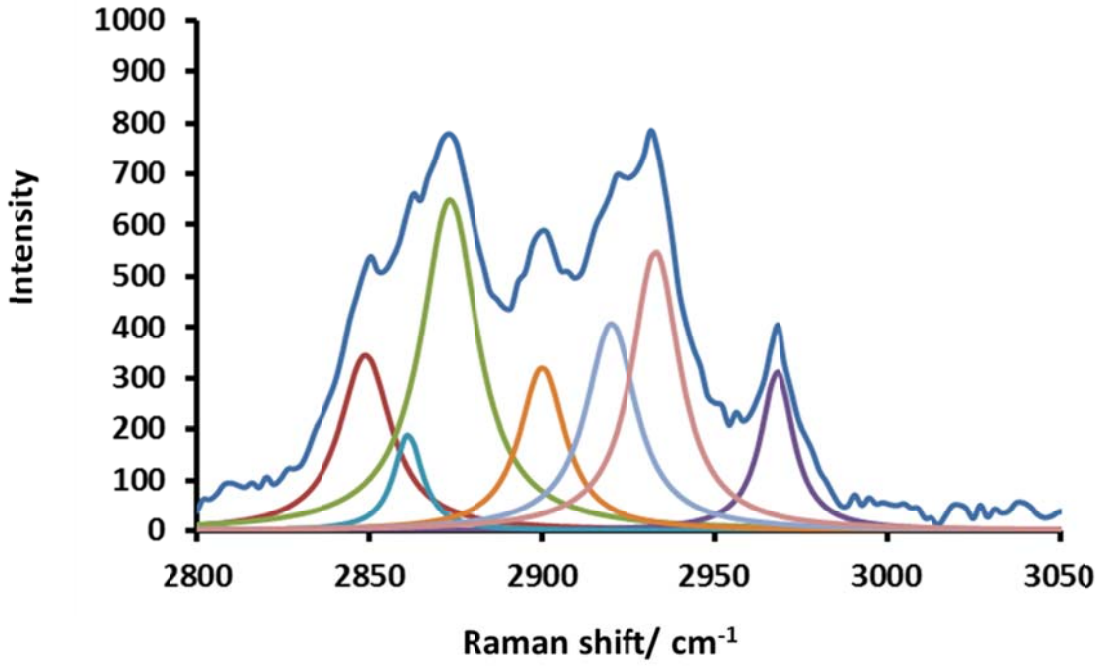

Figure 82. SERS spectra (dark blue) of 1-octanethiol and the corresponding fitting peak for $\nu_{sym}(CH_2)$ (red), $\nu_{sym}(CH_2)$ (light blue), $\nu_{sym}(CH_3)$ (green), $\nu_{asym}(CH_2)$ (orange), $\nu_{sym}(CH_2, FR)$ (grey), $\nu_{sym}(CH_3, FR)$ (pink), and $\nu_{asym}(CH_3)$ (purple).

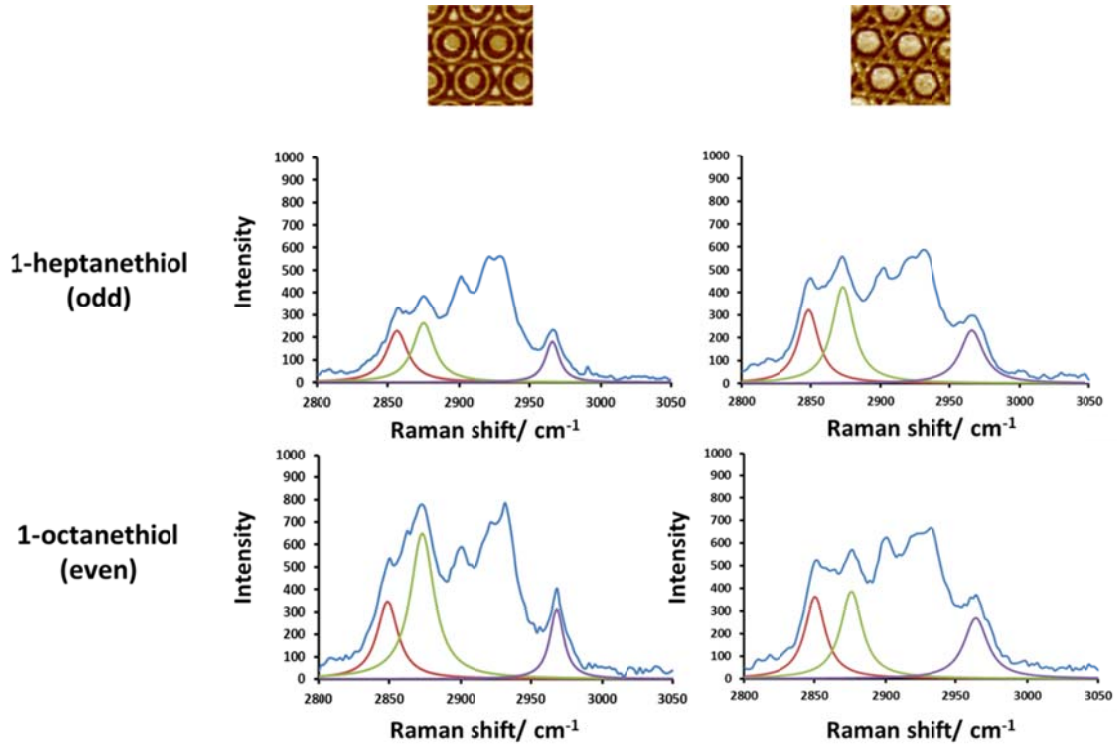

Figure 83. SERS spectra (blue) of 1-heptanethiol and 1-octanethiol on two substrates and the corresponding fitting peak for $\nu_{sym}(CH_2)$ (red), $\nu_{sym}(CH_3)$ (green) and $\nu_{asym}(CH_3)$ (purple).

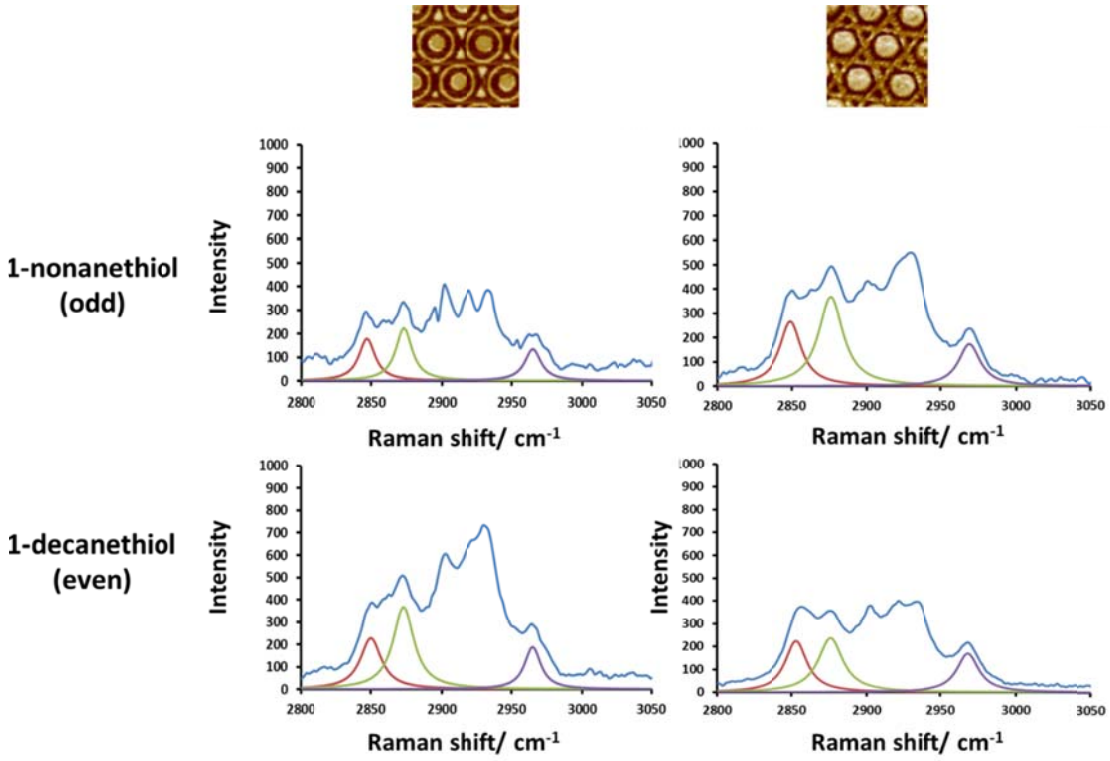

Figure 84. SERS spectra (blue) of 1-nonanethiol and 1-decanethiol on two substrates and the corresponding fitting peak for $\nu_{sym}(CH_2)$ (red), $\nu_{sym}(CH_3)$ (green) and $\nu_{asym}(CH_3)$ (purple).

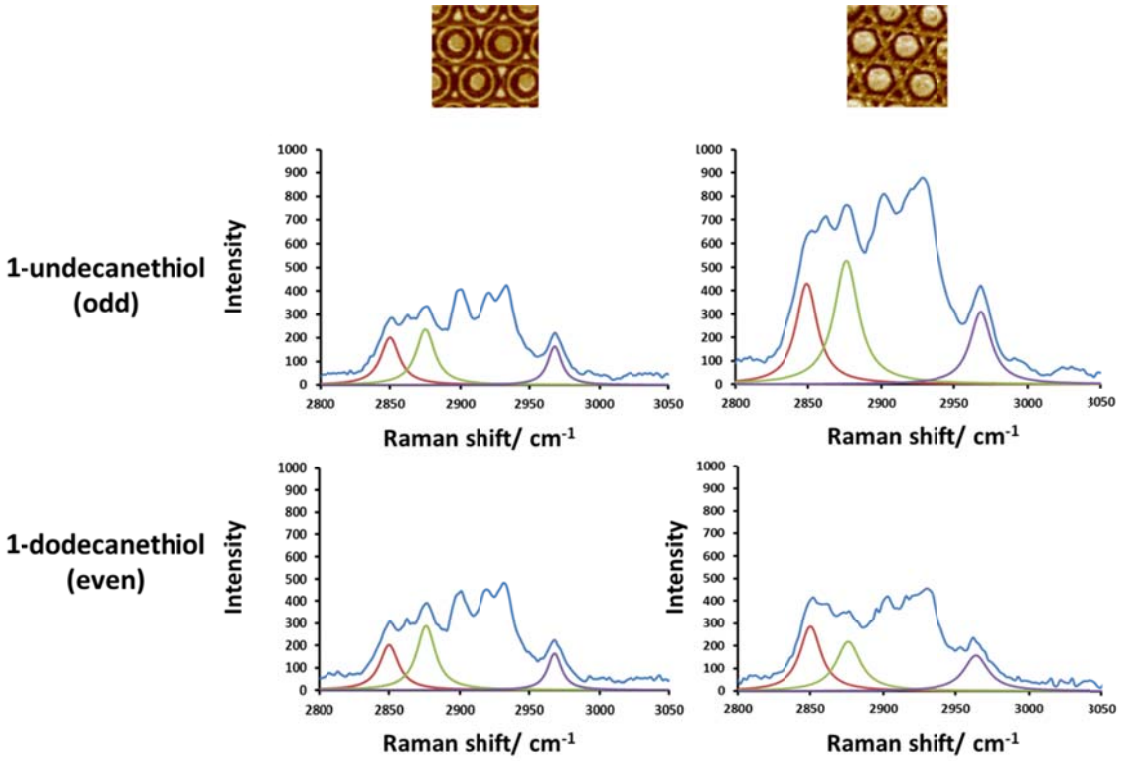

Figure 85. SERS spectra (blue) of 1-undecanethiol and 1-dodecanethiol on two substrates and the corresponding fitting peak for $\nu_{sym}(CH_2)$ (red), $\nu_{sym}(CH_3)$ (green) and $\nu_{asym}(CH_3)$ (purple).

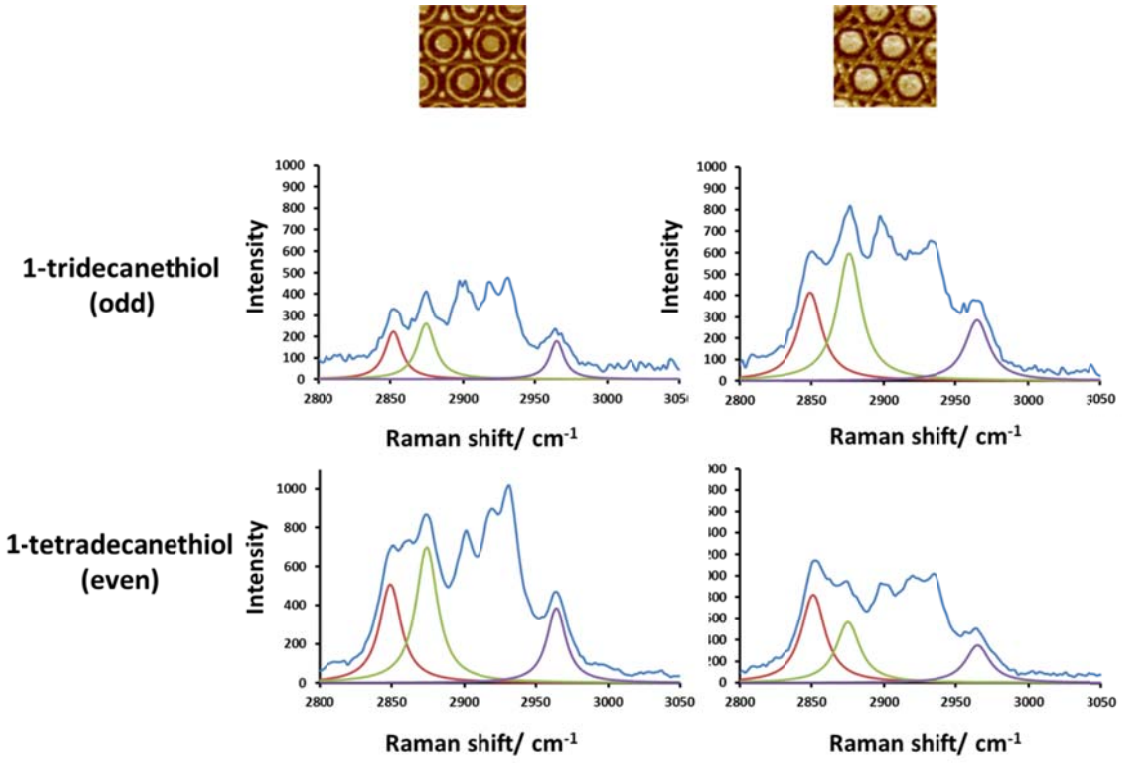

Figure 86. SERS spectra (blue) of 1-tridecanethiol and 1-tetradecanethiol on two substrates and the corresponding fitting peak for $\nu_{sym}(CH_2)$ (red), $\nu_{sym}(CH_3)$ (green) and $\nu_{asym}(CH_3)$ (purple).

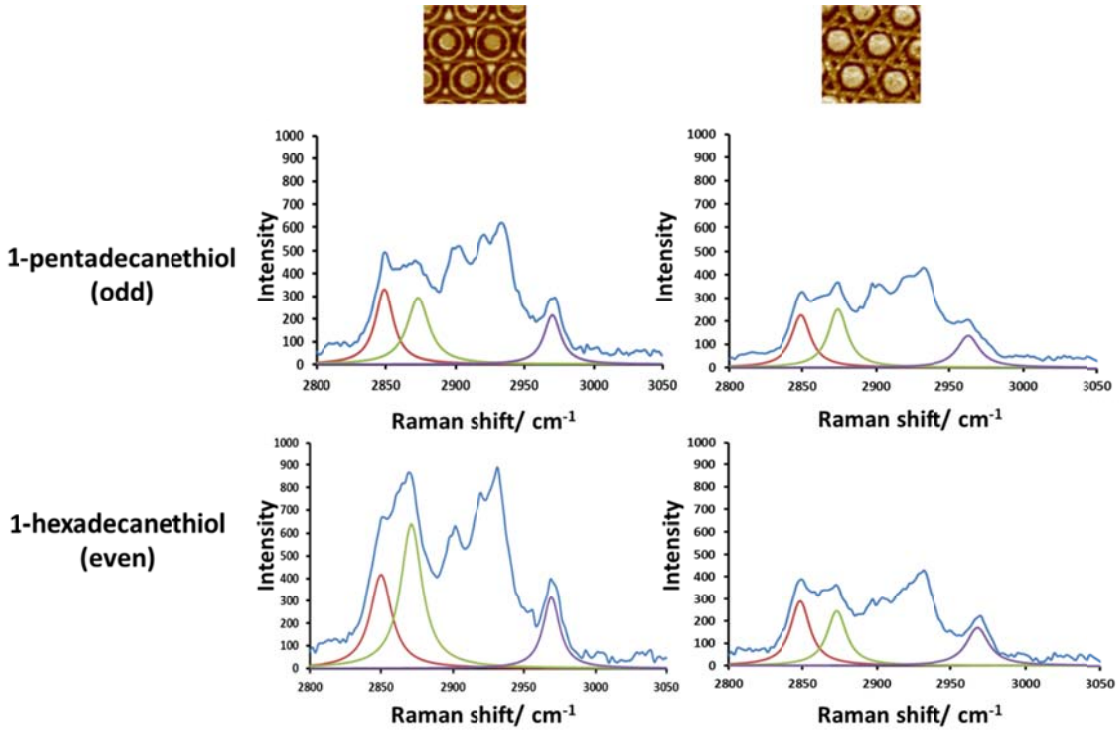

Figure 87. SERS spectra (blue) of 1-pentadecanethiol and 1-hexadecanethiol on two substrates and the corresponding fitting peak for $\nu_{sym}(CH_2)$ (red), $\nu_{sym}(CH_3)$ (green) and $\nu_{asym}(CH_3)$ (purple).

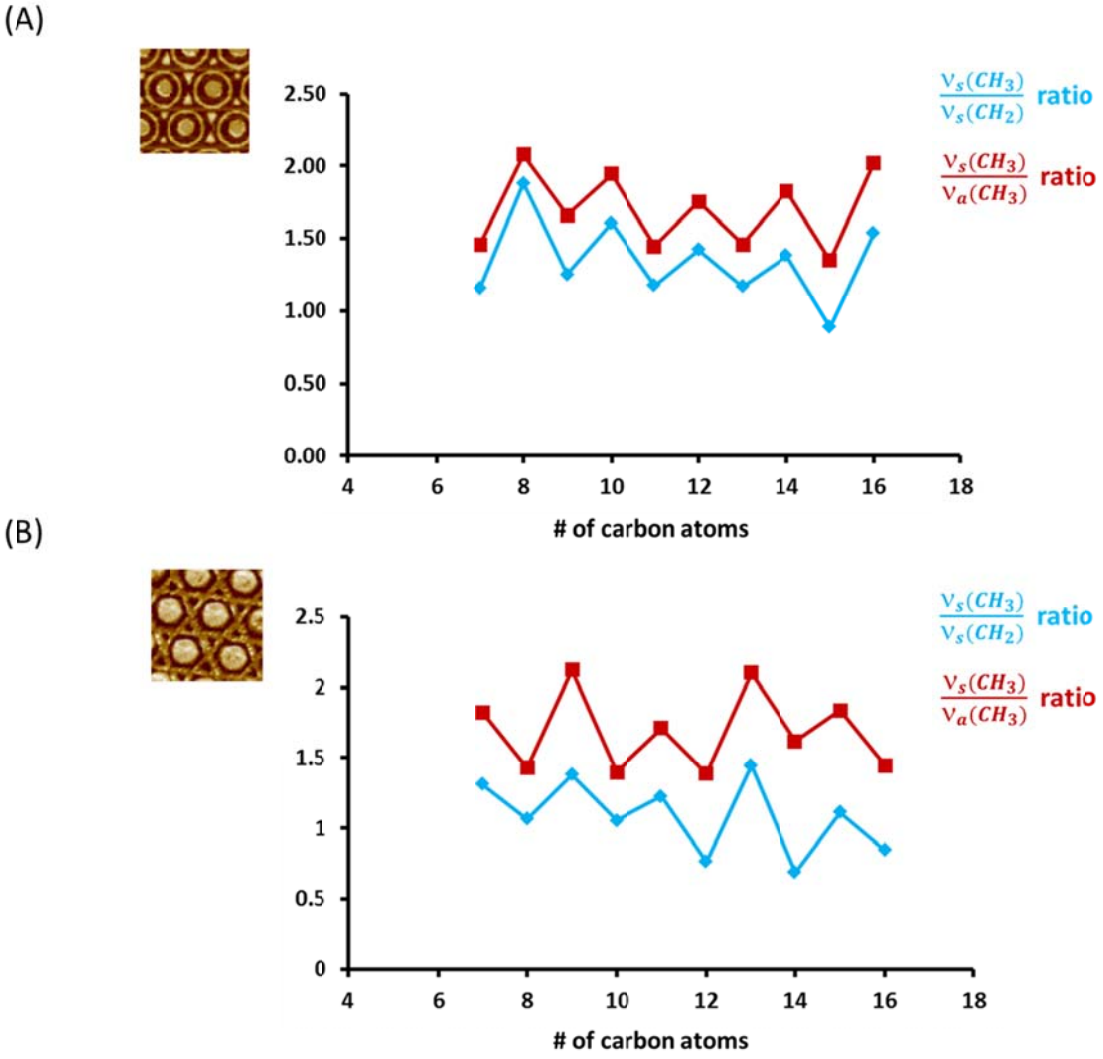

Figure 88. (A) Variation of $\nu_{sym}(CH_3)$: $\nu_{sym}(CH_2)$ and $\nu_{sym}(CH_3)$: $\nu_{asym}(CH_3)$ ratios as a function of carbon atom numbers on substrate 1. (B) Variation of $\nu_{sym}(CH_3)$: $\nu_{sym}(CH_2)$ and $\nu_{sym}(CH_3)$: $\nu_{asym}(CH_3)$ ratios as a function of carbon atom numbers on substrate 2.

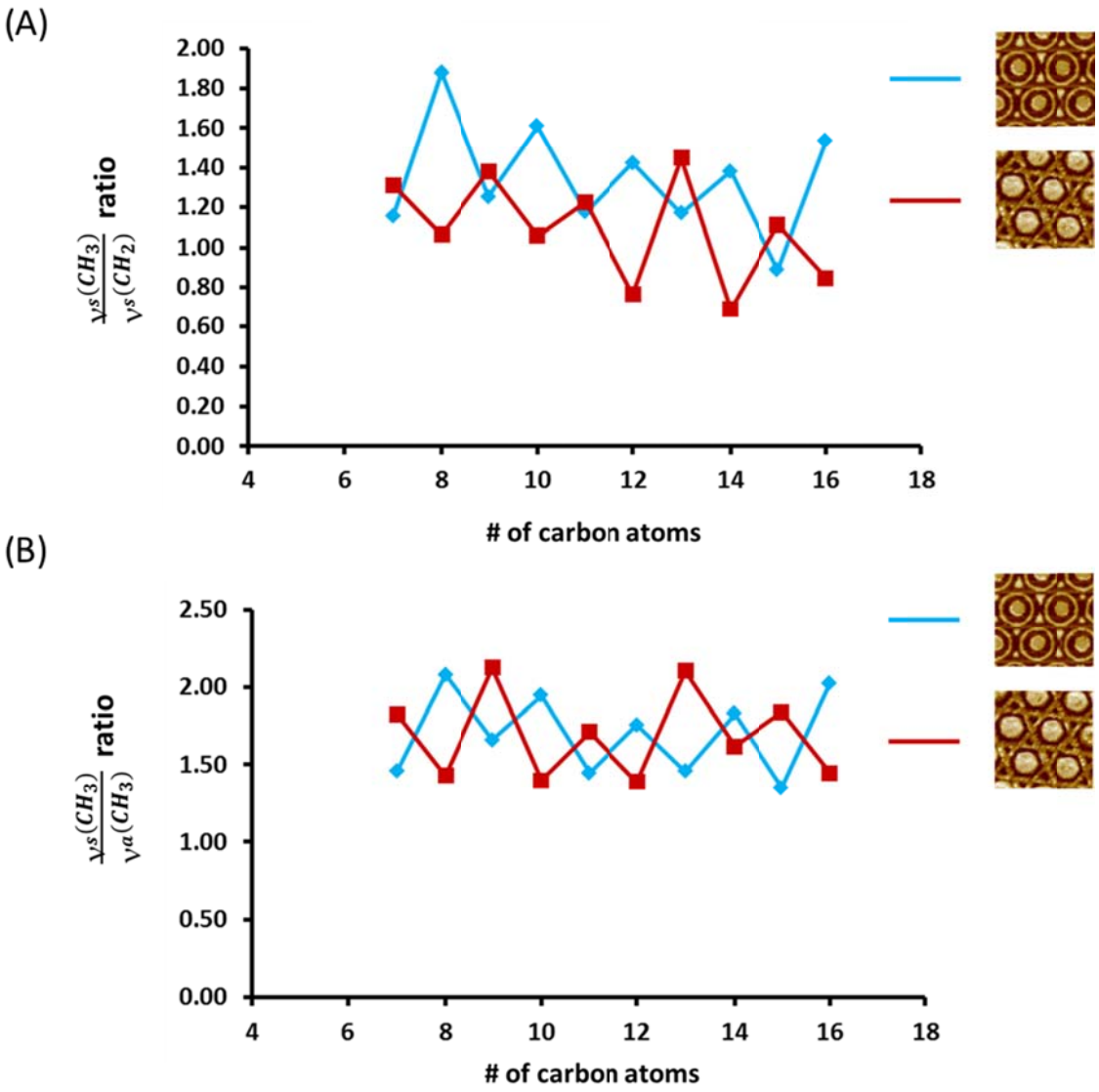

Figure 89. (A) Variation of $\nu_{sym}(CH_3)$: $\nu_{sym}(CH_2)$ ratio on two substrates. (B) Variation of $\nu_{sym}(CH_3)$: $\nu_{asym}(CH_3)$ ratio as a function of carbon atom numbers on two substrates.

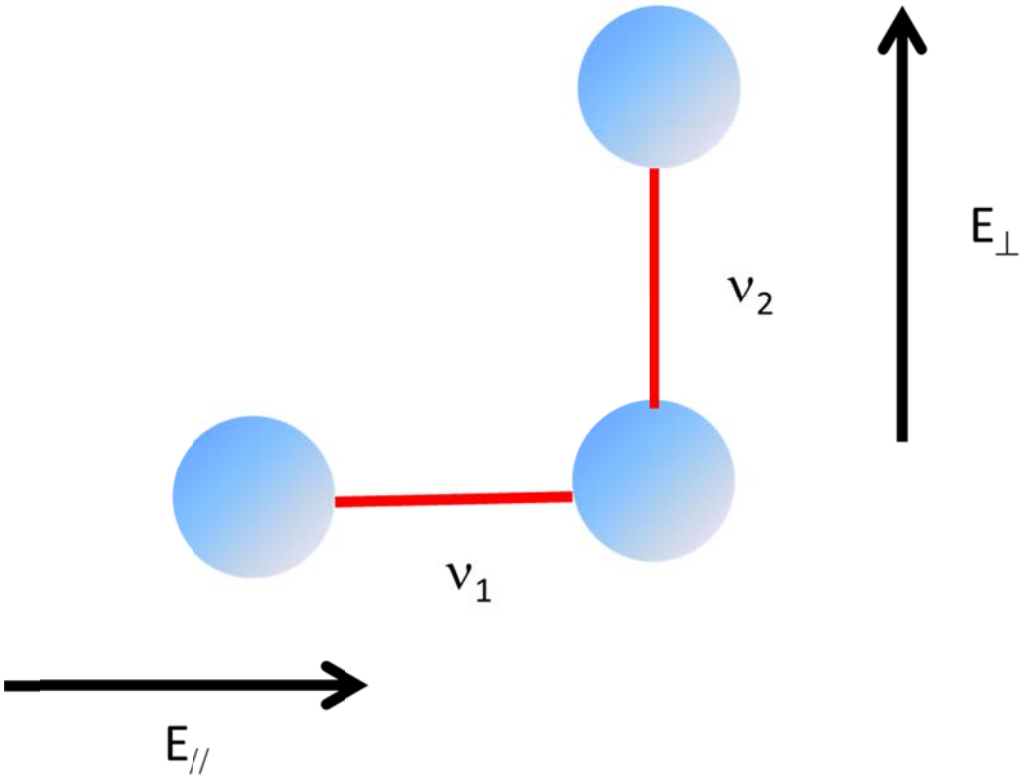

Figure 90. A model to estimate the sensitivity of mode-selective SERS.

We plotted the value ratio of $\nu_{sym}(CH_3)$: $\nu_{sym}(CH_2)$ and $\nu_{sym}(CH_3)$: $\nu_{asym}(CH_3)$ as a function of the number of methylene units for each of the substrate (Fig. 88). For substrate 1, both ratios went up from odd carbon number to even carbon number and then dropped for the next odd number. This trend was reversed as we changed the substrate into the hexagram-dot pattern. This comparison clearly demonstrated our assumption that the distinctive E-field on the two substrates would selectively enhance vibrations with different orientation. In addition, we plotted the value of each individual ratio for both substrate in the same plot (Fig. 89). The total opposite behavior for the

same vibrations on different substrates was extremely significant through this comparison.

The sensitivity of our mode-selective SERS in the detection of molecular structures could be briefly calculated as follows (Fig. 90). Assume that we have two orthogonal vibrations ν_1 and ν_2 whose intensity ratio was measured to determine the molecular conformation. The value of their intensity ratio could be written as ν_1 / ν_2. Consequently, the ratio of ν_1 / ν_2 under parallel and perpendicular excitations could be expressed as:

$$\frac{r_{/\!/}}{r_{\perp}} = \frac{\frac{I_1(parallel)}{I_2(perpendicular)}}{\frac{I_1(perpendicular)}{I_2(parallel)}} = \frac{I_1(parallel)}{I_1(perpendicular)} \times \frac{I_2(parallel)}{I_2(perpendicular)} = \frac{1}{\rho_1} \times \frac{1}{\rho_2} \qquad (4)$$

where $r_{/\!/}$ and $r_{\perp}$ are the ratio of ν_1 / ν_2 under parallel and perpendicular excitations; I_1, I_2 are the intensity of ν_1 and ν_2 and ρ_1, ρ_2 are the depolarization ratios of each vibration. The word parallel or perpendicular appeared in the parentheses indicate whether the E-field is parallel or perpendicular to the direction of vibrations. For example, the parallel E field is parallel to the orientation of ν_1 but perpendicular to the orientation of ν_2. Consequently, the annotation for I_1 would be parallel but perpendicular for I_2. The ratio of ν_1 / ν_2 under two orthogonal fields therefore is equal to the product of the reciprocal of two depolarization ratios. It is well known that the depolarization ratio is 0.75 for total symmetric vibrations and smaller than 0.75 for the rest of cases. Therefore, the minimum value for the ratio of ν_1 / ν_2 should be equal to ~1.8 when the two depolarization ratios are all 0.75. This result demonstrated that our technology

would be able to discriminate orthogonal vibrations by double their intensity ratio, which is much more sensitive than several currently used technique, including IR and SFG.[89, 93, 99]

CHAPTER IV

CONCLUSIONS*

In summary, we have devised two novel lithographic strategies to establish nano-pattern libraries. Our methodologies combine bottom-up and top-down techniques and are simple, versatile and cost-efficient. Our techniques possess several promising applications. We have demonstrated the distinctive SPR properties of our nano-features as well as a mode-selective SERS towards the sensitive detection of molecular structures.

First, we have developed a novel strategy to establish libraries of symmetric surface patterns. The approach used a combination of colloidal lithography, reactive ion etching and soft lithography for patterning a thin PS layer followed by etching an Au layer. Indeed, a wide variety of PS and Au patterns were fabricated on the micron and nanoscales. Unique and complex metal features, such as hexagonal webs and targets with triangles could be created by simply choosing a proper template and PS layer thicknesses. Such complex nanoscale features patterned over large areas would be difficult to create by other methods. Second, we developed a novel strategy to establish libraries of asymmetric and nonconcentric plasmonic structures. As far as we know, this is the first alternation of e-beam lithography in the patterning of multiple controllable,

---

*Part of the data reported in this chapter is reprinted with permission from "Stepwise Molding, Etching, and Imprinting to Form Libraries of Nanopatterned Substrates" by Zhao,Z.; Cai, Y.; Liao, W.; Cremer, P. S., 2013. *Langmuir*, 29, 6737-6745, Copyright [2013] by American Chemical Society.

nanosized non-concentric features. The approach used here combined the functions of colloidal lithography, reactive ion etching and soft lithography yet was more time and cost effective. It is also easy to be repeated in regular labs. The method could be further applied in create surface patterns of different material by combining with other lithographical methods. Indeed, a wide variety of polystyrene and Au patterns have already been fabricated on the micro and nanoscales. Unique and complex features, such as asymmetric hexagonal web and target with triangles, could be created by simply choosing a proper combination of template and polymer layer thickness. The same feature would be extremely difficult to be generated by other methods. With the precise control of parameters of features, our method would be capable to provide substrates for multiple applications in optics and electronics.

Finally, we have demonstrated a substrate dependent SERS in which the perpendicular and tangential vibrations of a molecule are selectively enhanced on different nano-patterns. This surface dependent Raman selection phenomenon should be attributed to the specific local orientations of E-field induced by each individual surface plasmon resonance. By measuring the intensity variation of orthogonal vibrations, this mode-selective SERS could be applied in the determination of molecular structures. We show here that the structural difference of n-alkanethiol SAMs could be easily told with this technique. An alternative variation of relative peak intensities have been observed on two substrates and the trends of the variation are opposite to each other. Molecular simulations have further confirmed our assumption.

REFERENCES

(1) Joannopoulos, J. D.; Villeneuve, P. R.; Fan, S. H. Photonic crystals: putting a new twist on light. *Nature* **1997**, 386, 143-149.

(2) Joannopoulos, J. D.; Meade, R. D.; Winn, J. N. *Photonic Crystals: Modeling the Flow of Light*, Princeton University Press: Princeton, NJ, 1995.

(3) Jacobs, H. O.; Whitesides, G. M. Submicrometer patterning of charge in thin-film electrets. *Science* **2001**, 291, 1763-1766.

(4) Thurn-Albrecht, T.; Schotter, J.; Kastle, C. A.; Emley, N.; Shibauchi, T.; Krusin-Elbaum, L.; Guarini, K.; Black, C. T.; Tuominen, M. T.; Russell, T. P. Ultrahigh-density nanowire arrays grown in self-assembled diblock copolymer templates. *Science* **2000**, 290, 2126-2129.

(5) Haes, A. J.; Van Duyne, R. P. A nanoscale optical biosensor: sensitivity and selectivity of an approach based on the localized surface plasmon resonance spectroscopy of triangular silver nanoparticles. *J. Am. Chem. Soc.* **2002**, 124, 10596-10604.

(6) Ostuni, E.; Chen, C. S.; Ingber, D.; Whitesides, G. M. Selective deposition of proteins and cells in arrays of microwells. *Langmuir* **2001**, 17, 2828-2834.

(7) Lee, K. B.; Park, S. J.; Mirkin, C. A.; Smith, J. C.; Mrksich, M. Protein nanoarrays generated by dip-pen nanolithography. *Science* **2002**, 295, 1702-1705.

(8) Kohli, P.; Harrell, C. C.; Cao, Z.; Gasparac, R.; Tan, W.; Martin, C. R. DNA-functionalized nanotube membranes with single-base mismatch selectivity. *Science* **2004**, 305, 984-986.

(9) Chan, W. C. W.; Nie, S. Quantum dot bioconjugates for ultrasensitive nonisotopic detection. *Science* **1998**, 281, 2016-2018.

(10) Han, M.; Gao, X.; Su, J. Z.; Nie, S. quantum-dot-tagged microbeads for multiplexed optical coding of biomolecules. *Nat. Biotechnol.* **2001**, 19, 631-635.

(11) Ebbesen, T. W.; Lezec, H. J.; Ghaemi, H. F.; Thio, T.; Wolff, P. A. Extraordinary optical transmission through sub-wavelength hole arrays. *Nature* **1998**, 391, 667-669.

(12) Farcau, C.; Astilean, S. Mapping the SERS efficiency and hot-spots localization on gold film over nanospheres substrates. *J. Phys. Chem. C* **2010**, 114, 11717-11722.

(13) Braun, G.; Pavel, I.; Morrill, A.R.; Seferos, D.S.; Bazan, B.C.; Reich, N.O.; Moskovits, M. Chemically patterned microspheres for controlled nanoparticle assembly in the construction of SERS hot spots. *J. Am. Chem. Soc.* **2007**, 129, 7760-7761.

(14) Link, S.; El-Sayed, M. A. Size and temperature dependence of the plasmon absorption of colloidal gold nanoparticles. *J. Phys. Chem. B* **1999**, 103, 4212-4217.

(15) Gao, H.; McMahon, J. M.; Lee, M. H.; Henzie, J.; Gray, S. K.; Schatz, G. C.; Odom, T. W. Rayleigh anomaly-surface plasmon polariton resonances in palladium and gold subwavelength hole arrays. *Opt. Express* **2009**, 17, 2334-2340.

(16) Stewart, M. E.; Anderton, C. R.; Thompson, L. B.; Maria, J.; Gray, S. K.; Rogers, J. A.; Nuzzo, R. G. Nanostructured plasmonic sensors. *Chem. Rev.* **2008**, 108, 494-521.

(17) Rechberger, W.; Hohenau, A.; Leitner, A.; Krenn, J. R.; Lamprecht, B. F.; Aussenegg, R. Optical properties of two interacting gold nanoparticles. *Opt. Commun.* **2003**, 220, 137-141.

(18) Grand, J.; Adam, P. M.; Grimault, A. S.; Vial, A.; de la Chapelle, M. L.; Bijeon, J. L.; Kostcheev, S.; Royer, P. Optical extinction spectroscopy of oblate, prolate and ellipsoid shaped gold nanoparticles: experiments and theory. *Plasmonics* **2006**, 1, 135-140.

(19) Duan, H.; Hu, H.; Kumar, K.; Shen, Z.; Yang, J. Direct and reliable patterning of plasmonic nanostructures with sub-10-nm gaps. *ACS Nano* **2011**, 5, 7593-7600.

(20) Ohno, T.; Bain, J. A.; Schlesinger, T. E.; Observation of geometrical resonance in optical throughput of very small aperture lasers associated with surface plasmons. *J. Appl. Phys.* **2007**, 101, 083107.

(21) Moreau, W. M. *Semiconductor Lithography,* Plenum: New York, 1989.

(22) Haynes, C. L.; Van Duyne, R. P. Nanosphere lithography: a versatile nanofabrication tool for studies of size-dependent nanoparticle optics. *J. Phys. Chem. B* **2001**, 105, 5599-5611.

(23) Geng, C.; Zheng, L.; Yu, J.; Yan, Q.; Wei, T.; Wang, X.; Shen, D. Thermal annealing of colloidal monolayer at the air/water interface: a facile approach to transferrable colloidal masks with tunable interstice size for nanosphere lithography. *J. Mater. Chem.* **2012**, 22, 22678-22685.

(24) Xia, Y.; Whitesides, G. M. Soft lithography. *Angew. Chem. Int. Ed.* **1998**, 37, 550-575.

(25) Huang, Y.; Paloczi, G. T.; Yariv, A.; Zhang, C.; Dalton, L. R. Fabrication and replication of polymer integrated optical devices using electron-beam lithography and soft lithography. *J. Phys. Chem. B* **2004**, 108, 8606-8613.

(26) Kim, Y. H.; Park, J.; Yoo, P. J.; Hammond, P. T. Selective assembly of colloidal particles on a nanostructured template coated with polyelectrolyte multilayers. *Adv. Mater.* **2007**, 19, 4426-4430.

(27) Li, X.; Peter, M.; Huskens, J.; Reinhoudt, D. N. Catalytic microcontact printing without ink. *Nano Lett*. **2003**, 3, 1449-1453.

(28) Chen, J. Y.; Klemic, J. F.; Elimelech, M. Micropatterning microscopic charge heterogeneity on flat surfaces for studying the interaction between colloidal particles and heterogeneously charged surfaces. *Nano Lett.* **2002**, 2, 393-396.

(29) Armani, A. M.; Kulkarni, R. P.; Fraser, S. E.; Flagan, R. C.; Vahala, K. J.; Moskovits, M. J.; Suh, S. Label-free, single-molecule detection with optical microcavities. *Science* **2007**, 317, 783-787.

(30) Blanchard-Dionne, A-P.; Guyot, L.; Patskovsky, S.; Gordon, R.; Meunier, M. Intensity based surface plasmon resonance sensor using a nanohole rectangular array. *Optics Express*, **2011**, 19, 15041-15046.

(31) Roh, S.; Chung, T.; Lee, B. Overview of the characteristics of micro- and nano-structured surface plasmon resonance sensors. *Sensors* **2011**, 11, 1565-1588.

(32) Zhang, M.; Qing, G.; Xiong, C.; Cui, R. Pang, D.; Sun, T. Dual-responsive gold nanoparticles for colorimetric recognition and testing of carbohydrates with a dispersion-dominated chromogenic process. *Adv. Mater* **2013**, 25, 749-754.

(33) Pang, L.; Hwang, G. M.; Slutsky, B.; Fainman, Y. Spectral sensitivity of two-dimensional nanohole array surface plasmon polariton resonance sensor. *App. Phys. Lett.* **2007**, 91, 123112.

(34) Yu, C.; Irudayaraj, J. Multiplex biosensor using gold nanorods. *Anal. Chem.* **2007**, 79, 572-579.

(35) Arlett, J. L.; Myers, E. B.; Roukes, M. L. Comparative advantages of mechanical biosensors. *Nat. Nanotechnol.* **2011**, 6, 203-215.

(36) Waldeisen, J. R.; Wang, T.; Ross, B. M.; Lee, L. P. Disassembly of a core–satellite nanoassembled substrate for colorimetric biomolecular detection. *ACS Nano* **2011**, 5, 5383-5389.

(37) Verellen, N.; Sonnefraud, Y.; Sobhani, H.; Hao, F.; Moshchalkov, V. V.; Van Dorpe, P.; Nordlander, P.; Maier. S. A. Fano resonances in individual coherent plasmonic nanocavities. *Nano Lett.* **2009**, 9, 1663-1667.

(38) Fedotov, V. A.; Rose, M.; Prosvirnin, S. L.; Papasimakis, N.; Zheludev, N. I. Sharp trapped-mode resonances in planar metamaterials with a broken structural symmetry. *Phys. Rev. Lett.* **2007**, 99, 147401.

(39) Zheludev, N. I.; Prosvirnin, S. L.; Papasimakis, N.; Fedotov, V. A. Lasing spaser. *Nature Photon* **2008**, 2, 351-354.

(40) Chu, M.; Myroshnychenko, V.; Chen, C. H.; Deng, J.; Mou, C.; Javier García de Abajo, F. Probing bright and dark surface-plasmon modes in individual and coupled noble metal nanoparticles using an electron beam. *Nano Lett.* **2009**, 9, 399-404.

(41) Nordlander, P.; Oubre, C.; Prodan, E.; Li, K.; Stockman, M. I. Plasmon hybridization in nanoparticle dimers. *Nano Lett.* **2004**, 4, 899-903.

(42) Ding, P.; Liang, E.; Cai, G.; Hu, W.; Fan, C.; Xue, Q. Dual-band perfect absorption and field enhancement by interaction between localized and propagating surface plasmons in optical metamaterials. *J. Opt.* **2011**, 075005.

(43) Hu, C.; Liu, L.; Zhao, Z.; Chen, X.; Luo, X. Mixed plasmons coupling for expanding the bandwidth of near-perfect absorption at visible frequencies. *Opt. Express* **2009**, 17, 16745-16749.

(44) Lukyanchuk, B.; Zheludev, N. I.; Maier, S. A.; Halas, N. J.; Nordlander, P.; Giessen, H.; Chong, C. T. The Fano resonance in plasmonic nanostructures and metamaterials. *Nature Materials* **2010**, 9, 707-715.

(45) Zhang, S.; Bao, K.; Halas, N. J.; Xu, H.; Nordlander P. Substrate-induced Fano resonances of a plasmonic nanocube: a route to increased-sensitivity localized surface plasmon resonance sensors revealed. *Nano Lett.* **2011**, 11, 1657-1663.

(46) Hao, F.; Sonnefraud, Y.; Van Dorpe, P.; Maier, S. A.; Halas, N. J.; Nordlander, P. Symmetry breaking in plasmonic nanocavities: subradiant LSPR sensing and a tunable Fano resonance. *Nano Lett.* **2008**, 8, 3983-3988.

(47) Cetin, A. E.; Altug, H. Fano resonant ring/disk plasmonic nanocavities on conducting substrates for advanced biosensing. *ACS Nano* **2012**, 6, 9989-9995.

(48) Zhang, S.; Genov, D. A.; Wang, Y.; Liu, M.; Zhang, X. Plasmon-induced transparency in metamaterials. *Phys. Rev. Lett.* **2008**, 101, 047401.

(49) Chang, W. S.; Lassiter, J. B.; Swanglap, P.; Sobhani, H.; Khatua, S.; Nordlander, P.; Halas, N. J.; Link, S. A plasmonic Fano switch. *Nano Lett.* **2012**, 12, 4977-4982.

(50) Malinsky, M. D.; Kelly, K. L.; Schatz, G. C.; Van Duyne, R. P. Nanosphere lithography: effect of substrate on the localized surface plasmon resonance spectrum of silver nanoparticles. *J. Phys. Chem. B* **2001**, 105, 2343-2350.

(51) Fredriksson, H.; Alaverdyan, Y.; Dmitriev, A.; Langhammer, C.; Sutherland, D. S.; Zaech, M.; Kasemo, B. Hole–mask colloidal lithography. *Adv. Mater.* **2007**, 19, 4297-4302.

(52) Hanarp, P.; Kaell, M.; Sutherland, D. S. Optical properties of short range ordered arrays of nanometer gold disks prepared by colloidal lithography. *J. Phys. Chem. B* **2003**, 107, 5768-5772.

(53) Sun, Z.; Li, Y.; Zhang, J.; Li, Y.; Zhao, Z.; Zhang, K.; Zhang, G.; Guo, J.; Yang, B. A universal approach to fabricate various nanoring arrays based on a colloidal-crystal-assisted-lithography strategy. *Adv. Funct. Mater.* **2008**, 18, 4036-4042.

(54) Liao, W. S.; Chen, X.; Chen, J.; Cremer, P. S. Templating water stains for nanolithography. *Nano Lett.* **2007**, 7, 2452-2458.

(55) McLellan Joseph, M.; Geissler, M.; Xia, Y. Edge Spreading lithography and its application to the fabrication of mesoscopic gold and silver rings. *J. Am. Chem. Soc.* **2004**, 126, 10830-10831.

(56) Chen, J.; Liao, W. S.; Chen, X.; Yang, T.; Wark, S. E.; Son, D. H.; Batteas, J. D.; Cremer, P. S. Evaporation-induced assembly of quantum dots into nanorings. *ACS Nano* **2009**, 3, 173-180.

(57) Lu, Y.; Yin, Y.; Xia, Y. Preparation and characterization of micrometer-sized "egg shells". *Adv. Mater.* **2001**, 13, 271-274.

(58) Jorgenson, R. C.; Yee, S. S. A fiber-optic chemical sensor based on surface plasmon resonance. *Sensors and Actuators B: Chemical* **1993**, 12, 213-220.

(59) Genet, C.; Ebbesen, T. W. Light in tiny holes. *Nature* **2007**, 445, 39-46.

(60) Degiron, A.; Ebbesen, T. W. The role of localized surface plasmon modes in the enhanced transmission of periodic subwavelength apertures. *Journal of Optics A-Pure and Applied Optics* **2005**, 7, S90-S96.

(61) Krishnan, A.; Thio, T.; Kima, T. J.; Lezec, H. J.; Ebbesen, T. W.; Wolff, P. A.; Pendry, J.; Martin-Moreno, L.; Garcia-Vidal, F. J. Evanescently coupled resonance in surface plasmon enhanced transmission. *Optics Communications* **2001**, 200, 1-7.

(62) Baida, F. I.; Van Labeke, D. Light transmission by subwavelength annular aperture arrays in metallic films. *Optics Communications* **2002**, 209, 17-22.

(63) Chang, S. H.; Gray, S. K.; Schatz, G. C. Surface plasmon generation and light transmission by isolated nanoholes and arrays of nanoholes in thin metal films. *Optics Express* **2005**, 13, 3150-3165.

(64) Chan, G. H.; Zhao, J.; Hicks, E. M.; Schatz, G. C.; Van Duyne, R. P. Plasmonic properties of copper nanoparticles fabricated by nanosphere lithography. *Nano Lett.* **2007**, 7, 1947-1952.

(65) Lassiter, J. B.; Sobhani, H.; Fan, J. A.; Kundu, J.; Capasso, F.; Nordlander, P.; Halas, N. J. Fano resonances in plasmonic nanoclusters: geometrical and chemical tenability. *Nano Lett.* **2010**, 10, 3184-3189.

(66) Raman, C. V.; Krishnan, K. S. A new type of secondary radiation. *Nature* **1928**, 121, 501-502.

(67) Kneipp, K.; Kneipp, H. Single molecule Raman scattering. *Appl. Spectroscopy* **2006**, 60, 322A-334A.

(68) Jeanmaire, D. L.; Van Duyne, R. P. Surface Raman electrochemistry part I. heterocyclic, aromatic and aliphatic amines adsorbed on the anodized silver electrode. *Journal of Electroanalytical Chemistry* **1977**, 84, 1–20.

(69) Grant Albrecht, M.; Alan Creighton, J. Anomalously intense Raman spectra of pyridine at a silver electrode. *J. Am. Chem. Soc.* **1977**, 99, 5215–5217.

(70) Campion, A.; Kambhampati, P. Surface-enhanced Raman scattering. *Chem. Soc. Rev.* **1998**, 27, 241-250

(71) Camden, J. P.; Dieringer, J. A. Wang, Y.; Masiello, D. J.; Marks, L. D.; Schatz, G. C.; Van Duyne R. P. Probing the structure of single-molecule surface-enhanced Raman scattering hot spots. *J. Am. Chem. Soc.* **2008**, 130, 12616-12617.

(72) Nie, S.; Emory, S. R. Probing Single molecules and single nanoparticles by surface-enhanced Raman scattering. *Science* **1997**, 275, 1102-1106.

(73) Zheng, Y. B.; Payton, J. L.; Chung, C. H.; Liu, R.; Cheunkar, S.; Krishna Pathem, B.; Yang, Y.; Jensen, L.; Weiss, P. S. Surface-enhanced Raman spectroscopy to probe reversibly photoswitchable azobenzene in controlled nanoscale environments. *Nano. Lett.* **2011**, 11, 3447-3452.

(74) Lu, L.; Sun, G.; Zhang, H.; Wang, H.; Xi, S.; Hu, J.; Tian, Z.; and Chen, R. Fabrication of core-shell Au-Pt nanoparticle film and its potential application as catalysis and SERS substrate. *J. Mater. Chem.* **2004**, 14, 1005-1009.

(75) Kneipp, K.; Kneipp, H.; Itzkan, I.; Dasari, R. R.; Feld, M. S. Surface-enhanced Raman scattering and biophysics. *J. Phys.: Condens. Matter* **2002**, 14, R597–R624.

(76) Xie, W.; Schlucker, S. Medical applications of surface-enhanced Raman scattering. *Phys. Chem. Chem. Phys.* **2013**, 15, 5329-5344.

(77) Fang, Y.; Seong, N.; Dlott, D.D. Measurement of the distribution of site enhancements in surface-enhanced Raman scattering. *Science* **2008**, 321, 388-392.

(78) Moskovits, M.; Suh, J.S. Surface selection rules for surface-enhanced Raman spectroscopy: calculations and application to the surface-enhanced Raman spectrum of phthalazine on silver. *J. Phys. Chem.* **1984**, 88, 5526

(79) Moskovits, M. Surface enhanced Raman spectroscopy. *Reviews of Modern Physics* **1985**, 57, 783-826.

(80) Álvarez-Puebla, R. A. Effects of the excitation wavelength on the SERS spectrum. *J. Phys. Chem. Lett.* **2012**, 3, 857-866.

(81) Mcquillan, A. J.; Henpra, D. J.; Fleischmann, M. Raman spectroscopic investigation of silver electrodes. *J. Electroanal. Chem.* **1975**, 65, 933-944.

(82) Wetzel, H.; Gerischer, H.; Pettinger, B. Comparison of the potential dependence of the surface-enhanced Raman effect at colloidal silver particles and bulk silver electrodes. *Chem. Phys. Lett.* **1982**, 85, 187-189.

(83) Zhao, Z.; Cai, Y.; Liao, W. S.; Cremer, P. S. Stepwise molding, etching and imprinting to form libraries of nano-patterned substrates. *Langmuir*, In press.

(84) Tao, F.; Bernasek, S. L. Understanding odd-even effects in organic self-assembled monolayers. *Chem. Rev.* **2007**, 107, 1408-1453.

(85) Nuzzo, R. G.; Allara, D. L. Adsorption of bifunctional organic disulfides on gold surfaces. *J. Am. Chem. Soc.* **1983**, 105, 4481-4483.

(86) Ulman, A. *Thin films: self-assembled monolayer of thiols*, Academic Press: San Diego, CA, 1998.

(87) Bowden, F. P. *The frication and lubrication of solids*, Oxford University Press: London, 1968.

(88) Flink, S.; Van Veggel, F. C. J. M.; Reinhoudt, D. N. Sensor functionalities in self-assembled monolayers. Adv. Mater. 2000, 12, 1315-1328.

(89) Walczak, M. M.; Chung, C.; Stole, S. M.; Widrig, C. A.; Porter, M. D. Structure and interfacial properties of spontaneously adsorbed n-alkanethiolate monolayers on evaporated silver surfaces. *J. Am. Chem. Soc.* **1991**, 113, 2370-2378.

(90) Mcgonigal, G. C.; Bernhardt, R. H.; Thomson, D. J. Imaging alkane layers at the liquid/graphite interface with the scanning tunneling microscope. *Appl. Phys. Lett.* **1990**, 57, 28-30.

(91) Bryant, M. A.; Pemberton, J. E. Surface Raman scattering of self-assembled monolayers formed from 1-alkanethiols: behavior of films at au and comparison to films at Ag. *J. Am. Chem. Soc.* **1991**, 113, 8284-8293.

(92) Yeganeh, M. S.; Dougal, S. M.; Polizzotti, R. S.; Rabinowitz, P. Interfacial atomic structure of a self-assembled alkyl thiol monolayer/Au(111): a sum-frequency generation study. *Phys. Rev. Lett.* **1995**, 74, 1811-1814.

(93) Porter, M. D.; Bright, T. B.; Allara, D. L.; Chidsey, C. E. D. Spontaneously organized molecular assemblies. 4. structural, characterization of n-Alkyl thiol

monolayers on gold by optical ellipsometry, infrared spectroscopy, and electrochemistry. *J. Am. Chem. Soc.* **1987**, 109, 3559-3568.

(94) Strong, L.; Whiteside, G. M. Structures of self-assembled monolayer films of organosulfur compounds adsorbed on gold single crystals: electron diffraction studies. *Langmuir*, **1988**, 4, 546-558.

(95) Wong, S. S.; Takano, H.; Porter, M. D. Mapping orientation differences of terminal functional groups by friction force microscopy. *Anal. Chem.* **1998**, 70, 5209-5212.

(96) Stoliar, P.; Kshirsagar, R.; Massi, M.; Annibale, P.; Albonetti, C.; de Leeuw, D. M.; Biscarini, F. Charge injection across self-Assembly monolayers in organic field-effect transistors: Odd−Even Effects. *J. Am. Chem. Soc.* **2007**, 129, 6477-6484.

(97) Worf, K. V.; Cole, D. A.; Bernasek, S. L.; Low-energy collisions of pyrazine and d6-benzene molecular ions with self-assembled monolayer surfaces: the odd−even chain length effect. *Langmuir*, **2001**, 17, 8254-8259.

(98) Hu, Z. G.; Prunici, P.; Patzner, P.; Hess, P. Infrared spectroscopic ellipsometry of n-alkylthiol (C5-C18) self-ssembled monolayers on gold. *J. Phys. Chem. B.* **2006**, 110, 14824-14831.

(99) Nishi, N.; Hobara. D.; Yamamoto, M.; Kakiuchi, T. Chain-length-dependent change in the structure of self-assembled monolayers of n-alkanethiols on Au(111) probed by broad-bandwidth sum frequency generation spectroscopy. *J. Chem. Phys.* **2003**, 118, 1904-1911.

(100) Pemberton, J. E.; Bryant, M. A.; Sobocinski, R. L.; Joa, S. L. A simple method for determination of orientation of adsorbed organics of low symmetry using surface-enhanced Raman scattering. *J. Phys. Chem.* **1992**, 96, 3776-3782.

(101) Deegan, R. D.; Bakajin, O.; Dupont, T. F.; Huber, G.; Nagel, S. R.; Witten, T. A. Capillary flow as the cause of ring stains from dried liquid drops. *Nature* **1997**, 389, 827-829.

(102) Deegan, R. D. Pattern formation in drying drops. *Phys. Rev. E* **2000** 61, 475-485.

(103) Deegan, R. D.; Bakajin, O.; Dupont, T. F.; Huber, G.; Nagel, S. R.; Witten, T. A. Contact line deposits in an evaporating drop. *Phys. Rev. E* **2000**, 62, 756-765.

(104) Wang, X.; Summers, C. J.; Wang, Z. Large-scale hexagonal-patterned growth of aligned ZnO nanorods for nano-optoelectronics and nanosensor arrays. *Nano Lett.* **2004**, 4, 423-426.

(105) Huang, Z. P.; Carnahan, D. L.; Rybczynski, J.; Giersig, M.; Sennett, M.; Wang, D. Z.; Wen, J. G.; Kempa, K.; Ren, Z. F. Growth of large periodic arrays of carbon nanotubes. *Applied Physics Lett.* **2003**, 82, 460-462.

(106) Mark, J. *Polymer Data Handbook*, Oxford Univ. Press, New York, 1999.

(107) *Elastic Properties and Young Modulus for some Materials The Engineering ToolBox*, Retrieved 2012-01-06.

(108) Wang, W. Polydimethylsiloxane mechanical properties measured by macroscopic compression and nanoindentation techniques. *Graduate School Theses and Dissertations* USF Graduate School, University of South Florida, Tampa, 2011.

(109) Garra, J.; Long, T.; Currie, J.; Schneider, T.; White, R.; Paranjape, M. Dry etching of polydimethylsiloxane for microfluidic systems. *J. Vac. Sci. Technol. A* **2002**, 20, 975-982.

(110) Glocker, D.A.; Shah, S.I. *Handbook of Thin Film Process Technology*, Institute of Physics: Bristol, 1995.

(111) Plettl, A.; Enderle, F.; Saitner, M.; Manzke, A.; Pfahler, C.; Wiedemann, S.; Ziemann, P. Non-close-packed crystals from self-assembled polystyrene spheres by isotropic plasma etching: adding flexibility to colloid lithography. *Adv. Funct. Mater.* **2009**, 19, 3279-3284.

(112) Zhang, H.; Bucknall, D.G.; Dupuis, A. Uniform nanoscopic polystyrene patterns Produced from a microscopic mold. *Nano. Lett.* **2004**, 4, 1513-1519.

(113) Mark, J.E. *Polymer Data Handbook 2nd Edition,* Oxford University Press: Oxford, England, 2009.

(114) Suh, K.Y.; Kim, Y.S.; Lee, H.H. Capillary force lithography. *Adv. Mater.* **2001**, 13, 1386-1389.

(115) Cai, Y.; Zhao, Z.; Chen, J.; Yang, T.; Cremer, P. S. Deflected capillary force lithography. *ACS Nano,* **2012**, 6, 1548–1556.

(116) Mata, A.; Fleischman, J.; Roy, S. Characterization of polydimethylsiloxane (PDMS) properties for biomedical micro/nanosystems. *Biomedical Microdevices*, **2005**, 7, 281-293.

(117) Geldhauser, T.; Ikegaya, S.; Kolloch, A.; Murazawa, N.; Ueno, K.; Boneberg, J.; Leiderer, P.; Scheer, E.; Misawa, H. Visualization of near-field enhancements of gold triangles by nonlinear photopolymerization. *Plasmonics* **2011**, 6, 207-212.

(118) Perentes, A.; Utke, I.; Dwir, B.; Leutenegger, M.; Lasser, T.; Hoffmann, P.; Baida, F.; Bernal, M-P.; Russey, M.; Salvi, J.; Van Labeke, D. Fabrication of arrays of sub-wavelength nano-apertures in an optically thick gold layer on glass slides for optical studies. *Nanotechnology* **2005**, 16, S273–S277.

(119) Poujet, Y.; Salvi, J.; and Baida, F. I. 90% Extraordinary optical transmission in the visible range through annular aperture metallic arrays. *Opt. Lett.* **2007**, 32, 2941-2944.

(120) Poujet, Y.; Roussey, M.; Salvi, J.; Baida, F. I.; Van Labeke, D.; Perentes, A.; Santschi, C.; Hoffmann, P. Super-transmission of light through subwavelength annular aperture arrays in metallic films: spectral analysis and near-field optical images in the visible range. *Photonics and Nanostructures – Fundamentals and Applications* **2006**, 4, 47–53.

(121) Sarrazin, M.; Vigneron, J. P.; Vigoureux, J.-M. Role of Wood anomalies in optical properties of thin metallic films with a bidimensional array of subwavelength holes. *Phys. Rev. B* **2003**, 67, 085415.

(122) Genet, C.; van Exter, M. P.; Woerdman, J. P. Fano-type interpretation of red shifts and red tails in hole array transmission spectra. *Opt. Commun.* **2003**, 225, 331-336.

(123) Hao, F.; Nordlander, P.; Sonnefraud, Y.; Van Dorpe, P.; Maier, S. A. Tunability of subradiant dipolar and Fano-type plasmon resonances in metallic ring/disk cavities: implications for nanoscale optical sensing. *ACS Nano* **2009**, 3, 643-652.

(124) Hao, F.; Nordlander, P.; Burnett, M. T.; Maier, S. A. Enhanced tunability and linewidth sharpening of plasmon resonances in hybridized metallic ring/disk nanocavities. *Physical Review B* **2007**, 76, 245417.

(125) Hu, X.; Wang, T.; Wang, L.; Dong, S. Surface-enhanced Raman scattering of 4-aminothiophenol self-assembled monolayers in sandwich structure with nanoparticle shape dependence: off-surface plasmon resonance condition. *J. Phys. Chem. C* **2007**, 111, 6962-6969.

(126) Huang, Y.; Zhu, H.; Liu, G.; Wu, D.; Ren, B.; Tian, Z. When the signal is not from the original molecule to be detected: chemical transformation of para-aminothiophenol on Ag during the SERS measurement. *J. Am. Chem. Soc.* **2010**, 132, 9244-9246.

(127) Wan, L.; Terashima, M.; Noda, H.; Osawa, M. Molecular orientation and ordered structure of benzenethiol adsorbed on gold(111). *J. Phys. Chem. B* **2000**, 104, 3563-3569.

(128) Nara, J.; Higai, S. Density functional theory investigation of benzenethiol adsorption on Au(111). *J. Chem. Phys.* **2004**, 120, 6705-6711.

(129) Allemand, C. D. Depolarization Ratio Measurements in Raman Spectrometry. *Applied Spectroscopy* **1970**, 24, 348–353.

(130) Moskovits, M.; Dilella, D. P.; Maynard, K. L. Surface Raman spectroscopy of a number of cyclic aromatic molecules adsorbed on silver: selection rules and molecular reorientation. *Langmuir* **1988**, 4, 67-76.

(131) Futamata, M.; Maruyama, Y.; Ishikawa, M. Microscopic morphology and SERS activity of Ag colloidal particles. *Vib. Spectrosc.* **2002**, 30, 17-23.

(132) Jiang, J.; Bosnick, K.; Maillard, M.; Brus, L. Single molecule Raman spectroscopy at the junctions of large Ag nanocrystals. *J. Phys. Chem. B* **2003**, 107, 9964-9972.

(133) Ramin, L.; Jabbarzadeh, A. Odd-even effects on the structure, stability, and phase transition of alkanethiol self-assembled monolayers. *Langmuir*, **2011**, 27, 9748-9759.